Structural and Electrochemical Studies on Metalladeca- and Undecaboranes

Stuart A. Macgregor

Thesis Presented for the Degree
of Doctor of Philosophy
University of Edinburgh
1991

Declaration

Except where specific reference is made to other sources, the work presented in this thesis is the original work of the author. It has not been submitted, in whole or in part, for any other degree. Certain of the results have been published, or have been accepted for publication (see Appendix 4)

Stuart A. Macgregor

To my parents, for all their help and support

"But... you've gotta' have a quote."

K.J.Taylor,1991

Acknowledgements

I would like to thank my supervisors, Dr Alan Welch and Dr Lesley Yellowlees, for all their help, encouragement and enthusiasm throughout the course of this work.

I am also grateful to Dr David Reed for running many n.m.r. spectra and for several useful discussions and comments. I would like to acknowledge the help of Professor C.D.Garner in obtaining the XANES data on the cobalt systems. Thanks also to all the departmental technical staff for their support.

In the lab., life wouldn't have been the same without Kenny-boy, The Pie, Brown, Zoers, Ken and the Wee-Man, and to them and other collegues over the last few years, I would also like to extend my thanks for their help and company.

Finally, I would like to thank the SERC for financial assistance and the Hope Foundation for a bursary.

Abstract

Chapter 1 begins with a review of the development of the ideas now used in the discussion of the electronic structures of cluster compounds. The structure and reactivity of *nido*-$B_{10}H_{14}$ is described, especially with regard to the formation of metalladeca- and undecaboranes. The problem of whether to describe the structures of $MB_{10}H_{12}$ metallaboranes as true *nido*-11-vertex clusters or simply as metal complexes of the *nido*-$[B_{10}H_{12}]^{2-}$ ligand is highlighted. Finally, a review of the electrochemical studies undertaken on boron-containing systems is presented.

Chapter 2 begins with a description of a new method of polyhedral borane analysis, the r.m.s. misfit method. This method is applied to a series of *nido*- and *arachno*-$\{B_{10}\}$ fragments and is shown to distinguish between these two structural forms. A new labelling scheme [B(a) to B(j)] is introduced because of the close structural relationship of these two systems. The structures of three $MB_{10}H_{12}$ metallaboranes, $[(CO)_3CoB_{10}H_{12}]^-$, **9**, $[Pd(B_{10}H_{12})_2]^{2-}$, **11** and $[Pt(B_{10}H_{12})_2]^{2-}$, **10**, are then presented and discussed in terms of the results of r.m.s. misfit calculations between the $\{B_{10}\}$ fragments of these species with the $\{B_{10}\}$ fragments of *nido*-$B_{10}H_{14}$ and *nido*-$[B_{11}H_{13}]^{2-}$. The concept of metal verticity is introduced to quantify the degree of interaction between the metal and borane fragments. For **9**, the borane fragment is found to be *arachno*-$\{B_{10}H_{12}\}^{4-}$ and the metal verticity is 69.1%. This implies a Co^{III} metal centre, a result later supported by a XANES study on a series of cobalt-containing species. The structures of the two *bis*-borane systems and their nickel analogue are compared *via* the r.m.s. misfit method.The borane fragments in these systems are found to be of intermediate structure, between *nido* and *arachno*. The study also shows that as the principle quantum number of the metal valence orbitals increase, so does the metal verticity. An initial comparison with certain cage parameters shows that the B(a)..B(b) non-bonded distance best reflects the results of the r.m.s. misfit calculations.

The results of a series of EHMO-FMO calculations on five metallaborane systems

are presented in *Chapter 3*. These show that the results of the r.m.s. misfit calculations can be understood in terms of the number of orbitals which the metal fragment uses in its interaction with the borane (the orbital contribution of the metal fragment). Thus, the $\{(PMe_2Ph)_3Pt\}^{2+}$ fragment in $(PMe_2Ph)_3PtB_{10}H_{12}$ has an orbital contribution of 3 and the platinum atom a high verticity of 73.1%. In contrast the $\{Cy_3PAu\}^+$ fragment in $[Cy_3PAuB_{10}H_{12}]^-$ has an orbital contribution of 1, and the gold atom a verticity of 13.3%. Between these two extremes a continuum of metallaborane structures is seen. Variation in the B(a)..B(b), B(c)-B(d) and B(h)-B(i) distances in $MB_{10}H_{12}$ metallaboranes can be best understood in terms of the occupancies of the frontier molecular orbitals of the $\{B_{10}H_{12}\}^{2-}$ fragments of these species. In general the B(a)..B(b) distance most closely follows the trend in metal verticities and, of the three criteria above, is therefore the best reflection of the overall nature of the metallaboranes analysed. However, the anomalous structure of $[Me_2TlB_{10}H_{12}]^-$ suggests that a complete understanding of the metallaborane structure may require EHMO-FMO studies.

Chapter 4 gives the results of electrochemical studies on 6,6,6-$(PMe_2Ph)_3$-6-*nido*-RuB_9H_{13}, **19**. At 290K in dichloromethane, this species exhibits a partially reversible two electron oxidation at, relative to Ag/AgCl, +0.97V, and a one electron partially reversible reduction at -1.54V. Bulk electrosynthesis at +1.00V yields several products. One of these is investigated by multinuclear n.m.r. spectroscopy and is believed to be 2-$(PMe_2C_6H_4)$-6,6-$(PMe_2Ph)_2$-6-*nido*-RuB_9H_{12}, **22**. The product of electrosynthesis at -1.75V is characterised by EPR and UV/visible spectroscopy. The preparation and characterisation of two chlorinated derivatives of 19, 2-Cl-6,6,6-$(PMe_2Ph)_3$-6-*nido*-RuB_9H_{12}, **20** and 2,5-Cl_2-6,6,6-$(PMe_2Ph)_3$-6-*nido*-RuB_9H_{11}, **21** are described, including the crystallographic characterisation of **20**. The electrochemical, n.m.r. and UV/visible properties of these species are compared to those of **19** and **22**.

Chapter 5 details gives the results of electrosynthetic studies on $[BTMA]_2[M(B_{10}H_{12})_2]$; M=Ni, **8**, Pd, **11** and Pt, **10**. All three species undergo a partially reversible oxidation but bulk electrolysis leads to decomposition. At 238K in dimethylformamide, $[BTMA]_2$**10** exhibits a one electron, chemically reversible reduction at -1.65V. The characterisation of the product of bulk electrolysis at -1.8V by *in-situ* EPR and UV/visible spectroelectrochemistry is presented. At 290K, the reduction of $[BTMA]_2$**10** affords a new species, thought to be binuclear. The one electron reduction of $[BTMA]_2$**11** is chemically irreversible giving EPR-silent product mixtures. Possible structures of these electrochemically-generated species are discussed in terms of their UV/visible spectra and the results of EHMO calculations on the parent species.

Chapter 6 outlines the experimental procedures and techniques employed in the course of this work. It can be conveniently divided into four parts. 1. Synthetic Methods. 2. Crystallographic Procedures, including details of Data Collection, Structure Solution and Crystal Data. 3. Details and brief background to the EHMO-FMO calculations employed. 4. Electrochemical Techniques and Analysis.

In addition, *Appendix 1*, the results of a semi-quantitatuve analysis of the ^{11}B n.m.r. parameters of $MB_{10}H_{12}$ metallaboranes compared to those of *nido*-$B_{10}H_{14}$ are presented. *Appendix 2* describes the synthesis and molecular structure of 5-(p-cymene)-6-OEt-5-*nido*-RuB_9H_{12}, **24**, prepared from the reaction of 6-(p-cymene)-6-*nido*-RuB_9H_{13} in alcoholic sodium hydroxide

Abbreviations

a.c.	alternating current
AO	atomic orbital
bipy	2-2'bipyridyl
BTMA	benzyltrimethylammonium
COD	1,5-*cyclo*-octadiene
COSY	correlated spectroscopy
Cy	*cyclo*-hexyl
d.c.	direct current
dkt	2-2'bipyridyl ketone
DMBD	2,3-dimethylbutadiene
DMF	*N*,*N*-dimethylformamide
ec	electron transfer/chemical reaction
en	ethylenediamine
e.s.d.	estimated standard deviation
EHMO	extended Hückel molecular orbital
EPR	electron paramagnetic resonance
EPRESISE	electron paramagnetic resonance *in-situ* electrochemistry
EXAFS	extended X-ray absorption fine structure
eV	electron volts
FMO	fragment molecular orbital
HOMO	highest occupied molecular orbital
ICCT	intra-cluster charge transfer
LCAO	linear combination of atomic orbitals
LUMO	lowest unoccupied molecular orbital
Me	methyl
MO	molecular orbital
n.m.r.	nuclear magnetic resonance

OTTLE	optically transparent thin layer electrode
p-cymene	p-[$(Me)_2CH$]-toluene
Ph	phenyl
p.p.m.	parts per million
PSEP	polyhedral skeletal electon pair
PTFE	polytetrafluoroethene
r.m.s.	root mean square
SEP	skeletal electron pair
UV	ultraviolet
VSIE	valence shell ionisation energy
XANES	X-ray absorption near edge spectroscopy

Abbreviations for Specific Compounds

1	*nido*-$B_{10}H_{14}$
2	*nido*-$[B_{11}H_{13}]^{2-}$
3	*nido*-$[B_{10}H_{13}]^{-}$
4	*nido*-6-NCS-$B_{10}H_{13}$
5	*nido*-$[B_{11}H_{14}]^{-}$
6	5,6-μ-(Cy_3PAu)-*nido*-$B_{10}H_{13}$
7	$[PCy_3AuB_{10}H_{12}]^{-*}$
8	$[Ni(B_{10}H_{12})_2]^{2-}$
9	$[(CO)_3CoB_{10}H_{12}]^{-}$
10	$[Pt(B_{10}H_{12})_2]^{2-}$
11	$[Pd(B_{10}H_{12})_2]^{2-}$
12	$[(CO)_3Co(DMBD)]^{+}$
13	$(PMe_2Ph)_2PtB_{10}H_{11}Cl$
14	$(PMe_2Ph)_2PtB_{10}H_{11}(B_{10}H_{13})$
15	$[Me_2TlB_{10}H_{12}]^{-}$
16	$(PMe_2Ph)_2B_{10}H_{12}$
17	$[Zn(B_{10}H_{12})_2]^{2-}$
18	$(PMe_2Ph)_3PtB_{10}H_{12}$
19	6,6,6-$(PMe_2Ph)_3$-6-*nido*-RuB_9H_{13}
20	2-Cl-6,6,6-$(PMe_2Ph)_3$-6-*nido*-RuB_9H_{12}
21	2,5-Cl_2-6,6,6-$(PMe_2Ph)_3$-6-*nido*-RuB_9H_{11}
22	2-$(PMe_2C_6H_4)$-6,6-$(PMe_2Ph)_2$-6-*nido*-RuB9H12
23	6-(p-cymene)-6-*nido*-RuB_9H_{13}
24	5-(p-cymene)-6-OEt-5-*nido*-RuB_9H_{12}

* because of the ambiguous nature of the $\{B_{10}\}$ fragments in $MB_{10}H_{12}$ metallaboranes, no formal nomenclature is adopted for these systems here. The reader is referred to specific areas of the text for a detailed description of these systems

Table of Contents

Figures

The labelling of figures in this work indicates the positions of those atoms discussed in the text only. ORTEP figures are drawn with 50% probability level, with hydrogen atoms given an artificial radius of 0.1Å for clarity. On schematic diagrams where terminal hydrogens have been omitted each boron vertex can be assumed to be bonded to one terminal hydrogen, unless otherwise indicated.

Chapter 1

Introduction

Boron Hydrides and the Rationalisation of Their Structures

The first major contribution to this area came from the work of Alfred Stock and co-workers who isolated a series of boron hydrides, or boranes, of general formula B_nH_{n+m}.[1] Later, as crystallographic data became increasingly available, it was seen that these species adopted structures based on a series of regular polyhedra with a {BH} fragment at each of the vertices. Classification of the borane structures was made in terms of their geometry:

closo, from the Greek meaning closed, used if the borane exhibits the structure of a regular deltahedral polyhedron. An example is the octahedral species $[B_6H_6]^{2-}$

nido, "nest", if the structure is that of a regular polyhedron with one vertex removed, for example $B_{10}H_{14}$. In this species the structure is that of an octadecahedron with the six-connected polyhedral vertex removed.

arachno, "network", for those with two vertices removed from a regular polyhedron. Thus removal of a three-connected vertex from the open face of *nido*-$B_{10}H_{14}$ gives the geometry upon which the structure of the *arachno* borane $[B_9H_{14}]^-$ is based.

Attempts to understand the structure of these and related systems have revolutionised the ways in which chemists think about bonding. The first step towards this understanding was the concept of the multicentre bond. This involved the realisation that the simple covalent, or two centre-two electron bond is simply a specific case of the general situation where linear combination of n atomic orbitals

(AO's) forms n molecular orbitals (MO's), which are either bonding, anti-bonding or non-bonding in character.

This new idea was developed by Lipscomb into his topological approach to the rationalisation of the structures of boranes.[2] This relies heavily on 3-centre 2-electron interactions (either BHB, open three centre BBB or central three centre BBB) to describe the bonding in a borane system and can be employed to discuss probable electronic structures. However, for more symmetrical species and especially for the higher polyhedral boranes, this localised approach breaks down.

To date, the most successful analysis of the structures of the boranes and related species is derived from molecular orbital theory and is encapsulated in the set of rules known as polyhedral skeletal electron pair (PSEP) theory. These rules, first proposed by Wade,[3] exploit the fact that the number of electron pairs used in cluster bonding (known as skeletal electron pairs, SEP's) is equal to the number of bonding interactions resulting from the combination of the AO's contributed by each of the polyhedral vertices. The number of electrons involved in cluster bonding is the sum of those contributed by each vertex plus those from bridging hydrogens (one per bridge) and the extra contribution resulting from the overall charge of the molecule. Dividing this number by two gives the number of SEP's.

This can be simply illustrated by consideration of *closo*- $[B_6H_6]^{2-}$, the structure of which is that of an octahedron with a {BH} fragment at each vertex. Figure 1.1 shows the frontier MO's of such a {BH} fragment. Mixing of the B 2s and $2p_z$ orbitals forms two $2sp_z$ hybrid orbitals, one of which interacts with the hydrogen 1s orbital to give an occupied bonding and an unoccupied anti-bonding combination. The other sp_z hybrid orbital is also occupied and points towards the centre of the octahedron, and is thus termed a radial orbital. The two remaining B 2p orbitals remain unoccupied and lie at a tangent to the cluster surface. In this way each {BH}

vertex contributes 3 orbitals and 2 electrons towards cluster bonding. Linear combination of the six radial orbitals then produces one strongly bonding MO, three weakly anti-bonding MO's and two strongly anti-bonding MO's. The twelve tangential orbitals likewise combine to give six bonding MO's, three weakly anti-bonding MO's and three strongly anti-bonding MO's (see Figure 1.2). Thus seven (or n+1, where n is the number of polyhedral vertices) bonding MO's arise, all of which are filled by the twelve electrons contributed from the six vertices and two from the dianionic nature of the borane. Similar analysis of the structures of *nido* and *arachno* boranes led to the relationships summarised below.

Number of SEP's	Terminology
n+1	*closo*
n+2	*nido*
n+3	*arachno*
n+4	*hypho*

In the same paper, Wade rationalised the structure of $[Ru_6(CO)_{18}]^{2-}$ in a similar way. In this ruthenium cluster each $\{Ru(CO)_3\}$ vertex contributes two electrons and three orbitals to skeletal bonding, in a manner analogous to the {BH} vertices in $[B_6H_6]^{2-}$. Each Ru centre has nine valence orbitals and eight valence electrons. Three two-centre two-electron interactions with the carbonyl ligands reduce the number of available orbitals to six. Three of these are the filled t_{2g} set which are involved in interaction with the π^* orbitals of the carbonyl ligands. Thus only the remaining three orbitals, which are d^2sp^3 hybrids, and two electrons are available for cluster bonding.

Figure 1.1 Fragment Molecular Orbitals of a {BH} Fragment.*

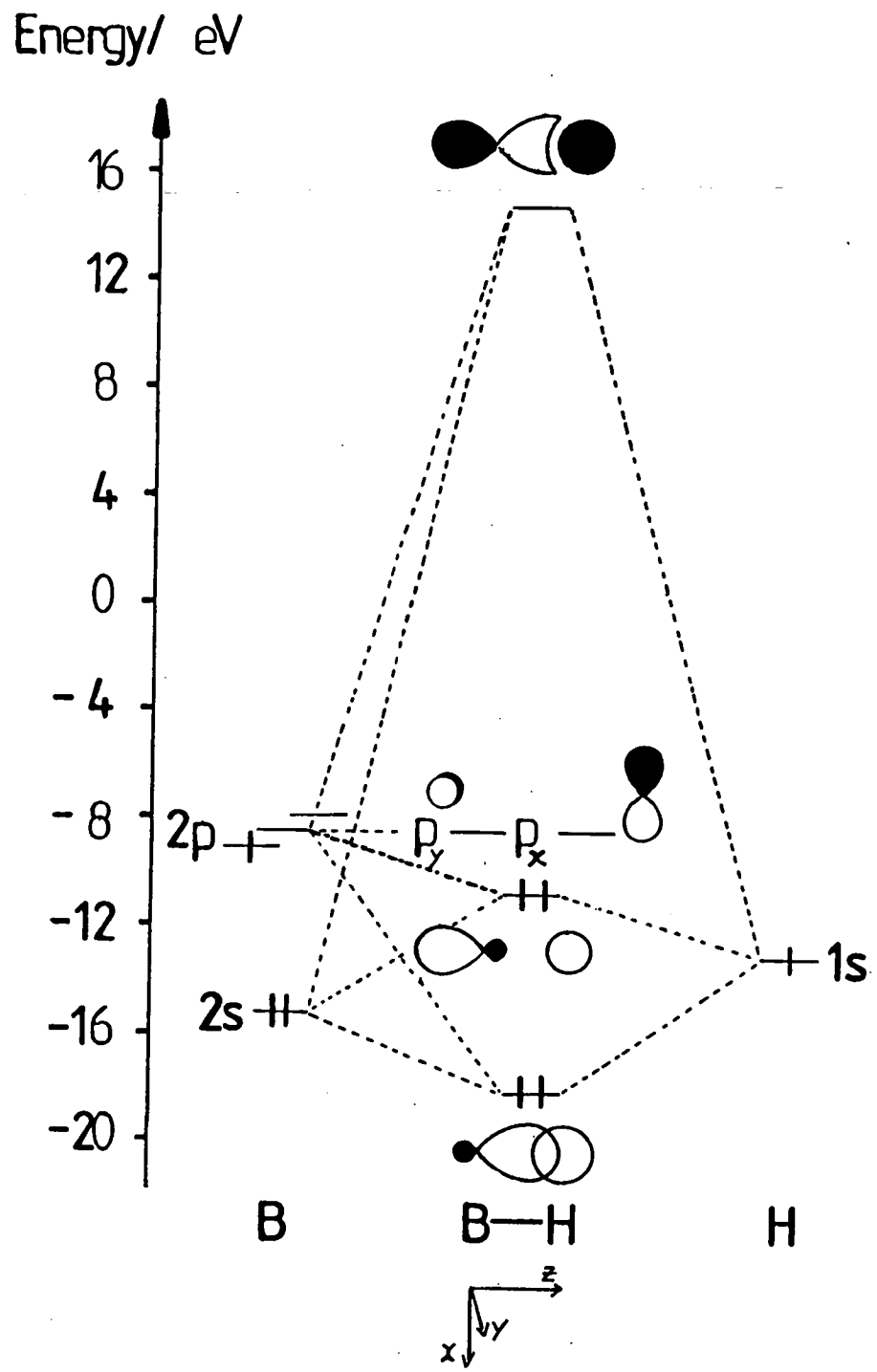

* Diagram derived from an EHMO calculation on a {BH} fragment with B-H=1.15Å.

Figure 1.2 Molecular Orbital Scheme for *closo*-$[B_6H_6]^{2-}$.

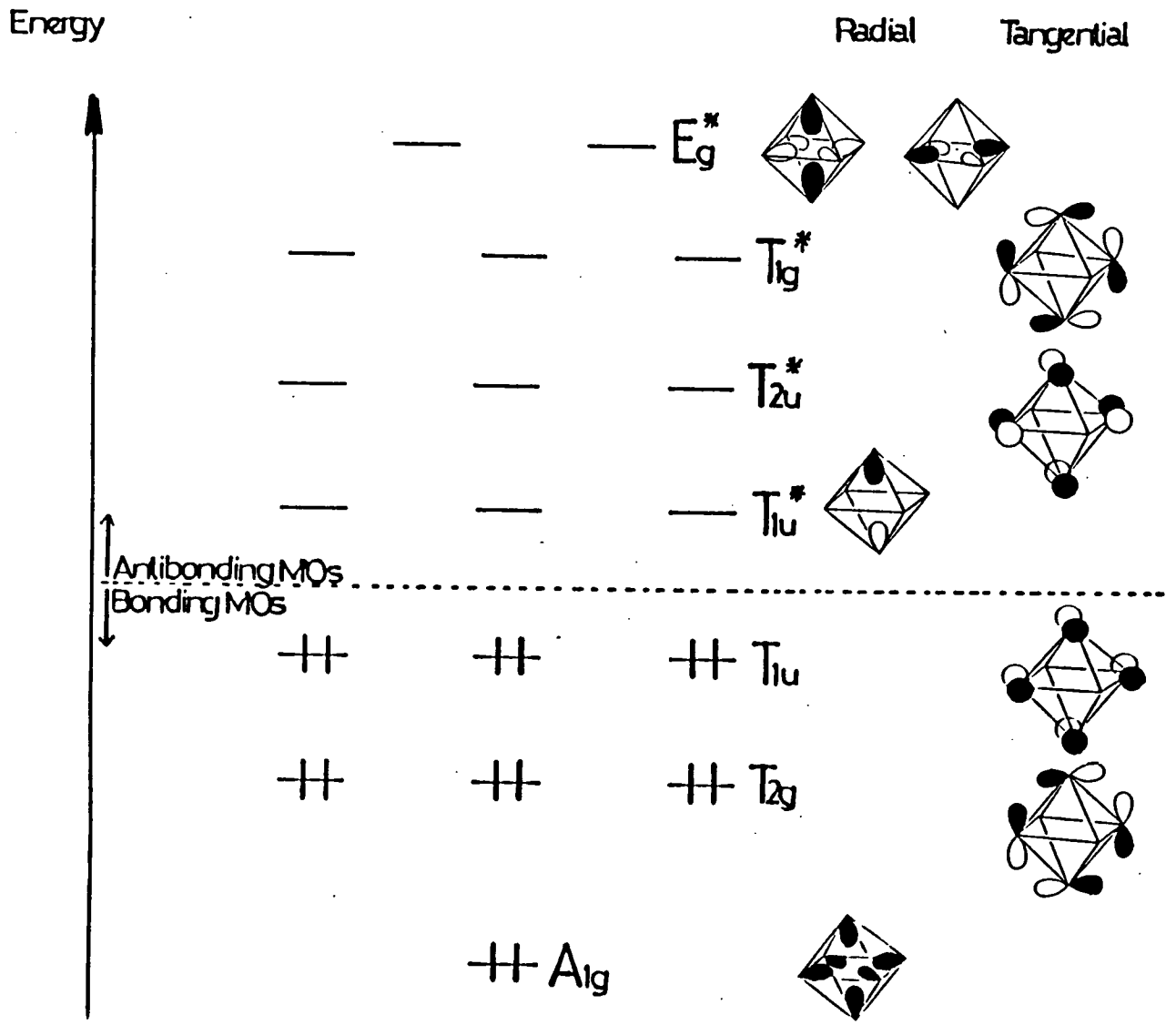

For a transition metal fragment in general, the number of electrons available for cluster bonding is given by the equation

$$v + x - 12$$

where v = number of valence electrons and x = number of electrons contributed by the *exo*-polyhedral ligand. For a main group fragment this takes the form

$$v + x - 2$$

In a similar way to the borane system, the structure of $[Ru_6(CO)_{18}]^{2-}$ contains n+1 SEP's and also exhibits a *closo* geometry.

This successful analysis of the structures of both borane and low-valent transition metal clusters points to the general applicability of the PSEP theory. Also, the noted similarity between a {BH} fragment and a $\{Ru(CO)_3\}$ fragment is central to another important development: the isolobal analogy proposed by Hoffmann.[4]

The Isolobal Analogy

This idea neatly rationalises the ideas implicit in Wade's rules and has provided a link between inorganic and organic chemistry. It states that two fragments are isolobal if the number, symmetry properties, approximate energy and shape of the frontier MO's, and the number of electrons contained within them, are similar. Thus {BH} is isolobal $\{Ru(CO)_3\}$ and both behave similarily in the examples given above, as two electron-three orbital donors. The isolobal analogy is of great use in both rationalising structures and suggesting the existance of new species. This will be evident in the following review of the chemistry of *nido*-decaborane and its derivatives.

Nido-Decaborane and Its Derivatives

Various crystallographic studies on *nido*-decaborane,[5,6] $B_{10}H_{14}$, including the most accurate neutron diffraction study[7], have shown its structure to consist of ten boron atoms each bonded to a terminal hydrogen with four bridging hydrogens in the open face (see Figure 1.3). The structure is that of a *nido* fragment of an octadecahedron; there are 12, or n+2, SEP's involved in cluster bonding arising from the twenty electrons contributed by the ten {BH} vertices and one each from the four bridging hydrogen atoms.

Nido-$B_{10}H_{14}$ is a colourless, volatile, toxic solid. It is readily available, easily handled and purified, all factors which contribute to the large amount of work done on characterising its chemistry and that of its derivatives. This is summarised in Scheme 1.[8-14]

In addition to the reactions shown in Scheme 1, substitution of terminal hydrogen atoms can also occur. These reactions are generally of two types. Firstly, substitution can occur in the open face, usually at B(6) and normally by an electrophilic attack or addition mechanism, as shown below.[15-19]

$$B_{10}H_{14} + MeLi \text{ ---> } B_{10}H_{13}Me$$

$$[B_{10}H_{13}]^- + RI \text{ ---> } B_{10}H_{13}R$$

$$[B_{10}H_{13}]^- + Ph_2PCl \text{ ---> } B_{10}H_{13}PPh_2$$

$$B_{10}H_{12}(SMe_2)_2 + HCl \text{ ---> } B_{10}H_{13}Cl$$

$$B_{10}H_{12}(SMe_2)_2 + H_2SO_4 \text{ ---> } (B_{10}H_{13})_2O$$

Secondly, under Friedel-Craft's alkylation conditions, substitution can occur at the four basal boron atoms. Several series of products of the general form $R_nB_{10}H_{14-n}$ are known (R = Cl[20], Br[21], I[22], n = 1, 2; R = D, n = 1 - 4;[23] R = Me, n = 1 to 4 [24]). With D_2O, further substitution can occur to give $B_{10}D_{14}$.[11]

Figure 1.3 Molecular Structure and Numbering Scheme for *nido*-$B_{10}H_{14}$.

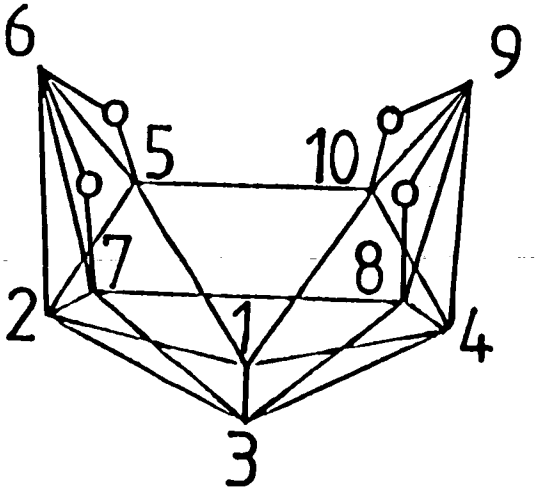

Scheme 1 Reaction Chemistry of *nido*-$B_{10}H_{14}$.

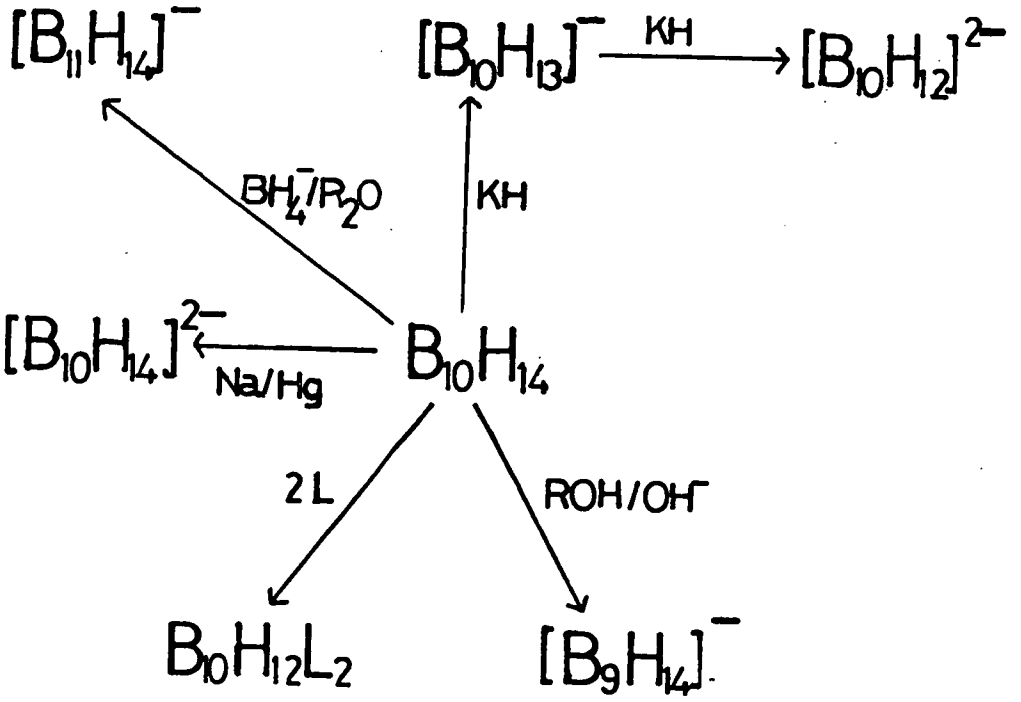

One of the most significant reactions shown in Scheme 1 is the formation of *arachno* borane adducts, $B_{10}H_{12}L_2$, where L is a two electron donor ligand.[25] The crystal structures where L = SMe_2[26], CH_3CN[27] have been determined and exhibit the general structure which is shown in Figure 1.4. The two electrons involved in the B-H_{endo} bonds are included in the electron count as the orbital in which they lie is tangential to the cluster surface. The structure of $[B_{10}H_{14}]^{2-}$ is interpreted in the same way as these adducts with, here, L = H^-.

The further reaction of these species with alkynes is one of the most common routes to *ortho*-carborane and its substituted derivatives.[28] Dehydroboronation of *ortho*-carborane yields *nido*-$[7,8\text{-}C_2B_9H_{11}]^{2-}$, the starting point for much carbametallaborane chemistry first studied by Hawthorne and co-workers in the 1960's.[29]

However, in the context of this work the most significant reactions contained in Scheme 1 are the deprotonation and dehydroboronation of *nido*-$B_{10}H_{14}$. These form the bases of the common syntheses of the metallaboranes studied here: the *nido*-6-metalladecaboranes and those of the general form $MB_{10}H_{12}$. The general area of metallaborane chemistry has been recently reviewed.[30]

Nido-$B_{10}H_{14}$ is a strong acid (pK_a = 2.70) and deprotonation can occur even with relatively weak bases such as NEt_3 to yield $[B_{10}H_{13}]^-$.[31] Further reaction of two equivalents of this species with metal halide complexes provides a common route to the synthesis of $MB_{10}H_{12}$ metallaboranes. Disproportionation of $[B_{10}H_{13}]^-$ generates the $\{B_{10}H_{12}\}^{2-}$ moiety *in-situ*. This then acts as a nucleophile towards the metal centre, displacing the halide ligands. *Nido*-$B_{10}H_{14}$ is therefore a side product of these reactions. For example:[32, 34]

$$(PMe_2Ph)_2PtCl_2 + 2[B_{10}H_{13}]^- \text{---> } (PMe_2Ph)_2PtB_{10}H_{12} + 2Cl^- + B_{10}H_{14}$$

$$IrCO(PPh_3)_2Cl + 2[B_{10}H_{13}]^- \text{---> } [(PPh_3)_2COIrB_{10}H_{12}]^- + Cl^- + B_{10}H_{14}$$

or, where the metal has a further weakly bound ligand, further displacement may occur:[34]

$$CODMCl_2 + 4[B_{10}H_{13}]^- \text{---> } [M(B_{10}H_{12})_2]^{2-} + 2Cl^- + 2B_{10}H_{14} + COD$$

where M = Pd, Pt and COD = 1,5-*cyclo*-octadiene.

Other routes to analogous metallaboranes are through the reaction of *nido*-decaborane with metal alkyls:[35]

$$2Me_3Tl + B_{10}H_{14} \text{---> } [Me_2Tl]^+[Me_2TlB_{10}H_{12}]^- + 2CH_4$$

The dehydroboronation of *nido*-$B_{10}H_{14}$ with alcoholic KOH produces the *arachno* borane $[B_9H_{14}]^-$. The formation of this species is thought to occur in a number of steps.[13]

$$B_{10}H_{14} + OH^- \text{---> } [B_{10}H_{13}]^- + H_2O$$

$$[B_{10}H_{13}]^- + OH^- \text{---> } [B_{10}H_{13}OH]^{2-}$$

$$[B_{10}H_{13}OH]^{2-} + H^+ + 2H_2O \text{---> } [B_9H_{14}]^- + B(OH)_3 + H_2$$

Reaction of *arachno*-$[B_9H_{14}]^-$ with metal halide complexes produces the *nido* -6-metalladecaboranes. This reaction is probably more complicated than the analogous reaction of metal halide complexes with the $[B_{10}H_{13}]^-$ anion as it involves both proton abstraction, probably by halide to form HX, and a rearrangement of the pattern of bridging hydrogens in the open face of the metallaborane (Figure 1.5).

Figure 1.4 Structure of *Arachno*-Borane Adducts, $B_{10}H_{12}L_2$.

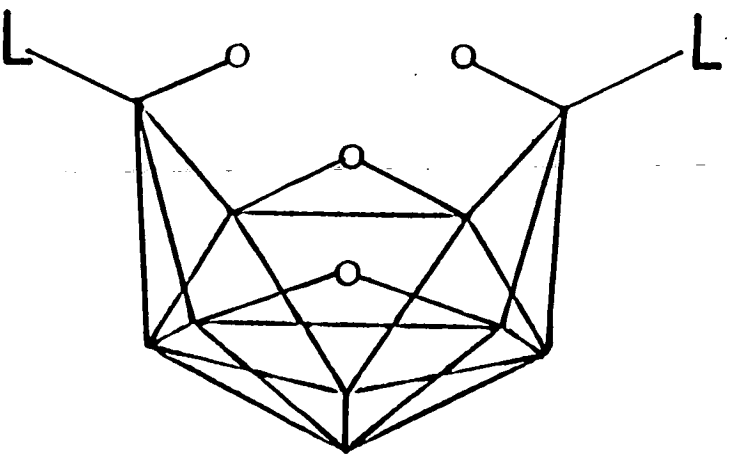

Figure 1.5 Formation and Structure of MB_9H_{13} Metallaboranes from *arachno*-$[B_9H_{14}]^-$.

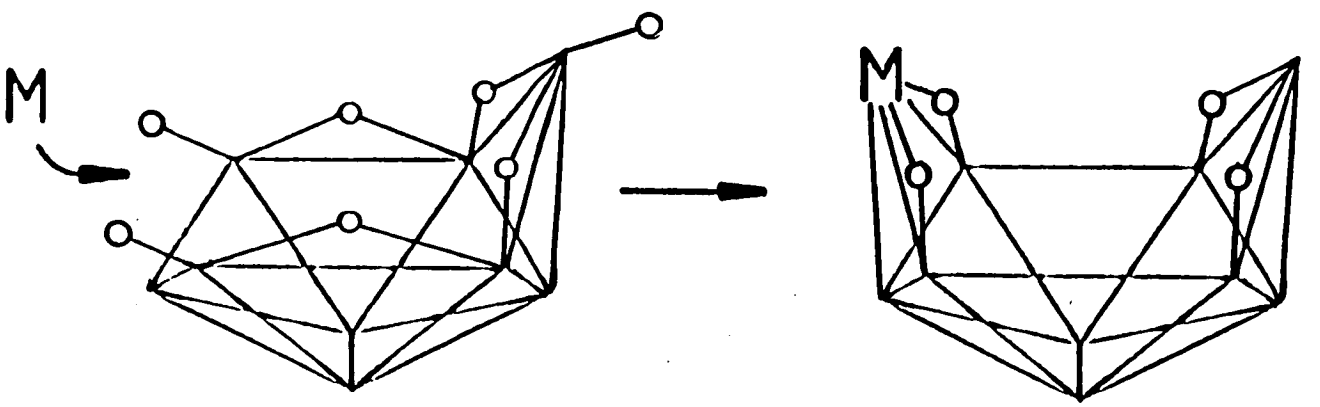

Thus species of the general form $L_nMB_9H_{13}$ are known, but, as yet, only where the $\{L_nM\}$ fragment acts as a two electron-three orbital source, that is, isolobal to {BH}. For example:[36, 37]

$$Mn(CO)_5Br + [B_9H_{14}]^- \text{---> } [(CO)_3MnB_9H_{13}]^- + HBr + 2CO$$

$$(PMe_2Ph)_3RuCl_3 + [B_9H_{14}]^- \text{ --EtOH-> } (PMe_2Ph)_3RuB_9H_{13} + HCl + 2Cl^-$$

Analogous species where the isolobal replacement of {BH} in *nido*-$B_{10}H_{14}$ has occurred at the 5- and 2- positions in the cage are also known.[38, 39]

Structures of Metallaboranes

Nido-6-metalladecaboranes

Figure 1.5 shows the structure of the *nido*-6-metalladecaboranes to be analogous to that of *nido*-$B_{10}H_{14}$, in terms of both the isolobal replacement of a {BH} vertex and of the pattern of the bridging hydrogens in the open face. Further evidence for this analogy can also be found. In *nido*-$B_{10}H_{14}$ the B(5)-B(10) and B(7)-B(8) connectivities are unusually long for a binary borane system, 1.987Å. These long distances are retained in the equivalent connectivities in the *nido*-6-metallaboranes; in $(PMe_2Ph)_3OsB_9H_{13}$ they average 2.045Å and in the wolfraborane, $(PMe_2Ph)_3H_2WB_9H_{13}$, 2.012Å. Comparison of the pattern of ^{11}B n.m.r. chemical shifts of these two metallaboranes and the rhena- and iridaborane analogues (where the metal fragments are $\{(PMe_2Ph)_3ReH\}$ and $\{(PMe_2Ph)_2IrH\}$ respectively) with those of *nido*-$B_{10}H_{14}$ also suggests the electronic structure to be similar in these two types of systems.[37] Finally, application of a new approach to the analysis of cluster systems, the root mean square (r.m.s.) misfit method, confirms the analogy. Using this technique, the positions in space of the nine boron atoms of these four metalladecaboranes are compared to those of the $\{B_9\}$ fragment derived from

nido-$B_{10}H_{14}$ by removal of B(6). The consistently low values obtained in these calculations, between 0.040 and 0.045Å, suggest that the $\{B_9\}$ fragments of the metalladecaboranes are indeed correctly described as *arachno* fragments of an octadecahedron. Therefore the overall geometry of these species is that of a *nido* fragment of an octadecahedron. A detailed description of the working of the r.m.s. misfit method is given in Chapter 2.

$MB_{10}H_{12}$ Metallaboranes

Whereas the interpretation of the structures of the *nido*-6-metalladecaboranes is unambiguous, that of the $MB_{10}H_{12}$ metallaboranes is made difficult by the classification of the $\{B_{10}H_{12}\}$ fragment. This problem is the subject of Chapters 2 and 3 of this thesis. A brief overview is related here.

A true *nido*-11-vertex metallaborane, with the metal in the 7-position, is isostructural to $[B_{11}H_{13}]^{2-}$[40] (see Figure 1.6). In this interpretation, the $\{B_{10}\}$ fragment is correctly described as an *arachno*-$\{B_{10}H_{12}\}^{4-}$ moiety. However, in most crystallographically characterised $MB_{10}H_{12}$ metallaboranes the connectivities equivalent to the B(5)-B(10) and B(7)-B(8) connectivities of *nido*-$B_{10}H_{14}$ retain the unusually long B-B distances observed in the latter. This suggests that the $\{B_{10}\}$ fragment in these metallaboranes is actually more correctly described as *nido*-$\{B_{10}H_{12}\}^{2-}$. Consideration of the geometries of these two borane fragments reveals the difficulty in structural analysis (see Figure 1.7). A *nido* fragment of an octadecahedron has exactly the same pattern of connectivities as an *arachno* fragment of an icosahedron. In addition, the pattern of bridging hydrogens in *nido*-$\{B_{10}H_{12}\}^{2-}$ and *arachno*-$\{B_{10}H_{12}\}^{4-}$, derived respectively from *nido*-$B_{10}H_{14}$ and *nido*-$[B_{11}H_{13}]^{2-}$, is the same, and is that seen in the $MB_{10}H_{12}$ metallaboranes.

Figure 1.6 Structure and Numbering Scheme for *nido*-$[B_{11}H_{13}]^{2-}$ and a True *nido*-7-Metallaundecaborane.

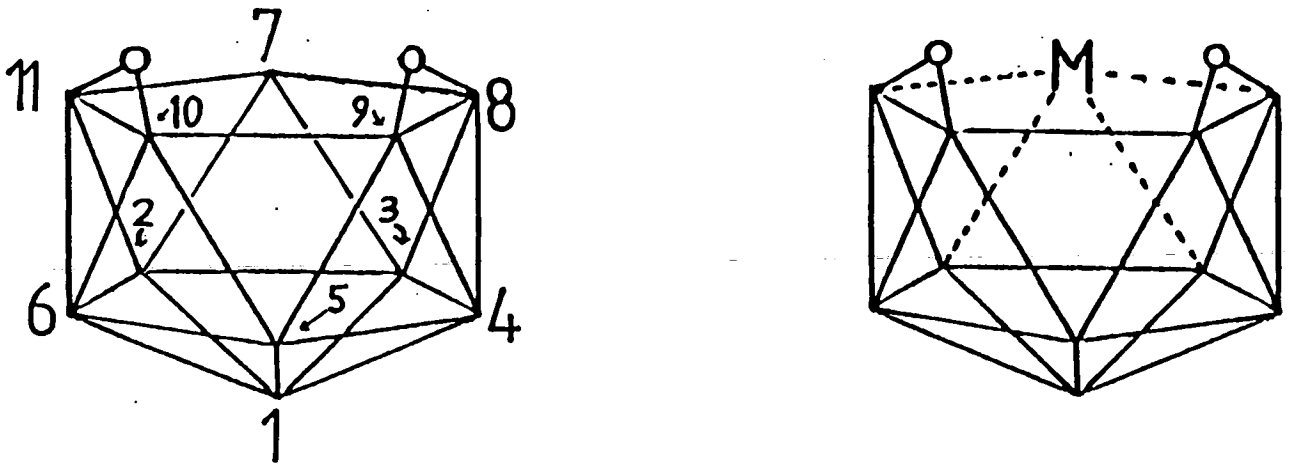

Figure 1.7 Derivation of $\{B_{10}\}$ Fragments from Parental *Closo*-Polyhedra.

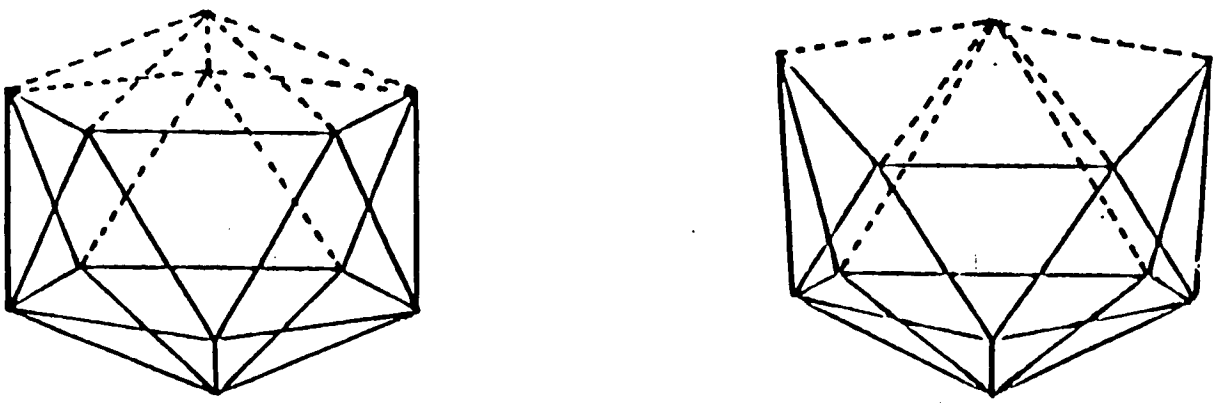

icosahedron. octadecahedron

Figure 1.8 Schlegel Diagrams Representing Different Binding Modes of the $\{B_{10}H_{12}\}$ Fragment.

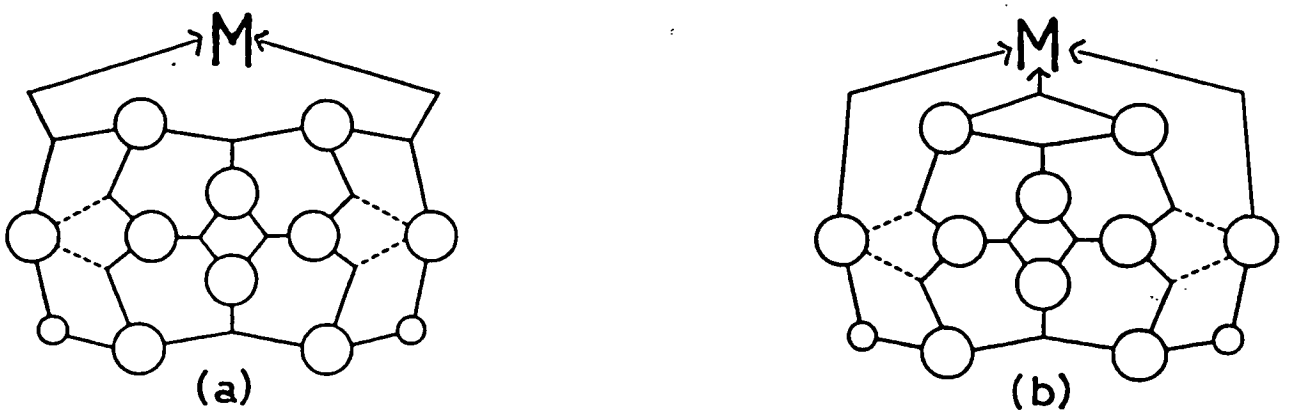

In his recent review,[30] Kennedy makes a distinction between those $MB_{10}H_{12}$ metallaboranes featuring main group metals and those featuring transition metals. This classification is made in terms of the number of orbitals donated to the $\{B_{10}\}$ fragment by the metal fragment. In this analysis a main group metal fragment makes a two electron-two orbital contribution. Bonding between the metal fragment and the borane takes place via two three centre-two electron interactions (see Figure 1.8a). The borane is described as an η^4, bidentate *nido*-$[B_{10}H_{12}]^{2-}$ ligand. For transition metal fragments three orbitals and two electrons are donated and, with significant back donation from metal to borane, the $\{B_{10}\}$ fragment is described as a tridentate, η^4 *arachno*-$[B_{10}H_{12}]^{4-}$ moiety (see Figure 1.8b).

The bases of Kennedy's classification of the $MB_{10}H_{12}$ metallaboranes are the variation of bond lengths within the borane fragment and the ^{11}B n.m.r. parameters. The validities of these approaches are discussed in Chapter 2.

Implications of Structure on Chemical Reactivity

As described above, the structures of the *nido*-6-metalladecaboranes can best be understood in terms of the replacement of {BH} by isolobal metal fragments. This begs the question as to what extent the chemistry of these *nido*-6- metalladecaboranes will resemble that of *nido*-$B_{10}H_{14}$; how much relevance does the isolobal analogy have on the chemistry of these isostructural species? One example of the similar reactivity of these two type of systems is given below:[41]

$$(PPh_3)_2HIrB_9H_{13} + 2KH + (PMe_3)_2PtCl_2 \rightarrow (PPh_3)_2HIrB_9H_{11}Pt(PMe_3)_2 + 2KCl + 2H_2$$

This is analogous to the deprotonation of *nido*-$B_{10}H_{14}$ and further reaction with $(PMe_2Ph)_2PtCl_2$ to give $(PMe_2Ph)_2PtB_{10}H_{12}$. In addition to this, could these, as yet unknown, reactions of the *nido*-6-metalladecaboranes be possible?

$$L_nMB_9H_{13} \text{ -}OH^-/EtOH\text{--> } [L_nMB_8H_{13}]^- \text{ -}\{L_nM\}\text{--> } (L_nM)_2B_8M_{12}$$

or,

$$L_nMB_9H_{13} \text{ -Na/Hg--> } [L_nMB_9H_{13}]^{2-}$$

The first of these proposed reactions suggests a route to *nido*-6,9-$M_2B_8H_{12}$ metallaboranes of which only one example is known: $(C_5Me_5)_2Co_2B_8H_{12}$.[42] This is made in very low yield (<1%) from the reaction of $CoCl_2$ with $[B_9H_{14}]^-$ and $Li^+[C_5Me_5]^-$. The pattern of bridging hydrogens in this species is the same as that exhibited in *nido*-$B_{10}H_{14}$. In the same reaction and in similar yield, the 5,7-isomer is also formed, along with $[C_5Me_5]CoB_9H_{13}$, the major product. However, many *arachno*-6,9-$M_2B_8H_{10}$ metallaboranes are known where M is a two electron-two orbital donor, such as $\{(PMe_2Ph)_2Pt\}$ or $\{SCSNEt_2Au\}^+$, and the structure is based on that of *arachno*-$[B_{10}H_{14}]^{2-}$. These species are formed from the reaction of *arachno*-MB_8H_{12} metallaboranes with a further equivalent of the appropriate metal halide complex. Examples are known where M_2 = Pt_2, PtPd, PtIr, PtAu and Au_2.[43-47] It is interesting to note that the formation of the nine-vertex *arachno* species usually occurs from the reaction of a metal halide complex with *arachno*-$[B_9H_{14}]^-$. A possible mechanism for this reaction may be the formation of a transient *nido*-10 vertex species, which then loses a {BH} vertex to give the *arachno*-MB_8 product. This preference for metal fragments which act as two orbital donors for the *arachno* MB_8 geometry and for those contributing three orbitals preferring the *nido* -MB_9 geometry is interesting and certainly suggests further investigation.

The reduction of a *nido*-6-metalladecaborane, either chemically or electrochemically, to a metallaborane analogue of *arachno*-$[B_{10}H_{14}]^{2-}$ has yet to be observed.

These ideas take the isolobal analogy to its extreme: the assumption is that isolobal replacement of {BH} with a metal fragment will not significantly alter the chemical reactivity of the system. Clearly, some changes in reactivity will be encountered, due both to the steric bulk of the metal fragments and the changes in electronic structure which, although the experimental evidence described above suggests may be small, will still be present.

Electrochemical Studies on Boron-Containing Compounds

The rationalisation of the structures of metallaboranes in terms of the number of SEP's used in cluster bonding immediately suggests that oxidation or reduction of these species may be a way to induce structural change. One known example of such a process is the reduction of *nido*-$B_{10}H_{14}$, and in general this principle may be shown in the following way:

$$\textit{closo} \overset{2e}{\rightleftharpoons} \textit{nido} \overset{2e}{\rightleftharpoons} \textit{arachno} \overset{2e}{\rightleftharpoons} \textit{hypho}$$

In the case of *nido*-$B_{10}H_{14}$ the "predicted" structural change from *nido* to *arachno* is seen.[48] However, despite this promising example, very few detailed electrochemical studies have been carried out on other borane or metallaborane systems. The majority of the work in this area has been done on carbametallaboranes.[49, 50]

Carbametallaboranes

The electrochemical studies carried out on the carbametallaboranes have been dominated by the analogy between metal complexes of the cyclopentadienyl anion, $[C_5H_5]^-$ (Cp^-), and the $[7,8\text{-}C_2B_9H_{11}]^{2-}$ dianion. Although it is difficult to gauge the relevance of specific data from these studies to any subsequent study of metallaboranes, some general points of interest do emerge from the body of

electrochemical data in the literature.

In comparison with its metallocene analogue, a carbametallaborane is generally easier to oxidise by approximately 0.5V. This shows the carbametallaboranes to be better at stabilizing high metal oxidation states, a fact which is usually attributed to the higher charge on the $[C_2B_9H_{11}]^{2-}$ ligand. Indeed, a recent study on a monoanionic carbaborane analogue of Cp^-, $[7,8\text{-}C_2B_9H_{10}SMe_2]^-$, found that the one-electron oxidation of $(C_2B_9H_{10}SMe_2)_2Fe$ occurred, versus Ag/AgCl, at +0.57V.[51] The analogous ferrocene/ferrocinium couple occurs at +0.55V. The importance of the charge of the ligand may also be seen in the metallaborane systems to be discussed in this work, where the borane fragment has a formal charge of -2 or -4. The carbametallaboranes are typified by $(C_2B_9H_{11})_2Ni$ which exhibits three reversible one-electron reductions to $[(C_2B_9H_{11})_2Ni]^{3-}$.[52] Such formal cage reduction should, in terms of the discussion above, cause an opening of the *closo* cage geometries of these species. However such a gross structural change is unlikely to be occurring, given the reversible nature of the observed electrochemical waves. A more likely scenario, especially in the highly reduced forms of these carbametallaboranes, is slippage of the metal centre relative to the carbaborane bonding face. This is well documented in non-reduced species of this type involving several late transition metal fragments.[53] In the context of the observed electrochemistry, this, relatively small, structural change must be concomitant with, or occur rapidly after, the electroreduction, implying a low activation barrier to the slippage of the metal centre. It also strongly implies that these reductive processes are primarily metal based.

Also, some studies have been carried out on the effect of substitution of the carbaborane cage on the position of the redox potential. The best example of this is the comparison of the one electron (formally $Co^{II/I}$) reduction of $[(C_2B_9H_{11})_2Co]^{2-}$[52] and the tri-bromo analogue $[(C_2B_9H_8Br_3)_2Co]^{2-}$.[54] In the former, this process occurs at -2.52V. The effect of substitution is to cause a positive shift in this potential to

-1.52V. This certainly shows the degree of control which may potentially be exerted on metallaboron systems by cage substitution.

Finally, although the electrochemical characterisation of many carbametallaborane systems has been performed, very little work has been done in pursuing the nature of the redox-synthesised products, either by bulk electrosynthesis or by the action of chemical oxidants or reductants. One example of such a chemical synthesis is the oxidation of the nine vertex carbacobaltaborane, $[CpCoCB_7H_8]^-$, with $FeCl_3$ to give a neutral, relatively air stable, product.[55] However further data on the nature of this product are not available.

Boranes

The number of electrochemical studies on boranes containing more than one B atom are relative few. In the presence of donor ligands, L (e.g. CH_3CN or dimethylformamide, DMF), $[B_3H_8]^-$[56] and $[B_9H_{14}]^-$[57] both undergo a one electron irreversible oxidation to form adducts of the type B_3H_7L and $B_9H_{13}L$ with evolution of H_2 gas.

An example of an electrochemically induced structural change occurs in the reduction of *arachno*-$B_{10}H_{12}(CH_3CN)_2$.[58] This exhibits an irreversible two electron oxidation with E_p at +0.75 (Pt working electrode, versus $Ag/AgNO_3$). Electrosynthesis at +0.9V gives a mixture of products, a major constituent of which is $B_{10}H_{10}(CH_3CN)_2$. Thus the oxidation, at least in part, procedes as:

$$B_{10}H_{12}(CH_3CN)_2 \text{ ---> } B_{10}H_{10}(CH_3CN)_2 + 2H^+$$

a formal *arachno* to *nido* oxidation.

The most extensively studied borane system is *nido*-$B_{10}H_{14}$.[48, 59, 60] On paper the

reduction of this species is simple:

$$B_{10}H_{14} + 2e \text{ ---> } [B_{10}H_{14}]^{2-}$$

However, detailed study of this reduction shows it to be mechanistically complex.

At the dropping mercury electrode, using 1,2-dimethoxyethane as solvent, $B_{10}H_{14}$ exhibits an electrochemically reversible one electron reduction at -1.54V. However the product rapidly disproportionates:[48]

$$B_{10}H_{14} + e \text{ ---> } [B_{10}H_{14}]^{-}$$
$$2B_{10}H_{14}^{-\cdot} \text{ ---> } [B_{10}H_{13}]^{-} + [B_{10}H_{15}]^{-}$$

Further reduction of $[B_{10}H_{13}]^{-}$ to $[B_{10}H_{13}]^{2-}$ then occurs once again with disproportionation of the product. This results in a second polarographic wave at -2.75V.[60]

$$[B_{10}H_{13}]^{-} + e \text{ ---> } [B_{10}H_{13}]^{2-}$$
$$2[B_{10}H_{13}]^{2-} \text{ --->} [B_{10}H_{12}]^{2-} + [B_{10}H_{14}]^{2-}$$

Further reaction of $[B_{10}H_{14}]^{2-}$ with $B_{10}H_{14}$ and the reaction of $[B_{10}H_{15}]^{-}$ with $[B_{10}H_{12}]^{2-}$ regenerates $[B_{10}H_{13}]^{-}$ and over longer reaction times the formal *nido* to *arachno* reduction goes to completion.

The implications of the above mechanism for the analogous reduction of *nido*-6-metalladecaboranes are unclear. The suggestion is that analogous metallaborane intermediates will need to be formed if a similar reduction is to occur, and how accessible such species may be is uncertain.

Metallaboranes

The amount of electrochemical data available on metallaboranes is extremely limited. A number of small metallaboranes have been synthesised at sacrificial electrodes,[61] but from the point of view of the synthesis of structurally-altered metallaboranes, a review of the literature is fruitless. A number of *closo*-nickelaboranes have been studied, all of which feature formal Ni^{IV} centres and consequently are dominated by what have been attributed to metal-based reductive processes.[62] How valid even this assumption is, in a highly delocalised metallaborane system, is a point of debate. No following work-up on the nature of the reduced products has been reported. One of the few *nido* species to be studied, $[Ni(B_{10}H_{12})_2]^{2-}$,[63] exhibits a chemically irreversible oxidation, although no coulometric details were given. However, isolation of the product of this oxidation may be of interest; the irreversible nature of the chemical process occurring upon electron transfer implies a structural change. Application of Wade's rules would predict a closure of the cage structure.

It seems, therefore, that the field of metallaboron compounds and especially metallaboranes has great potential for electrochemical study. Possible areas of study could be the isolation of electrochemically generated species, the study of substituent effects at the borane cage and the more fundamental investigation into electron transfer rates.

Chapter 2

The R.m.s. Misfit Method and Analysis of $MB_{12}H_{10}$ Structures

The R.m.s. Misfit Method

The problem of the structure of the $\{B_{10}H_{12}\}$ fragment of $MB_{10}H_{12}$ metallaboranes can be simply envisaged by comparison of the structures of the parental *closo* boranes $[B_{12}H_{12}]^{2-}$ and $[B_{11}H_{11}]^{2-}$. Removal of two adjacent BH^{2+} vertices from the former and one from the latter gives two ten vertex species *arachno*-$\{B_{10}H_{10}\}^{6-}$ and *nido*-$\{B_{10}H_{10}\}^{4-}$. The $\{B_{10}H_{12}\}$ moiety can be generated from both of these experimentally unknown species to give two ten vertex boranes in which the pattern of connectivities is exactly the same and the variation in geometry is only slight . The important difference is that the *arachno* species has one extra pair of electrons involved in skeletal bonding. The question that the first part of this thesis addresses is to which of these two extreme cases are $\{B_{10}\}$ moieties in the $MB_{10}H_{12}$ metallaboranes more correctly related.

These two $\{B_{10}H_{12}\}$ species are best known indirectly within the framework of other boranes: addition of two bridging protons onto the open face of *nido*-$\{B_{10}H_{12}\}^{2-}$ generates *nido*-$B_{10}H_{14}$. Similarily, *arachno*-$\{B_{10}H_{12}\}^{4-}$ is observed as a fragment of both *nido*-$[B_{11}H_{13}]^{2-}$ and *nido*-$[B_{11}H_{14}]^{-}$. Figure 2.1 shows the two numbering schemes conventionally adopted for these two classes of experimentally known species. Replacement of B(7) with a metal fragment in the *nido*-icosahedral 11-vertex borane produces the accepted numbering for an ideal *nido*-icosahedral metallaborane. It is clear that comparison of the two, superficially similar, $\{B_{10}H_{12}\}$

fragments contained within these structures is potentially confusing. Also, the adoption of one of these conventions naturally prejudices any discussion of structure. For these reasons, throughout this work a new non-prejudicial scheme will be used for labelling the borane fragment. This is shown in Figure 2.2.

This Chapter will begin by discussing the reasons for using, and the mechanism and preliminary testing of, a new method of polyhedral borane analysis; the root mean square (r.m.s.) misfit method. This method will then be applied to a number of newly crystallographically characterised $MB_{10}H_{12}$ metallaboranes and the implications of the results obtained examined.

The Need for the R.m.s. Misfit Method

As previously described, the pattern of connectivities in *arachno*-$[B_{10}H_{12}]^{4-}$ and *nido*-$[B_{10}H_{12}]^{2-}$ is exactly the same, the important distinction being that the former is a fragment of an icosahedron containing 13 SEP's and the latter a fragment of an octadecahedron containing 12 SEP's. Despite this subtle difference, analysis of the nature of the borane fragment in $MB_{10}H_{12}$ metallaboranes has mainly focused on the length of certain connectivities within the borane framework and a non-quantitative comparison of ^{11}B n.m.r. parameters with those of *nido*-$B_{10}H_{14}$, **1**. The connectivities most frequently used in cage analysis are B(h)-B(i) and B(c)-B(d).

Figure 2.1 Numbering Schemes for a *Nido*-10-Vertex System (1) and a *Nido*-11-Vertex System (2).

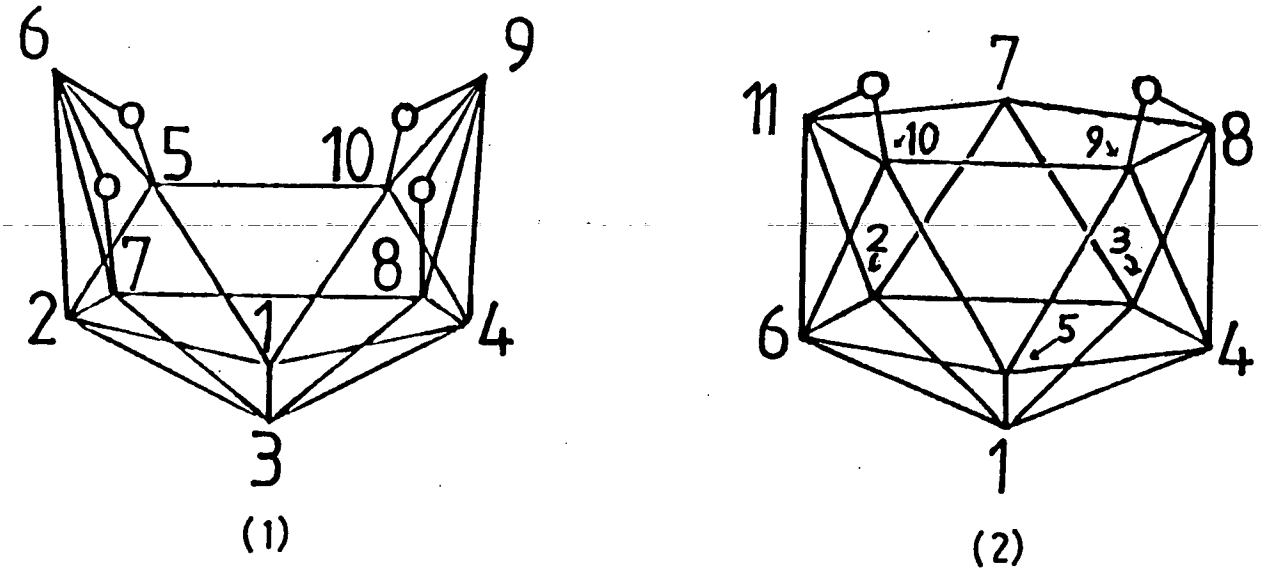

Figure 2.2 Non-Prejudicial Labelling Scheme Adopted Throughout This Work.

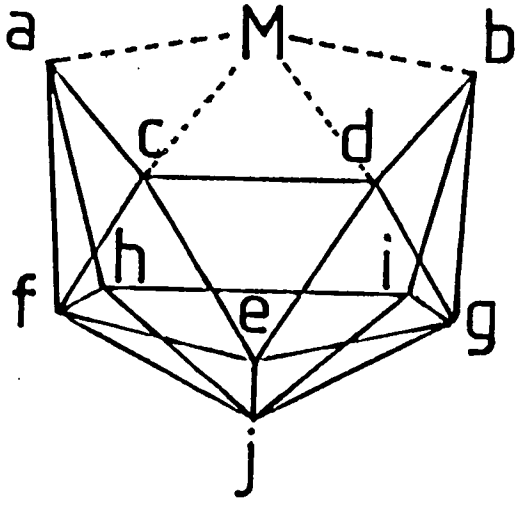

There are several problems with these approaches. Firstly, by selecting only two boron-boron connectivities as criteria for the nature of the cage, the atomic positions of the remaining six boron atoms are effectively being ignored. Given that the PSEP theory describes the total geometries of borane and heteroborane polyhedra, an analysis taking account of the variation in position of all ten boron atoms, as the r.m.s. misfit method does, would seem more appropriate.

Secondly, a wide range is observed for the B(h)-B(i) and B(c)-B(d) distances in $MB_{10}H_{12}$ species. These are relatively short in the platinaborane, $(Me_2PhP)_2PtB_{10}H_{12}$,[32] 1.976Å and 1.818Å respectively. At the other extreme is the thallaborane, $[Me_2TlB_{10}H_{12}]^-$,[64] where the corresponding distances are 2.06Å and 1.97Å. In between a whole range of intermediate distances are observed for these connectivities in the other known, structurally characterised, metallaboranes of this type. These distances compare with 1.987Å in **1**,[7] where these two connectivities are equivalent, and with 1.820Å [B(h)-B(i)] and 1.770Å [B(c)-B(d)] in the *arachno* $\{B_{10}\}$ fragment formed here, and in the subsequent discussion, by the removal of the BH^{2+} unit not associated with any bridging hydrogen atoms from the open face of *nido*-$[B_{11}H_{13}]^{2-}$, **2**.[40] Accordingly, the platinaborane has been interpreted as a *nido*-icosahedron involving an *arachno*-$\{B_{10}\}$ fragment, and the thallaborane as a four coordinate tetrahedral thallium(III) complex involving two methyl ligands and a *nido*-$[B_{10}H_{12}]^{2-}$ ligand. It is clear that the B(c)-B(d) distances in the metallaboranes lie within the extremes defined by the equivalent distances in the appropriate boranes. However, the considerably longer B(h)-B(i) connectivities in the metallaboranes lie mostly outside the range of those of the boranes and the relationship between these two classes of compounds, in this respect, is not immediately apparent. Thus, the platinaborane exhibits an "*arachno*-like" B(c)-B(d) distance and a "*nido*-like" B(h)-B(i) distance. The B(c)-B(d) distance in the thallaborane is certainly reminiscent of that of **1**, but how does one account for the very long B(h)-B(i)

distance?

Here we see the difficulties with selective connectivity analysis: which connectivity best reflects the overall cage geometry, and can the effects of other distances within the borane framework be ignored? Furthermore, most of these specific distances in metallaboranes of this type are of intermediate length, making analysis, in these terms, even more confused.

Thirdly, use of ^{11}B n.m.r. spectroscopy as a tool to assign the nature of the borane cage in $MB_{10}H_{12}$ species has mostly been limited to a qualitative comparison with **1**.[65] At the simplest level, in terms of molecular symmetry and connectivity pattern, a *nido*-$[B_{10}H_{12}]^{2-}$ cage is equivalent to an *arachno*-$[B_{10}H_{12}]^{4-}$ cage, so no obvious change in the ^{11}B n.m.r. properties will be observed. A deeper analysis of individual ^{11}B chemical shifts *via* ^{11}B-^{11}B COSY (correlated spectroscopy) and selectively decoupled-boron proton n.m.r. spectroscopy has, as yet, shed little light on the factors which determine the chemical shift of a ^{11}B nucleus. In specific cases[66], empirical correlations between structure and chemical shift have been made, as well as the potentially useful observation that the order of chemical shifts in **1** is exactly the reverse of that of *arachno*-$[B_{10}H_{14}]^{2-}$.[67] However the precise relationship between electronic structure and chemical shift is still not clear.

In this case, where the cage structures are so similar and yet electronically distinct, the use of ^{11}B n.m.r. shifts to differentiate between the possible roles of the $\{B_{10}\}$ fragment must be treated with caution. For example, Greenwood *et al.*[32] cite the variation in the chemical shift of the B(c) and B(d) atoms in $(Me_2PhP)_2PtB_{10}H_{12}$, $[Ni(B_{10}H_{12})_2]^{2-}$ and $[Me_2TlB_{10}H_{12}]^-$ compared to those in **1** as evidence for an increased 3-centre M-B(c)-B(d) interaction, and, by implication, increased *nido*-icosahedral character in the former two structures. Table 2.1 below shows that in the platinum and nickel species, these boron atoms are deshielded relative to **1**,

whereas they show increased shielding in the ^{11}B n.m.r. spectrum of the thallaborane[68].

Table 2.1: N.m.r. Parameters (p.p.m.) of Metallaboranes and *nido*-$B_{10}H_{14}$.

System	B(a,b)	B(c,d)	B(j)	B(e)	B(h,i)	B(f,g)
[a]$(PMe_2Ph)_2PtB_{10}H_{12}$ [32]	+9.3	+15.1	+16.1	+2.3	-3.1	-26.9
[b]$[Ni(B_{10}H_{12})_2]^{2-}$	+11.6	+10.9	+8.7	+1.0	-3.5	-21.1
[c]$[Me_2TlB_{10}H_{12}]^-$ [68]	+8.2	-3.1	-2.8	+3.0	-4.7	-31.7
[b]$B_{10}H_{14}$ [65]	+11.5	-0.2	+11.5	+11.5	-0.2	-35.3

a: in CD_2Cl_2; b: in CD_3CN; c: in $(CD_3)_2CO$

The conclusion reached, within these premises, appears valid. However, the analysis of n.m.r. parameters has been rather limited in that it is once again very selective. Inspection of the other ^{11}B n.m.r. parameters of these species, also displayed in Table 2.1, shows that, relative to **1**, in all three cases B(e), B(h) and B(i) all experience increased shielding, B(a) and B(b) remain fairly constant (although if anything experience increased shielding) and B(f) and B(g) are more strongly deshielded in the nickel and platinum compounds. However, whilst B(j) is deshielded in the platinaborane, this boron atom is more shielded in the nickel and thallium species. There is no obvious trend in these data when they are viewed as a whole. To follow the argument of these authors, the assumption must once again be made that one local variation in the cage is diagnostic of an overall change in the cage structure.

In Appendix 1 of this work we attempt a semi-quantitative analysis of ^{11}B n.m.r. parameters in comparison to **1**, in which all ten ^{11}B resonances are taken into account.

Mechanics of the R.m.s. Misfit Method.

R.m.s. misfit calculations are performed with IDEAL, a subroutine inlaid in the program CALC.[69] This programme was designed to enable the comparison of structurally similar groups, and finds the closest fit between two sets of coordinates containing at least three similarily-numbered atoms common to both sets. The r.m.s. misfit calculations used in this study require as input the positions of two sets of ten boron atoms, either in orthogonalised Å space or as fractional coordinates with unit cell data, from a crystal structure.

An initial fit is achieved by conversion of the first set of coordinates to orthogonalised Å units with the origin at the centre of gravity. The model is then rotated to make the atom furthest from the origin lie on the z-axis and the atom furthest from the z-axis lie in the xz plane to positive x. The second set is then treated in a similar fashion with the corresponding atoms defining the positive z and x directions. The best fit is found by an iterative least squares procedure, rotating the second set around the x, y and z axes, minimising $\Sigma\delta_i^2$, where δ_i is the distance between the corresponding members of an atom pair. The r.m.s. misfit between two sets of n atoms, defined as the square root of $[\Sigma_i(\delta_i^2)/n]$, is then calculated. This typically gives a value of less than 1Å for structurally similar groups. Individual misfits for each atom pair are also obtained as output.

The result of this approach is one number which, in principle, is a measure of the overall geometrical similarity between two borane fragments. To investigate whether this method can distinguish between *arachno* and *nido* $\{B_{10}\}$ fragments it was applied to a number of borane systems of unambiguous structure. The systems studied were **1**, *nido*-$[B_{10}H_{13}]^-$,[70] **3**, *nido*-$(SCN)B_{10}H_{13}$,[71] **4**, two *arachno*-$\{B_{10}\}$ fragments derived from **2** and from *nido*-$[B_{11}H_{14}]^-$,[72] **5**, and the auraborane, 5,6-μ-(Cy_3PAu)-*nido*-$B_{10}H_{13}$ (Cy = *cyclo*-C_6H_{11}), **6**.[73] A feature of these boranes is

that the pattern of bridging hydrogen atoms in the open face is constant and the same as that observed in $MB_{10}H_{12}$ species. For this reason *arachno*-$[B_{10}H_{14}]^{2-}$[74] was not studied.

In all cases the models had full molecular symmetry imposed on them, if not already present crystallographically. In this way for molecules which deviate from full molecular symmetry and which crystallise in a centrosymmetric space group, any ambiguity between "left-handed" and "right-handed" forms in the unit cell is avoided. This is not important when considering the r.m.s. misfit between two molecules; for individual misfits, however, the comparison between two sets of effectively symmetry related pairs of molecules generates two possible values for the individual misfit between atom pairs. For example, the results of misfit calculations between **3** and the two forms of **5** both gave an r.m.s. misfit of 0.142Å. However, two values are obtained for each of the individual misfits: for B(a) these are 0.213Å and 0.201Å, averaging 0.207Å, and for B(b), 0.291Å and 0.299Å, averaging 0.295Å.The imposition of full molecular symmetry avoids this problem. In the comparable calculation, with C_s symmetry imposed on the *arachno*-$\{B_{10}\}$ fragment of **5**, formed by the removal of the $\{BH_2^{3+}\}$ fragment in the 5-membered open face of this species, the value for the r.m.s. misfit is 0.146Å with individual misfits for B(a) and B(b) of 0.202Å and 0.293Å respectively.

Thus, the models for **3** and **6** contained no molecular symmetry. The *arachno*-$\{B_{10}\}$ fragment derived from **2** had C_s symmetry present crystallographically. C_s symmetry was imposed on the models for **4** and, as described above, the *arachno*-$\{B_{10}\}$ unit of **5**. The model for **1** had full C_{2v} symmetry. For simplification, an arbitrary choice between the two independent molecules observed in the crystal structure of **1** has been made. This step is justified when the r.m.s. misfit between these two molecules is calculated: the very low value of 0.002Å obtained suggests any difference between the two is insignificant.

For ease of comparison, the area of chemical change in these models has been kept constant; in **3**, the B(a)-B(c) connectivity has no bridging hydrogen atom, it is this connectivity which is bridged by the gold-phosphine unit in **6**, and in **4**, the NCS group has replaced the terminal hydrogen on B(a).

The interpretation of the structure of **6** as an analogue of **1** has been confirmed by Mössbauer spectroscopy.[75] This shows the gold atom to be in the +1 oxidation state and the structure can be envisaged to be derived from **1** by the isolobal replacement of a bridging proton with a $\{(Cy_3P)Au\}^+$ moiety. By implication, the cage is present as a *nido*-$[B_{10}H_{13}]^-$ fragment.

R.m.s. Misfit Calculations Between *Nido* and *Arachno* Ten Vertex Boranes.

The results of the r.m.s. misfit calculations between the six borane systems described above are shown in Table 2.2. This displays both the overall r.m.s. misfit and the individual misfits between atom pairs.

Considering first the r.m.s. misfit values, one trend is immediately apparent. The result of a calculation between two cages of a similar geometry is at least a factor of two times smaller than that between an *arachno* and a *nido* cage. Between two *nido* or *arachno* cages the average r.m.s. misfit is 0.061Å; between an *arachno* and a *nido* cage the average result is 0.183Å. The small geometrical variations between these *nido* and *arachno* species are clearly measurable *via* the r.m.s. misfit method; the method distinguishes between *nido* and *arachno* character.

Secondly, comparison of the r.m.s. misfit values obtained between the *nido* and *arachno* cages shows those involving **5** to be consistently lower than those involving **2**. Clearly the $\{B_{10}\}$ unit in both these species is correctly described as *arachno* but the degree of this *arachno* character is greater in the latter.

Table 2.2 R.m.s. Misfits and Individual Misfits (Å) Between Boranes and Substituted Boranes Containing *nido*-$\{B_{10}H_{12}\}^{2-}$ and *arachno*-$\{B_{10}H_{12}\}^{4-}$ Fragments.

R.m.s. misfit		δ_a	δ_b	δ_c	δ_d	δ_e	δ_f	δ_g	δ_h	δ_i	δ_j
1/3	0.074	0.145	0.034	0.037	0.151	0.045	0.046	0.045	0.032	0.034	0.016
1/4	0.026	0.018	0.012	0.009	0.023	0.018	0.009	0.066	0.009	0.023	0.018
1/6	0.059	0.046	0.106	0.073	0.063	0.044	0.036	0.031	0.045	0.071	0.030
3/4	0.080	0.151	0.026	0.033	0.132	0.056	0.052	0.109	0.025	0.056	0.029
3/6	0.067	0.104	0.086	0.098	0.088	0.052	0.019	0.024	0.015	0.067	0.023
4/6	0.067	0.059	0.104	0.075	0.045	0.060	0.040	0.095	0.039	0.074	0.035
2/5	0.052	0.084	0.089	0.024	0.024	0.058	0.045	0.045	0.032	0.032	0.020
1/2	0.199	0.377	0.377	0.123	0.123	0.164	0.076	0.076	0.137	0.137	0.081
1/5	0.166	0.297	0.297	0.116	0.116	0.108	0.113	0.113	0.112	0.112	0.101
3/2	0.180	0.290	0.371	0.112	0.140	0.132	0.086	0.042	0.161	0.127	0.078
3/5	0.146	0.202	0.293	0.100	0.124	0.078	0.107	0.074	0.138	0.100	0.098
4/2	0.209	0.390	0.377	0.129	0.127	0.180	0.073	0.139	0.143	0.151	0.098
4/5	0.178	0.310	0.297	0.120	0.117	0.124	0.112	0.178	0.119	0.129	0.118
6/2	0.206	0.338	0.413	0.168	0.110	0.143	0.075	0.045	0.175	0.183	0.093
6/5	0.176	0.255	0.346	0.168	0.095	0.087	0.102	0.084	0.153	0.160	0.111

1 *nido*-$B_{10}H_{14}$ **4** *nido*-6-NCS-$B_{10}H_{13}$

2 *nido*-$[B_{11}H_{13}]^{2-}$ **5** *nido*-$[B_{11}H_{14}]^{-}$

3 *nido*-$[B_{10}H_{13}]^{-}$ **6** 5,6-μ-(Cy_3PAu)-*nido*-$B_{10}H_{13}$

Analysis of the individual misfits shows that the r.m.s. misfit is not uniformly distributed throughout the cage. Indeed, some relationship between high individual misfit and the area of chemical change may be expected, in terms of local steric and electronic effects. Such a relationship may be seen in the individual misfits between **1** and **3**. The highest values occur at B(a) and B(d), and, despite the fact that the B(a)-B(c) connectivity loses a bridging proton in **3**, the individual misfit at B(c) is low. This phenomenon has been successfully explained by inspection of the HOMO of **3**.[70] This is primarily located and bonding between, B(a) and B(c) with a smaller, in phase, contribution on B(d).

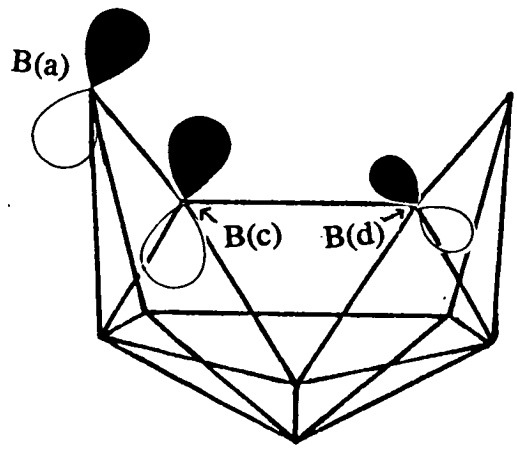

Depopulation of this orbital, *via* protonation to form **1**, causes lengthening of both the B(a)-B(c) and B(c)-B(d) connectivities. The net result is a high misfit at B(a) and B(d), but B(c) remains, relative to the centre of gravity, static. A similar argument should apply to the depopulation of this orbital by the bridging $\{(Cy_3P)Au\}^+$ moiety, although the higher lying gold-based a_1 acceptor orbital should be less efficient in this role than the hydrogen 1s orbital of a proton. Now we see the highest misfit at B(a), but this is only marginally greater than those at B(b), B(c) and B(d), a result not easily interpreted in the same terms as those of the previous argument. Also, the B(a)-B(c) and B(c)-B(d) connectivities in **3** are considerably shorter than those in **1**

and **6**.

System	B(a)-B(c)/Å	B(c)-B(d)/Å
1	1.782(3)	1.987(4)
3	1.657(5)	1.848(5)
6	1.80(3)	2.04(3)

How these variations reflect on the overall interpretation of the cage structures, if at all, is not clear. Only the r.m.s. misfit clearly shows that **3** and **6** can both be correctly treated as derivatives of **1**.

Similarily in **4**, B(g) is remote from the area of chemical change yet this position has a relatively high misfit in the calculations involving this species with **1**, **3** and **6**.

Overall it seems that the r.m.s. misfit approach gives a better indication of cage structure than does the analysis of local effects in terms of connectivity lengths, ^{11}B n.m.r. parameters or individual misfits. This is perhaps not surprising when the delocalised nature of these species is taken into account; it appears global trends are more important than local ones.

In summary, two alike $\{B_{10}\}$ fragments give an r.m.s. misfit of around 0.06Å. This figure represents the "noise level" of these calculations due to the errors inherent in the atomic positions and the random effects of packing forces on the models used. For the borane systems studied an r.m.s. misfit of around 0.180Å is indicative of two cages that are fundamentally different, and the distinction between *nido* and *arachno* character has been made.

Calculations on Auraboranes: Implications for Oxidation State.

The nature of the borane fragment in **6** has already been inferred from independent

assessment of the gold oxidation state *via* Mössbauer spectroscopy. This complementary relationship between cage geometry and metal oxidation state will exist for any $MB_{10}H_{12}$ species and leads to a further method of testing the validity of the r.m.s. misfit method.

Several auraboranes have been made in recent years in Edinburgh.[75] One such species, $[\{(Cy_3P)Au\}B_{10}H_{12}]^-$, **7**, is obtained as the triethylammonium salt by deprotonation of **6** with NEt_3. In **7**, the gold-phosphine unit is found to lie symmetrically over the B(a)B(c)B(d)B(b) face. R.m.s. misfits of this species with **1** and the *arachno* $\{B_{10}\}$ unit of **2** gave the following results:

vs **1**: 0.046Å, *vs* **2**: 0.192Å

Comparison of these results with those discussed in the previous section suggests that the $\{B_{10}\}$ unit of **7** is best described as a *nido*-$[B_{10}H_{12}]^{2-}$ rather than an *arachno*-$[B_{10}H_{12}]^{4-}$ fragment. This has implications not only for the cage and the metal, but also for the interaction between the two.

If the $\{B_{10}\}$ cage in **7** is effectively a *nido*-$[B_{10}H_{12}]^{2-}$ fragment then the gold atom is best described in the role of an μ_4 bridge over the bonding face of the borane. This is clearly different from the role of a metal in a true *nido*-icosahedral species where the former is best regarded as a cluster vertex interacting with an *arachno*-$[B_{10}H_{12}]^{4-}$ unit. Of course, a test of this interpretation is once again available through Mössbauer spectroscopy and it has been shown elsewhere that the gold atom in **7** is indeed present in the +1 oxidation state.[75]

Two important points arise from this. Firstly, the r.m.s. misfit method may be useful in determining metal oxidation states. Secondly, a metal can clearly adopt one of two possible roles in these metallaboranes; either that of a true cluster vertex, as in a true *nido*-icosahedral metallaborane, or as a bridging species over a

nido-decaboranyl ligand. The major difference between these two extremes seems to lie in the extent of formal electron donation from the metal fragment to the borane cage. A metal bridges a *nido*-$[B_{10}H_{12}]^{2-}$ unit but a true cluster vertex interacts with a formally reduced *arachno*-$[B_{10}H_{12}]^{4-}$ fragment, this formal two electron reduction being complemented by a two electron oxidation of the metal.

In the following discussion of $MB_{10}H_{12}$ species we have attempted to quantify the extent of this interaction in terms of the "verticity" of the metal. To do this we compare, *via* the r.m.s. misfit method, the geometry of the metallaborane with that of the archetypal *nido*-$[B_{10}H_{12}]^{2-}$ and *arachno*-$[B_{10}H_{12}]^{4-}$ units which are fragments of **1** and **2** respectively. In the former, an eleventh boron can be viewed as being removed to infinity, and has a verticity of 0%. The unique BH unit in the open face of **2** is said to have a verticity of 100%. (**2**, as opposed to **5**, is used as a standard because, as shown above, its *arachno*-$[B_{10}H_{12}]^{4-}$ fragment displays the greater *arachno* character).

The verticity of a metallaborane, X can now be defined as:

$$\frac{\text{(r.m.s. misfit 1 } vs \text{ 2)+(r.m.s. misfit X } vs \text{ 1)-(r.m.s. misfit X } vs \text{ 2)}}{\text{2(r.m.s. misfit 1 } vs \text{ 2)}} \times 100\%$$

On this basis the verticity of the gold atom in **7** is calculated to be 13.3%. The overall strategy for analysis of $MB_{10}H_{12}$ metallaboranes can now be summarised.

Metallaborane Analysis.

Whilst a reasonably large number of $MB_{10}H_{12}$ metallaboranes are known, accurate crystallographic studies have not always been carried out. In these cases the structure has usually been assigned by analogy with other crystallographically characterised $MB_{10}H_{12}$ species, *via* n.m.r. spectroscopy.[35] However, for the present work accurate crystal data are clearly necessary, so the resynthesis and accurate crystallographic study of several species already known in the literature was undertaken in order to provide a wider array of structures for comparative purposes.

The relationship between cage geometry and metal oxidation state, as described above, is important and so the synthesis of metallaboranes in which the metal oxidation state may be independently assessed was a major aim. To this end, the electrochemistry of $MB_{10}H_{12}$ species, as yet rarely studied, was viewed as perhaps the only generally applicable method of probing the metal oxidation state in a series of metallaborane species. The electrochemistry of four $MB_{10}H_{12}$ metallaboranes, with regard to the question of metal oxidation state, is described in this chapter, and discussed in more detail in Chapter 5. Finally, the results of the r.m.s. misfit calculations are related to certain molecular parameters of the borane cage. These parameters will include the B(a)...B(b) non-bonded distance, the B(c)-B(d) and B(h)-B(i) distances and the height of the metal above the least-squares plane through B(a)B(h)B(i)B(b), H. A rationalisation of the effects of a variety of metal fragments on the structure of the $\{B_{10}\}$ unit is attempted *via* a series of EHMO and FMO calculations and the utility of the various cage parameters described above for metallaborane analysis is assessed.

Crystallographic Studies on Some $MB_{10}H_{12}$ Species

The number of structural studies on species of the general form $MB_{10}H_{12}$, where M is a transition metal, is very limited. At the start of this work only three were known : $(PMe_2Ph)_2PtB_{10}H_{12}$[32] and the bis-borane species $[Ni(B_{10}H_{12})_2]^{2-}$,[77] **8**, and $[Au(B_{10}H_{12})_2]^-$,[76] although several further $\{MB_{10}\}$ species featuring derivatised cages have been structurally characterised. These are $CO(PPh_3)_3IrB_{10}H_{11}$,[78] where a phosphine has substituted a terminal hydrogen on B(e), $(PMe_2Ph)_2PtB_{10}H_{11}Cl$,[79] where B(a) is bonded to a terminal chlorine atom, $(PMe_2Ph)(S_2CNEt_2)PtB_{10}H_{11}$,[80] the dithiocarbamate moiety bridging between the Pt and B(d) atoms, $(PMe_2Ph)_2PtB_{10}H_{11}(B_{10}H_{13})$,[32] the $\{B_{10}H_{13}\}$ moiety being bonded to B(f) on the metallaborane, through B(2), adopting a decaboranyl nomenclature for this pendant ligand, and $(PMe_2Ph)(Ph_2PC_6H_4)PtB_{10}H_{11}O$,[78] where B(a) is oxy-bridged to an *ortho* carbon of one of the *exo*-polyhedral phenyl rings. In all these species the pattern of the hydrogen atoms is assumed to be as that observed in $MB_{10}H_{12}$ species. In the only other structurally characterised $\{MB_{10}\}$-containing, metallaborane, $Cp^*RhCl(PMe_2Ph)B_{10}H_{11}$,[81] this is not the case.

Here the crystal structures of three more $MB_{10}H_{12}$ metallaboranes are presented. These are $[(CO)_3CoB_{10}H_{12}]^-$, **9**, $[Pt(B_{10}H_{12})_2]^{2-}$, **10** and $[Pd(B_{10}H_{12})_2]^{2-}$, **11**. All of these species have been previously synthesised by Muetterties and co-workers.[34]

Considering first the *bis*-borane species, the studies of **10** and **11** and their comparison with the nickel analogue complete a series down a transition metal triad, allowing the effects of the increase in principle quantum number of the metal valence orbitals to be monitored. Comparison will not be drawn with the gold species as some disorder was noted in the structure, rendering such comparison invalid. The metal centres in the Pd and Pt species are most usually described as square planar d^8 and, therefore, the $\{MB_{10}H_{12}\}$ fragments are not isolobal with {BH}, the classic

borane vertex. It was proposed that, in **9**, the $[Co(CO)_3]^+$ moiety would act as a 2 electron-3 orbital source, isolobal to {BH}, the first such metal fragment to be structurally characterised within the framework of an $MB_{10}H_{12}$ species.

Details of data collection and processing and of the crystallographic procedures used in the solution and refinement of the structures discussed here are presented in Chapter 6. The numbering scheme employed for the borane fragments in the text is the same as that shown in Figure 2.2 above, with the terminal and bridging hydrogen atoms taking the letter of the boron(s) to which they are attached.

The Structure of $[PhCH_2N(CH_3)_3]^+$ 9, [BTMA]9.

A perspective view of the anion is presented in Figure 2.3. Table 2.3 details the atomic positions of refined atoms with equivalent thermal parameters, Table 2.4 gives selected interatomic distances and interbond angles, Table 2.5 anisotropic thermal parameters and Table 2.6 lists the calculated positions of hydrogen atoms.

Four ion pairs of BTMA **9** crystallise in the unit cell of the monoclinic space group $P2_1/c$. The anion has effective, non-crystallographically imposed C_s molecular symmetry about the plane defined by Co, B(e) and B(j). The estimated standard deviations (e.s.d.'s) on the atomic positions are somewhat higher than would normally be expected; we attribute this to the poor quality of the crystals available for the crystallographic study. The gross structure of the borane fragment is as expected. The longest B-B connectivity is observed, as is usual in these systems, between B(h) and B(i). However this distance, 1.924(21)Å, is the shortest of its type as yet observed in an $MB_{10}H_{12}$ metallaborane. The B(a)...B(b) and B(c)-B(d) distances are 3.136(20)Å and 1.790(21)Å respectively. Average Co - B distances are longer to B(a) and B(b) than to B(c) and B(d), although the difference is not significant. H for this species is 0.321(15)Å.

Figure 2.3 Molecular Structure of **9**.

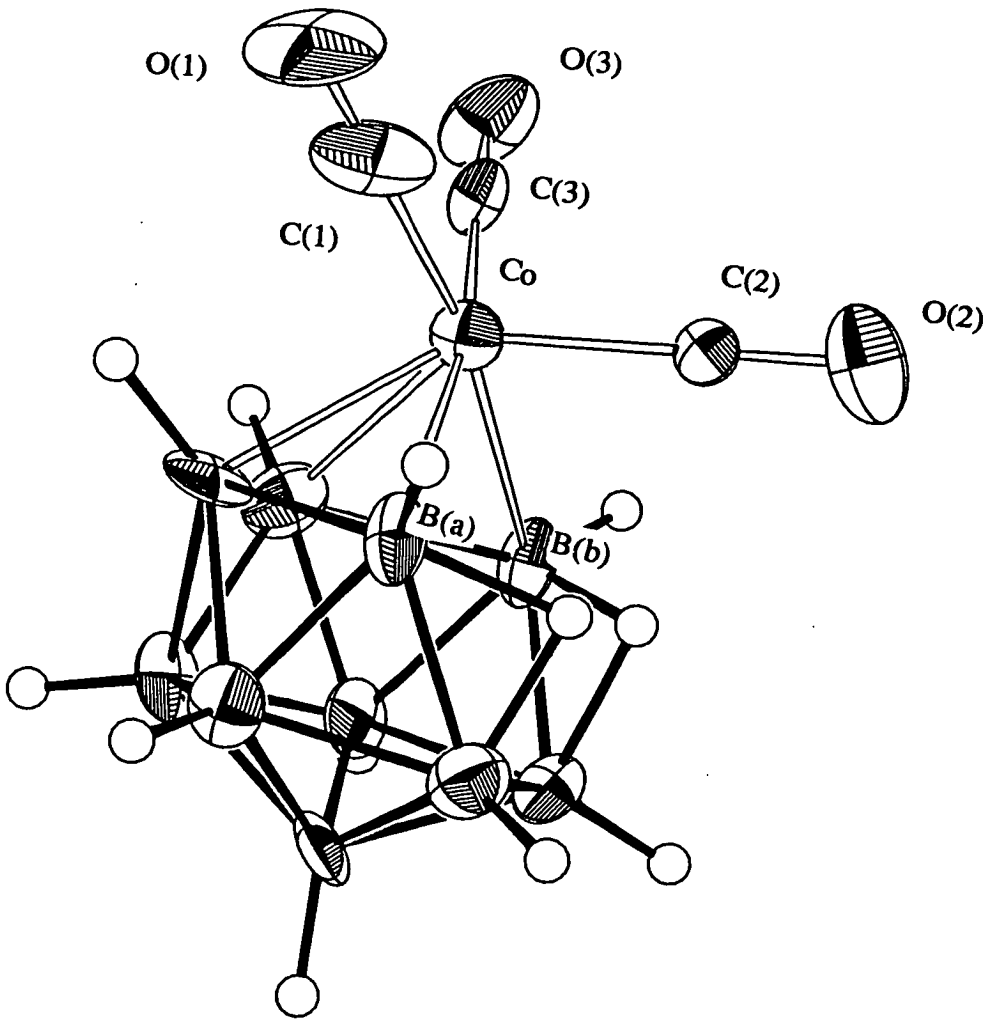

Table 2.3 Atomic Positions and Equivalent Isotropic Thermal Parameters ($Å^2$) of Refined Atoms in [BTMA]9.

	x	y	z	Ueq
Co	0.24060(16)	0.09793(13)	0.02488(11)	0.0272(8)
C(3)	0.1186(12)	0.0919(10)	0.1115(8)	0.035(7)
O(3)	0.0437(9)	0.0923(8)	0.1666(7)	0.052(6)
C(1)	0.2480(13)	-0.0270(11)	0.0047(10)	0.046(9)
O(1)	0.2585(12)	-0.1056(7)	-0.0096(8)	0.067(8)
C(2)	0.3785(12)	0.1193(7)	0.0940(7)	0.025(6)
O(2)	0.4700(9)	0.1334(8)	0.1393(7)	0.054(7)
B(e)	0.1382(13)	0.2187(12)	-0.1682(10)	0.032(8)
B(c)	0.1912(12)	0.1041(11)	-0.1239(9)	0.030(7)
B(d)	0.1065(15)	0.1871(12)	-0.0546(11)	0.038(9)
B(g)	0.1554(13)	0.3037(11)	-0.0803(10)	0.031(8)
B(j)	0.2699(14)	0.2938(10)	-0.1690(9)	0.029(8)
B(f)	0.2903(14)	0.1716(12)	-0.1970(9)	0.033(8)
B(b)	0.2139(14)	0.2538(10)	0.0256(10)	0.031(8)
B(i)	0.3189(13)	0.3225(10)	-0.0528(10)	0.028(8)
B(h)	0.4066(15)	0.2341(11)	-0.1304(10)	0.034(8)
B(a)	0.3587(13)	0.1120(10)	-0.1022(9)	0.029(7)
C(2)	0.6362(6)	0.3520(6)	0.0755(5)	0.033(3)
C(3)	0.6220(6)	0.3772(6)	0.1697(5)	0.041(3)
C(4)	0.7269(6)	0.4028(6)	0.2255(5)	0.044(3)
C(5)	0.8461(6)	0.4033(6)	0.1871(5)	0.040(3)
C(6)	0.8603(6)	0.3781(6)	0.0928(5)	0.034(3)
C(1)	0.7554(6)	0.3524(6)	0.0370(5)	0.027(3)
C(7)	0.7716(11)	0.3232(9)	-0.0646(8)	0.027(3)
N(1)	0.7568(8)	0.4026(7)	-0.1370(6)	0.026(5)
C(8)	0.7726(14)	0.3593(11)	-0.2326(9)	0.045(9)
C(9)	0.8522(12)	0.4808(8)	-0.1203(10)	0.039(8)
C(10)	0.6257(11)	0.4476(9)	-0.1355(9)	0.034(7)

Table 2.4 Interatomic Distances (Å) and Selected Interbond Angles (°) for [BTMA]**9**.

Co	- C(3)	1.816(13)	B(d)	- B(g)	1.768(22)
Co	- O(3)	2.948(10)	B(d)	- B(b)	1.844(21)
Co	- C(1)	1.788(15)	B(g)	- B(j)	1.783(20)
Co	- O(1)	2.922(12)	B(g)	- B(b)	1.754(21)
Co	- C(2)	1.763(11)	B(g)	- B(i)	1.789(20)
Co	- O(2)	2.929(10)	B(j)	- B(f)	1.785(21)
Co	- B(c)	2.158(14)	B(j)	- B(i)	1.758(20)
Co	- B(d)	2.187(16)	B(j)	- B(h)	1.753(21)
Co	- B(b)	2.219(15)	B(f)	- B(h)	1.768(21)
Co	- B(a)	2.237(14)	B(f)	- B(a)	1.726(20)
C(3)	- O(3)	1.133(16)	B(b)	- B(i)	1.871(20)
C(3)	- C(1)	2.670(20)	B(i)	- B(h)	1.924(21)
C(3)	- C(2)	2.809(17)	B(h)	- B(a)	1.845(21)
C(1)	- O(1)	1.135(19)	C(2)	- C(3)	1.395(11)
C(1)	- C(2)	2.771(18)	C(2)	- C(1)	1.395(11)
C(1)	- B(c)	2.653(20)	C(3)	- C(4)	1.395(11)
C(2)	- O(2)	1.165(15)	C(4)	- C(5)	1.395(11)
B(e)	- B(c)	1.818(20)	C(5)	- C(6)	1.395(11)
B(e)	- B(d)	1.714(22)	C(6)	- C(1)	1.395(11)
B(e)	- B(g)	1.735(21)	C(1)	- C(7)	1.512(14)
B(e)	- B(j)	1.756(21)	C(7)	- N(1)	1.525(15)
B(e)	- B(f)	1.807(21)	N(1)	- C(8)	1.500(17)
B(c)	- B(d)	1.790(21)	N(1)	- C(9)	1.513(16)
B(c)	- B(f)	1.778(20)	N(1)	-C(10)	1.533(16)
B(c)	- B(a)	1.801(20)			

C(3)	- Co	- C(1)	95.6(6)	B(d)	- B(g)	- B(b)	63.1(9)
C(3)	- Co	- C(2)	103.4(6)	B(j)	- B(g)	- B(i)	59.0(8)
C(3)	- Co	- B(c)	120.4(6)	B(b)	- B(g)	- B(i)	63.8(8)
C(3)	- Co	- B(d)	84.7(6)	B(e)	- B(j)	- B(g)	58.7(8)
C(3)	- Co	- B(b)	87.1(6)	B(e)	- B(j)	- B(f)	61.4(8)
C(3)	- Co	- B(a)	168.5(6)	B(g)	- B(j)	- B(i)	60.7(8)
C(1)	- Co	- C(2)	102.6(6)	B(f)	- B(j)	- B(h)	60.0(8)
C(1)	- Co	- B(c)	83.9(6)	B(i)	- B(j)	- B(h)	66.5(8)
C(1)	- Co	- B(d)	121.1(6)	B(e)	- B(f)	- B(c)	61.0(8)
C(1)	- Co	- B(b)	170.0(6)	B(e)	- B(f)	- B(j)	58.5(8)
C(1)	- Co	- B(a)	86.0(6)	B(c)	- B(f)	- B(a)	61.8(8)
C(2)	- Co	- B(c)	135.1(5)	B(j)	- B(f)	- B(h)	59.1(8)
C(2)	- Co	- B(d)	134.8(6)	B(h)	- B(f)	- B(a)	63.7(9)
C(2)	- Co	- B(b)	86.1(5)	Co	- B(b)	- B(d)	64.4(7)
C(2)	- Co	- B(a)	87.4(5)	B(d)	- B(b)	- B(g)	58.8(8)
B(c)	- Co	- B(d)	48.7(6)	B(g)	- B(b)	- B(i)	59.0(8)
B(c)	- Co	- B(b)	86.4(5)	B(g)	- B(i)	- B(j)	60.3(8)
B(c)	- Co	- B(a)	48.3(5)	B(g)	- B(i)	- B(b)	57.2(8)
B(d)	- Co	- B(b)	49.5(6)	B(j)	- B(i)	- B(h)	56.7(8)
B(d)	- Co	- B(a)	84.7(5)	B(j)	- B(h)	- B(f)	60.9(8)
B(b)	- Co	- B(a)	89.5(5)	B(j)	- B(h)	- B(i)	56.9(8)
Co	- C(3)	- O(3)	176.8(12)	B(f)	- B(h)	- B(a)	57.0(8)
Co	- C(1)	- O(1)	176.6(13)	Co	- B(a)	- B(c)	63.5(6)
Co	- C(2)	- O(2)	179.6(10)	B(c)	- B(a)	- B(f)	60.5(8)
B(c)	- B(e)	- B(d)	60.8(8)	B(f)	- B(a)	- B(h)	59.2(8)
B(c)	- B(e)	- B(f)	58.7(8)	C(3)	- C(2)	- C(1)	120.0(7)
B(d)	- B(e)	- B(g)	61.7(9)	C(2)	- C(3)	- C(4)	120.0(7)
B(g)	- B(e)	- B(j)	61.4(8)	C(3)	- C(4)	- C(5)	120.0(7)
B(j)	- B(e)	- B(f)	60.1(8)	C(4)	- C(5)	- C(6)	120.0(7)
Co	- B(c)	- B(d)	66.5(7)	C(5)	- C(6)	- C(1)	120.0(7)
Co	- B(c)	- B(a)	68.1(6)	C(2)	- C(1)	- C(6)	120.0(7)
B(e)	- B(c)	- B(d)	56.7(8)	C(2)	- C(1)	- C(7)	120.2(7)

B(e)	- B(c)	- B(f)	60.3(8)	C(6)	- C(1)	- C(7)	119.8(7)
B(f)	- B(c)	- B(a)	57.7(8)	C(1)	- C(7)	- N(1)	115.3(9)
Co	- B(d)	- B(c)	64.8(7)	C(7)	- N(1)	- C(8)	107.2(9)
Co	- B(d)	- B(b)	66.2(7)	C(7)	- N(1)	- C(9)	112.1(9)
B(e)	- B(d)	- B(c)	62.5(9)	C(7)	- N(1)	-C(10)	111.7(9)
B(e)	- B(d)	- B(g)	59.8(9)	C(8)	- N(1)	- C(9)	110.3(9)
B(g)	- B(d)	- B(b)	58.1(8)	C(8)	- N(1)	-C(10)	108.1(9)
B(e)	- B(g)	- B(d)	58.6(8)	C(9)	- N(1)	-C(10)	107.5(9)
B(e)	- B(g)	- B(j)	59.9(8)				

Table 2.5 Anisotropic Thermal Parameters ($Å^2$) for [BTMA]9.

	U11	U22	U33	U23	U13	U12
Co	0.0284(8)	0.0272(8)	0.0259(8)	-0.0008(9)	0.0032(6)	0.0013(9)
C(3)	0.0420(78)	0.0290(70)	0.0345(67)	-0.0065(64)	-0.0091(60)	-0.0110(67)
O(3)	0.0418(56)	0.0581(67)	0.0565(59)	-0.0127(58)	0.0252(48)	-0.0184(57)
C(1)	0.0343(82)	0.052 (10)	0.0514(93)	0.0204(73)	0.0267(72)	0.0067(73)
O(1)	0.1128(99)	0.0144(54)	0.0750(78)	0.0034(52)	0.0159(65)	0.0084(67)
C(2)	0.0386(73)	0.0112(60)	0.0237(57)	-0.0063(44)	-0.0040(54)	0.0017(50)
O(2)	0.0419(60)	0.0724(78)	0.0481(58)	-0.0036(53)	-0.0146(49)	0.0112(54)
B(e)	0.0154(71)	0.0430(91)	0.0378(80)	0.0000(69)	-0.0128(59)	0.0097(68)
B(c)	0.0270(72)	0.0296(73)	0.0325(68)	0.0207(72)	-0.0005(56)	0.0121(74)
B(d)	0.0266(81)	0.0421(94)	0.0461(89)	0.0030(78)	0.0076(68)	-0.0086(72)
B(g)	0.0140(67)	0.0428(89)	0.0359(76)	0.0026(68)	-0.0080(56)	0.0011(63)
B(j)	0.0390(86)	0.0310(81)	0.0170(63)	0.0040(57)	-0.0135(58)	0.0050(67)
B(f)	0.0305(83)	0.0448(92)	0.0242(69)	-0.0082(66)	0.0095(60)	-0.0040(72)
B(b)	0.0331(99)	0.0294(81)	0.0306(73)	-0.0217(66)	-0.0010(66)	0.0001(61)
B(i)	0.0213(75)	0.0183(69)	0.0451(86)	0.0015(62)	-0.0052(61)	0.0019(58)
B(h)	0.0339(88)	0.0337(81)	0.0346(78)	-0.0007(67)	0.0041(64)	-0.0049(70)
B(a)	0.0317(74)	0.0239(77)	0.0303(67)	-0.0160(64)	-0.0064(57)	0.0070(68)
N(1)	0.0256(51)	0.0222(50)	0.0306(49)	-0.0005(49)	0.0025(39)	-0.0035(50)
C(8)	0.0578(97)	0.0530(91)	0.0247(66)	-0.0089(64)	0.0089(64)	-0.0049(78)
C(9)	0.0310(74)	0.0168(67)	0.0676(94)	0.0080(60)	-0.0127(66)	-0.0104(55)
C(10)	0.0222(64)	0.0283(68)	0.0520(80)	0.0074(61)	0.0004(56)	0.0072(57)

Table 2.6 Calculated Positions of Hydrogen Atoms for [BTMA]**9**.

	x	y	z
H(e)	0.0556	0.2162	-0.2162
H(c)	0.1583	0.0289	-0.1361
H(d)	0.0185	0.1685	-0.0207
H(g)	0.0907	0.3614	-0.0615
H(j)	0.2892	0.3506	-0.2196
H(f)	0.3217	0.1382	-0.2632
H(b)	0.1944	0.2733	0.0991
H(i)	0.3646	0.3845	-0.0194
H(h)	0.5081	0.2427	-0.1457
H(a)	0.4241	0.0506	-0.1001
H(bi)	0.3391	0.2576	0.0203
H(ah)	0.4217	0.1788	-0.0512
H(2)	0.5550	0.3321	0.0322
H(3)	0.5298	0.3768	0.1995
H(4)	0.7159	0.4223	0.2985
H(5)	0.9273	0.4232	0.2303
H(6)	0.9526	0.3784	0.0631
H(71)	0.8649	0.2938	-0.0702
H(72)	0.7024	0.2694	-0.0818

The symmetry of the $\{Co(CO)_3\}$ moiety conforms to the overall molecular symmetry with the unique *endo* C(2)O(2) carbonyl ligand lying in the plane of symmetry. That the coordination around the central cobalt atom is distorted away from octahedral is evidenced by the C-Co-C angles. Those involving C(2) average 103.0(8)°, whilst the C(3)-Co-C(1) angle is 95.6(6)°. The angle which the vector defined by the positions of the Co and O(2) atoms makes with the least-squares plane through B(a)B(c)B(d)B(b) is 11.0°, considerably less than 35.2°, the expected value if the Co atom exhibited ideal octahedral geometry. Similar vectors through the metal and O(3) and O(1) make angles of 34.7° and 35.0° respectively with the plane through the bonded borane face.

Variation in the Co-C and C-O distances is also apparent. The Co-C(2) distance is shortest at 1.763(11)Å, the Co-C(1) distance is 1.788(15)Å and Co-C(3) is the longest at 1.810(13)Å. Although, due to the general inaccuracy of the model, these differences are not statistically significant, a similar, opposite trend is seen in the intra-carbonyl distances, suggesting that the trends in Co - C distances are due to variation in the extent of π-backbonding from the metal to the π^* acceptor orbitals of the carbonyl ligands. A more detailed account of the frontier MO's of metal fragments will be given in Chapter 3.

However, the main interest in the structure of **9** lies in the overall geometry of the cage. R.m.s. misfit calculations between **9** and **1** and between **9** and the *arachno*-$\{B_{10}\}$ fragment of **2** give values of 0.147Å and 0.070Å respectively, leading to a verticity of 69.1%. This suggests that the borane moiety in **9** is best described as an *arachno*-$\{B_{10}H_{12}\}^{4-}$fragment and that the overall geometry of the metallaborane is that of a true *nido*-icosahedron. Within this formulation, the cobalt is functioning as a true cluster vertex and is formally present in the +3 oxidation state. This final point is contentious. The presence of three strongly π-acidic carbonyl ligands around a Co^{III} centre is unusual, indeed no precedent is available in the literature. Confirmation of

the conclusion drawn from the r.m.s. misfit calculations was therefore sought by independent assessment of the cobalt oxidation state. This is discussed below, although the initial observation that the carbonyl stretching frequencies of **9** are of quite high energy (2002, 2020 and 2065cm^{-1}) is consistent with a generally low degree of π-backbonding and a metal centre with a relatively low electron density.

Molecular Structures of [BTMA]$_2$**10** and [BTMA]$_2$**11**.2CH$_3$CN.

Both these species crystallise in the triclinic space group Pbar1 with the metal centres located on crystallographic inversion centres. An ion-pair of [BTMA]**10** is shown in Figure 2.4. Table 2.7 lists atomic positions of refined non-hydrogen atoms with equivalent isotropic thermal parameters, Table 2.8 selected interatomic distances and interbond angles, Table 2.9 shows anisotropic thermal parameters and Table 2.10 the positions of refined hydrogen atoms. Tables 2.11 to 2.14 detail the corresponding information for the palladium analogue, the unit cell contents of which are shown in Figure 2.5. Figures 2.4 and 2.5 shows the overall gross isostructural nature of **10** and **11**. The two can be discussed together, except for the small, but significant, deviation from effective C_{2h} symmetry observed in **10**. This distortion results in the metal lying closer to B(a) than to B(b), but also results in a Pt-B(d) distance which is shorter than Pt-B(c). An explanation is afforded in terms of crystal packing effects. Firstly, although there are no inter-ion distances of less than 2.6Å, Figure 2.4 clearly shows that the sides of the borane cages experience different crystal environments. Also, the fortuitous incorporation of two solvent molecules in the unit cell of [BTMA]$_2$**11** removes this asymmetry, altering the packing and allowing the adoption of effective C_{2h} symmetry in the latter.

Figure 2.4 Ion Pair of [BTMA]10.

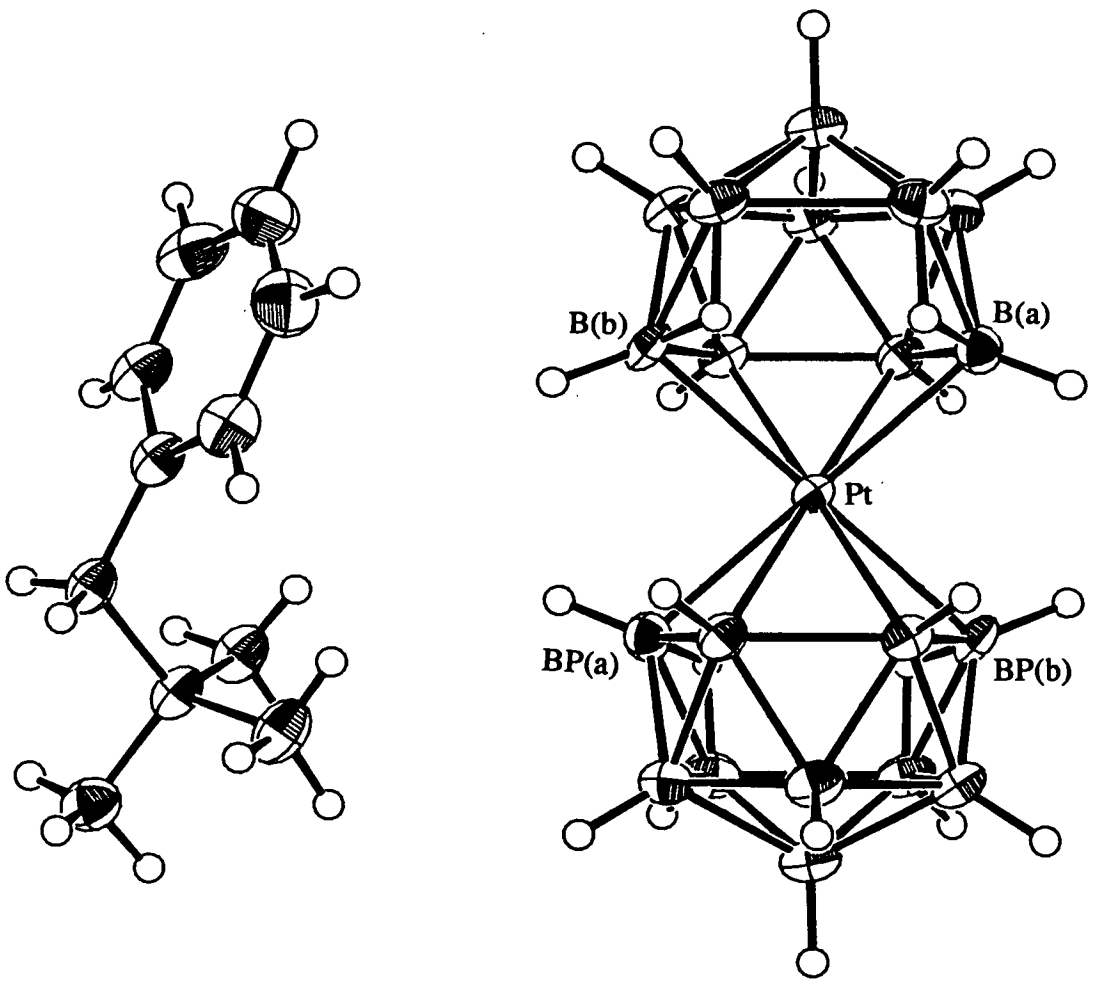

Table 2.7 Atomic Positions and Equivalent Isotropic Thermal Parameters ($Å^2$) of Refined Non-Hydrogen Atoms for $[BTMA]_2$**10**.

	x	y	z	Ueq
Pt	0.00000	0.00000	0.00000	0.0218(1)
C(1)	0.7779(3)	0.4894(3)	0.3868(3)	0.0351(17)
C(2)	0.7429(4)	0.3618(3)	0.2671(3)	0.0444(20)
C(3)	0.7363(4)	0.2313(4)	0.2751(4)	0.0576(25)
C(4)	0.7666(4)	0.2291(4)	0.4028(5)	0.066(3)
C(5)	0.8051(4)	0.3564(4)	0.5237(4)	0.062(3)
C(6)	0.8090(4)	0.4861(4)	0.5154(3)	0.0449(20)
C(7)	0.7967(3)	0.6335(3)	0.3830(3)	0.0340(17)
N(1)	0.6346(3)	0.66296(25)	0.33214(23)	0.0331(14)
C(8)	0.6803(4)	0.8187(3)	0.3547(4)	0.0445(21)
C(9)	0.5272(4)	0.5620(4)	0.1775(3)	0.0436(21)
C(10)	0.5377(4)	0.6451(4)	0.4148(3)	0.0417(20)
B(a)	0.1163(4)	0.2424(3)	0.0634(3)	0.0307(17)
B(c)	0.0954(3)	0.1181(3)	-0.1060(3)	0.0290(17)
B(d)	-0.1101(4)	-0.0279(3)	-0.2201(3)	0.0293(17)
B(b)	-0.2605(3)	-0.0253(3)	-0.1484(3)	0.0317(18)
B(i)	-0.2739(4)	0.1574(4)	-0.0997(3)	0.0368(19)
B(j)	-0.1517(4)	0.2480(3)	-0.1597(3)	0.0368(19)
B(e)	-0.0583(4)	0.1316(3)	-0.2430(3)	0.0337(18)
B(g)	-0.2627(4)	0.0548(3)	-0.2619(3)	0.0334(18)
B(f)	0.0675(4)	0.2894(3)	-0.0763(3)	0.0346(19)
B(h)	-0.0505(4)	0.3169(3)	0.0253(3)	0.0377(20)

Table 2.8 Selected Interbond Distances (Å) and Angles (°) for $[BTMA]_2$**10**.

Pt	- B(a)	2.274(3)	B(a)	- B(h)	1.828(5)
Pt	- B(c)	2.232(3)	B(a)	- H(a)	1.03(4)
Pt	- B(d)	2.215(3)	B(a)	-H(ah)	1.38(4)
Pt	- B(b)	2.294(3)	B(c)	- B(d)	1.823(5)
C(1)	- C(2)	1.385(5)	B(c)	- B(e)	1.773(5)
C(1)	- C(6)	1.387(5)	B(c)	- B(f)	1.777(5)
C(1)	- C(7)	1.498(4)	B(c)	- H(c)	1.07(4)
C(2)	- C(3)	1.388(6)	B(d)	- B(b)	1.783(5)
C(2)	-HC(2)	0.92(5)	B(d)	- B(e)	1.772(5)
C(3)	- C(4)	1.373(6)	B(d)	- B(g)	1.791(5)
C(3)	-HC(3)	0.98(5)	B(d)	- H(d)	1.10(4)
C(4)	- C(5)	1.382(6)	B(b)	- B(i)	1.824(5)
C(4)	-HC(4)	0.93(5)	B(b)	- B(g)	1.753(5)
C(5)	- C(6)	1.386(6)	B(b)	- H(b)	1.09(4)
C(5)	-HC(5)	0.94(5)	B(b)	-H(bi)	1.30(4)
C(6)	-HC(6)	0.92(5)	B(i)	- B(j)	1.758(5)
C(7)	- N(1)	1.525(4)	B(i)	- B(g)	1.783(5)
C(7)	-H(71)	0.91(5)	B(i)	- B(h)	1.988(5)
C(7)	-H(72)	0.97(5)	B(i)	- H(i)	1.09(4)
N(1)	- C(8)	1.499(4)	B(i)	-H(bi)	1.22(4)
N(1)	- C(9)	1.489(5)	B(j)	- B(e)	1.769(5)
N(1)	-C(10)	1.495(4)	B(j)	- B(g)	1.776(5)
C(8)	-HC(81)	0.91(4)	B(j)	- B(f)	1.776(5)
C(8)	-HC(82)	0.96(5)	B(j)	- B(h)	1.749(5)
C(8)	-HC(83)	0.97(4)	B(j)	- H(j)	1.09(4)
C(9)	-HC(91)	0.90(4)	B(e)	- B(g)	1.771(5)
C(9)	-HC(92)	0.93(4)	B(e)	- B(f)	1.767(5)
C(9)	-HC(93)	0.97(4)	B(e)	- H(e)	1.07(4)
C(10)	-HC(10)	0.94(4)	B(g)	- H(g)	1.09(4)
C(10)	-HC(10)	0.93(5)	B(f)	- B(h)	1.780(5)
C(10)	-HC(10)	0.95(4)	B(f)	- H(f)	1.10(4)
B(a)	- B(c)	1.780(5)	B(h)	- H(h)	1.07(4)
B(a)	- B(f)	1.753(5)	B(h)	-H(ah)	1.22(4)

B(a)	- Pt	- B(c)	46.54(12)	B(b)	- B(d)	- B(g)	58.76(18)
B(a)	- Pt	- B(d)	84.85(12)	B(e)	- B(d)	- B(g)	59.62(19)
B(a)	- Pt	- B(b)	94.23(12)	Pt	- B(b)	- B(d)	64.39(14)
B(c)	- Pt	- B(d)	48.41(12)	B(d)	- B(b)	- B(g)	60.86(19)
B(c)	- Pt	- B(b)	85.17(12)	B(i)	- B(b)	- B(g)	59.76(19)
B(d)	- Pt	- B(b)	46.54(12)	B(b)	- B(i)	- B(g)	58.16(19)
C(2)	- C(1)	- C(6)	119.2(3)	B(j)	- B(i)	- B(g)	60.17(20)
C(2)	- C(1)	- C(7)	121.3(3)	B(j)	- B(i)	- B(h)	55.25(19)
C(6)	- C(1)	- C(7)	119.3(3)	B(i)	- B(j)	- B(g)	60.61(20)
C(1)	- C(2)	- C(3)	120.4(3)	B(i)	- B(j)	- B(h)	69.04(21)
C(2)	- C(3)	- C(4)	119.8(4)	B(e)	- B(j)	- B(g)	59.98(19)
C(3)	- C(4)	- C(5)	120.3(4)	B(e)	- B(j)	- B(f)	59.81(19)
C(4)	- C(5)	- C(6)	119.8(4)	B(f)	- B(j)	- B(h)	60.63(20)
C(1)	- C(6)	- C(5)	120.3(3)	B(c)	- B(e)	- B(d)	61.90(18)
C(1)	- C(7)	- N(1)	115.68(25)	B(c)	- B(e)	- B(f)	60.26(19)
C(7)	- N(1)	- C(9)	111.00(24)	B(d)	- B(e)	- B(g)	60.74(19)
C(7)	- N(1)	-C(10)	111.24(24)	B(j)	- B(e)	- B(g)	60.21(19)
C(8)	- N(1)	- C(9)	108.8(3)	B(j)	- B(e)	- B(f)	60.32(19)
C(8)	- N(1)	-C(10)	108.8(3)	B(d)	- B(g)	- B(b)	60.38(19)
C(9)	- N(1)	-C(10)	109.1(3)	B(d)	- B(g)	- B(e)	59.64(19)
C(7)	- N(1)	- C(8)	107.85(24)	B(b)	- B(g)	- B(i)	62.08(19)
Pt	- B(a)	- B(c)	65.47(15)	B(i)	- B(g)	- B(j)	59.22(20)
B(c)	- B(a)	- B(f)	60.39(19)	B(j)	- B(g)	- B(e)	59.82(19)
B(f)	- B(a)	- B(h)	59.55(19)	B(a)	- B(f)	- B(c)	60.56(19)
Pt	- B(c)	- B(a)	67.99(15)	B(a)	- B(f)	- B(h)	62.33(20)

Pt - B(c) - B(d)	65.31(14)	B(c) - B(f) - B(e)	60.04(19)
B(a) - B(c) - B(f)	59.04(19)	B(j) - B(f) - B(e)	59.87(19)
B(d) - B(c) - B(e)	59.00(18)	B(j) - B(f) - B(h)	58.91(20)
B(e) - B(c) - B(f)	59.70(19)	B(a) - B(h) - B(f)	58.13(19)
Pt - B(d) - B(c)	66.28(14)	B(i) - B(h) - B(j)	55.70(19)
Pt - B(d) - B(b)	69.06(15)	B(j) - B(h) - B(f)	60.45(20)
B(c) - B(d) - B(e)	59.10(18)		

Table 2.9 Anisotropic Thermal Parameters ($Å^2$) for $[BTMA]_2$**10**.

	U11	U22	U33	U23	U13	U12
Pt	0.0179(1)	0.0210(1)	0.0169(1)	0.0089(1)	0.0061(1)	0.0084(1)
C(1)	0.0221(11)	0.0408(14)	0.0302(13)	0.0166(11)	0.0171(10)	0.0156(10)
C(2)	0.0369(15)	0.0432(15)	0.0340(15)	0.0131(13)	0.0195(12)	0.0184(12)
C(3)	0.0455(18)	0.0402(16)	0.0590(21)	0.0157(16)	0.0228(16)	0.0179(14)
C(4)	0.0387(16)	0.0522(19)	0.0866(28)	0.0434(20)	0.0341(18)	0.0229(15)
C(5)	0.0348(15)	0.0784(23)	0.0613(21)	0.0505(20)	0.0329(15)	0.0323(16)
C(6)	0.0304(14)	0.0560(18)	0.0335(15)	0.0226(14)	0.0204(12)	0.0228(13)
C(7)	0.0213(11)	0.0397(14)	0.0267(13)	0.0140(11)	0.0130(10)	0.0127(10)
N(1)	0.0230(10)	0.0404(12)	0.0223(10)	0.0134(9)	0.0116(8)	0.0137(9)
C(8)	0.0351(15)	0.0423(15)	0.0396(16)	0.0218(14)	0.0185(13)	0.0187(12)
C(9)	0.0338(15)	0.0514(18)	0.0231(14)	0.0113(13)	0.0087(12)	0.0148(13)
C(10)	0.0267(13)	0.0508(17)	0.0323(15)	0.0191(13)	0.0183(12)	0.0179(12)
B(a)	0.0266(13)	0.0261(12)	0.0243(13)	0.0101(11)	0.0092(11)	0.0072(11)
B(c)	0.0219(12)	0.0294(13)	0.0240(13)	0.0123(11)	0.0113(11)	0.0113(10)
B(d)	0.0255(13)	0.0283(13)	0.0222(13)	0.0117(11)	0.0101(11)	0.0129(11)
B(b)	0.0154(11)	0.0383(15)	0.0254(13)	0.0152(12)	0.0032(10)	0.0097(11)
B(i)	0.0291(14)	0.0397(15)	0.0310(15)	0.0215(13)	0.0167(12)	0.0214(12)
B(j)	0.0337(15)	0.0359(14)	0.0303(15)	0.0210(12)	0.0173(12)	0.0209(12)
B(e)	0.0303(14)	0.0363(14)	0.0241(13)	0.0178(12)	0.0157(11)	0.0167(12)
B(g)	0.0252(13)	0.0383(15)	0.0236(13)	0.0169(12)	0.0091(11)	0.0160(11)
B(f)	0.0313(14)	0.0295(13)	0.0306(14)	0.0178(12)	0.0145(12)	0.0135(11)
B(h)	0.0399(16)	0.0288(14)	0.0310(15)	0.0154(12)	0.0184(13)	0.0175(12)

Table 2.10 Atomic Positions of Refined Hydrogen Atoms for $[BTMA]_2$**10**.

	x	y	z
H(a)	0.225(4)	0.302(4)	0.157(4)
H(b)	-0.366(4)	-0.116(4)	-0.169(4)
H(c)	0.210(4)	0.104(4)	-0.115(4)
H(d)	-0.120(4)	-0.131(4)	-0.303(4)
H(e)	-0.041(4)	0.125(4)	-0.335(4)
H(f)	0.158(4)	0.381(4)	-0.069(4)
H(g)	-0.368(4)	0.008(4)	-0.366(4)
H(h)	-0.042(4)	0.419(4)	0.100(4)
H(i)	-0.385(4)	0.182(4)	-0.096(4)
H(j)	-0.204(4)	0.320(4)	-0.195(4)
H(ah)	-0.016(4)	0.255(4)	0.098(4)
H(bi)	-0.238(4)	0.088(4)	-0.035(4)
HC(2)	0.720(5)	0.365(4)	0.182(4)
HC(3)	0.703(5)	0.142(4)	0.187(4)
HC(4)	0.764(5)	0.141(5)	0.405(4)
HC(5)	0.828(5)	0.360(4)	0.613(5)
HC(6)	0.835(5)	0.572(5)	0.596(5)
HC(71)	0.840(5)	0.641(4)	0.322(4)
HC(72)	0.863(5)	0.715(4)	0.479(4)
HC(81)	0.733(5)	0.823(4)	0.299(4)
HC(82)	0.747(5)	0.880(4)	0.456(4)
HC(83)	0.574(5)	0.832(4)	0.320(4)
HC(91)	0.505(5)	0.468(4)	0.164(4)
HC(92)	0.590(5)	0.576(4)	0.129(4)
HC(93)	0.431(5)	0.589(4)	0.146(4)
HC(10)	0.507(5)	0.545(5)	0.391(4)
HC(10)	0.608(5)	0.709(4)	0.511(4)
HC(10)	0.441(5)	0.668(4)	0.382(4)

Figure 2.5 Unit Cell Contents of $[BTMA]_2$**11**.$2CH_3CN$.

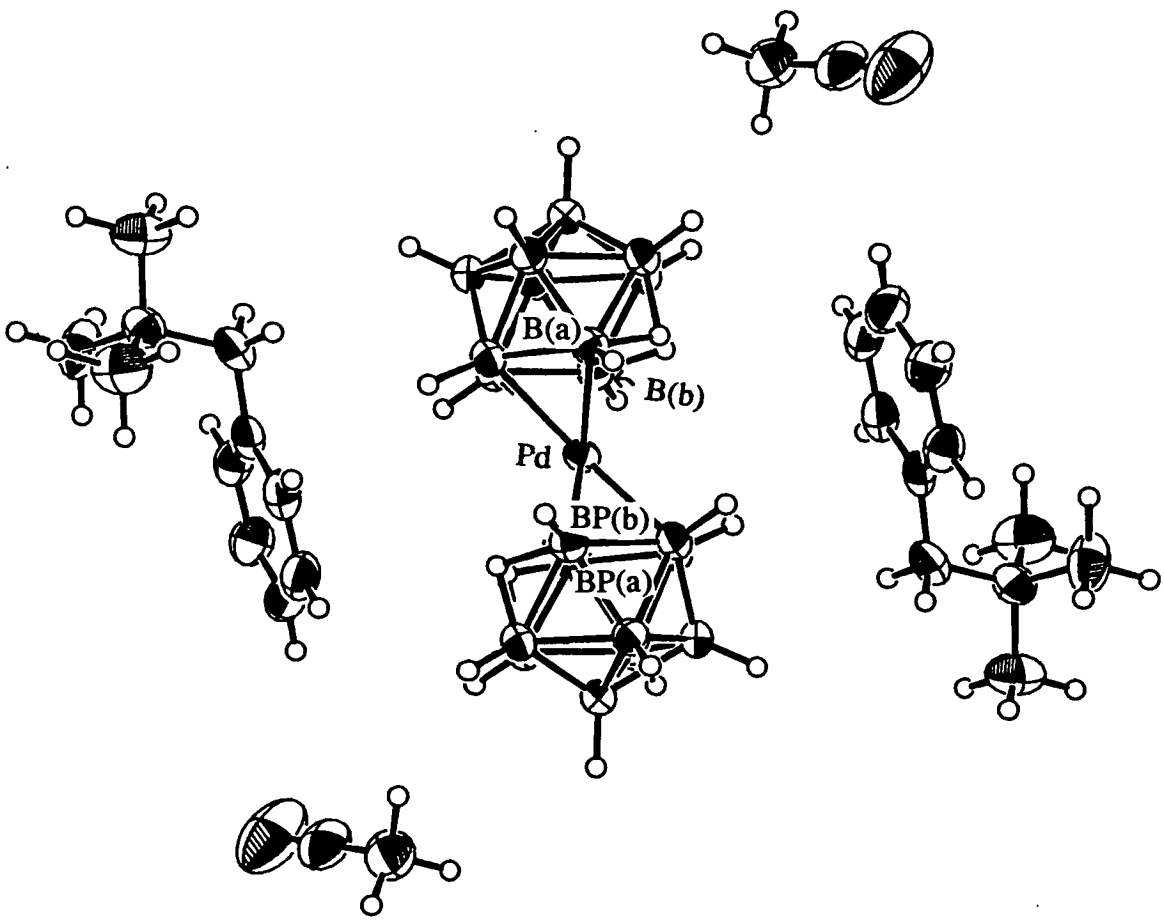

Table 2.11 Atomic Positions and Equivalent Isotropic Thermal Parameters ($Å^2$) of Non-Hydrogen Atoms of $[BTMA]_2 11.2CH_3CN$.

	x	y	z	Ueq
Pd	0.00000	0.00000	0.00000	0.0318(1)
B(a)	0.05941(14)	-0.22922(12)	0.11364(12)	0.0379(3)
B(b)	0.22174(13)	0.01148(12)	-0.11556(11)	0.0373(3)
B(c)	0.00450(14)	-0.18732(13)	-0.04241(12)	0.0380(3)
B(d)	0.09237(13)	-0.05590(13)	-0.16722(11)	0.0367(3)
B(j)	0.31487(14)	-0.27865(13)	-0.04638(12)	0.0404(3)
B(g)	0.28606(14)	-0.11884(13)	-0.17461(11)	0.0393(3)
B(i)	0.35679(14)	-0.13439(13)	-0.02919(12)	0.0398(3)
B(e)	0.15571(14)	-0.23081(13)	-0.13862(12)	0.0405(3)
B(f)	0.14379(15)	-0.33020(12)	0.02590(13)	0.0406(3)
B(h)	0.26101(14)	-0.27731(13)	0.10615(12)	0.0393(3)
C(1)	0.22667(13)	0.06314(14)	0.36903(12)	0.0469(3)
C(2)	0.20236(15)	-0.04673(14)	0.48024(13)	0.0531(3)
C(3)	0.31791(15)	0.03825(16)	0.27166(12)	0.0559(3)
C(4)	0.26626(17)	-0.17689(15)	0.49152(15)	0.0614(3)
C(5)	0.35606(17)	-0.20146(16)	0.39376(16)	0.0673(3)
C(6)	0.38256(16)	-0.09320(17)	0.28410(14)	0.0667(3)
C(7)	0.14763(14)	0.20338(15)	0.35198(13)	0.0532(3)
N(1)	0.22615(14)	0.28558(12)	0.40039(11)	0.0495(3)
C(8)	0.12703(20)	0.41814(16)	0.38372(18)	0.0735(3)
C(9)	0.25637(22)	0.21256(16)	0.53771(15)	0.0835(3)
C(10)	0.36641(18)	0.31553(18)	0.32580(19)	0.0820(3)
C(A1)	0.70103(20)	-0.40641(17)	0.13582(17)	0.0735(3)
C(A2)	0.69530(21)	-0.44438(16)	0.27029(18)	0.0758(3)
N(A1)	0.69141(25)	-0.47402(19)	0.37764(19)	0.1333(3)

Table 2.12 Selected Interatomic Distances (Å) and Interbond Angles (°) for $[BTMA]_2B_{11}H_{11}.2CH_3CN$.

Pd	- B(a)	2.2988(13)	B(i)	- B(h)	1.9837(19)
Pd	- B(b)	2.2955(12)	B(i)	- H(i)	1.050(3)
Pd	- B(c)	2.2375(14)	B(i)	-H(bi)	1.252(3)
Pd	- B(d)	2.2357(13)	B(e)	- B(f)	1.7713(19)
B(a)	- B(c)	1.7659(19)	B(e)	- H(e)	1.029(3)
B(a)	- B(f)	1.7603(19)	B(f)	- B(h)	1.7839(19)
B(a)	- B(h)	1.8292(19)	B(f)	- H(f)	0.984(3)
B(a)	- H(a)	1.131(3)	B(h)	-H(ah)	1.302(3)
B(a)	-H(ah)	1.214(3)	B(h)	- H(h)	1.053(3)
B(b)	- B(d)	1.7639(18)	C(1)	- C(2)	1.3974(20)
B(b)	- B(g)	1.7528(18)	C(1)	- C(3)	1.3883(20)
B(b)	- B(i)	1.8254(18)	C(1)	- C(7)	1.4942(20)
B(b)	-H(bi)	1.283(3)	C(2)	- C(4)	1.3744(22)
B(b)	- H(b)	1.101(3)	C(2)	-H(2C)	1.007(3)
B(c)	- B(d)	1.8249(19)	C(3)	- C(6)	1.3854(22)
B(c)	- B(e)	1.7720(19)	C(3)	-H(3C)	0.938(3)
B(c)	- B(f)	1.7814(19)	C(4)	- C(5)	1.3843(24)
B(c)	- H(c)	1.158(3)	C(4)	-H(4C)	0.731(4)
B(d)	- B(g)	1.7854(18)	C(5)	- C(6)	1.3828(24)
B(d)	- B(e)	1.7743(19)	C(5)	-H(5C)	0.926(4)
B(d)	- H(d)	1.096(3)	C(6)	-H(6C)	0.904(4)
B(j)	- B(g)	1.7799(19)	C(7)	-H(1C7)	0.897(3)
B(j)	- B(i)	1.7558(19)	C(7)	-H(2C7)	0.991(3)
B(j)	- B(e)	1.7789(19)	C(7)	- N(1)	1.5231(19)
B(j)	- B(f)	1.7782(19)	N(1)	- C(8)	1.4955(23)
B(j)	- B(h)	1.7529(19)	N(1)	- C(9)	1.4893(22)
B(j)	- H(j)	1.114(3)	N(1)	- C(0)	1.4813(23)
B(g)	- B(i)	1.7838(19)	AC(1)	-AC(2)	1.422(3)
B(g)	- B(e)	1.7716(19)	AC(2)	- AN	1.137(3)
B(g)	- H(g)	1.009(3)			

B(a)	- Pd	- B(c)	45.80(5)	B(j)	- B(i)	- B(h)	55.50(7)
B(b)	- Pd	- B(c)	84.05(5)	B(c)	- B(e)	- B(d)	61.94(7)
B(b)	- Pd	- B(d)	45.80(5)	B(c)	- B(e)	- B(f)	60.36(8)
B(c)	- Pd	- B(d)	48.15(5)	B(d)	- B(e)	- B(g)	60.46(7)
Pd	- B(a)	- B(c)	65.27(6)	B(j)	- B(e)	- B(g)	60.17(7)
B(c)	- B(a)	- B(f)	60.69(8)	B(j)	- B(e)	- B(f)	60.11(8)
B(f)	- B(a)	- B(h)	59.56(7)	B(a)	- B(f)	- B(c)	59.81(8)
Pd	- B(b)	- B(d)	65.31(6)	B(a)	- B(f)	- B(h)	62.14(8)
B(d)	- B(b)	- B(g)	61.02(7)	B(c)	- B(f)	- B(e)	59.84(8)
B(g)	- B(b)	- B(i)	59.76(7)	B(j)	- B(f)	- B(e)	60.15(8)
Pd	- B(c)	- B(a)	68.93(6)	B(j)	- B(f)	- B(h)	58.96(8)
Pd	- B(c)	- B(d)	65.87(6)	B(a)	- B(h)	- B(f)	58.29(7)
B(a)	- B(c)	- B(f)	59.50(7)	B(j)	- B(h)	- B(i)	55.64(7)
B(d)	- B(c)	- B(e)	59.09(7)	B(j)	- B(h)	- B(f)	60.36(8)
B(e)	- B(c)	- B(f)	59.80(8)	C(2)	- C(1)	- C(3)	118.76(13)
Pd	- B(d)	- B(b)	68.89(6)	C(2)	- C(1)	- C(7)	120.45(13)
Pd	- B(d)	- B(c)	65.97(6)	C(3)	- C(1)	- C(7)	120.66(13)
B(b)	- B(d)	- B(g)	59.18(7)	C(1)	- C(2)	- C(4)	120.27(14)
B(c)	- B(d)	- B(e)	58.97(7)	C(1)	- C(3)	- C(6)	120.60(14)
B(g)	- B(j)	- B(i)	60.59(7)	C(2)	- C(4)	- C(5)	120.82(15)
B(g)	- B(j)	- B(e)	59.71(7)	C(4)	- C(5)	- C(6)	119.34(15)
B(i)	- B(j)	- B(h)	68.86(8)	C(3)	- C(6)	- C(5)	120.21(15)
B(e)	- B(j)	- B(f)	59.73(8)	C(1)	- C(7)	- N(1)	115.49(12)
B(f)	- B(j)	- B(h)	60.68(8)	C(7)	- N(1)	- C(8)	108.01(12)
B(b)	- B(g)	- B(d)	59.80(7)	C(7)	- N(1)	- C(9)	110.90(12)
B(b)	- B(g)	- B(i)	62.14(7)	C(7)	- N(1)	-C(10)	111.15(12)
B(d)	- B(g)	- B(e)	59.84(7)	C(8)	- N(1)	- C(9)	108.99(13)

B(j) - B(g) - B(i)	59.03(7)	C(8) - N(1) -C(10)	107.82(13)
B(j) - B(g) - B(e)	60.12(7)	C(9) - N(1) -C(10)	109.87(13)
B(b) - B(i) - B(g)	58.10(7)	AC(1) -AC(2) - AN	179.48(22)
B(j) - B(i) - B(g)	60.37(7)		

Table 2.13 Anisotropic Thermal Parameters ($Å^2$) for $[BTMA]_2$**11.2**CH_3CN.

	U11	U22	U33	U23	U13	U12
Pd	0.0292(1)	0.0293(1)	0.0291(1)	-0.0079(1)	-0.0011(1)	-0.0028(1)
B(a)	0.0393(3)	0.0325(3)	0.0330(3)	-0.0074(2)	-0.0032(3)	-0.0052(2)
B(b)	0.0329(3)	0.0372(3)	0.0344(3)	-0.0129(2)	-0.0004(2)	-0.0071(2)
B(c)	0.0327(3)	0.0371(3)	0.0368(3)	-0.0119(2)	-0.0055(2)	-0.0069(2)
B(d)	0.0317(3)	0.0397(3)	0.0307(3)	-0.0110(2)	-0.0042(2)	-0.0042(2)
B(j)	0.0356(3)	0.0380(3)	0.0406(3)	-0.0177(2)	-0.0081(3)	0.0001(3)
B(g)	0.0328(3)	0.0443(3)	0.0334(3)	-0.0164(2)	-0.0017(2)	-0.0036(3)
B(i)	0.0315(3)	0.0424(3)	0.0387(3)	-0.0170(2)	-0.0063(2)	-0.0047(2)
B(e)	0.0375(3)	0.0415(3)	0.0367(3)	-0.0188(2)	-0.0078(2)	-0.0041(3)
B(f)	0.0409(3)	0.0317(3)	0.0420(3)	-0.0132(2)	-0.0085(3)	-0.0047(2)
B(h)	0.0397(3)	0.0351(3)	0.0354(3)	-0.0117(2)	-0.0111(2)	-0.0018(3)
C(1)	0.0338(3)	0.0596(3)	0.0406(3)	-0.0214(2)	-0.0069(2)	-0.0136(3)
C(2)	0.0460(3)	0.0599(3)	0.0463(3)	-0.0244(2)	0.0028(3)	-0.0186(3)
C(3)	0.0451(3)	0.0747(3)	0.0393(3)	-0.0243(3)	-0.0038(3)	-0.0169(3)
C(4)	0.0626(3)	0.0566(3)	0.0558(3)	-0.0219(3)	-0.0002(3)	-0.0201(3)
C(5)	0.0591(3)	0.0666(3)	0.0701(3)	-0.0404(3)	-0.0038(3)	-0.0129(3)
C(6)	0.0510(3)	0.0865(3)	0.0567(3)	-0.0446(3)	0.0005(3)	-0.0147(3)
C(7)	0.0353(3)	0.0628(3)	0.0488(3)	-0.0163(3)	-0.0104(3)	-0.0053(3)
N(1)	0.0486(3)	0.0422(3)	0.0450(3)	-0.0081(2)	-0.0072(3)	-0.0046(3)
C(8)	0.0730(3)	0.0519(3)	0.0756(3)	-0.0168(3)	-0.0006(3)	0.0066(3)
C(9)	0.1340(3)	0.0524(3)	0.0529(3)	-0.0109(3)	-0.0360(3)	-0.0207(3)
C(10)	0.0542(3)	0.0675(3)	0.1080(3)	-0.0324(3)	0.0116(3)	-0.0217(3)
C(A1)	0.0745(3)	0.0591(3)	0.0741(3)	-0.0250(3)	-0.0085(3)	-0.0118(3)
C(A2)	0.0925(3)	0.0447(3)	0.0798(3)	-0.0262(3)	-0.0068(3)	-0.0149(3)
N(A1)	0.2251(3)	0.0749(3)	0.0827(3)	-0.0286(3)	-0.0059(3)	-0.0353(3)

Table 2.14 Atomic Positions and Equivalent Isotropic Thermal Parameters (Å^2) of Refined and Calculated Hydrogen Atoms of [BTMA]$_2$**11**.2CH_3CN.

	x	y	z	Ueq
H(A1)	0.63900	-0.46774	0.11129	
H(A2)	0.81488	-0.42217	0.10174	
H(A3)	0.65360	-0.30047	0.09235	
H(a)	-0.0010(3)	-0.2714(3)	0.2091(3)	0.0436(3)
H(c)	-0.1105(3)	-0.2035(3)	-0.0602(3)	0.0563(3)
H(d)	0.0331(3)	0.0107(3)	-0.2528(3)	0.0398(3)
H(j)	0.4074(3)	-0.3621(3)	-0.0473(3)	0.0467(3)
H(i)	0.4646(3)	-0.1208(3)	-0.0214(3)	0.0522(3)
H(e)	0.1430(3)	-0.2753(3)	-0.2017(3)	0.0539(3)
H(ah)	0.1627(3)	-0.1909(3)	0.1397(3)	0.0473(3)
H(bi)	0.2769(3)	-0.0377(3)	-0.0054(3)	0.0496(3)
H(g)	0.3531(3)	-0.1007(3)	-0.2539(3)	0.0502(3)
H(f)	0.1306(3)	-0.4258(3)	0.0539(3)	0.0655(3)
H(h)	0.3201(3)	-0.3392(3)	0.1878(3)	0.0461(3)
H(b)	0.2569(3)	0.1119(3)	-0.1589(3)	0.0436(3)
H(2C)	0.1381(3)	-0.0337(3)	0.5539(3)	0.0497(3)
H(3C)	0.3378(3)	0.1111(3)	0.1974(3)	0.0561(3)
H(4C)	0.2554(3)	-0.2336(3)	0.5509(3)	0.0779(3)
H(5C)	0.4015(3)	-0.2896(3)	0.4051(3)	0.0664(3)
H(6C)	0.4438(3)	-0.0933(3)	0.2160(3)	0.0648(3)
H(1C7)	0.0581(3)	0.2065(3)	0.3923(3)	0.0552(3)
H(2C7)	0.1351(3)	0.2610(3)	0.2609(3)	0.0705(3)
H(1C8)	0.02360	0.39940	0.43721	
H(2C8)	0.10578	0.47242	0.28416	
H(3C8)	0.18013	0.47834	0.41776	
H(1C9)	0.32794	0.11664	0.55058	
H(2C9)	0.15324	0.19430	0.59189	
H(3C9)	0.30982	0.27375	0.57023	
H(1C10)	0.44037	0.22137	0.33609	
H(2C10)	0.41774	0.37648	0.36026	
H(3C10)	0.34338	0.37055	0.22667	

The metal centres of **10** and **11** both exhibit the expected formal square planar coordination. Two metal to boron distances are observed, the M-B(a), B(b) distances being significantly longer than the M-B(c), B(d) distances. The longest borane connectivity is again B(h)-B(i); 1.987(5)Å in **10** and 1.9837(19)Å in **11**.

The results of r.m.s. misfit calculations between the three *bis*-borane systems and **1** and **2** are shown in Table 2.15, along with the B(a)...B(b), B(h)-B(i) and B(c)-B(d) distances and **H** for these metallaboranes.

Considering first the r.m.s. misfits, certain trends are immediately apparent. Although actual differences may not be statistically significant, as the triad is descended, the increasingly good fit with the *arachno*-$[B_{10}H_{12}]^{4-}$ fragment coupled with the poorer fit against *nido*-$[B_{10}H_{12}]^{2-}$, suggests the greatest *arachno* character is seen in the borane fragment of **10**. This is necessarily reflected in the verticities with the Pt centre behaving as the best cluster vertex. A simple explanation of these observations is possible; as the principle quantum number of the metal valence orbitals increases from Ni through to Pt, the extent of overlap of these metal orbitals with the borane cage increases, resulting in greater interaction between metal and cage.

However, the absolute nature of the borane fragment is not so clear. The r.m.s. misfit values are consistently lower against *nido*-$[B_{10}H_{12}]^{2-}$, but, when compared with the values obtained above between unambiguously *nido*-$\{B_{10}\}$ cages, they appear somewhat too high to indicate true *nido* character. Likewise, the results against *arachno*-$[B_{10}H_{12}]^{4-}$ are lower than would be expected for a true *nido* species. The structure of the $\{B_{10}\}$ fragments of **8**, **10** and **11** appear therefore to be intermediate between *nido*-$[B_{10}H_{12}]^{2-}$ and *arachno*-$[B_{10}H_{12}]^{4-}$. This is the first indication that the problem of the geometry of $B_{10}H_{12}$ cages is not simply a question of assigning pure *nido* or *arachno* character.

Table 2.15 Comparison of R.m.s. Misfits(Å), Metal Verticities(%) and Selected Cage Parameters (Å) for the Ni Triad *Bis*-Boranes.

Metallaborane	R.m.s. Misfit		Verticity	B(a)...B(b)	B(c)-B(d)	B(h)-B(i)	H
	vs 1	*vs* 2					
8	0.074	0.134	34.9%	3.392	1.870	1.973	0.4737
11	0.081	0.127	38.4%	3.352	1.825	1.984	0.5693
10	0.083	0.124	39.4%	3.347	1.825	1.988	0.5370

Analysis of the various intramolecular distances in Table 2.15 suggests further intricasies. Whilst certain trends are discernable, most notably in the B(a)...B(b) and B(c)-B(d) distances, no correlation between **H** and verticity is seen. The comparable values of **H** for **9** (0.321Å, verticity = 69.1%) and **7** (0.717Å, verticity = 13.3%) show that this parameter reflects general trends in verticity. However, as a tool for metallaborane analysis, it requires the assumption that a change in the degree of interaction of the metal with the cage will be accurately reflected in the height of the metal above the B(a)B(h)B(i)B(b) face. This appears to be the case when **10** and **11** are compared; the Pd atom in **11** exhibits both a lower verticity and a higher value of **H** than the Pt atom in **10**. However in **8**, the Ni atom, despite having the lowest verticity of the three, also has the lowest value of **H**. An important factor in these results may be the variation in size of the metal centre. This is most marked in moving from Ni to Pd; thus the low value of **H** in **8** can be attributed to the smaller size of the Ni atom rather than being indicative of a greater interaction with the borane. In moving from second to third row transition metal elements, the variation in atomic size is not so marked and so the electronic effects of varying the metal centre are more greatly reflected in the magnitude of **H**. From the point of view of assessing the nature of $MB_{10}H_{12}$ metallaboranes in general, **H** will only be of use when the metals involved are of a comparable size. Clearly more data would aid development of these ideas.

Assessment of Metal Oxidation States

Several approaches, most of which focused on the cobaltaborane, were employed in an attempt to assign the metal oxidation state in these species.

Electrochemistry

The electrochemistry discussed here has been performed, in conjunction with

EHMO studies, purely to assess the likely metal oxidation states in the $MB_{10}H_{12}$ species described above. For a fuller discussion of the redox behaviour of the *bis*-borane systems see Chapter 5.

Here, and elsewhere in this work, all $E_{1/2}$ values are quoted relative to Ag/AgCl reference electrode against which the ferrocene/ferrocinium couple appears at +0.55V. The previously reported electrochemical study on the *bis*-borane nickel species, **8**,[63] was repeated under the same experimental conditions as those employed for the studies of **10** and **11** and is included for comparative purposes. The electrochemical oxidative potentials for **8**, **10** and **11** in acetonitrile and that of **9** in dichloromethane are shown below:

Metallaborane	E_p^a
8	+1.24V
9	+1.18V
10	+1.40V
11	+1.28V

In all cases the structure of the electrochemical wave was very similar, there being no evidence for a return wave. Thus, a reversible electron transfer step is being followed by a very fast chemical reaction; an ec (electron transfer-chemical reaction) mechanism. The chemical reaction of the oxidised species cannot be slowed down sufficiently for the electrochemical characterisation of the products and only in the case of **9** was a redox-active daughter product observed on the timescale of the cyclic voltammogram. The results of coulometric studies carried out on these oxidative couples were unclear. In all four cases the solution decolourised during the course of the electrosynthesis and at least 5 electrons per mole of metallaborane were passed. Cyclic voltammetry of the product solutions was complicated and indicated the

presence of a number of degradation products.

The reductive behaviour of the systems exhibits more variation. In acetonitrile, **10** and **11** exhibit reversible couples at -1.53V and -1.67V respectively and coulometric studies show that one electron is involved in the transfer process. **9** shows a broad, irreversible reductive response in the d.c. cyclic voltammogram, whilst no reductive response for **8** was observed in the potential range of 0 to -2.5V in either acetonitrile or dimethylformamide (DMF).

The electrochemical behaviour was also examined using a series of EHMO calculations to determine the nature of the frontier MO's of these metallaborane systems. In all four cases the HOMO of the system was primarily located (>90% in the bisboranes, 75% in **9**) on, and bonding within, the borane framework. Inspection of the LUMO's of these species indicated a higher degree of metal based character, but extensive delocalisation onto the boron atoms directly bonded to the metal precluded a simple interpretation of the electrochemical reductions in terms of a metal-based mechanism.

The delocalised nature of the frontier MO's of these four metallaboranes means that, for the specific goal of assessing metal oxidation states, these electrochemical studies are of little value.

The Synthesis and Structure of $[(CO)_3Co(DMBD)]^+[FeCl_3(CH_3CN)]^-$, $12[FeCl_3(CH_3CN)]^-$ (DMBD = 2,3-dimethylbutadiene).

The synthesis and structural characterisation of this cationic Co^I species was undertaken in the expectation that the coordination sphere around the cobalt centre would be analogous to that observed in **9** and that, therefore, any variations within the $Co(CO)_3$ unit would be attributable to a change in formal oxidation state.

Synthesis

Spectroscopic evidence for the cation had been previously reported.[82] However the bulk preparation and isolation of this species, by means of the chemical oxidation of the $[Co(CO)_2(DMBD)]_2$ dimer with ferric chloride, was not known. This synthesis occurs only in low yield and the isolation of **12** as the $[FeCl_3(CH_3CN)]^-$ salt was unexpected. This novel anion appears to be formed by the complimentary reduction of ferric chloride by the cobalt starting material and subsequent ligation by acetonitrile upon dissolution in this solvent. It has not previously been structurally characterised.

Structure of the $[FeCl_3(CH_3CN)]^-$ Anion.

The structure of the anion is unexceptional: the coordination of the central iron atom is only slightly distorted away from tetrahedral. Cl-Fe-Cl angles average 113.49(9)° and N-Fe-Cl angles 105.09(22)°. The geometry of the ligating acetonitrile nitrogen atom is non-linear, Fe-N(1)-C(10) = 170.6(4)°, although the sequence N(1)-C(10)-C(11) is linear. These angles and the N(1)-C(10) and C(10)-C(11) distances are unexceptional in comparison with other examples of bound acetonitrile.[83] A view of the anion is presented in Figure 2.6 and data from the X-ray study are tabulated along with that for **12**.

Molecular Structure of 12.

12 is shown in Figure 2.7. Table 2.16 lists the atomic positions of refined atoms along with equivalent isotropic thermal parameters. Table 2.17 details interatomic distances and interbond angles, Table 2.18 anisotropic thermal parameters and Table 2.19 the positions of refined and calculated hydrogen atoms for both **12** and the anion discussed above.

Figure 2.6 Molecular Structure of $[FeCl_3(CH_3CN]^-$.

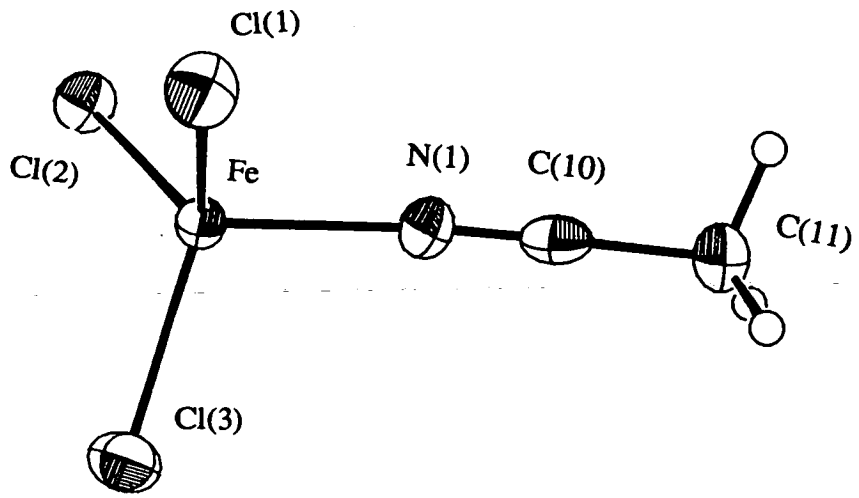

Figure 2.7 Molecular Structure of **12**.

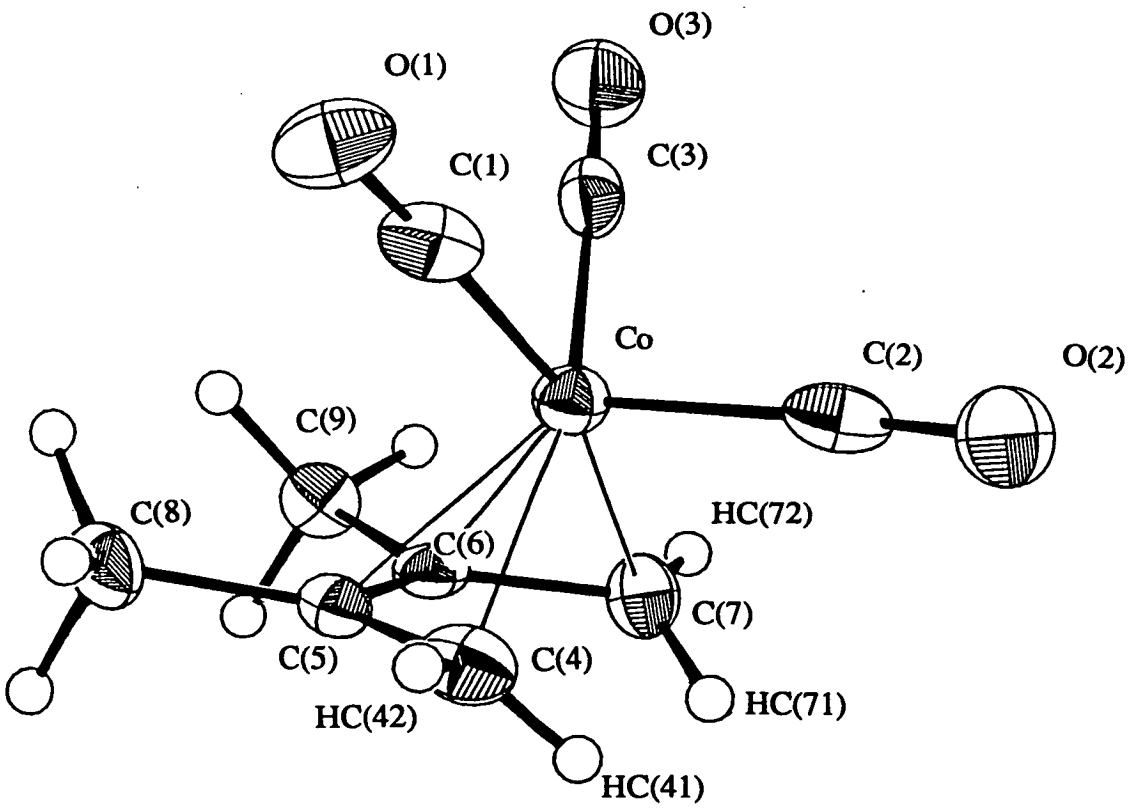

Table 2.16 Atomic Positions and Equivalent Isotropic Thermal Parameters ($Å^2$) of Refined Non-Hydrogen Atoms of **12**[$FeCl_3CH_3CN$].

	x	y	z	Ueq
Fe	0.22731(6)	0.52612(5)	0.69958(5)	0.0231(4)
Cl(1)	0.33475(12)	0.46608(11)	0.57326(9)	0.0409(8)
Cl(2)	0.34165(11)	0.61722(10)	0.83185(9)	0.0328(8)
Cl(3)	0.10651(12)	0.40022(11)	0.76295(10)	0.0414(9)
N(1)	0.1174(4)	0.6387(4)	0.6165(3)	0.035(3)
C(10)	0.0509(5)	0.6898(4)	0.5610(4)	0.034(3)
C(11)	-0.0364(4)	0.7552(4)	0.4906(4)	0.039(3)
Co	0.69182(6)	0.43230(6)	0.81949(5)	0.0251(4)
C(1)	0.7827(5)	0.3509(4)	0.9218(4)	0.034(4)
O(1)	0.8410(4)	0.3033(3)	0.9855(3)	0.045(3)
C(2)	0.5438(6)	0.3696(4)	0.8211(4)	0.034(4)
O(2)	0.4504(4)	0.3338(3)	0.8254(3)	0.049(3)
C(3)	0.7531(4)	0.3602(4)	0.7113(4)	0.028(3)
O(3)	0.7927(3)	0.3197(3)	0.6445(3)	0.042(3)
C(4)	0.6628(5)	0.5538(4)	0.9292(4)	0.034(4)
C(5)	0.7608(4)	0.5837(4)	0.8768(4)	0.022(3)
C(6)	0.7399(4)	0.5865(4)	0.7645(4)	0.023(3)
C(7)	0.6222(5)	0.5584(4)	0.7177(4)	0.028(3)
C(8)	0.8848(4)	0.6017(4)	0.9367(4)	0.033(3)
C(9)	0.8387(4)	0.6087(4)	0.6983(4)	0.031(3)

Table 2.17 Selected Interatomic Distances (Å) and Interbond Angles (°) for **12**[$FeCl_3CH_3CN$].

Fe	-Cl(1)	2.2540(14)	C(1)	- O(1)	1.130(7)
Fe	-Cl(2)	2.2642(14)	C(2)	- O(2)	1.144(7)
Fe	-Cl(3)	2.2554(15)	C(3)	- O(3)	1.122(6)
Fe	- N(1)	2.035(4)	C(4)	- C(5)	1.408(7)
N(1)	-C(10)	1.140(7)	C(4)	-HC(41)	0.94(5)
C(10)	-C(11)	1.469(7)	C(4)	-HC(42)	0.99(5)
Co	- C(1)	1.831(5)	C(5)	- C(6)	1.418(7)
Co	- C(2)	1.832(6)	C(5)	- C(8)	1.516(7)
Co	- C(3)	1.837(5)	C(6)	- C(7)	1.420(7)
Co	- C(4)	2.077(6)	C(6)	- C(9)	1.504(7)
Co	- C(5)	2.076(5)	C(7)	-HC(71)	0.97(5)
Co	- C(6)	2.082(5)	C(7)	-HC(72)	0.85(5)
Co	- C(7)	2.082(5)			

Cl(1)	- Fe	-Cl(2)	112.32(5)	C(6)	- Co - C(7) 39.90(20)
Cl(1)	- Fe	-Cl(3)	116.40(5)	Co	- C(1) - O(1) 177.9(5)
Cl(1)	- Fe	- N(1)	100.94(13)	Co	- C(2) - O(2) 177.0(5)
Cl(2)	- Fe	-Cl(3)	111.76(5)	Co	- C(3) - O(3) 177.4(5)
Cl(2)	- Fe	- N(1)	108.13(13)	Co	- C(4) - C(5) 70.2(3)
Cl(3)	- Fe	- N(1)	106.22(13)	Co	- C(4) -HC(41) 105.2(30)
Fe	- N(1)	-C(10)	170.6(4)	Co	- C(4) -HC(42) 119.0(28)
N(1)	-C(10)	-C(11)	179.0(6)	C(5)	- C(4) -HC(41) 121.0(30)
C(1)	- Co	- C(2)	101.27(25)	C(5)	- C(4) -HC(42) 122.8(28)
C(1)	- Co	- C(3)	92.85(24)	HC(41)	- C(4) -HC(42) 110.8(41)
C(1)	- Co	- C(4)	91.26(23)	Co	- C(5) - C(4) 70.2(3)
C(1)	- Co	- C(5)	94.16(22)	Co	- C(5) - C(6) 70.3(3)
C(1)	- Co	- C(6)	124.83(22)	Co	- C(5) - C(8) 125.4(3)
C(1)	- Co	- C(7)	164.30(23)	C(4)	- C(5) - C(6) 116.6(4)
C(2)	- Co	- C(3)	104.20(24)	C(4)	- C(5) - C(8) 121.7(4)
C(2)	- Co	- C(4)	93.41(24)	C(6)	- C(5) - C(8) 121.6(4)
C(2)	- Co	- C(5)	131.06(22)	Co	- C(6) - C(5) 69.9(3)
C(2)	- Co	- C(6)	130.45(22)	Co	- C(6) - C(7) 70.0(3)
C(2)	- Co	- C(7)	92.24(23)	Co	- C(6) - C(9) 126.2(3)
C(3)	- Co	- C(4)	160.74(23)	C(5)	- C(6) - C(7) 116.0(4)
C(3)	- Co	- C(5)	121.21(21)	C(5)	- C(6) - C(9) 122.1(4)
C(3)	- Co	- C(6)	91.69(21)	C(7)	- C(6) - C(9) 121.7(4)
C(3)	- Co	- C(7)	91.51(22)	Co	- C(7) - C(6) 70.1(3)
C(4)	- Co	- C(5)	39.64(20)	Co	- C(7) -HC(71) 100.3(28)
C(4)	- Co	- C(6)	70.63(20)	Co	- C(7) -HC(72) 119.3(34)
C(4)	- Co	- C(7)	79.90(22)	C(6)	- C(7) -HC(71) 120.3(28)
C(5)	- Co	- C(6)	39.88(18)	C(6)	- C(7) -HC(72) 111.2(34)
C(5)	- Co	- C(7)	70.75(20)	HC(71)	- C(7) -HC(72) 123.1(44)

Table 2.18 Anisotropic Thermal Parameters (Å^2) for **12**[$FeCl_3CH_3CN$].

	U11	U22	U33	U23	U13	U12
Fe	0.0216(4)	0.0250(4)	0.0223(4)	0.0020(3)	0.0022(3)	0.0011(3)
Cl(1)	0.0434(8)	0.0496(9)	0.0296(7)	-0.0038(7)	0.0076(6)	0.0050(7)
Cl(2)	0.0344(8)	0.0319(7)	0.0314(7)	-0.0047(6)	0.0018(6)	-0.0015(6)
Cl(3)	0.0422(8)	0.0381(9)	0.0435(8)	0.0043(7)	0.0079(7)	-0.0080(7)
N(1)	0.0252(27)	0.0378(28)	0.0399(27)	0.0090(24)	0.0025(22)	0.0067(23)
C(10)	0.0263(33)	0.0368(34)	0.0387(34)	0.0001(30)	0.0138(29)	-0.0050(30)
C(11)	0.0352(35)	0.0423(36)	0.0387(32)	0.0103(30)	-0.0006(28)	0.0052(29)
Co	0.0259(4)	0.0228(4)	0.0263(4)	0.0004(3)	0.0038(3)	0.0006(3)
C(1)	0.0429(39)	0.0262(34)	0.0323(34)	0.0014(29)	0.0147(30)	-0.0005(29)
O(1)	0.0511(27)	0.0407(26)	0.0422(25)	0.0122(21)	0.0057(21)	0.0156(22)
C(2)	0.0501(42)	0.0198(31)	0.0332(33)	0.0025(26)	0.0126(30)	0.0055(30)
O(2)	0.0382(26)	0.0376(25)	0.0731(30)	0.0025(21)	0.0218(23)	-0.0095(22)
C(3)	0.0240(33)	0.0267(33)	0.0318(32)	0.0056(28)	-0.0026(27)	-0.0060(27)
O(3)	0.0410(25)	0.0470(26)	0.0377(23)	-0.0133(21)	0.0099(20)	-0.0003(20)
C(4)	0.0455(39)	0.0282(34)	0.0276(32)	-0.0006(27)	0.0041(32)	0.0032(30)
C(5)	0.0279(32)	0.0187(29)	0.0202(30)	-0.0003(24)	0.0018(26)	0.0011(25)
C(6)	0.0245(32)	0.0148(29)	0.0309(33)	0.0010(24)	0.0074(26)	0.0025(25)
C(7)	0.0295(34)	0.0336(35)	0.0200(30)	0.0011(29)	-0.0016(29)	-0.0035(28)
C(8)	0.0390(37)	0.0295(34)	0.0283(30)	-0.0011(26)	-0.0124(27)	-0.0008(28)
C(9)	0.0340(35)	0.0309(34)	0.0291(30)	-0.0003(26)	0.0061(26)	-0.0016(27)

Table 2.19 Positions of Refined and Calculated Hydrogen Atoms for **12**[$FeCl_3CH_3CN$].

	x	y	z
HCN(1)	0.0151	0.8090	0.4461
HCN(2)	-0.0965	0.8045	0.5310
HCN(3)	-0.0878	0.6981	0.4372
HC(81)	0.9563	0.5612	0.9026
HC(82)	0.8842	0.5731	1.0170
HC(83)	0.8986	0.6905	0.9368
HC(91)	0.9185	0.5652	0.7322
HC(92)	0.8552	0.6971	0.7016
HC(93)	0.8152	0.5834	0.6168
HC(41)	0.585(4)	0.581(4)	0.906(4)
HC(42)	0.672(4)	0.534(4)	1.006(4)
HC(71)	0.554(4)	0.580(4)	0.752(4)
HC(72)	0.619(4)	0.549(4)	0.651(4)

From Figure 2.7 it is clear that the coordination of the cobalt atom in **12** is analogous to that in **9**. The cation adopts effective, non-crystallographically imposed C_s symmetry, about the plane through Co, C(2), O(2) and the midpoint of the C(5)-C(6) bond. The position of the unique carbonyl ligand, *endo* to the μ_4 ligand, is the same as that seen in **9**. The structure of the DMBD moiety is entirely consistent with that in a large number of isoelectronic iron analogues.[84] The displacement of the *syn* and *anti* hydrogens atoms out of the C(4)C(5)C(6)C(7) plane has also been noted in iron butadiene systems.[85] Here, the former are an average of 0.172Å away from the cobalt atom, the latter an average of 0.516Å towards the metal.

Comparison of the $\{Co(CO)_3\}$ units of **12** and **9** is drawn in Table 2.20. The only significant differences are a narrowing of the C(1)-Co-C(3) angle and a lengthening of the Co-C(2) bond in the former. The consistently shorter Co-C bonds in **9** may be interpreted as reflecting a smaller metal centre, suggesting the presence of Co^{III} as opposed to Co^{I}. However, other differences between the two species, not least the general inaccuracy of the model for **9**, invalidate such a simple approach. The shorter Co-C distances in **9** could also result from the difference in overall charge between the two species. Moreover, the variation in the nature of the μ_4 ligand will clearly effect the structure of the $Co(CO)_3$ unit. A recent study[86] of the interaction of a $Mn(CO)_3$ unit with a Cp^- ring and the monoanionic carbaborane $[C_2B_9H_{10}S(Me)_2]^-$, showed the latter to be the better donor due to the contribution to the frontier MO's from relatively higher lying boron 2p orbitals. By the same argument it seems reasonable that the borane in **9** will increase electron density on the metal centre relative to that in **12** and so increase the extent of π-backbonding to the carbonyl ligands.

Table 2.20 Comparison of the $\{(CO)_3Co\}$ Fragments of **9** and **12**.

Bonds/Å	**9**	**12**
Co-C(1,3)	1.802(14)	1.834(5)
Co-C(2)	1.763(11)	1.832(6)
C(1,3)-O(1,3)	1.134(18)	1.126(7)
C(2)-O(2)	1.165(15)	1.144(7)
Angles(°)		
C(2)-Co-C(1,3)	102.97(58)	102.74(25)
C(1)-Co-C(3)	95.58(63)	92.85(24)

To assess the effect of overall charge on Co-CO backbonding a series of d^6 complexes $[CpM(CO)_3]^n$ [M=Fe, n=+1;[87] M=Mn, n= 0;[88] M=Cr, n=-1[89]] were considered. In these the effective symmetry of the $\{M(CO)_3\}$ fragment is C_{3v}, giving rise to C-O vibrations of a_1 and e symmetry. As the electron density on the metal increases in moving from the iron to chromium complex, the frequency of the a_1 C-O stretch in the infrared spectrum decreases by 170cm^{-1} and that of the e C-O stretch by 250cm^{-1}. The difference in these stretching frequencies is not so marked in the isoelectronic cobalt systems, **9** and **12** (65cm^{-1} and 80cm^{-1} respectively, see Table 2.21 below). This suggests that less electron density is available for π-backbonding in **9** than would be expected from overall charge considerations alone. Indeed, as Table 2.21 indicates, and as mentioned previously, the carbonyl stretches for **9** do occur at a relatively high energy. Taking into account the stronger donor qualities of the μ_4 borane moiety, this variation in carbonyl stretching frequencies is only consistent with the cobalt atom in **9** being present in a higher formal oxidation state than that in **12**.

Table 2.21 Carbonyl Infrared Stretching Frequencies (cm^{-1}) in Complexes Containing $\{M(CO)_3\}$ Fragments.

Complex	a_1 stretch	e stretch
$[CpFe(CO)_3]^+$	2070	2027
$CpMn(CO)_3$	2025	1945
$[CpCr(CO)_3]^-$	1900	1776*
12	2130	2090*
9	2065	2010*

* components of 'e' stretch resolved and average taken.

K-edge X-ray Absorption Near Edge Spectroscopy (XANES) of 9.

The XANES Technique

The process involved in the K-edge XANES experiment is the excitation of metal core 1s electrons by X-rays. The electron can either be excited to higher lying metal orbitals or fully ejected from the metal atom. The position of the absorption edge is calculated as the midpoint between that where absorption starts and that where the electron has been fully emitted. The energy of the absorption edge depends largely on the oxidation state of the metal. Fine structure within the absorption edge is more dependent on the nature of the surrounding ligands, as it involves the higher lying metal orbitals where the influence of the ligands will be felt. Further information on the environment of the metal can be obtained from the fine structure beyond the absorption edge. This is the extended X-ray absorption fine structure (EXAFS) experiment.

Calibration Species

Little work has been done in this area on cobalt systems. Therefore, it was necessary to use two well defined cobalt species to calibrate the results. A Co^{I} and Co^{III} species were used as these were the likely oxidation states of the cobalt in **9**. Although an effort was made to retain a similar coordination sphere to that in **9**, this proved impossible, firstly due to there being no other $\{(CO)_3Co^{III}\}^+$ containing species available in the literature and, secondly, because the air-sensitive nature and low yield synthesis of **12** precluded its use as a Co^{I} standard.

However, considering the crucial importance of oxidation state, rather than metal environment in the XANES experiment, it was felt that the standards used, $[(CO)_3Co(PPh_3)_2]^+[BPh_4]^-$[90] ($Co^{I}$) and $[Co(en)_3]^{3+}3Br^-$[91] (Co^{III}, en =

ethylenediamine), were adequate.

Results

The values obtained for the position of the absorption edge in **9** and the Co^{I} and Co^{III} standards are shown below. The figures are quoted relative to cobalt foil at 0eV. From these results it appears that the cobalt atom in **9** is indeed present in the 3+ oxidation state, giving, thus far, the most conclusive validation of the results of the r.m.s. misfit calculations on **9**.

Compound	Position of Absorption Edge/eV
9	13.2
$[Co(en)_3]Br_3$	13.2
$[(CO)_3Co(PPh_3)_2][BPh_4]$	10.0

Summary

That the r.m.s. method is successful in distinguishing between *nido* and *arachno* $\{B_{10}\}$ fragments has been shown by the results of calculations between well characterised *nido* and *arachno* borane systems. Further evidence of the utility of this technique is found in the independent assessment of the metal oxidation state in **6**, its conjugate base, **7**, and in **9**. These last two give, respectively, examples of a metal with a high verticity, acting as a true cluster vertex, and a low verticity, where the metal is bridging the borane face. However, the *bis*-boranes of the Ni triad give rise to metallaboranes where the role of the metal is intermediate between these two extremes.

Chapter 3

Extended Hückel and Fragment Molecular Orbital Studies on $MB_{10}H_{12}$ Metallaboranes.

This chapter begins with the collation of structural data from all the crystallographically characterised $MB_{10}H_{12}$ metallaboranes. The relationships between the verticity of the metal and the structural parameters mentioned in Chapter 2, the B(a)...B(b), B(c)-B(d) and B(h)-B(i) distances in the borane fragment, are discussed. The variation in verticity in $MB_{10}H_{12}$ species is then investigated *via* a series of EHMO-FMO calculations in which the interaction of a common borane fragment, $\{B_{10}H_{12}\}^{2-}$, with various metal fragments is studied. The relationships between the metal verticity and the above structural parameters are then discussed in terms of the results of the EHMO-FMO studies.

Review of the Structures of $MB_{10}H_{12}$ Metallaboranes

Table 3.1 displays the r.m.s. misfits and metal verticities for all the known, crystallographically characterised $MB_{10}H_{12}$ metallaboranes. The two substituted platinaboranes, discussed in Chapter 2, are included to assess the effect of substitution at the borane cage, either in the bonding face, as in $(PMe_2Ph)_2PtB_{10}H_{11}Cl$,[79] **13**, or remote from the position of the metal as in $(PMe_2Ph)_2PtB_{10}H_{11}(B_{10}H_{13})$,[32] **14**. In addition to these, and to results from $[Me_2TlB_{10}H_{12}]^-$,[64] **15**, and $(PMe_2Ph)_2PtB_{10}H_{12}$,[32] **16**, also mentioned above, Table 3.1 contains data on $[Zn(B_{10}H_{12})_2]^{2-}$,[92] **17**, and $(PMe_2Ph)_3PtB_{10}H_{12}$,[93] **18**. **17** was one of the first $MB_{10}H_{12}$ metallaboranes to be structurally characterised and has been interpreted as featuring a tetrahedrally coordinated Zn metal centre with the two B_{10}

cages twisted relative to each other by an angle of 87.90°. The synthesis and crystallographic characterisation of **18** was intimated during the course of this work.

Inspection of Table 3.1 reaffirms the relationship of these metallaboranes to the *nido* and *arachno* exemplars contained within **1** and **2**. As the r.m.s. misfit against the $\{B_{10}\}$ fragment of **1** decreases so that against the $\{B_{10}\}$ fragment of **2** increases. The only inconsistencies are in the values obtained for **7** and **15**. That **9** and **18** display the highest metal verticities is not surprising; these two species contain the conical $\{(CO)_3Co\}^+$ and $\{(PMe_2Ph)_3Pt\}^{2+}$ fragments, isolobal with {BH}. However, excepting **7**, the remaining metallaboranes all feature formally four coordinate metal centres. These have either been thought of as being square-planar, in the case of the four platinaboranes, **10**, **13**, **14** and **16**, as well as **8** and **11**, or tetrahedral, in the case of **15** and **17**. Despite this apparently similar extent of coordination, these species exhibit a wide range of structures as evidenced in the r.m.s. misfits and verticities shown in Table 3.1. Table 3.1 also relates verticity to selected B-B distances of the borane fragment. All three parameters appear related to the verticity, the distances lengthening as the verticity decreases. The B(a)...B(b) distance shows the strongest correlation and, although some deviation is observed in the B(c)-B(d) and B(h)-B(i) distances, the general trend still follows the metal verticity. Once again the structures of **7** and **15** show the greatest deviation.

EHMO-FMO calculations were carried out on five metallaboranes: **7**, **10**, **15**, **16** and **18**. The choice of these species gave a wide variety in metal verticity whilst maintaining a common principle quantum number for the metal valence orbitals.

Table 3.1 R.m.s.Misfits (Å), Metal Verticities (%) and Borane Cage Parameters (Å) of $MB_{10}H_{12}$ Metallaboranes.

Metallaborane	vs 1	vs 2	Metal Verticity	B(a)...B(b)	B(c)-B(d)	B(h)-B(i)
$(PMe_2Ph)_3PtB_{10}H_{12}$, **18**	0.150	0.058	73.1	3.115	1.819	1.889
$[(CO)_3CoB_{10}H_{12}]^-$, **9**	0.143	0.067	69.1	3.136	1.790	1.924
$(PMe_2Ph)_2PtB_{10}H_{11}$-$(B_{10}H_{13})$, **14**	0.101	0.117	54.0	3.257	1.813	1.970
$(PMe_2Ph)_2PtB_{10}H_{11}Cl$, **13**	0.111	0.099	53.0	3.234	1.851	1.951
$(PMe_2Ph)_2PtB_{10}H_{12}$, **16**	0.105	0.103	50.5	3.239	1.818	1.976
$[Pt(B_{10}H_{12})_2]^{2-}$, **10**	0.083	0.124	39.7	3.347	1.825	1.987
$[Pd(B_{10}H_{12})_2]^{2-}$, **11**	0.081	0.127	38.4	3.352	1.825	1.984
$[Ni(B_{10}H_{12})_2]^{2-}$, **8**	0.074	0.134	34.9	3.392	1.870	1.973
$[Zn(B_{10}H_{12})_2]^{2-}$, **17***	0.047	0.183	15.8	3.494	1.926	2.068
$[Cy_3PAuB_{10}H_{12}]^-$, **7**	0.046	0.191	13.3	3.551	1.903	2.074
$[Me_2TlB_{10}H_{12}]^-$, **15**	0.034	0.191	10.6	3.54	1.97	2.06

* Average values obtained from both borane cages.

EHMO-FMO Studies.

Preliminary EHMO-FMO Studies on 2.

Before EHMO-FMO studies were undertaken on the metallaboranes, a number of calculations were performed on **2**. These assessed the effects of the overall charge of the model and of the charge iteration procedure performed on the heavy atom of the "metal" fragment (here {BH} or $\{CH\}^+$) on the occupation of the frontier MO's of the $\{B_{10}H_{12}\}^{2-}$ fragment.

Three models of **2** were studied and calculations performed both with and without charge iteration on the "metal" fragment. These were $[B_{11}H_{13}]^{2-}$ [(*i*) and (*ii*) in Table 3.2], $[B_{10}H_{13}C]^-$ with the carbon atom given boron exponents and orbital energies [(*iii*) and (*iv*)] and $[B_{10}H_{13}C]^-$, where the carbon atom is the usual carbon exponents and energies [(*v*) and (*vi*)]. All the models were derived from the experimental geometry of **2**,[40] with the {BH} or $\{CH\}^+$ fragments corresponding to the unique boron atom in the five-membered open face.

The frontier MO's of $\{B_{10}H_{12}\}^{2-}$, shown in Figure 3.1, are from a study of this fragment derived from **1** by removal of the bridging protons from the B(a)-B(c) and B(b)-B(d) connectivities. As has been noted elsewhere,[73] analogy can be drawn with the frontier MO's of *cis*-butadiene, the main difference lying in the orientation and relative coefficients of the atomic orbitals, due to contributions from the boron atoms lying below the bonding face. These result in the **a'** occupied and **a"** unoccupied orbitals of *cis*-butadiene appearing as two components in the borane, the **1a'** and **2a'** occupied MO's and the **2a"** and **3a"** unoccupied MO's respectively. The frontier MO's of $\{B_{10}H_{12}\}^{2-}$ are primarily located on the B(a)B(c)B(d)B(b) face, with particularily large contributions to the HOMO and LUMO on B(a) and B(b) and a large contribution to the second HOMO on B(c) and B(d).

Table 3.2 Effects of Charge Iteration and Overall Charge on the Occupancies (e) of the Frontier MO's of the $\{B_{10}H_{12}\}^{2-}$ Fragment in **2**.

Borane Model	"Metal"Fragment	1a'	2a'	1a"(HOMO)	3a'(LUMO)
(*i*)[a]: $[B_{11}H_{13}]^{2-}$	{BH}	1.750	1.946	1.329	0.978
(*ii*)[b]: $[B_{11}H_{13}]^{2-}$	**{BH}**	1.737	1.949	1.397	1.060
(*iii*)[a]: $[B_{10}CH_{13}]^{-}$	$\{CH\}^{+}$	1.750	1.946	1.329	0.978
(*iv*)[c]: $[B_{10}CH_{13}]^{-}$	**$\{CH\}^{+}$**	1.713	1.935	1.204	0.814
(*v*)[d]: $[B_{10}CH_{13}]^{-}$	$\{CH\}^{+}$	1.584	1.913	0.935	0.524
(*vi*)[e]: $[B_{10}CH_{13}]^{-}$	**$\{CH\}^{+}$**	1.616	1.926	1.158	0.743

a: "normal" boron exponents (ζ=1.3) and energies [H_{ii}(2s)=-15.2eV, H_{ii}(2p)=-8.5eV]; b: ζ=1.3, H_{ii}(2s)=-15.32, H_{ii}(2p)=-8.62eV; c: ζ=1.3, H_{ii}(2s)=-19.79, H_{ii}(2p)=-9.99eV; d: "normal" carbon exponents (ζ=1.625) and energies [H_{ii}(2s)=-21.4, H_{ii}(2p)=-11.4eV]; e: ζ=1.625, H_{ii}(2s)=-19.08, H_{ii}(2p)=-9.28eV

Bold type indicates those calculations where charge iteration was performed

Figure 3.1 Frontier MO's of the $\{B_{10}H_{12}\}^{2-}$ Fragment.

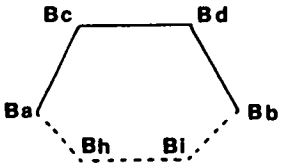

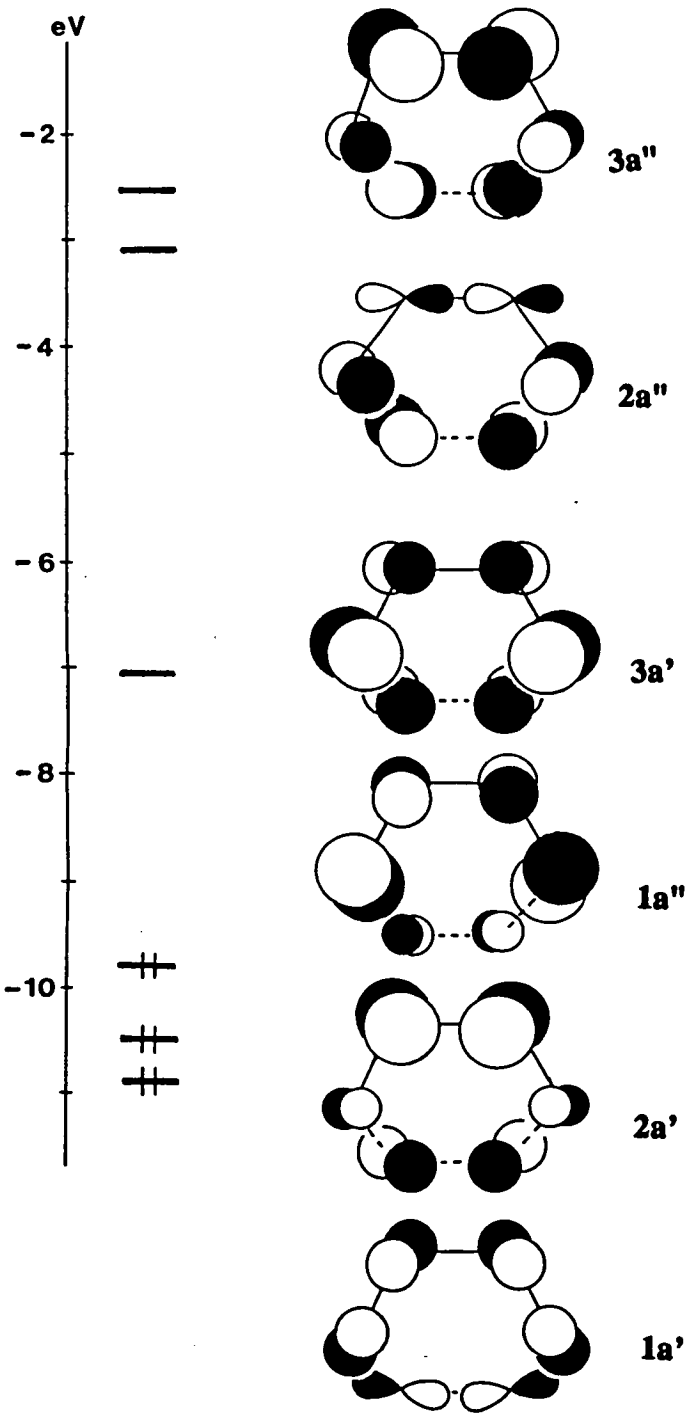

The results of the six calculations given in Table 3.2 show calculations (*i*) and (*iii*) to give the same values for the occupancies of the frontier MO's of the $\{B_{10}\}$ fragment, the only difference in these two calculations lying in the overall charge of the molecule; dianionic in (*i*), monoanionic in (*iii*). Clearly, in the absence of charge iteration, this difference in overall charge has no effect on the results of the calculation. When (*i*) is compared to (*iv*), however, the observed variation in the occupancies of the $\{B_{10}\}$ fragment must originate in the charge iteration performed on the carbon atom of the $\{CH\}^+$ fragment. The effects of the overall charge on the model when charge iteration is performed must therefore be taken into account when considering models for the EHMO-FMO studies on metallaboranes. Comparison of calculations performed with and in the absence of charge iteration on the three models above shows the effect of this process on the distribution of electron density in the borane fragment orbitals. From the results of these studies it was decided that dianionic metallaborane species would be modelled with the type of system shown in (*vi*) in Table 3.2.

Metallaborane Models

In light of the results of the EHMO calculations on **2** a series of monoanionic models the five metallaboranes under study were employed:

$[Cy_3PAuB_{10}H_{12}]^-$, **7** modelled by $[H_3PAuB_{10}H_{12}]^-$, **7'**,

$[Pt(B_{10}H_{12})_2]^{2-}$, **10** by $[Au(B_{10}H_{12})_2]^-$, **10'**,

$[Me_2TlB_{10}H_{12}]^-$, **15**,

$(PMe_2Ph)_2PtB_{10}H_{12}$, **16** by $[(H_3P)_2IrB_{10}H_{12}]^-$, **16'**,

and $(PMe_2Ph)_3PtB_{10}H_{12}$, **18** by $[(H_3P)_3IrB_{10}H_{12}]^-$, **18'**.

These were then partitioned as $\{B_{10}H_{12}\}^{2-}$ and the appropriate monocationic metal fragment. Charge iteration was then performed on the metal. Details of the orbital

exponents and energies used in these calculations are shown in Table 3.3.

Because the ICON8 programme employed in these studies has a maximum of 50 atoms as input, phosphine groups were modelled as H_3P with M-P-H = H-P-H = 109.47° and P-H = 1.42A. In **15**, the inaccuracy of the crystallographic determination was such that the H atoms were placed in idealised positions with $B\text{-}H_{terminal}$ = 1.15A, $B\text{-}H_{bridge}$ = 1.31 - 1.36Å. A range for $B\text{-}H_{bridge}$ distances is obtained because bridging hydrogen positions, calculated using average bond lengths, angles and torsions found in the structure of **1**, are set relative to only one of the B atoms in the bridged connectivity of the metallaborane. Methyl hydrogens were also set in calculated positions, with M-C-H = H-C-H = 109.42° and C-H = 1.08Å. With these exceptions, the experimental model, with full molecular symmetry imposed (see Chapter 6), was used throughout.

Results

The occupations of the frontier MO's of the $\{B_{10}H_{12}\}^{2-}$ fragment in these metallaborane models are displayed in Table 3.4. This shows that, with the exception of **15**, the extent of depopulation of the **1a'** and **2a'** orbitals is similar in all cases. However, as we move from **7'** to **18'** there is a general increase in both the depopulation of the **1a"** HOMO and the occupation of the **3a'** LUMO of the borane. Analysis of these trends was attempted by studying the nature of the metal fragment frontier MO's.

The frontier MO's of the d^8 conical $\{(H_3P)_3Ir\}^+$ and angular $\{(H_3P)_2Ir\}^+$ fragments and the d^{10} linear $\{H_3PAu\}^+$ fragment are well known.[94, 95] These are sketched, along with those of the $\{Au(B_{10}H_{12})\}^+$ and $\{Me_2Tl\}^+$ fragments, in Figure 3.2.

Table 3.3 Metal AO Parameters Used in EHMO Calculations.

Atom	Orbital	H_{ii}(eV)	ζ_1[a]	ζ_2[a]	c_1[b]	c_2[b]
Au (in **7'**)	6s	-10.37	2.602			
	6p	-5.35	2.504			
	5d	-13.44	6.163	2.794	0.64418	0.53558
Au (in **10'**)	6s	-11.24	2.602			
	6p	-6.02	2.504			
	5d	-14.65	6.163	2.794	0.64418	0.53558
Tl (in **15**)	6s	-14.80	2.300			
	6p	-11.36	1.600			
Ir (in **16'**)	6s	-10.18	2.500			
	6p	-5.73	2.200			
	5d	-10.09	5.796	2.557	0.6350	0.55561
Ir (in **18'**)	6s	-9.31	2.500			
	6p	-5.73	2.200			
	5d	-8.97	5.796	2.557	0.63506	0.55561

[a,b] exponents(a) and coefficients(b) in the double ζ function for d-orbitals.

Table 3.4 Occupations (e) of the Frontier MO's of $\{B_{10}H_{12}\}^{2-}$ in Metallaboranes.

Metallaborane	Metal Fragment	1a'	2a'	1a"(HOMO)	3a'(LUMO)
18'	$\{Ir(PH_3)_3\}^+$	1.800	1.939	1.269	0.766
16'	$\{Ir(PH_3)_2\}^+$	1.773	1.939	1.180	0.260
10'	$\{Au(B_{10}H_{12})\}^+$	1.791	1.895	0.970	0.082
15	$\{TlMe_2\}^+$	1.913	1.647	1.568	0.010
7'	$\{AuPH_3\}^+$	1.826	1.853	1.861	0.054

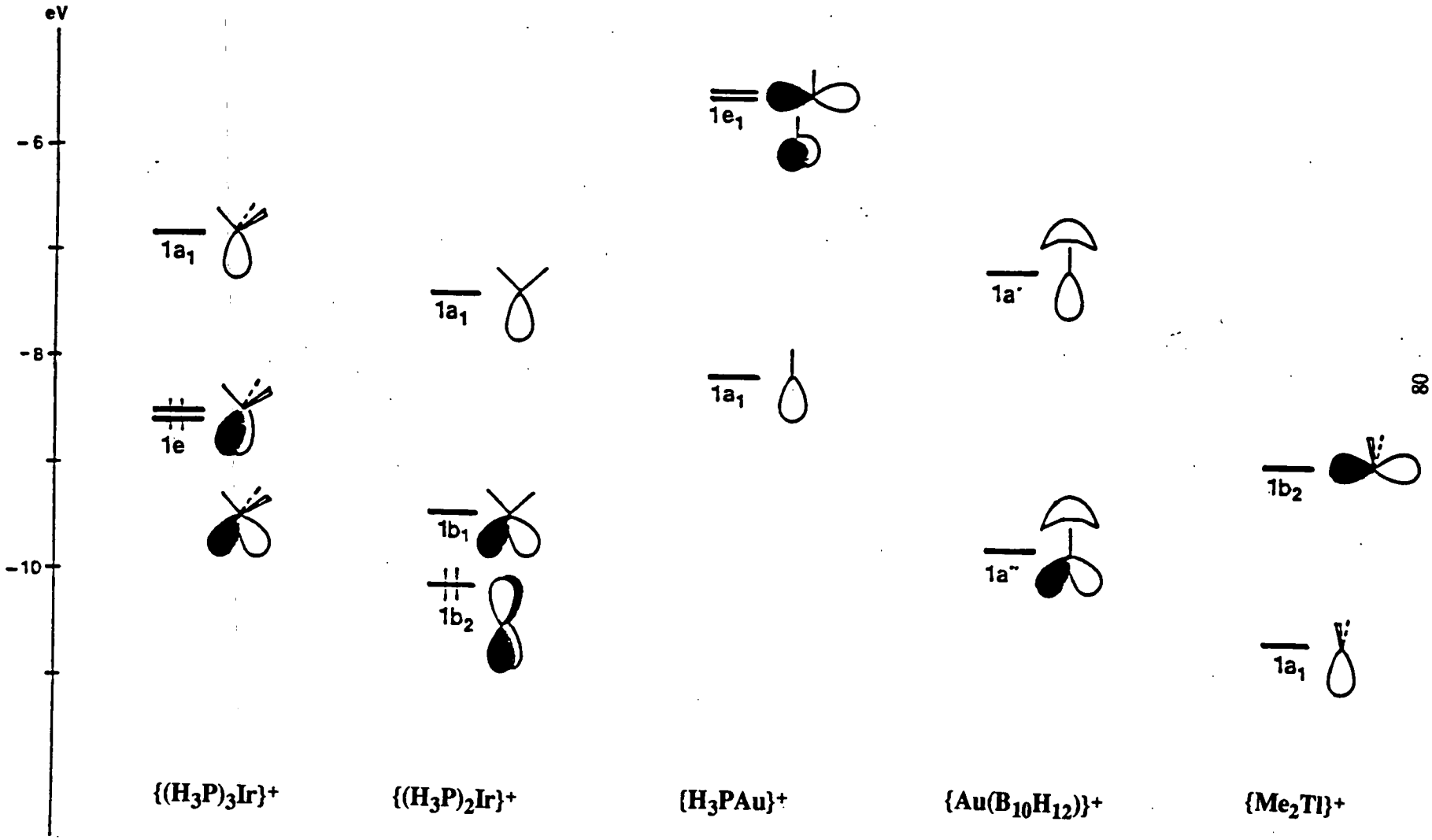

Figure 3.2 Frontier MO's for Metal Fragments.

From Figure 3.2, it can be seen that all the metal fragments have in common an acceptor orbital of a local symmetry. This can interact with the **1a'** and **2a'** orbitals of the borane fragment resulting in their partial deoccupation. In **7'** this is the major effect; the deoccupation of **1a'** and **2a'** being more marked than the deoccupation of the **1a"** orbital. The occupation of the **3a'** orbital is negligible. The low deoccupation of the **1a"** orbital results from the Au $6p_x$ orbital being of too high an energy for efficient interaction. Similarily, the buried Au 5d orbitals are too low lying to populate the **3a'** borane orbital significantly. Therefore, the number of orbitals employed in interaction with the borane fragment by, or orbital contribution of, the $\{H_3PAu\}^+$ fragment is 1. By analogy the orbital contribution of the $\{Cy_3PAu\}^+$ moiety in **7** is also 1.

As well as a similar depopulation of the **1a'** and **2a'** borane orbitals, the $\{(H_3P)_2Ir\}^+$ fragment both depopulates the **1a"** HOMO and significantly populates the **3a'** LUMO of the borane system. The depopulation of the HOMO is effected by the $\mathbf{1b_1}$ orbital of the metal fragment. This metal $5d_{xz}$-$6p_x$ hybrid is both of a suitable symmetry and energy for interaction with the borane **1a"** orbital due to the mixing in of $6p_x$ character. This results in a better energy match with the borane orbital and also in the metal orbital being directed towards the borane face. The interaction of the $\mathbf{1b_2}$ $5d_{yz}$ orbital with the **3a'** borane LUMO increases the occupation of the latter to 0.26e. However, this effect is not as great as that arising from the $\mathbf{1b_1}$ orbital because, for an angular fragment in the xz plane, no mixing in of Ir $6p_y$ character occurs. Compared to the $\mathbf{1b_1}$ orbital, the $\mathbf{1b_2}$ orbital is both deeper buried and not hybridised towards the borane, resulting in it being less well organised for interaction with the latter. The number of orbitals employed by the $\{(H_3P)_2Ir\}^+$ fragment in interaction with the borane can only be said to be somewhat greater than two. By implication, the orbital contribution of the $\{(PMe_2Ph)_2Pt\}^{2+}$ fragment in **16** is also between 2 and 3.

In **18'**, the conical $\{(H_3P)_3Ir\}^+$ fragment efficiently deoccupies the **1a'**, **2a'** and **1a"** orbitals, and in addition populates the **3a'** orbital significantly more than in **16'**. This last effect arises through two two-orbital two-electron interactions between the **1e** degenerate pair of singly occupied MO's of the metal fragment and the HOMO and LUMO of the borane system. The **e** pair are both 5d-6p hybrids and, as a result, exhibit the favourable raising in energy and orientation seen in the $\mathbf{1b_1}$ orbital of the $\{(H_3P)_2Ir\}^+$ fragment above. Here, however, we see three metal fragment orbitals strongly interacting with the borane. The orbital contribution of the $\{(PMe_2Ph)_3Pt\}^{2+}$ in **18** is therefore 3.

The explanation for the trends in metal verticity is now clear. The Pt atom in **18** functions as a good cluster vertex because it has three orbitals available for strong interaction with the borane fragment; in **7** the gold atom has only one such orbital available and consequently is a poor cluster vertex. In **16**, the Pt atom is of intermediate verticity, having two orbitals available for strong interaction and a third, weakly interacting, orbital. Subtle variations within these general trends are discernable. For instance, of the three systems discussed so far, the total depopulation of the **1a'** and **2a'** borane orbitals is greatest in **7'**, whilst the deoccupation of the **1a"** orbital by the $\mathbf{1b_1}$ orbital of **16'** is greater than that by one of the components of the **e** pair in **18'**. In these cases this seems to reflect the relative energies of the orbitals involved; of the $\mathbf{a_1}$ acceptor orbitals of these metal fragments, that of the Au fragment is the lowest in energy. Similarily, the mis-match in energy between the $\mathbf{1b_1}$ orbital in **16'** and the borane **1a"** orbital is less than that between the borane **1a"** and the **e** pair in **18'**, resulting in the former acting as the better acceptor orbital. The relative sizes of the metal fragment orbitals will also result in variation in the extent of their interaction with the borane fragment. However, despite this, the overall relationship between verticity and orbital contribution is clear, as is further evidenced by the studies of **10'** and **15**.

The verticity of the Pt atom in **10** is intermediate, as are those of the metals in the Ni and Pd analogues. The EHMO-FMO study of **10'** reveals a deoccupation of the borane **1a'** and **2a'** orbitals similar to that seen previously. The **1a"** borane orbital is efficiently deoccupied, but the occupation of the **3a'** orbital is low. Inspection of the frontier MO's of the $\{Au(B_{10}H_{12})\}^+$ fragment shows the presence of two acceptor orbitals: the usual **a'** orbital and an especially low lying **a"** orbital, accounting for the efficient depopulation of the borane **1a"** orbital. No suitable metal donor orbital is available for interaction with the borane LUMO and so the orbital contribution of the Au atom in **10'** and, by implication, the Pt atom in **10** is 2.

Finally, in **15** the low lying Tl based $\mathbf{a}_1$ orbital shows the most efficient deoccupation of the borane **1a'** and **2a'** orbitals. The $\mathbf{1b}_2$ $6p_x$ orbital is of the correct symmetry to depopulate the borane **1a"** orbital, however, this effect, although clearly measurable, is not substantial due to the tangential nature of the $\mathbf{1b}_2$ orbital which limits the extent of overlap . Because of this, the orbital contribution of the Tl atom is only somewhat greater than 1. This is anomalous in terms of the Tl verticity, the lowest at 10.6%. Despite having a higher orbital contribution than that of the Au atom in **7**, the latter exhibits a higher verticity, 13.3%. This inconsistency, also apparent in the individual connectivity distances shown in Table 3.1, will be addressed below.

The results of the EHMO-FMO study are summarised in Table 3.5. Of the five metal fragments, only $\{(PMe_2Ph)_3Pt\}^{2+}$ is isolobal with {BH}. Comparison with the occupation of the frontier MO's of $\{B_{10}H_{12}\}^{2-}$ in **2**, modelled by the monoanionic carbaborane, $[B_{10}H_{13}C]^-$, **2'**, shows that the deoccupation of the **1a"** orbital and occupation of the **3a'** orbital are very similar to those in **18** (see Table 3.6). The only significant difference is in the somewhat greater deoccupation of the **1a'** and **2a'** orbitals by the low lying $\mathbf{a}_1$ acceptor orbital of the $\{CH\}^+$ fragment.

Table 3.5 Orbital Contribution and Metal Verticity.

Metal Fragment	Metal verticity(%)	Orbital Number
$\{Pt(PMe_2Ph)_3\}^{2+}$	73.3	3
$\{Pt(PMe_2Ph)_2\}^{2+}$	50.5	>2
$\{Pt(B_{10}H_{12}\}^{2+}$	39.7	2
$\{TlMe_2\}^{+}$	10.6	>1
$\{AuPCy_3\}^{+}$	13.3	1

Table 3.6 Occupations (e) of the Frontier MO's of $\{B_{10}H_{12}\}^{2-}$ in **1** and **2'**.

Borane	Added Fragment	1a'	2a'	1a"(HOMO)	3a'(LUMO)
$B_{10}H_{14}$	$\{H..H\}^{2+}$	1.607	1.585	1.124	0.010
$[B_{10}CH_{13}]^{-}$	$\{CH\}^{+}$	1.616	1.926	1.157	0.743

The structures of the other metallaboranes listed in Table 3.1 can now be interpreted in the same terms using the arguments developed above. The cobaltaborane, **9**, appears entirely analogous to **18**. Both feature conical metal fragments with an orbital contribution of 3. The similar verticities of the Pt atoms in the monocage platinaboranes, suggest that the orbital contribution of >2 in the parent species, **16**, is only slightly perturbed in the substituted derivatives, **13** and **14**. Similarily, the structures of the Ni triad *bis*-boranes can all be interpreted in the same way, specifically, in terms of a metal centre of orbital contribution 2. Comparison of these three species also indicates that, although the size of the metal centre causes some variation in the interaction of the metal with the cage, by far the most important factor in determining the nature of the borane cage is the orbital contribution of the metal fragment. Finally, the structure of **17** suggests that the orbital contribution of the Zn atom is between 1 and 2. This implies that the coordination around the Zn site is not tetrahedral, but rather lies towards two-coordinate, that is, a linear Zn^{II} centre. Such a conclusion certainly warrants further investigation. One approach could be the measurement, through variable temperature n.m.r. experiments, of the barrier of rotation of the borane cages around the axis defined by the Zn and B(j) atoms. The results of the misfit study suggest that the value obtained should be relatively low, as the main interaction between metal and cage, that of the $\mathbf{a}_1$ acceptor orbital with the borane **1a'** and **2a'** orbitals, is independent of rotational conformation. Therefore, comparison with the value obtained from an analogous compound containing a tetrahedrally coordinated zinc atom, for example the, as yet unknown, species $(en)ZnB_{10}H_{12}$, could show the *bis*-borane species to have the lower barrier.

In a similar way, implications about the coordination of the metal centres in the other metallaboranes can now be made. The high verticity species, **9** and **18**, feature octahedral metal centres. The Ni triad *bis*-boranes exhibit square planar metal centres and the auraborane, **7**, a linearly coordinated Au atom. These are common

coordination modes for these metal centres. However, the interpretation of the structures of the three monocage platinaboranes and the thallaborane is not so clear. Rather than involving a simple four coordinate square planar metal centre, **13**, **14** and **16** contain a Pt atom the coordination number of which is greater than four, although not as high as six. Likewise, in **15** the Tl atom, rather than being a tetrahedral centre, is more correctly described as lying between trigonal and "T"-shaped. It seems that the flexibility of the bonding of the borane fragment is reflected in a similar flexibility of the metal centre, which may adopt coordination modes with which it is not normally associated.

Relationship of Orbital Contribution to Other Metallaborane Features

Metal Oxidation States

In Chapter 2 of this work the XANES study on **9** gave evidence for a Co^{III} metal centre and thus for the structure of **9** being that of a true *nido*-icosahedron. Previously, the Mössbauer study on **7** had shown the Au atom to be in the +1 oxidation state and therefore to be acting as a bridge over the borane fragment. In light of the patterns arising from the EHMO-FMO studies described in the previous section, the formal oxidation states of the metals in other metallaboranes can now be discussed.

By analogy to the $\{(CO)_3Co\}^+$ moiety in **9**, the isolobal $\{(PMe_2Ph)_3Pt\}^{2+}$ fragment contains a Pt^{IV} centre. From similar considerations, the Tl atom in **15** is in the +3 oxidation state. These two examples represent the extreme cases of high and low verticity respectively, where these inferences are backed up by the independent evidence on the metal oxidation states in **9** and **7**. The interpretation of the metal oxidation state in **10** and **16** is not so straightforward.

In **10** the orbital contribution of the metal is 2: the borane **1a"** orbital is

deoccupied but occupation of the **3a'** does not occur to any great extent. Occupation of this latter orbital in **16** is more significant, but still not as great as that in **18**. This is reflected in the intermediate verticities of the metal in these systems, for which assignment of a formal integer oxidation state seems impossible. In **10**, the cage geometry exhibits greater *nido* character, but of the two possible extreme oxidation states, Pt^{II} and Pt^{VI}, only a greater degree of Pt^{II} character can be inferred. Similarily, in **16**, the significant occupation of the borane **3a'** orbital is consistent with the increased *arachno* character of the $\{B_{10}\}$ moiety; however, in terms of the Pt oxidation state, this can only be taken to imply an oxidation state somewhat greater than two. This is consistent with the ideas of other authors who have interpreted ^{11}B n.m.r. parameters and the relatively short length of the B(c)-B(d) connectivity in terms of "enhanced" [(Pt-B(c)-B(d)] "three centre bonding contributions which probably occurs *via* additional d-orbital occupation".[32] Here we clearly see that the nature of this extra contribution is the interaction of the Pt d_{yz} orbital with the **3a'** borane LUMO.

Metallaborane Geometry

The relationship between verticity and the B(a)...B(b), B(c)-B(d) and B(h)-B(i) distances was noted above. These trends can now be re-interpreted in terms of the orbital contribution of the metal.

From Figure 3.1 the effects of depopulation of the borane occupied MO's and the population of the LUMO can be assessed. These are summarised overleaf:

Orbital Change	B(a)...B(b)	B(c)-B(d)	B(h)-B(i)
1a' deoccupied	lengthens	lengthens	lengthens
2a' deoccupied	lengthens	*lengthens*	lengthens
1a" deoccupied	*shortens*	shortens	shortens
3a' occupied	*shortens*	shortens	shortens

The major effects (italics) reflect a higher percentage of the MO being located on the atoms in question. The most significant effects occur within the bonding B(a)B(c)B(d)B(b) face.

Table 3.1 shows that the variation in B(a)...B(b) distance most closely follows that of the metal verticity. If the metallaboranes are grouped into those containing a metal of orbital contribution of 3, between 2 and 3, 2, and less than 2, the pattern of the B(a)...B(b) is seen to follow this delineation exactly. This is not the case for the B(c)-B(d) and B(h)-B(i) distances. For metals with orbital contributions of 2 or more, no real trend is apparent in these two parameters. However, for these distances a clear distinction is apparent when metals of orbital contribution less than 2 are considered.

The B(a)...B(b) distance is most dependent on the occupation of the borane **1a"** and **3a'** orbitals. This explains the very close relationship of this distance to the metal orbital contribution. For an orbital contribution of 3 the B(a)...B(b) distance is shortest due to both the occupation of the **3a'** orbital and the deoccupation of the **1a"** orbital. As the orbital contribution decreases, first of all by the weakened interaction with the borane LUMO (as in **16**, orbital contribution >2) then to no interaction with this orbital (as in **10**, orbital contribution = 2) a stepwise increase in the B(a)...B(b) distance is observed. Finally for orbital contributions of less than 2, the longest distances are observed, for example in **7**. In these species interaction with the borane

1a" and **3a'** orbitals is minimal.

For the B(c)-B(d) and B(h)-B(i) distances similar arguments can be adopted. The most important factor in determining the length of the B(c)-B(d) distance is the deoccupation of the borane **2a'** orbital. From the results of the EHMO-FMO studies, there seems to be little real variation in the occupation of this orbital. Therefore, for metals of orbital contribution of 2 or more, the shorter B(c)-B(d) distances reflect the deoccupation and occupation of the borane **1a"** and **3a'** orbitals respectively. However, this distance is not so dependent on these orbital occupations and no real trend emerges. Only when interaction with these orbitals ceases, as for metals of orbital contribution less than 2, does a significant and, in terms of orbital contribution, meaningful lengthening of this connectivity occur. Similarily, the virtual continuum of B(h)-B(i) distance for metal of orbital contribution of 2 or more reflects the varying interaction with the borane **1a"** and **3a'** orbitals. Once again, when this interaction ceases for metals of orbital contribution less than 2, a lengthening of the B(h)-B(i) distance is seen which can be interpreted meaningfully in terms of the structure of the metallaborane.

Clearly then, as a tool for analysis of the structures of the $MB_{10}H_{12}$ metallaboranes, the B(a)...B(b) distance is most useful as it most closely reflects a wide range of metal-borane interactions and is interpretable in terms of the metal fragment orbital contribution. The B(c)-B(d) and B(h)-B(i) distances may have potential for distinguishing between metals of orbital contribution less than 2 and those of 2 or more. However, it seems likely that in the above discussion the grouping of metallaboranes into distinct classes in this way is artificial and possibly more a function of the relatively low number of crystallographically characterised species than a true feature of these systems. With the variation possible in *exo*-polyhedral ligands (even if restricted to phosphines bound to the metal centres) and substituents on the cage , it seems likely that continua for both the metal

verticities and the interboron distances discussed here will be formed. In these circumstances, it seems likely that the use of these parameters for structural analysis in these systems will become increasingly arbitrary and fuller understanding of the metallaborane structure will only be achieved by adoption of a molecular orbital approach similar to that used in this chapter.

These conclusions become even more valid when the anomalous structure of **15** is considered. This species, as mentioned previously, exhibits relative to **7** an unusually low metal verticity. In terms of orbital contribution, however, the B(a)...B(b) and B(h)-B(i) distances, being both shorter than the equivalent distances in **7**, are "correct". Only the B(c)-B(d) distance is anomalously long and this must be connected to the very efficient depopulation of the borane **2a'** orbital noted in Table 3.4 by the $\mathbf{a_1}$ acceptor orbital of the $\{Me_2Tl\}^+$ fragment. The crystal structure of **15** indicates that this orbital points directly at the centre of the B(c)-B(d) connectivity.[64] Thus, although in **15** the metal fragment interacts more strongly with $\{B_{10}H_{12}\}^{2-}$ than does that in **7**, the more important factor in the former is the increased interaction of the $\mathbf{a_1}$ orbital rather than the (weak) interaction of the metal fragment $\mathbf{1b_2}$ orbital with the borane **1a"** orbital, which would usually increase the degree of *arachno* character of the cage. Rather, in this case, the increased interaction of metal with cage results in increased *nido* character. This is an example where analysis by the r.m.s. misfit method gives a misleading answer: the Tl atom in **15** is a better cluster vertex than this approach suggests and it requires a deeper analysis to reveal the nature of the interaction between the metal fragment and the borane cage. It is possible that similar anomalies may exist in the other metallaborane systems, especially other main group-containing species. The crystallographic characterisation of more such species, many of which are known synthetically,[30] would be desirable.

Comparison with Boranes

Table 3.7 compares the B(a)...B(b), B(c)-B(d) and B(h)-B(i) distances of the metallaboranes with those of some borane systems. With the exception of **3**, the B(a)...B(b) and B(c)-B(d) distances of the metallaboranes lie within the limits described by the boranes. **1** and its simple derivatives exhibit longer distances, whilst those for the *arachno*-$\{B_{10}\}$ fragments contained within **2** and **5** are shorter. It seems that a metal fragment can never cause a $\{B_{10}\}$ unit to be as decaborane-like as decaborane itself or cause the B(a)...B(b) distance to shorten as much as does {BH}. Table 3.6 gave the occupation of the frontier MO's of the $\{B_{10}H_{12}\}^{2-}$ fragment in **1** and **2** (the latter modelled by $[B_{10}H_{13}C]^-$, **2'**). The deoccupation of the borane **1a'** and **2a'** orbitals by $\{H...H\}^{2+}$ in **1** is as efficient as that of the **1a"** orbital. No metallaborane, except perhaps **15**, the most decaborane-like, exhibits this behaviour when the depopulation of the **1a"** orbital is significant. This is due to the radial metal fragment orbitals being generally too high lying for an interaction as efficient as that of the $\{H...H\}^{2+}$ fragment **a'** orbital. The efficient deoccupation of the **1a'** and **2a'** orbitals in **1**, and by analogy its simple derivatives, results in longer B(a)...B(b) and B(c)-B(d) distances. Deoccupation of this orbital by one proton, as in **3**, is considerably less, resulting in shorter distances.

The shorter B(a)...B(b) and B(c)-B(d) distances in the *arachno*-$\{B_{10}\}$ fragments of **2** and **5** cannot be explained in terms of orbital occupancy. A possible explanation is that, compared to those of boron and carbon, the greater radial characteristics of the valence orbitals of the metal fragments result in maximum overlap between the metal fragment orbitals and borane orbitals being achieved with a more open B(a)B(c)B(d)B(b) face. Comparison of the overlap integrals for the frontier MO's of the $\{(H_3P)_3Ir\}^+$ and the $\{CH\}^+$ fragments with those of the $\{B_{10}H_{12}\}^{2-}$ moiety shows that a similar degree of overlap occurs in both systems. Thus the extent of the

interaction is comparable, but the borane systems still exhibit shorter distances. Very accurate analysis of the structure of the indenyl-cobaltacarbaborane, 3-(μ-C_9H_7)-3,1,2-$CoC_2B_9H_{11}$ shows that the C_2B_3 face capped by the cobalt atom contains sides of average 1.7320Å whilst that capped by B(6) is less open, having an average side of 1.7145Å (the maximum e.s.d. on an individual connectivity is 0.0024Å).[96]

Finally two points arise concerning the B(h)-B(i) distances. Those for the metallaborane do not lie within the limits set by the boranes: metallaboranes containing a metal centre of orbital contribution less than 2 give examples where this connectivity is especially long. This is related to the occupancy of the **1a"** orbital of the $\{B_{10}H_{12}\}^{2-}$ fragment. In **1** deoccupation of the **1a'**, **2a'** and **1a"** orbitals is efficient and it is only when metallaboranes of orbital contribution less than 2 are considered that the **1a"** orbital is poorly deoccupied. The effect of this is to lengthen the B(h)-B(i) connectivity. In other metallaboranes the effect of a greater occupancy of the **1a"** orbital, for example in **18**, is more than offset by the occupation of the **3a'** orbital of the borane fragment.

The second point concerning the B(h)-B(i) distances is that they are, without exception, longer than the B(c)-B(d) connectivity in the same molecule. This once again reflects the greater interaction of the $\{H...H\}^{2+}$ fragment than any metal fragment. Starting from a model of $[B_{10}H_{10}]^{4-}$, depopulation of the frontier MO's occurs first by $\{H...H\}^{2+}$, adding over the B(a)B(h)B(i)B(b) face to give $\{B_{10}H_{12}\}^{2-}$, then by a metal fragment to give the metallaborane. The more efficient interaction of the former fragment results in the longer B(h)-B(i) distances.

Table 3.7 Cage Parameters (Å) of Boranes and Metallaboranes.

Compound	Verticity(%)	B(a)..B(b)	B(c)-B(d)	B(h)-B(i)
$[B_{11}H_{13}]^{2-}$, **2**		2.914	1.770	1.820
$[B_{11}H_{14}]^{-}$, **5**		3.049	1.774	1.896
$(PMe_2Ph)_3PtB_{10}H_{12}$, **18**	73.1	3.115	1.819	1.889
$[(CO)_3CoB_{10}H_{12}]^{-}$, **9**	69.1	3.136	1.790	1.924
$(PMe_2Ph)_2PtB_{10}H_{11}$-$(B_{10}H_{13})$, **14**	54.0	3.257	1.813	1.970
$(PMe_2Ph)_2PtB_{10}H_{11}Cl$, **13**	53.0	3.234	1.851	1.951
$(PMe_2Ph)_2PtB_{10}H_{12}$, **16**	50.5	3.239	1.818	1.976
$[Pt(B_{10}H_{12})_2]^{2-}$, **10**	39.7	3.347	1.825	1.987
$[Pd(B_{10}H_{12})_2]^{2-}$,**11**	38.4	3.352	1.825	1.984
$[Ni(B_{10}H_{12})_2]^{2-}$, **8**	34.9	3.392	1.870	1.973
$[B_{10}H_{13}]^{-}$, **3**		3.462	1.848	2.003
$[Zn(B_{10}H_{12})_2]^{2-}$, **17***	15.8	3.494	1.926	2.068
$[Cy_3PAuB_{10}H_{12}]^{-}$,**7**	13.3	3.551	1.903	2.074
$[Me_2TlB_{10}H_{12}]$-, **15**	10.6	3.541	1.97	2.06
$Cy_3PAuB_{10}H_{13}$ **6**		3.563	1.994	2.010
$B_{10}H_{14}$, **1**		3.590	1.987	1.987
NCS-$B_{10}H_{13}$, **4**		3.590	1.982	1.982

* average taken from both inequivalent $\{B_{10}\}$ cages.

Summary

This chapter has shown that the verticities of metals in $MB_{10}H_{12}$ metallaboranes are related to its orbital contribution, that is the number of orbital available for interaction with the borane cage. Trends in the B(a)...B(b), B(c)-B(d) and B(h)-B(i) distances have been discussed in terms of this parameter. Of these, the B(a)...B(b) distance shows most potential as a tool for analysing of the $MB_{10}H_{12}$ structures. Some indication that care is required in the interpretation of metal verticities is given by the anomalous structure of **15**. However, this structure can be rationalised in terms of the orientation of the $\{Me_2Tl\}^+$ fragment relative to the borane cage.

Chapter 4

Electrochemical Studies

on 6,6,6-$(PMe_2Ph)_3$-6-*nido*-RuB_9H_{13}, 19.

The synthesis of $(PMe_2Ph)_3RuB_9H_{13}$, **19**, was first reported by Greenwood, Kennedy and co-workers in 1986.[37] Its structure was found by multinuclear n.m.r. spectroscopy to be analogous to that of *nido*-$B_{10}H_{14}$ and is shown below.

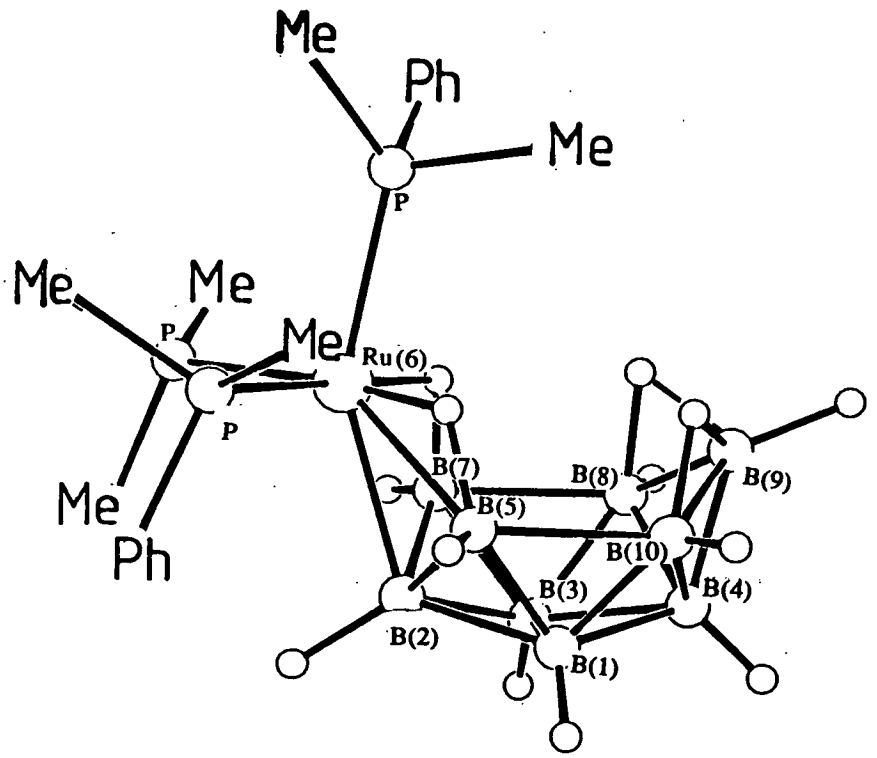

The synthesis of this species was originally undertaken as part of a systematic study of the structural and spectroscopic properties of *nido*-6-metalladecaboranes, MB_9H_{13} [M=$WH_2(PMe_2Ph)_3$, $ReH(PMe_2Ph)_3$, $Os(PMe_2Ph)_3$ and $IrH(PMe_2Ph)_2$]. Of particular interest was the comparison of these systems with *nido*-$B_{10}H_{14}$. However since this work, little further investigation into the properties of these molecules has

been reported in the literature. We undertook the electrochemical study of **19** to investigate the applicability of PSEP methods in predicting the products of redox changes in these cluster systems. In addition to this, given the structural relationship between *nido*-decaborane and this *nido*-6-metalladecaborane, these studies also assessed to what extent, if any, the analogy persists in their electrochemical behaviour.

Synthesis

19 was originally prepared in 38% yield from the reaction of *mer*-$RuCl_3(PMe_2Ph)_3$ with a ten-fold excess of $[NBu_4][B_9H_{14}]$ in refluxing, degassed ethanol. This method was found to be extremely time consuming, requiring several chromatographic separations before pure **19** could be obtained. Moreover, the necessity of increasing the scale of reaction to prepare sufficient amounts of material for a number of electrochemical studies exacerbated this problem. The large excess of *arachno*-$[B_9H_{14}]^-$ required in the reaction was thought to be the reason behind the laborious purification steps. Therefore, the reactions of a number of different salts of *arachno*-$[B_9H_{14}]^-$ in various ratios relative to the amount of *mer*-$RuCl_3(PMe_2Ph)_3$ present were assessed in order to improve the synthetic procedure. That finally arrived at employed a seven-fold excess of the $[BTMA]^+$ salt of the *arachno* borane under the same conditions used in the original method. The increased solubility of this salt resulted in the desired metallaborane product precipitating out of the cooling ethanolic solution. Recrystallisation from dichloromethane/n-hexane then gave **19** in pure form. The overall yield by this procedure (*circa* 40%) is not a significant improvement on that originally obtained, but for large scale syntheses the work up procedure is much simplified.

The ratio of borane to ruthenium was found to be crucial for the preparation of **19**. If a 2:1 reaction mixture is used then the major product formed is

$[Ru_2Cl_3(PMe_2Ph)_6][B_9H_{14}]$, as identified by ^{11}B, ^{31}P and ^{1}H n.m.r. spectroscopies and microanalysis. It seems that the borane is not a very strong nucleophile and the reduced form of *mer*-$RuCl_3(PMe_2Ph)_3$ produced in the reaction prefers to dimerise, with loss of chloride, rather than form the metallaborane. In general the formation of the latter required at least a five-fold excess of borane.

Electrochemical Response of 19

In dichloromethane at 290K, **19** exhibits both a partially reversible oxidation at +0.97V and reduction at -1.54V. Both processes have daughter products associated with them. Anodic a.c. voltammetry shows the presence of a second oxidative process at +1.08V, which is implied by variable scan rate experiments to be linked to the initial oxidation of **19**. In addition, cyclic voltametry of more concentrated solutions exhibited a desorption peak centred at +0.1V on the return sweep. Two daughter product waves at -1.07 and -0.06V are seen on the reverse sweep of the reductive cyclic voltammogram. Neither of these redox processes are observed if the reductive scan is reversed at -1.4V.

At 238K the reduction exhibits greater chemical reversibility and evidence is seen on the cyclic voltametric timescale for the first daughter product at -1.07V only. At this reduced temperature, no increase in chemical reversibility is seen for the oxidative process at +0.97V. These observations are summarised in Figures 4.1a and 4.1b

Figure 4.1 Electrochemical Response of **19** in Dichloromethane.

(a) Anodic Response.

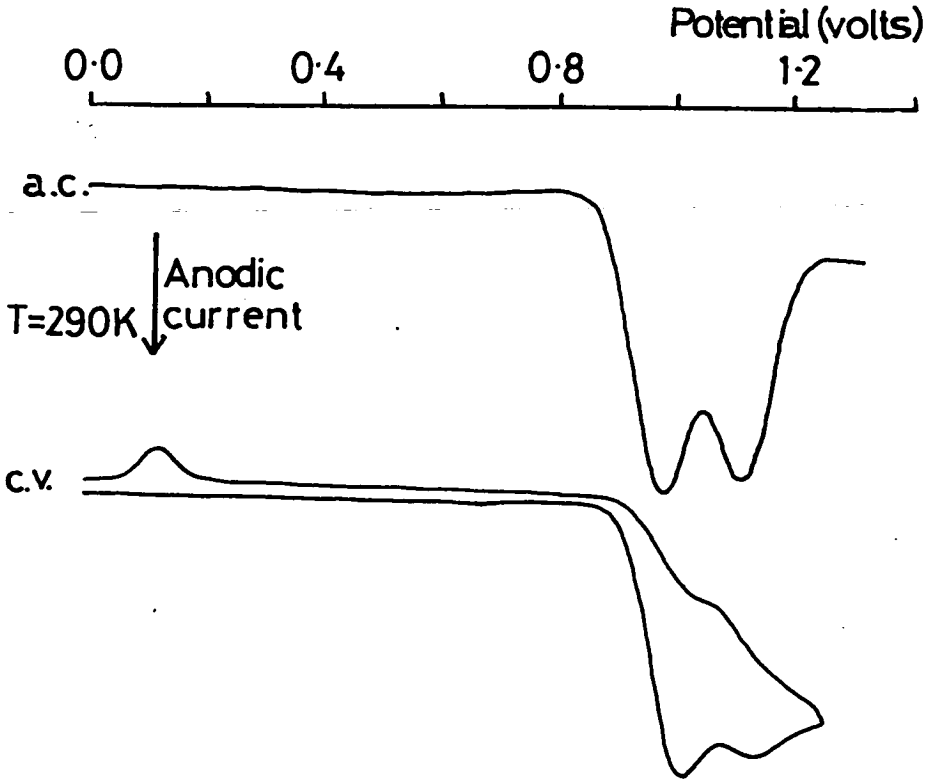

(b) Cathodic Response.

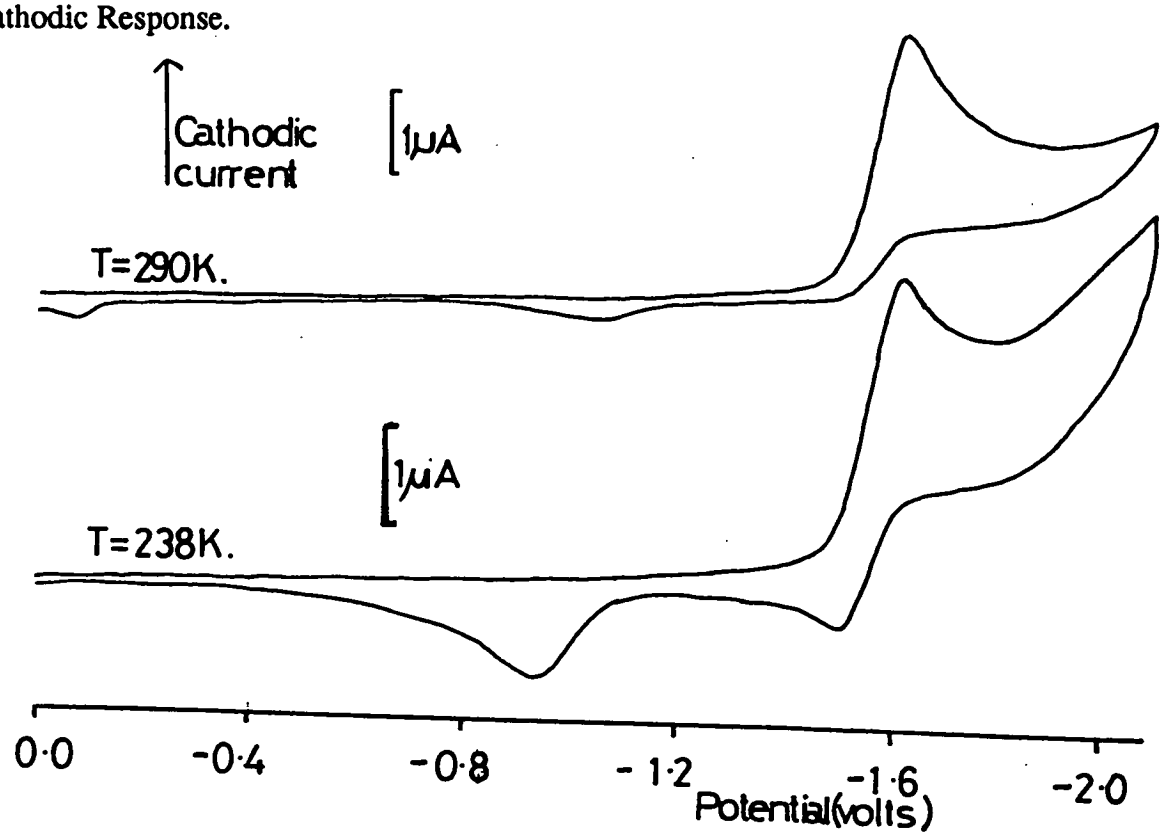

Bulk Electrolysis on 19 at +1.00V.

The bulk electrosynthesis of **19** at +1.00V and 290K in dichloromethane resulted in the solution changing colour from red to orange. Coulometric measurements on this process were complicated by the proximity of the second oxidative process at +1.08V; however, analysis of the results consistently gave a value of two electrons per mole of **19** present to be involved in the oxidative process at +0.97V. A.c. voltammetry of the oxidised solution revealed that a number of redox-active products had been formed. Two redox processes occured at +1.08V and -1.50V, 110mV and 40mV respectively to positive potential of the equivalent redox processes of **19**. These separations suggest both product processes may be derived from a single species. In addition to these, a broad asymmetric wave was seen at +0.4V. The shape of this wave and of the corresponding cyclic voltammetric wave indicates that a number of partially reversible electron transfer processes are involved. The relative sizes of the waves seen in the cyclic voltammagram also suggests that this mixture of products giving rise to the wave at +0.4V forms the majority of the electrogenerated species. ^{11}B n.m.r. of this EPR-silent mixture, generated in $[PF_6]^-$ electrolyte, yielded little information other than to confirm that a mixture of products had been formed. It was clear that separation of the mixture of products was required before characterisation of the individual species formed could be achieved. Alternatively, another approach was to attempt the chemical oxidation of **19**.

Reactions of 19 with Cl_2

Addition of a saturated solution of Cl_2 in carbon tetrachloride to **19** in dichloromethane results in a colour change from red to orange. Subsequent chromatographic separation yielded one major product. Anodic a.c. voltammetry of this species was indistinguishable from that of the electrochemically generated daughter product giving rise to the oxidative process at +1.08V described above. The

UV/visible spectrum of this product was also superimposable on that obtained from the mixture of electrogenerated species.

The ^{11}B and $^{11}B-\{^1H\}$ n.m.r. spectra of this product species are displayed in Figure 4.2. Four resonances are seen in the decoupled spectrum, of relative integral 4:3:1:1. In the coupled spectrum three of these resonances show evidence for terminal hydrogen coupling; none is seen to the resonance at -8.68p.p.m. These spectra indicate the presence of nine boron atoms, one of which has undergone a terminal hydrogen substitution. Because of the number of coincident resonances and the rapid relaxation of the ^{11}B n.m.r. signal, a problem common to all the derivatised systems discussed in this chapter, a $^{11}B-^{11}B$ COSY experiment yielded little further information on the structure of this species. Accordingly, a single crystal X-ray study was undertaken.

Crystallographic Characterisation

The crystallographic study on the product of the reaction of Cl_2 with **19** showed it to be a chlorinated derivative of the starting material, 2-Cl-6,6,6-$(PMe_2Ph)_3$-6-*nido*-RuB_9H_{12}, **20**. A perspective view of this molecule is shown in Figure 4.3. Table 4.1 lists the positions of non-hydrogen atoms with associated equivalent isotropic thermal parameters. Table 4.2 details selected interatomic distances and interbond angles. Anisotropic thermal parameters are given in Table 4.3 and the refined and calculated positions of hydrogen atoms are listed in Table 4.4.

Figure 4.2 ^{11}B and $^{11}B-\{^1H\}$ N.m.r. Spectra of the Product of Reaction of **19** with Cl_2.

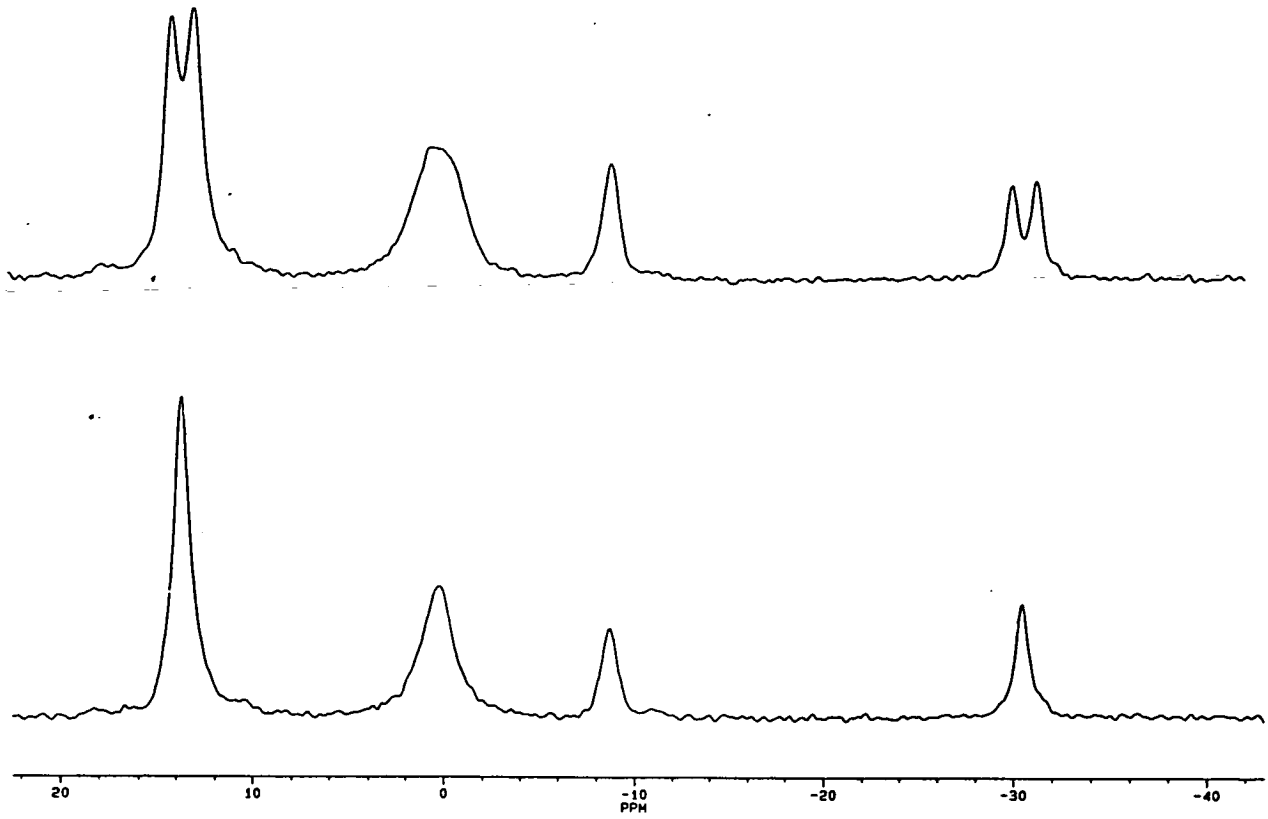

Figure 4.3 Molecular Structure of **20**.

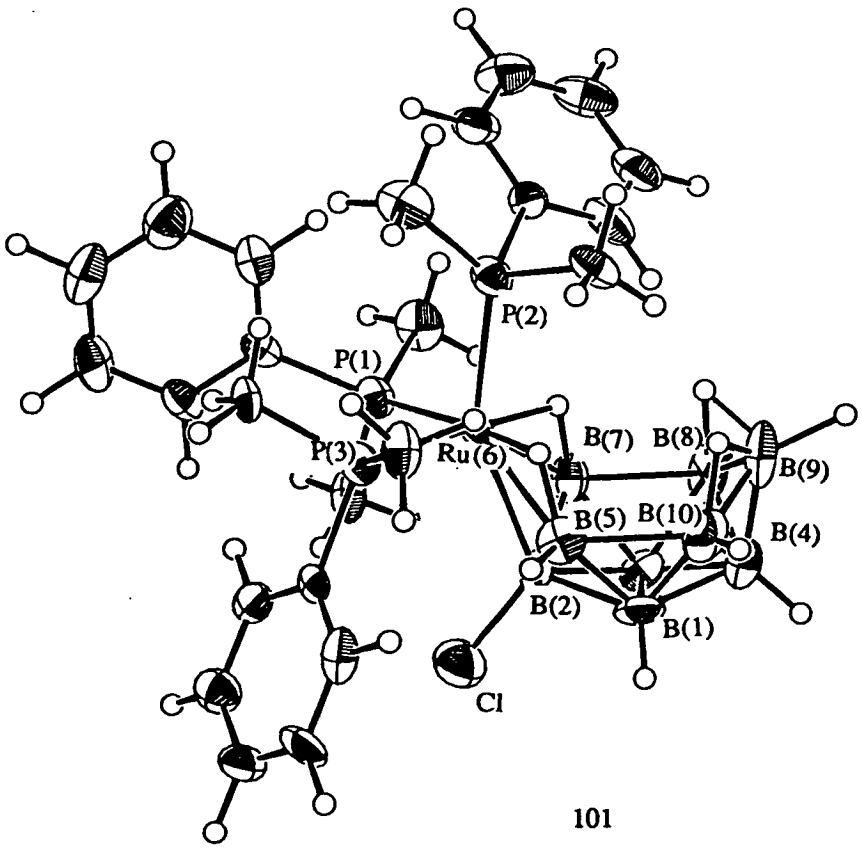

Table 4.1 Atomic Positions and Equivalent Isotropic Thermal Parameters ($Å^2$) of Refined Non-Hydrogen Atoms in **20**.

	x	y	z	Ueq
Ru(6)	0.52544(10)	0.32129(5)	0.77095(5)	0.0269(6)
P(1)	0.4003(3)	0.37588(17)	0.67527(16)	0.0367(21)
Cl	0.2533(4)	0.41685(18)	0.86181(18)	0.065(3)
P(2)	0.6967(4)	0.25655(17)	0.71628(16)	0.0365(21)
P(3)	0.6881(3)	0.41940(17)	0.80260(15)	0.0344(20)
B(2)	0.3462(14)	0.3298(8)	0.8474(6)	0.036(9)
B(7)	0.2974(17)	0.2672(8)	0.7784(7)	0.042(10)
B(5)	0.5298(15)	0.3075(8)	0.8846(7)	0.042(10)
B(9)	0.4499(20)	0.1326(9)	0.8723(8)	0.059(13)
B(1)	0.3787(16)	0.2758(8)	0.9211(7)	0.043(10)
B(4)	0.3213(18)	0.1823(9)	0.9100(8)	0.055(11)
B(10)	0.5063(19)	0.2070(9)	0.9253(8)	0.054(12)
B(8)	0.2953(20)	0.1678(9)	0.8248(8)	0.060(12)
B(3)	0.2383(18)	0.2518(8)	0.8567(8)	0.048(11)
C(11)	0.3178(12)	0.3115(7)	0.6118(5)	0.047(8)
C(12)	0.2390(13)	0.4302(6)	0.6928(6)	0.048(9)
C(14)	0.6080(9)	0.4121(4)	0.5886(4)	0.048(9)
C(15)	0.6921(9)	0.4603(4)	0.5537(4)	0.059(11)
C(16)	0.6653(9)	0.5363(4)	0.5548(4)	0.055(10)
C(17)	0.5544(9)	0.5642(4)	0.5907(4)	0.053(10)
C(18)	0.4703(9)	0.5161(4)	0.6256(4)	0.040(9)
C(13)	0.4971(9)	0.4400(4)	0.6245(4)	0.036(8)
C(21)	0.7867(12)	0.1879(6)	0.7734(5)	0.046(8)
C(22)	0.8640(12)	0.2939(6)	0.6838(6)	0.053(9)
C(24)	0.5156(9)	0.1430(5)	0.6639(4)	0.048(9)
C(25)	0.4487(9)	0.0969(5)	0.6140(4)	0.054(10)
C(26)	0.4841(9)	0.1041(5)	0.5486(4)	0.060(11)
C(27)	0.5866(9)	0.1575(5)	0.5333(4)	0.062(11)
C(28)	0.6536(9)	0.2036(5)	0.5833(4)	0.051(10)
C(23)	0.6181(9)	0.1964(5)	0.6486(4)	0.035(8)
C(31)	0.8550(12)	0.3906(6)	0.8563(5)	0.041(8)
C(32)	0.7767(13)	0.4747(6)	0.7418(5)	0.041(8)
C(34)	0.5097(9)	0.5426(5)	0.8130(3)	0.040(8)
C(35)	0.4441(9)	0.6000(5)	0.8458(3)	0.047(9)
C(36)	0.4772(9)	0.6089(5)	0.9145(3)	0.051(10)
C(37)	0.5759(9)	0.5605(5)	0.9504(3)	0.054(10)
C(38)	0.6414(9)	0.5032(5)	0.9175(3)	0.047(9)
C(33)	0.6083(9)	0.4942(5)	0.8488(3)	0.026(8)

Table 4.2 Interatomic Distances (Å) and Selected Interbond Angles (°) for **20**.

Ru(6)	- P(1)	2.347(3)	B(5)	- B(1)	1.720(21)
Ru(6)	- P(2)	2.315(3)	B(5)	- H(5)	1.06(8)
Ru(6)	- P(3)	2.348(3)	B(5)	-HB(56)	1.25(8)
Ru(6)	- B(2)	2.362(13)	B(9)	- B(4)	1.712(23)
Ru(6)	- B(7)	2.306(15)	B(9)	-B(10)	1.758(24)
Ru(6)	- B(5)	2.302(15)	B(9)	- B(8)	1.731(24)
Ru(6)	-HB(67)	1.58(8)	B(9)	- H(9)	1.36(8)
Ru(6)	-HB(56)	1.39(8)	B(9)	-HB(89)	1.50(8)
P(1)	-C(11)	1.829(12)	B(9)	-HB(910)	1.22(9)
P(1)	-C(12)	1.827(12)	B(1)	- B(4)	1.773(22)
P(1)	-C(13)	1.830(8)	B(1)	-B(10)	1.693(22)
Cl	- B(2)	1.821(13)	B(1)	- B(3)	1.771(21)
P(2)	-C(21)	1.824(12)	B(1)	- H(1)	1.03(8)
P(2)	-C(22)	1.843(12)	B(4)	-B(10)	1.730(23)
P(2)	-C(23)	1.828(9)	B(4)	- B(8)	1.729(24)
P(3)	-C(31)	1.838(11)	B(4)	- B(3)	1.767(23)
P(3)	-C(32)	1.832(11)	B(4)	- H(4)	1.02(8)
P(3)	-C(33)	1.833(8)	B(10)	-H(10)	0.94(9)
B(2)	- B(7)	1.810(20)	B(10)	-HB(910)	1.40(9)
B(2)	- B(5)	1.796(19)	B(8)	- B(3)	1.746(23)
B(2)	- B(1)	1.774(19)	B(8)	- H(8)	0.84(9)
B(2)	- B(3)	1.736(20)	B(8)	-HB(89)	1.37(8)
B(7)	- B(3)	1.742(22)	B(3)	- H(3)	0.99(9)
B(7)	- H(7)	1.10(9)	B(5)	-B(10)	2.011(22)
B(7)	-HB(67)	1.31(8)	B(7)	- B(8)	2.023(23)

P(1)	-Ru(6) - P(2)	96.31(12)	B(2)	- B(1) - B(3)	58.6(8)
P(1)	-Ru(6) - P(3)	98.08(11)	B(5)	- B(1) -B(10)	72.2(9)
P(2)	-Ru(6) - P(3)	94.38(11)	B(4)	- B(1) -B(10)	59.8(9)
B(2)	-Ru(6) - B(7)	45.6(5)	B(4)	- B(1) - B(3)	59.8(9)
B(2)	-Ru(6) - B(5)	45.3(5)	B(9)	- B(4) -B(10)	61.4(10)
B(7)	-Ru(6) - B(5)	79.0(5)	B(9)	- B(4) - B(8)	60.4(10)
Ru(6)	- B(2) - B(7)	65.6(6)	B(1)	- B(4) -B(10)	57.8(9)
Ru(6)	- B(2) - B(5)	65.6(6)	B(1)	- B(4) - B(3)	60.0(9)
B(7)	- B(2) - B(3)	58.8(8)	B(8)	- B(4) - B(3)	59.9(9)
B(5)	- B(2) - B(1)	57.6(8)	B(9)	-B(10) - B(4)	58.8(9)
B(1)	- B(2) - B(3)	60.6(8)	B(1)	-B(10) - B(4)	62.4(9)
Ru(6)	- B(7) - B(2)	68.8(6)	B(9)	- B(8) - B(4)	59.3(10)
B(2)	- B(7) - B(3)	58.5(8)	B(4)	- B(8) - B(3)	61.1(9)
Ru(6)	- B(5) - B(2)	69.1(6)	B(2)	- B(3) - B(7)	62.7(8)
B(2)	- B(5) - B(1)	60.6(8)	B(2)	- B(3) - B(1)	60.8(8)
B(4)	- B(9) -B(10)	59.8(9)	B(7)	- B(3) - B(8)	70.9(10)
B(4)	- B(9) - B(8)	60.3(10)	B(1)	- B(3) - B(4)	60.1(9)
B(2)	- B(1) - B(5)	61.8(8)	B(4)	- B(3) - B(8)	59.0(9)
Cl	- B(2) - B(7)	125.5(9)	Cl	- B(2) - B(5)	123.5(9)
Cl	- B(2) - B(1)	112.3(8)	Cl	- B(2) - B(3)	114.0(9)

Table 4.3 Anisotropic Thermal Parameters ($Å^2$) of Refined Non-Hydrogen Atoms for **20**.

	U11	U22	U33	U23	U13	U12
Ru(6)	0.0245(5)	0.0234(5)	0.0323(6)	-0.0011(6)	0.0002(4)	-0.0014(6)
P(1)	0.0310(20)	0.0338(20)	0.0443(22)	0.0032(17)	-0.0005(17)	0.0035(17)
Cl	0.0588(26)	0.0532(23)	0.0842(28)	-0.0064(21)	0.0217(22)	0.0067(20)
P(2)	0.0308(21)	0.0307(20)	0.0474(22)	-0.0025(17)	0.0043(17)	0.0024(16)
P(3)	0.0307(21)	0.0305(20)	0.0410(21)	-0.0010(17)	-0.0008(17)	-0.0031(16)
B(2)	0.0408(87)	0.0291(84)	0.0364(83)	0.0066(77)	0.0053(69)	-0.0090(78)
B(7)	0.041 (10)	0.040 (10)	0.0426(99)	0.0140(82)	-0.0076(85)	-0.0002(82)
B(5)	0.0286(90)	0.047 (10)	0.0491(99)	-0.0060(85)	0.0004(77)	-0.0060(81)
B(9)	0.072 (13)	0.043 (11)	0.061 (13)	0.0274(96)	-0.006 (10)	-0.013 (10)
B(1)	0.048 (11)	0.050 (10)	0.0319(92)	-0.0196(81)	0.0160(83)	-0.0052(83)
B(4)	0.073 (12)	0.046 (10)	0.048 (10)	0.020 (10)	0.0186(91)	-0.002 (11)
B(10)	0.066 (13)	0.062 (12)	0.032 (10)	0.0160(90)	-0.0044(94)	-0.0047(98)
B(8)	0.082 (14)	0.0 04(11)	0.056 (11)	-0.0074(97)	0.001 (10)	-0.054 (11)
B(3)	0.0317(98)	0.053 (11)	0.063 (12)	-0.0006(92)	0.0304(92)	-0.0089(88)
C(11)	0.0455(80)	0.0501(83)	0.0423(75)	-0.0081(70)	-0.0159(63)	-0.0130(74)
C(12)	0.0505(88)	0.0357(81)	0.0575(88)	0.0206(69)	0.0003(72)	-0.0006(70)
C(14)	0.0506(93)	0.0404(86)	0.0530(93)	0.0059(74)	0.0056(76)	0.0021(77)
C(15)	0.072 (11)	0.063 (11)	0.0422(94)	-0.0009(81)	0.0039(81)	-0.0151(93)
C(16)	0.066 (11)	0.063 (11)	0.0348(89)	0.0172(77)	-0.0074(77)	-0.0263(88)
C(17)	0.070 (11)	0.0359(88)	0.0496(97)	0.0212(77)	-0.0134(83)	0.0057(85)
C(18)	0.0505(89)	0.0307(83)	0.0368(83)	-0.0014(68)	-0.0044(69)	0.0117(73)
C(13)	0.0419(83)	0.0280(84)	0.0368(77)	-0.0050(62)	0.0015(65)	0.0048(64)
C(21)	0.0520(81)	0.0338(76)	0.0522(82)	-0.0069(70)	0.0047(67)	0.0159(73)
C(22)	0.0321(78)	0.0530(89)	0.0738(96)	-0.0139(73)	0.0044(71)	-0.0054(66)
C(24)	0.0314(82)	0.0288(76)	0.084 (11)	-0.0171(78)	0.0017(78)	-0.0040(67)
C(25)	0.0440(92)	0.0376(88)	0.081 (11)	-0.0124(85)	0.0135(88)	0.0116(74)
C(26)	0.0515(99)	0.063 (11)	0.064 (11)	-0.0400(85)	-0.0022(81)	-0.0007(83)
C(27)	0.061 (11)	0.075 (10)	0.0498(97)	-0.0177(86)	0.0127(83)	-0.0040(88)
C(28)	0.0505(92)	0.0416(90)	0.060 (10)	-0.0148(79)	0.0162(85)	0.0017(70)
C(23)	0.0386(80)	0.0309(85)	0.0364(83)	-0.0121(61)	0.0089(63)	-0.0112(66)
C(31)	0.0314(78)	0.0361(76)	0.0530(83)	0.0142(65)	-0.0086(64)	-0.0049(62)
C(32)	0.0535(87)	0.0191(69)	0.0492(80)	0.0032(61)	0.0105(68)	-0.0096(63)
C(34)	0.0488(90)	0.0374(81)	0.0347(76)	-0.0092(74)	0.0073(72)	-0.0166(71)
C(35)	0.0478(90)	0.0457(93)	0.0475(94)	-0.0089(73)	0.0018(75)	-0.0057(74)
C(36)	0.0523(94)	0.0384(86)	0.063 (11)	-0.0106(80)	0.0283(80)	-0.0004(75)
C(37)	0.091 (12)	0.0258(80)	0.0430(87)	-0.0166(73)	0.0074(85)	0.0024(80)
C(38)	0.0556(92)	0.0390(88)	0.0442(91)	0.0128(71)	-0.0056(75)	-0.0128(74)
C(33)	0.0224(72)	0.0199(69)	0.0361(81)	-0.0018(59)	0.0019(60)	-0.0087(57)

Table 4.4 Refined and Calculated Positions of Hydrogen Atoms in **20**

	x	y	z
H(7)	0.204(10)	0.275(5)	0.740(4)
H(5)	0.604(9)	0.341(4)	0.916(4)
H(9)	0.475(9)	0.059(5)	0.883(4)
H(1)	0.358(9)	0.299(4)	0.966(4)
H(10)	0.566(10)	0.194(5)	0.964(4)
H(4)	0.273(9)	0.162(5)	0.950(4)
H(8)	0.246(10)	0.134(5)	0.804(5)
H(3)	0.133(10)	0.263(5)	0.860(4)
HB(89)	0.420(10)	0.144(4)	0.798(4)
HB(910)	0.571(10)	0.163(5)	0.878(4)
HB(56)	0.423(10)	0.251(4)	0.755(4)
HB(67)	0.582(9)	0.290(4)	0.832(4)
HM(11)	0.2558(12)	0.2695(7)	0.6351(5)
HM(12)	0.4041(12)	0.2854(7)	0.5870(5)
HM(13)	0.2441(12)	0.3415(7)	0.5757(5)
HM(14)	0.2725(13)	0.4713(6)	0.7304(6)
HM(15)	0.1570(13)	0.3940(6)	0.7106(6)
HM(16)	0.1919(13)	0.4575(6)	0.6477(6)
HP(14)	0.6288(9)	0.3532(4)	0.5877(4)
HP(15)	0.7780(9)	0.4386(4)	0.5259(4)
HP(16)	0.7304(9)	0.5736(4)	0.5278(4)
HP(17)	0.5336(9)	0.6231(4)	0.5915(4)
HP(18)	0.3845(9)	0.5377(4)	0.6534(4)
HM(21)	0.7039(12)	0.1589(6)	0.7982(5)
HM(22)	0.8633(12)	0.2154(6)	0.8101(5)
HM(33)	0.8463(12)	0.1487(6)	0.7458(5)
HM(24)	0.8323(12)	0.3368(6)	0.6478(6)
HM(25)	0.9204(12)	0.2500(6)	0.6601(6)
HM(26)	0.9374(12)	0.3167(6)	0.7244(6)
HP(24)	0.4881(9)	0.1374(5)	0.7145(4)
HP(25)	0.3693(9)	0.0556(5)	0.6258(4)
HP(26)	0.4323(9)	0.0684(5)	0.5099(4)
HP(27)	0.6141(9)	0.1630(5)	0.4827(4)
HP(28)	0.7329(9)	0.2449(5)	0.5714(4)
HM(31)	0.8235(12)	0.3563(6)	0.8963(5)
HM(32)	0.9125(12)	0.4392(6)	0.8769(5)
HM(33)	0.9272(12)	0.3597(6)	0.8272(5)
HM(34)	0.6930(13)	0.4968(6)	0.7049(5)
HM(35)	0.8522(13)	0.4402(6)	0.7175(5)
HM(36)	0.8375(13)	0.5197(6)	0.7672(5)
HP(34)	0.4841(9)	0.5357(5)	0.7598(3)
HP(35)	0.3677(9)	0.6374(5)	0.8180(3)
HP(36)	0.4265(9)	0.6533(5)	0.9399(3)
HP(37)	0.6015(9)	0.5674(5)	1.0036(3)
HP(38)	0.7178(9)	0.4657(5)	0.9453(3)

The structure of **20** is derived from that of **19** by the substitution at B(2) of a terminal hydrogen atom by a chlorine atom. The conformation of the phosphine groups is such that **20** contains no molecular symmetry in the solid state, although, on the n.m.r. timescale at 290K, **20** clearly does have C_s symmetry in solution. In the absence of a crystal structure of **19**, detailed comparison between these two ruthenaboranes is not possible. However, comparison with the structures of the *nido*-6-metalladecaboranes mentioned in the beginning of this chapter shows that the effect of the chlorine on the overall structure of the metallaborane is minimal. The B(5)-B(10) and B(7)-B(8) connectivities are characteristically long, averaging 2.02(3)Å. An r.m.s. misfit calculation comparing the equivalent *arachno*-$\{B_9\}$ fragments of **20** and *nido*-$B_{10}H_{14}$ gives a value of 0.046Å. Both these are good indications of *nido*-6-metalladecaboranyl character (see Chapter 1). Individual misfits are greatest at the B(5), B(10), B(7) and B(8) positions, whilst that at B(2) is very small (0.022Å). Comparison of the metal environment in **20** with the underivatised osmium analogue reveals no significant difference between the two systems.

Returning to the ^{11}B n.m.r. spectrum of **20**, an attempt at assignment can be made by comparison with the ^{11}B spectrum of **19**.

Metallaborane:	**19**/p.p.m.[Assignment]	**20**/p.p.m.(Intensity)
	12.91 [B(5), B(7)]	13.74 (4B)
	10.25 [B(1), B(3)]	
	2.38 [B(9)]	0.23 (3B)
	-1.39 [B(8), B(10]	
	-23.23 [B(2)]	-8.68 (1B)
	-31.27 [B(4)]	-30.46 (1B)

The two spectra are, in fact, very similar, the major difference between the two appearing to be derived from the general deshielding effect of the electronegative chlorine atom. This causes all but one of the resonances [the exception being that due to B(9)] to move to higher frequency, although the major effect is seen at B(2), the site of substitution, the shift here being almost 15p.p.m. B(1) and B(3) are more affected than B(5) and B(7) resulting in the overlap of the two signals. Similarily the resonances arising from B(8), B(10) and B(9) merge. Thus the n.m.r. study confirms the conclusions of the single crystal analysis in that the overall structure of **19** is unchanged by chlorination. Furthermore, this spectroscopic study suggests the major electronic difference between the two species lies in the different B(2)-X σ interactions [X=H (**19**), X=Cl (**20**)] in the two systems.

EHMO studies on **19** and **20** were performed using models derived from the experimental geometry of **20**, with PMe_2Ph groups replaced by PH_3 moieties (P-H=1.42Å, Ru-P-H= 109.47°). In the model for **19** the B-Cl bond was replaced by a B-H bond along the same vector (B-H=1.15Å). Ruthenium H_{ii}'s were optimised by charge iteration; for **19**, H_{ii}(5s)=-8.74, H_{ii}(5p)=-5.29, H_{ii}(4d)=-8.94eV; for **20**, H_{ii}(5s)=-8.70, H_{ii}(5p)=-5.25, H_{ii}(4d)=-8.88eV. The models were oriented such that the positions of the B(2), B(5) and B(7) atoms defined the xy plane.

The results of these studies confirm the trends seen in the ^{11}B n.m.r. spectra of the two species. B(2) shows a significant change in net charge between the two studies; -0.11 in **19** and +0.33 in **20**. The orientation of the two models is such that the B(2)-X σ interaction will involve the 2s and $2p_y$ AO's, with some mixing in of $2p_z$ character, and so all three AO's are deoccupied:

Atomic Orbital	Occupancy (e):	19	20
2s		0.98	0.86
$2p_y$		0.67	0.44
$2p_z$		0.75	0.69

No other significant change is seen between the two systems, and again the electronic effect of the electronegative chloride atom is restricted to the boron atom to which it is bonded. In addition to this, B(2) in **19** carries by far the greatest negative charge and it seems likely that this is related to the high specificity of the chlorination reaction to produce **20**.

The frontier molecular orbitals of **19** and **20** are mostly metal based (>94% for both HOMO's and 44% for both LUMO's) and in none of these orbitals is there more than a 1% contribution from B(2). Not surprisingly therefore, these orbitals differ little between the two systems, with those of the chlorinated species being slightly thermodynamically more stable. This is reflected in the electrochemical data; **20** is both easier to reduce and harder to oxidise than **19**. The precise role of the chloride in effecting these differences is not clear and the lack of comparable data on similar systems means assessment of the relative size of this effect cannot be made. However, one might anticipate that both the shifts in $E_{1/2}$ potentials as well as the variation in the chemical nature of any redox change would be greater in systems were the frontier molecular orbitals are more greatly perturbed (for example, halogenation at the bonding face of the *bis*-borane species discussed in Chapter 5).

Reaction of 19 with Excess Cl_2

If an excess of Cl_2 is added to a solution of **19** in dichloromethane, a number of new products are formed in addition to the monochlorinated species, **20**. Separation

of this mixture was performed using preparative thin layer chromatography (t.l.c.). The ^{11}B and $^{11}B-\{^1H\}$ n.m.r. spectra of one of the major new products, presented in Figure 4.4 along with, for comparison, the $^{11}B-\{^1H\}$ n.m.r. spectrum **20**, suggest that a second substutution of a terminal hydrogen atom by chlorine has occured. The number of resonances in the ^{11}B spectrum indicates the site of this second substitution must lie off the molecular mirror plane. Two resonances clearly show no $B-H_{terminal}$ coupling in this spectrum; that at -12.69p.p.m., assigned to B(2) by comparison with the spectra of **19** and **20**, and that at +16.38p.p.m. This resonance broadens slightly in the coupled spectrum, although this may, in part, be due to the overlap with a second boron resonance to lower frequency. Irradiation at the frequency corresponding to the peak at 16.38p.p.m., leads to enhancement of two proton signals in the ^1H n.m.r. spectrum, one at a frequency indicative of a terminal hydrogen, and therefore associated with the overlapping lower frequency boron resonance, the other at a frequency indicative of a hydrogen bridge, -9.05p.p.m. Thus the position of the second substitution must be in the open face as the boron atom involved is associated with a hydrogen bridge. Moreover, the low frequency of this ^1H n.m.r. resonance suggests it arises from a hydrogen atom bridging a ruthenium-boron connectivity. The similarity of the broad resonance centred around 0p.p.m. in this spectrum with that of **20** also suggests that B(8) and B(10) remain unchanged in the two species. Therefore, all the evidence suggests that the second chlorine atom is bonded to B(5).

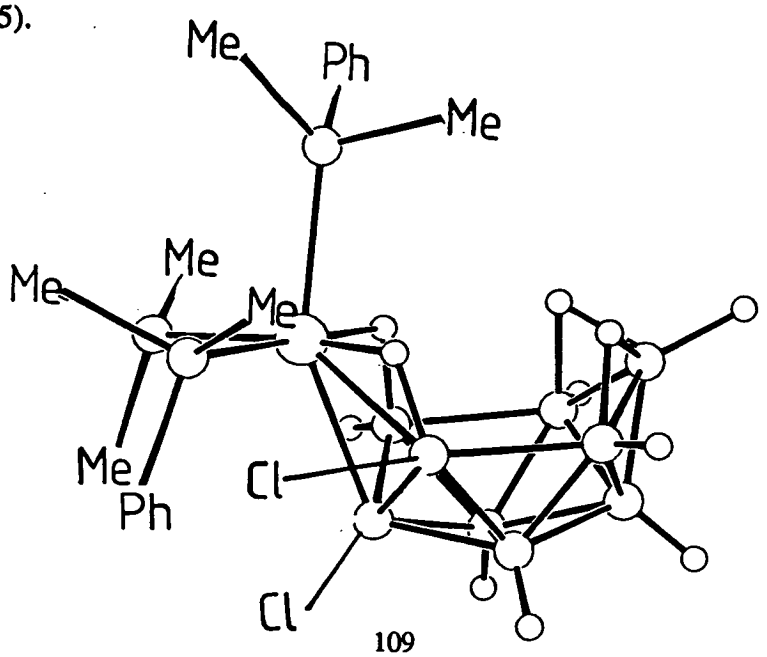

Figure 4.4 ^{11}B and ^{11}B-{^{1}H} N.m.r Spectra of the Product of Reaction of **19** with Excess Cl_2.

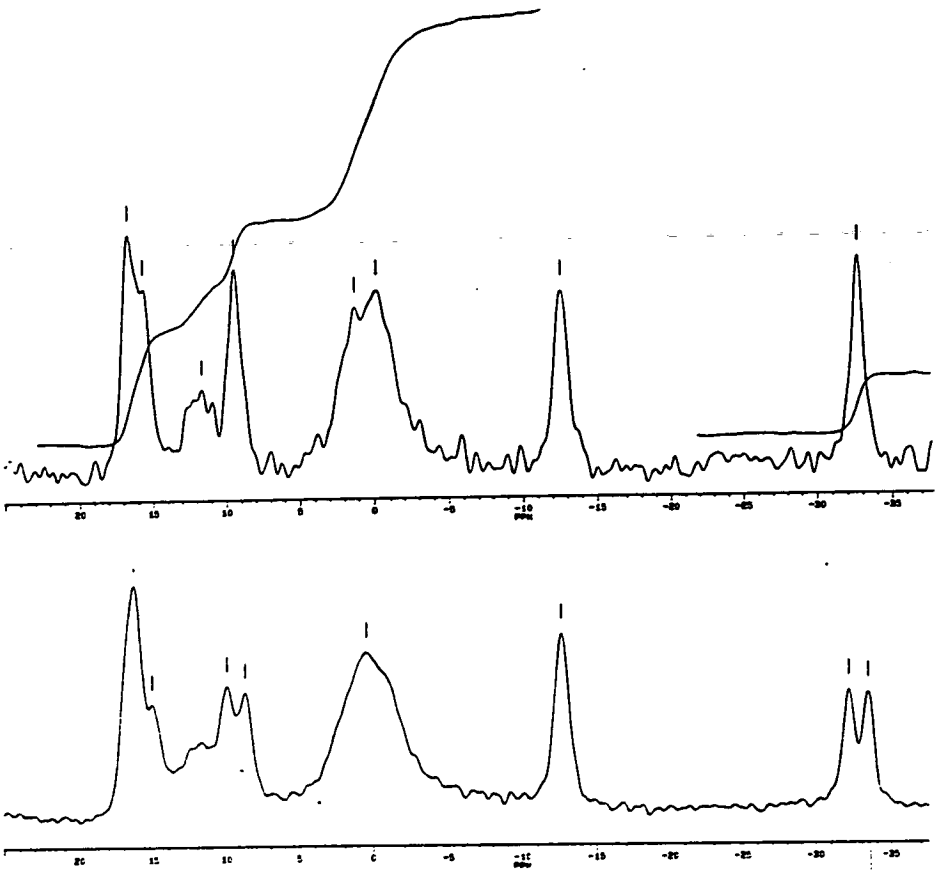

^{11}B-{^{1}H} N.m.r Spectrum of **20**.

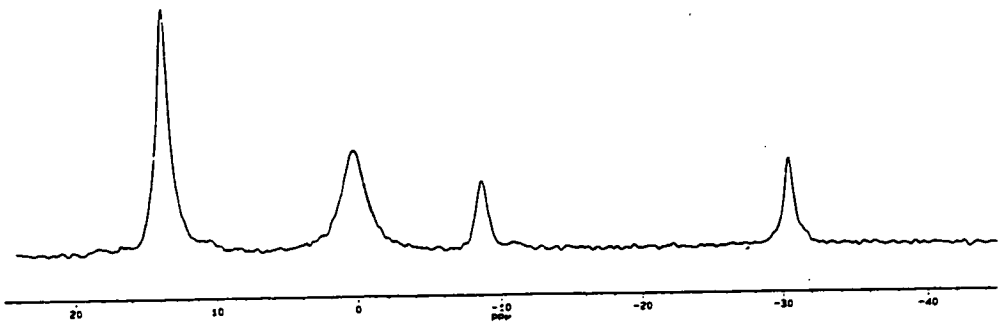

The formation of this species, 2,5Cl_2-6,6,6-$(PMe_2Ph)_3$-6-*nido*-RuB_9H_{11}, **21**, as the most likely dichlorinated species, might have been predicted from the EHMO studies on **19** and **20**. These reveal that the B(5) and B(7) sites in the latter are the least δ+, an observation correlated with a high likelihood of chlorine substitution, as seen above in the selective substitution of **19** at the B(2) position. The electrochemical response and electronic absorption data of **21** are discussed below.

The reactions of **19** can be compared with the chlorination reactions of *nido*-$B_{10}H_{14}$, **1**. Two mono-chloro derivatives of **1** have been reported with chlorination occuring at the 1 and 2 positions. In addition, the preparation of a di-substituted species, 1,2-$Cl_2B_{10}H_{12}$, is known; however all these reactions require the presence of $AlCl_3$ to proceed.[20] This is in contrast to the reactions of **19** described above in which no Friedel-Craft's catalyst was required. Also, in the metallaborane the site of the second substitution is at the 5 position. Both these differences must stem from the presence of the metal. The apparent greater reactivity of **19** with Cl_2 reflects the more electropositive ruthenium centre which, calculations show, creates a net negative charge at B(2). Similarily, although several products are formed in the presence of excess Cl_2, the directing influence of the metal causes a second chlorine substitution to occur at B(5), in contrast with $ClB_{10}H_{13}$, where the most electron-rich boron atoms appear to be in the basal positions.

Isolation and Spectroscopic Characterisation of Electrochemically Oxidised Products

The electrochemical response of **20** was indistinguishable from one of the daughter products of the electro-oxidation of **19**. If indeed these two species are the same, then the electrosynthetic mechanism of formation of **20** must be complex, involving a two-electron oxidation and subsequent reduction, as well as cleavage of the dichloromethane solvent. Renewed efforts directed towards the purification and

spectroscopic characterisation of the electrogenerated products were therefore undertaken.

An initial separation of the products formed by electrogeneration on **19** at +1.00V in dichloromethane can be achieved by the addition of diethylether to the product solution. This removes the majority of the bulk electrolyte, $[NBu_4][PF_6]$, as a precipitate which was then isolated by filtration. A.c. voltammetry on this regenerated electrolyte revealed it to contain one of the electrogenerated products, subsequently shown by ^{11}B n.m.r. spectroscopy to be borane-free. Removal of the dichloromethane from the original electrolysed solution gave a red gum which, when chromatographed using chloroform as eluant, realised at least 15 bands. The major band (R_f=0.7) was, in fact, the only species present in sufficient amounts to merit further work-up. A.c. voltammetry on this product showed it to be the species giving rise to the waves at +1.08 and -1.50V in the original electrogeneration and its UV/visible spectrum was superimposable on that of **20**. The ^{11}B and ^{11}B-{^1H} n.m.r. spectra of this species are shown in Figure 4.5. Although the appearence of these spectra is similar to those of **20** (see Figure 4.3), the two species are clearly not the same. The first difference is the coupling to the signal at +2.37p.p.m. in both spectra of the electrogenerated product. The coupling must arise through the interaction of an I=1/2 nucleus and the most likely explanation is the substitution of a terminal hydrogen by a phosphine group. The coupling constant of 83Hz is consistent with this assertion.[97] Secondly, whilst the four signals integrate in a similar way to those in the ^{11}B spectrum of **20**, the pattern of chemical shifts varies between the two systems. However, the overall similarity in the ^{11}B n.m.r. spectra of **20** and this new product does suggest the *nido*-decaboranyl structure is retained in the latter and allows the tentative assignment of its ^{11}B spectrum by analogy with that of **20**:

Metallaborane:	20/p.p.m.	Electrochemical Oxidation Product/p.p.m.
Boron Position		
B(1), B(3), B(5), B(7)	13.74	11.44
B(8), B(9), B(10)	0.23	-3.96
B(2)	-8.68	2.37
B(4)	-30.46	-31.64

Figure 4.5 ^{11}B and $^{11}B-\{^{1}H\}$ N.m.r. Spectra of the Isolated Product of the Electrochemical Oxidation of **19** at +1.00V.

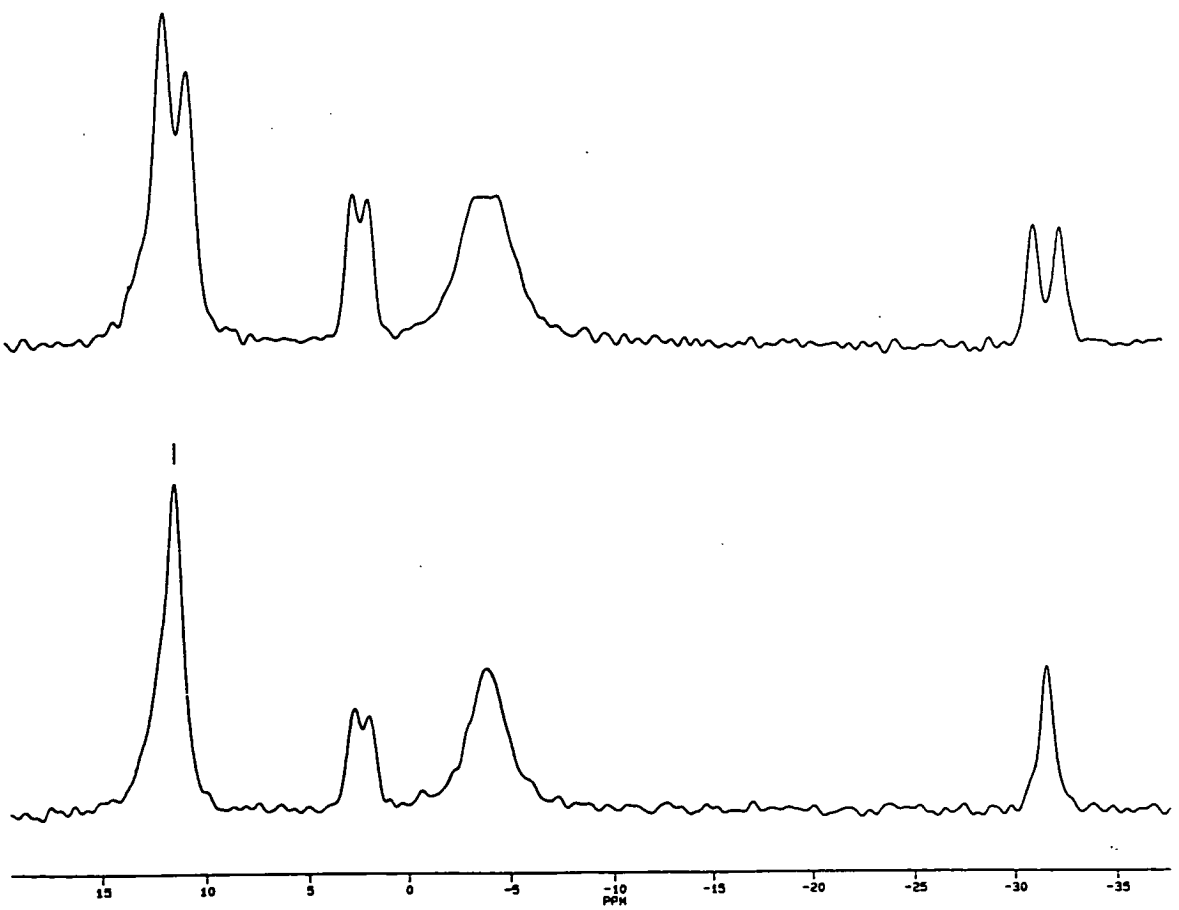

Comparing the two systems on this basis, we see little variation in the position of the highest and lowest frequency resonances (a slight shielding effect is seen in the new product). However, the B(2) position is markedly deshielded (by 11p.p.m.) whilst B(8), B(9) and B(10) show increased shielding. This cannot be explained in terms of any B(2)-P σ interaction as phosphorous is not as electronegative as chlorine and yet the B(2) position shows increased deshielding in what appears to be a phosphine-derivatised cage. It seems likely that this apparent inconsistency arises from the availability of the vacant phosphorous 3d orbitals. Unfortunately, due to the limited solubility of the material, as well as the problem of rapid relaxation of the ^{11}B signal, a ^{11}B-^{11}B COSY experiment yielded no further information on the structure of this species.

Another example of a phosphine substituted system is the ruthenaborane, 6,6,6-(CO)$(PPh_3)_2$-6-*nido*-$RuB_9H_{11}(PPh_3)$,[97] in which substitution is thought to occur at either B(8) or B(10). Although the ^{11}B-{^1H} n.m.r. spectrum of this species, and that of the parent, 6,6,6-(CO)$(PPh_3)_2$-6-*nido*-RuB_9H_{13}, have not been fully assigned, the B(8) and B(10) atoms in these two species are thought to give rise to resonances at -8.9 and 26.0p.p.m. and 1.7 and -2.1p.p.m. respectively. In the light of the spectroscopic studies on the electrochemically-generated species above, it is likely that it is the site of substitution in the published ruthenaborane that gives rise to the higher frequency resonance (26.0p.p.m.) with, again, the phosphine substituent causing strong deshielding of the boron to which it is attached.

The ^1H n.m.r spectrum of the electrochemically-generated species (Figure 4.6) displays the expected resonances in the methyl and phenyl regions arising from the PMe_2Ph groups. In addition to these, two broad signals can be seen at -3.60 and -10.95p.p.m., assigned to hydrogen atoms bridging B-B and B-Ru connectivities respectively.

Figure 4.6 ^{1}H N.m.r. Spectrum of the Electrochemical Oxidation Product.

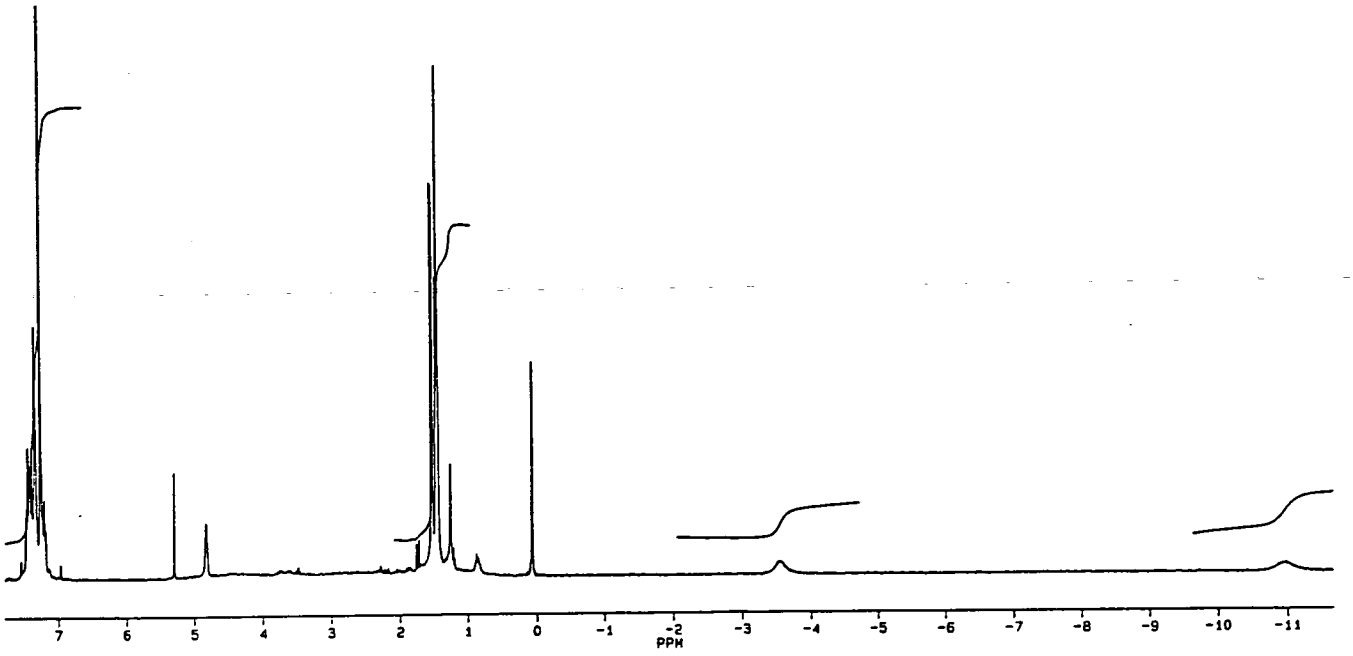

Figure 4.7 ^{31}P N.m.r. Spectrum of the Electrochemical Oxidation Product.

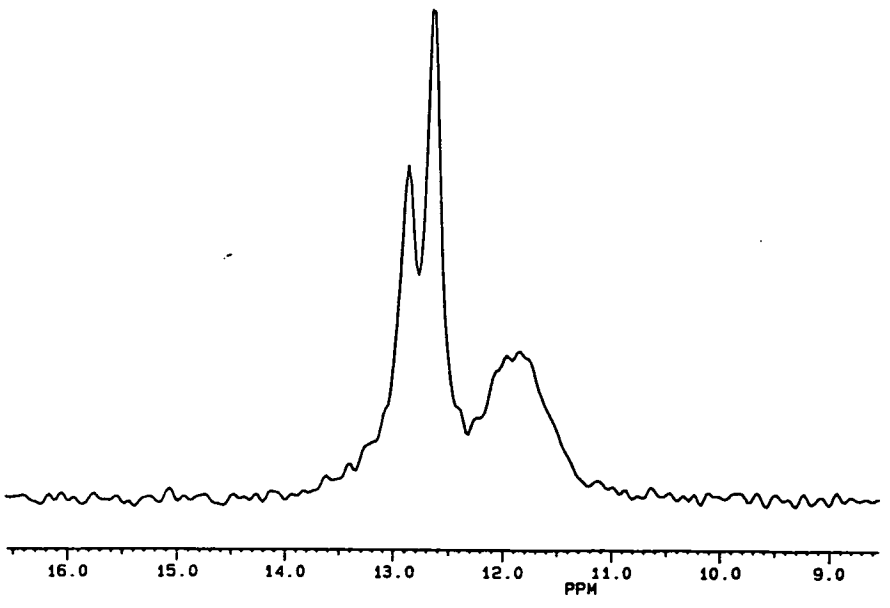

That only two bridge environments are apparent is again consistent with the retention of a *nido*-decaboranyl cage architecture and a molecular mirror plane. If this is so, these signals must arise from two pairs of hydrogen bridges and, returning to the methyl and phenyl areas, integration implies the presence of three rather than four PMe_2Ph units. The methyl region itself consists of three doublets, two of which overlap to form a triplet. There are therefore three methyl environments present, each of which give rise to a doublet through coupling to a phosphorus nucleus.

The ^{31}P n.m.r. spectrum of this species is shown in Figure 4.7 and exhibits three signals. The broad resonance centred on 11.67p.p.m. is likely to originate from the cage-bound phosphine, the broadening of the signal arising from the one bond coupling to a boron nucleus. Assignment of the other two peaks (of integral two) in this spectrum to two inequivalent phosphorus environments is not consistent with the interpretation of the ^{11}B and ^{1}H spectra above. If the molecule retains mirror symmetry, then these two signals in the ^{31}P spectrum must arise from one phosphorus environment, with coupling to the third (cage-bound) phosphorus to give a doublet. One method to confirm this would be to obtain the ^{31}P spectrum at a different field strength; no change in the phosphorus-phosphorus coupling should be observed.

From these spectroscopic studies a structure for this daughter product in solution can be proposed:

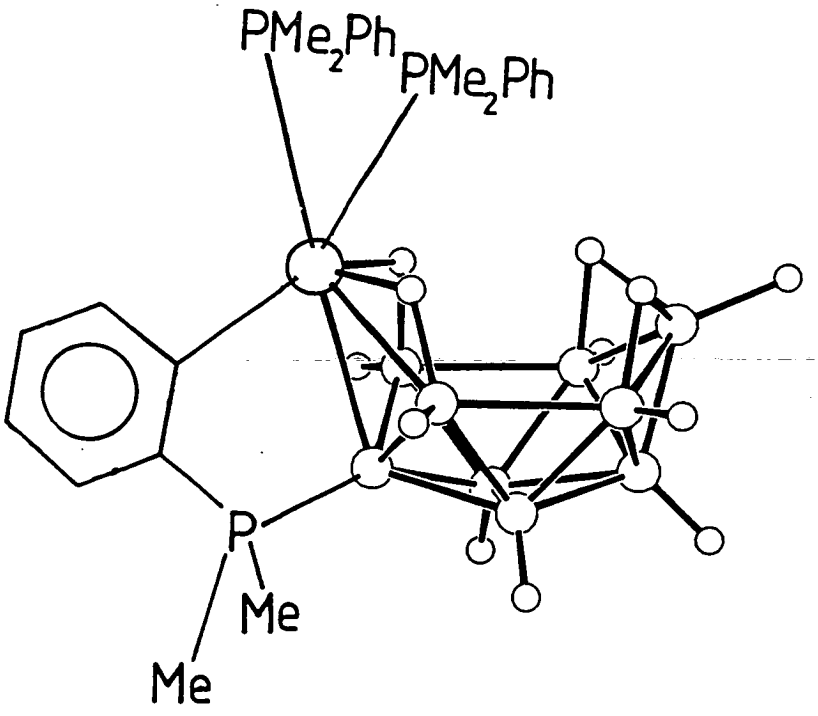

This represents the "average" structure observed on the n.m.r. timescale. The proposed molecule, 2-($PMe_2C_6H_4$)-6,6-(PMe_2Ph)$_2$-6-*nido*-RuB_9H_{12}, **22**, displays the *nido*-decaboranyl architecture suggested by the ^{11}B and ^1H n.m.r. spectra. In addition, the conformation of the phosphine groups maintains that mirror symmetry and means that each metal-bound phosphine group is bonded to two inequivalent methyl groups, explaining the occurrence of three doublets in the methyl region of the ^1H n.m.r. spectrum. In this interpretation, the two metal-bound phosphorus atoms exhibit a coupling to the cage-bound phosphorus atom of 34Hz. For the structure as drawn this coupling will be facilitated by the π system of the phenyl ring. Evidence in support of *ortho*-metallation can be found in the similarity of the ^{11}B n.m.r. spectra of **19** and **20** with that of **22**. If a five coordinate ruthenium centre was involved in **22**, greater variation may be expected in these spectra. Also, such a structure is without precedent in the literature and the metal-phenyl carbon linkage maintains a metal centre truely isolobal to {BH}. The spectra of **19** and **20** imply that the {RuP_3}

units in these species are spinning, such that a mirror plane is present on the n.m.r. timescale. For **22**, such rotation is limited to approximately 120° by the Ru-C_{phenyl} bond, but this is enough to make the two metal-bound phosphorus atoms equivalent.

The structure established above is consistent with the n.m.r. data. In the solid state however, such a trigonal prismatic coordination of the metal centre is likely to only represent an intermediate between two enantiomeric forms involving a *pseudo*-octahedrally coordinated ruthenium atom, similar to that seen in analogous systems.[30,37] One such enantiomeric form is shown below:

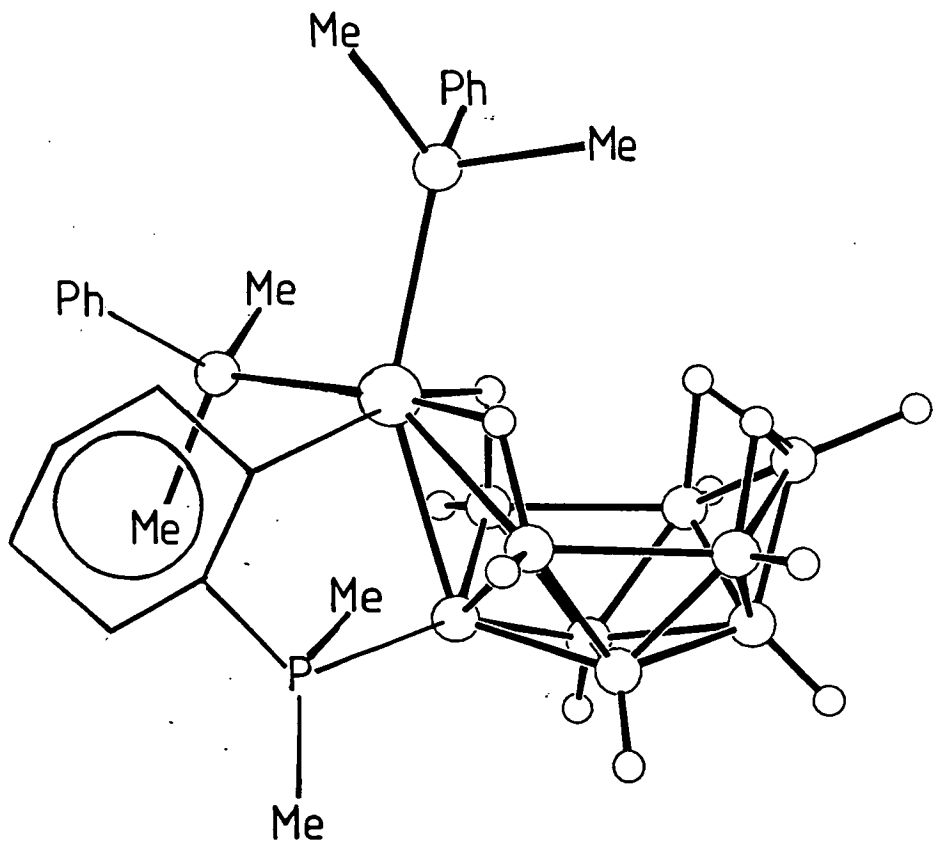

Electrochemical Study of 22

At 290K in dichloromethane **22** exhibits a quasi-reversible oxidative electron transfer at +1.08V and a partially reversible reduction at -1.50V, with an associated daughter product wave at -1.02V in the return wave of the reductive cyclic voltammogram. Both exhibit greater chemical reversibility at 238K, with no evidence of the reductive daughter product being seen at this temperature. A second partially reversible oxidative process occurs at +1.40V and associated with this is a desorption peak centred at +0.1V, very similar in shape to that seen in the cyclic voltammogram of **19**. This second oxidation remained partially reversible even at reduced temperatures. The electrochemical response of **22** is shown in Figure 4.8.

The electrochemical oxidation of **22** is much more chemically reversible than that of **19**. This point was further studied by a bulk electrolysis at +1.2V and 238K. During the course of this electrogeneration the solution was seen to darken markedly and coulometry indicated the passage of two moles of electrons per mole of **22** present. Voltammetry of the resultant solution initially gave no evidence for the presence of any redox-active species. When the potential was removed, however, the solution began to lighten in colour and a.c. voltammetry indicated that partial regeneration of **22** had occurred, as well as the appearence of a broad wave centred at +0.4V. Overall, the a.c. voltammetry of the final solution was similar to that obtained from the bulk oxidation of **19**, the implication being that the oxidation of both **19** and **22** result in the formation of the same species. This explains the increased chemical reversibility of the oxidation of **22** compared to **19**.

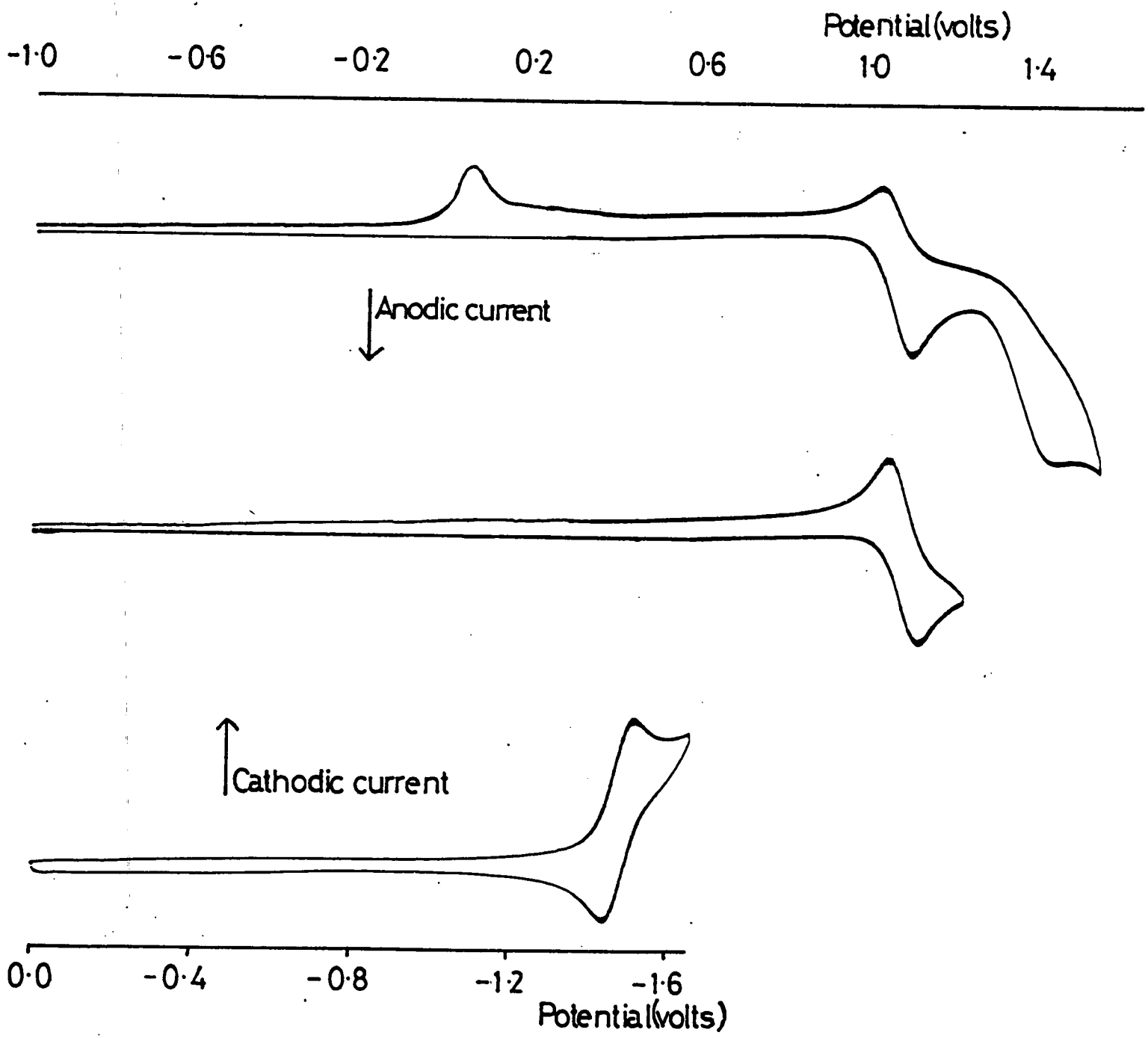

Figure 4.8 Electrochemical Response of **22** in Dichloromethane at 238K.

The mechanism of formation of **22** is clearly very complex. The EHMO calculation on **19** indicates the HOMO of that system to have a high degree of metal character. Thus the initial product of oxidation of that species, "19^{2+}", contains, formally, a Ru^{IV} metal centre, making the Ru-P bonds extremely labile. To yield **22**, a reduction of this, or a related, species must occur, and one possible mechanism may involve a disproportionation reaction. If the same intermediate is found in both the oxidation of **19** and **22**, either its disproportionation or oxidation would give rise to the same species. The presence of the very similar waves at +0.1V associated with the oxidation of **19** and the second oxidation of **22** supports this idea. Further characterisation of the many other products formed in the course of the oxidation of **19** may illuminate further the mechanism of formation of **22**.

The electrosynthetic oxidation of **19** was also carried out in the presence of one equivalent of PMe_2Ph, $P(OMe)_3$ and in a dichloromethane solution saturated with CO. However, from all these studies **22** was formed in a similar yield to that using only **19** and no evidence for any compounds related to **22** incorporating any of these dopants could be obtained. These results imply that the conversion of **19** to **22** is an intramolecular process.

Electrosynthesis of 19 in Acetonitrile

In acetonitrile, a similar oxidation step to that seen in dichloromethane is observed at +0.99V. However, on a cyclic voltametric timescale two daughter products at +1.35V and +1.50V are observed. Both these processes are partially reversible at 290K but become chemically reversible at 238K. Bulk electrosynthesis at +1.2V and 290K yielded the species giving rise to the oxidation at +1.35V with an associated partially reversible reduction at -1.38V. The oxidation of **19** in acetonitrile appears much cleaner, with fewer redox-active products being formed than that in dichloromethane. Although the ^{11}B and $^{11}B-\{^1H\}$ spectra of the product solution

were complicated by the presence of several minor products (see Figure 4.9), comparison with the n.m.r. spectra of **19** and **20** suggests that terminal hydrogen substitution at the 2 position has once again occured, the resonance at -20.45p.p.m. exhibiting no coupling in the $^{11}B-\{^{1}H\}$ spectrum. The fact that this resonance and a similar one at +21.56p.p.m. show no B-P coupling indicates that substitution has occured by another species, probably acetonitrile. This, and the simplified nature of the product mixture formed in this solvent, suggests the role of this stongly coordinating solvent is important in the oxidative procedure. Preparative t.l.c. on the product mixture, however, resulted in decomposition of the major product and no further characterisation of this species could be achieved.

Figure 4.9 ^{11}B and $^{11}B-\{^{1}H\}$ N.m.r. Spectra of the Mixture Formed from the Electrochemical Oxidation of **19** in Acetonitrile at 290K.

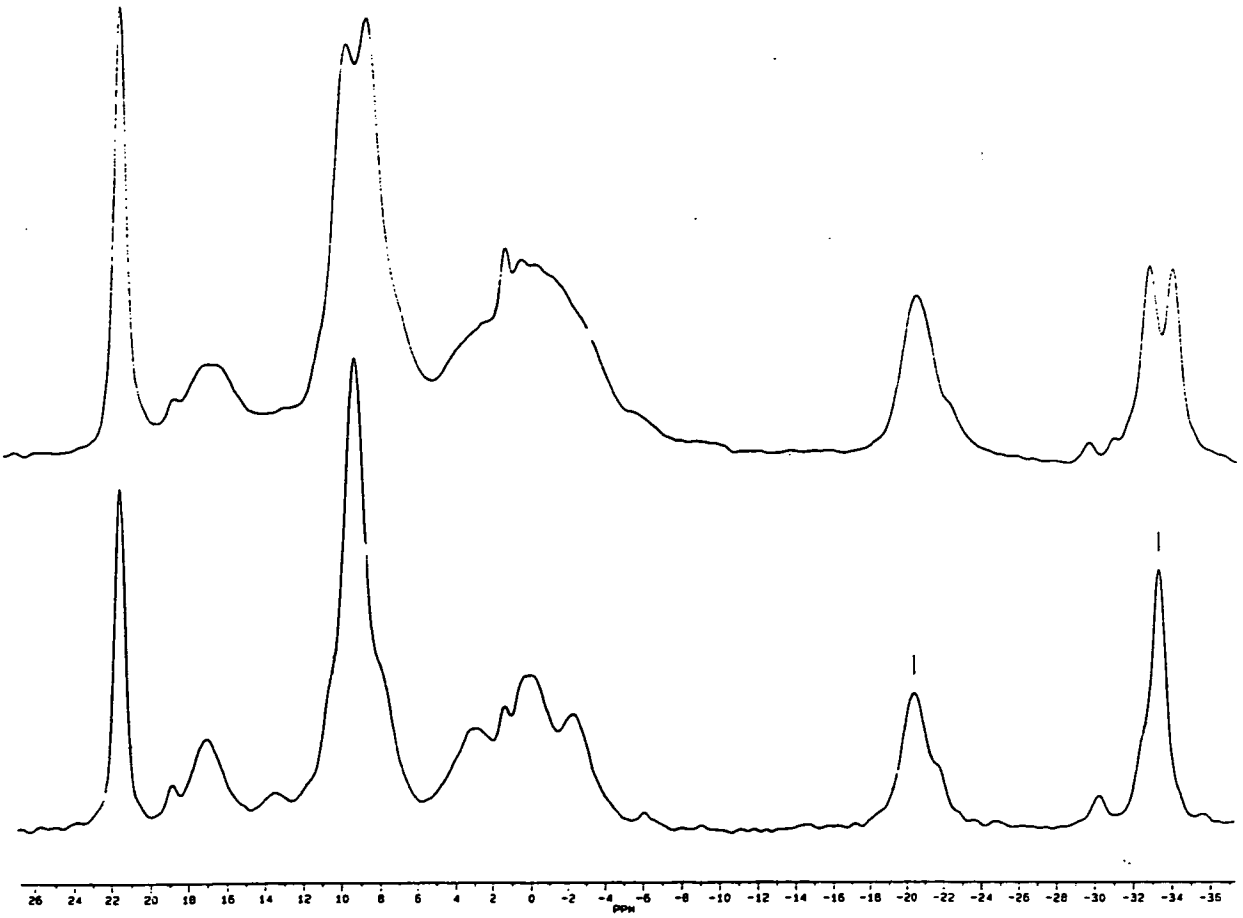

Substituent Effects

Three substituted derivatives of **19** have been prepared here and the electrochemical and electronic absorption data are collated in Table 4.5 below.

Table 4.5 Electrochemical and UV/Visible Data for **19**, **20**, **21** and **22**

	E_p^a	E_p^c	ν_{max}/cm^{-1} (ϵ, $moll^{-1}cm^{-1}$)
19	+0.97V	-1.54V	21700 (1900), 33000 (9900)
20	+1.10V	-1.43V	21500 (2100), 32500 (7800)
21	+1.16V	-1.31V	21100 (2100), 32400 (7100)
22	+1.08V	-1.50V	21400 (2300), 32300 (8300)

Considering first the electrochemical data, the oxidative and reductive potentials of each system bear a similar relationship to those of **19**. EHMO calculations on **19** and **20** showed this to be related to the thermodynamic stability of the frontier MO's, rather than any specific change in electronic structure. A second chlorine substituent causes further electron withdrawal from the cage and, again, the electrochemical data suggest a thermodynamic stabilisation occurs. The data on **22** could be similarily rationalised in terms of, relative to chlorine, a less electronegative phosphorous substituent. However, the nature of the ^{11}B n.m.r. spectrum of this species suggests the interaction between cage and substituent is more complicated in this case. In addition, the different metal environment also makes comparison between **22** and the other three metallaboranes more difficult.

The chemical nature of the oxidation of **19**, **20** and **21** is similar and only in **22** is any degree of chemical reversibility encountered, for the reasons discussed above. In **20** and **21** the 2 position is substituted and as no evidence for the formation of **22** is seen in the cyclic voltammogram of these species, it appears that the B(2)-Cl bond in this species is much less susceptable to substitution than the B(2)-H bond in **19**. It would be interesting to see if bulk electrolysis of these chlorinated species resulted in substitution at this position over longer timescales, and, if not, whether the distribution of the other products formed is different to that seen from the oxidation of **19**.

Unlike the other three species, the reduction of **21** exhibits some chemical reversibility at 290K. Whether this is retained over the period of an electrogeneration was not studied, however, it is likely that the relatively greater stability of the initial reduced form of **21** is linked to the nature of the frontier MO's of this system. It was noted above that the LUMO's of **19** and **20** contained little contribution from the B(2) position and therefore substitution at this position caused little variation in the behaviour of these systems. The LUMO's do have a significant contribution from the B(5) and B(7) positions, however, and if this is also the case in **21**, then the ability of the chlorine substituent to withdraw electron density should aid the stability of its reduced form.

The UV/visible spectra of these four systems show very little variation, indicative of little perturbation of the MO's involved in the absorption processes. Assignment of these spectra suffers form the lack of data on comparative systems. The related parent boranes, *arachno*-$[B_9H_{14}]^-$ and *nido*-$B_{10}H_{14}$, exhibit absorption maxima at 36900cm^{-1} (ε=3980$moll^{-1}cm^{-1}$)[13] and 37300cm^{-1} (ε=2700$moll^{-1}cm^{-1}$) respectively. The bands at around 32000-33000cm^{-1} in the spectra of the metallaboranes are more intense and so cannot be ascribed completely to any intra-borane transition. Rather, these processes may be described as intra-cluster charge transfer (ICCT) bands,

occurring between two cluster MO's of varying metal and borane character. Assignment of the bands around 21500cm^{-1} in these spectra is not so simple. Similar bands, although at higher energy, have been noted in the spectra of several systems of the type $[(PR_3)_3Ru^{II}X_3Ru^{II}(PR_3)_3]^+$, where X is typically a halide. Variation of the phosphine groups in these systems indicated that these processes are due to intra-phosphine transitions.[98] However, the bands at 21500cm^{-1} may be of too low an energy for such a process. Also, one might anticipate a greater change in the spectrum of **22**, where one phosphine group is effectively bridging between the metal and cage. An alternative interpretation is that these bands are due to (Laporte forbidden) metal to phosphine transitions. This is consistent both with the intensity of these bands and the retention of the band in the spectrum of **22**. Indeed, the minor changes in the UV/visible spectra of these four species reflect the peripheral role of the substituents in the electronic structure of the frontier MO's of these systems.

Reductive Electrosynthetic Studies

The bulk electrochemical reduction of **19** was studied in dimethylformamide (DMF), since this solvent affords a greater negative potential range than dichloromethane. **19** exhibits a partially reversible electron transfer at -1.54V in DMF, and, as in dichloromethane, evidence for two daughter products at -1.07 and -0.06V are seen in the return sweep of the reductive cyclic voltammogram at 290K. An increased chemical reversibility is observed at 238K, again, as is the case in dichloromethane.

Bulk electrolysis of a solution of **19** in DMF at -1.75V and 238K revealed that the reductive step involved one electron per mole of **19** present. Electrochemical analysis of the orange solution formed as a result of this electrogeneration showed that a structurally altered, new species had been produced. This species exhibited a partially reversible oxidation at -0.06V and bulk oxidation at potentials positive of

this regenerated **19** in full. This new, air-sensitive reduction product was found to be EPR-active and, although it could also be formed by the chemical reduction of **19** with sodium wire, repeated attempts at crystallisation afforded no suitable crystals for an crystallographic study.

The EPR spectrum of the electrogenerated product is shown in Figure 4.10 and was later confirmed by an *in-situ* electrogeneration using the Electron Paramagnetic Resonance *in-situ* Electrochemical (EPRESISE) cell. Two signals are seen at g=2.144 and 2.081, and overall the shape of this spectrum is typical of a d^7 axial system with a $d_{x^2-y^2}$ ground state. The EHMO calculation on **19** confirms the LUMO of this system to have a high degree of metal character and the greatest contribution to this coming from the $d_{x^2-y^2}$ orbital. However, the electrogeneration does not produce "**19**$^-$", a structural analogue of **19**, but a structurally different species, the EPR signal of which is indicative of a species with an even higher degree of metal character in the singly occupied MO. Any delocalisation on the cage would broaden the signal considerably due to superhyperfine coupling to the boron atoms (compare, for example, the EPR spectrum of **10**$^-$, Chapter 5). In addition, no obvious evidence is seen for coupling to the phosphorous nuclei.

The UV/visible spectra of **19** and the reduced product are compared in Figure 4.11. Several changes occur upon reduction. The band at 21700cm^{-1} grows in intensity and moves to higher energy, whilst that at 33000cm^{-1} is lost with concomitant growth of two new bands in this area. The two bands at 35500cm^{-1} and 29100cm^{-1} may be assigned to ICCT processes described above, and as such, are indicative of a major change occuring in the overall nature of the cluster. This is in contrast to the spectra of **19, 20, 21** and **22** where the same basic cluster structure gave rise to very similar UV/visible spectra. The movement to higher energy of the band at 21700cm^{-1} in the spectrum of the reduced form is not consistent with its above assignment to a metal to phosphine charge transfer process. As the electron density at the metal is increased,

so any charge transfer from that metal should show a decrease in energy.

Interpretation of the changes observed in these spectra upon reduction suffers from the lack of structural information on the product, and further analysis may well have to wait upon structural data.

All the data obtained on this reduction product, therefore, suggest a major structural difference between it and **19**. Cyclic voltammetry indicates that at least two intermediates are formed in the reduction process; "**19**$^{-}$", which can be stabilised briefly at 238K, as well as the intermediate at -1.07V (see Figure 4.1). The EPR spectrum suggests a tetragonally compressed ruthenium environment and the overall reversibility of the reduction/oxidation procedure demands that the integrity of the $\{P_3RuB_9\}$ unit remains intact.

The initial reduction product, "**19**$^{-}$", is, formally, an analogue of $[B_{10}H_{14}]^{-}$, a species invoked in the mechanism of the electrochemical reduction of *nido*-$B_{10}H_{14}$ to *arachno*-$[B_{10}H_{14}]^{2-}$, but otherwise uncharacterised.[48] In contrast, the ruthenaborane does not undergo any further reduction, but undergoes a structural change to give a monoanionic species. Thus the electrochemical behaviour of *nido*-decaborane and this *nido*-6-metalladecaborane cannot be said to be analogous.

Figure 4.10 EPR Spectrum of the Product of Reduction of **19** in DMF at -1.75V. Recorded as a Frozen Glass at 78K.

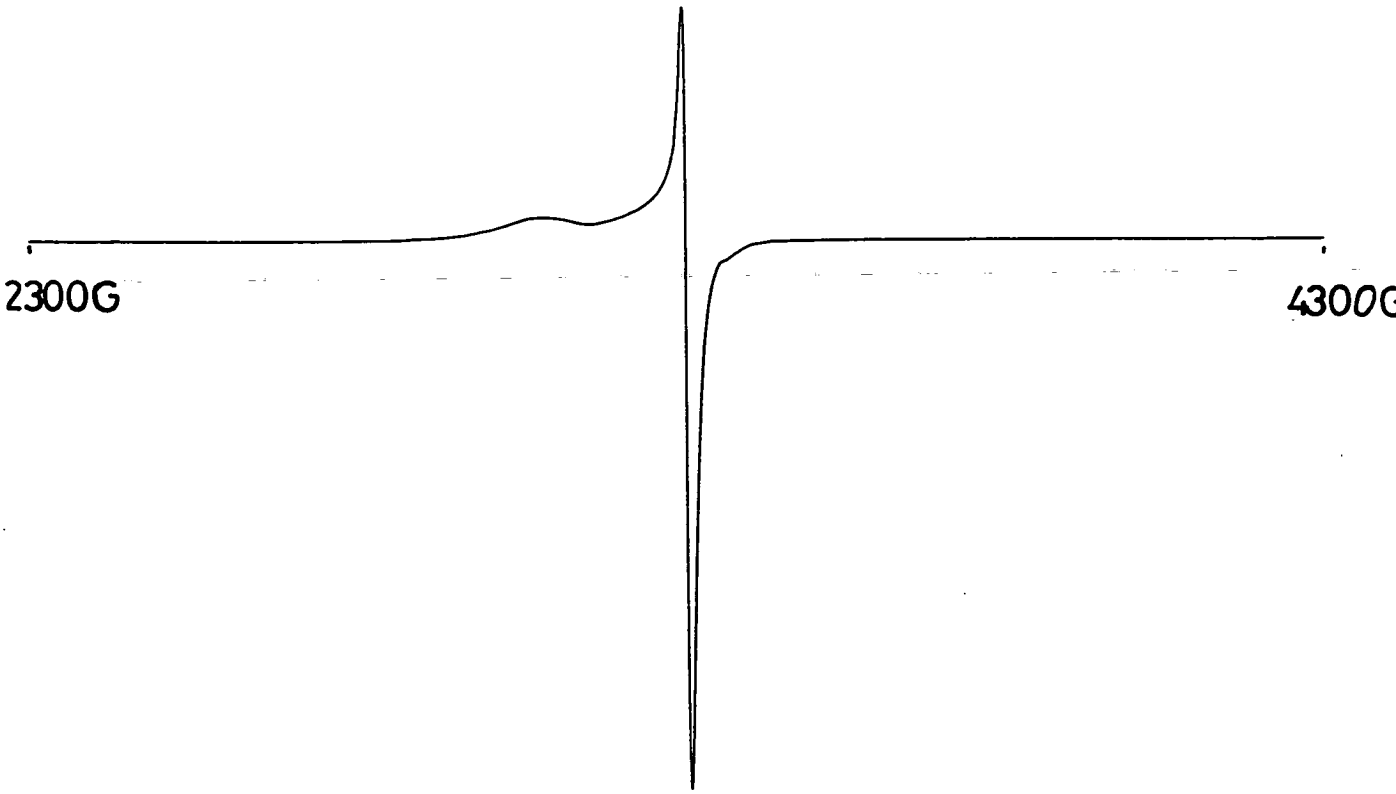

Figure 4.11 UV/Visible Spectra of **19** (i) and its Reduction Product (ii) in Dichloromethane at 238K.

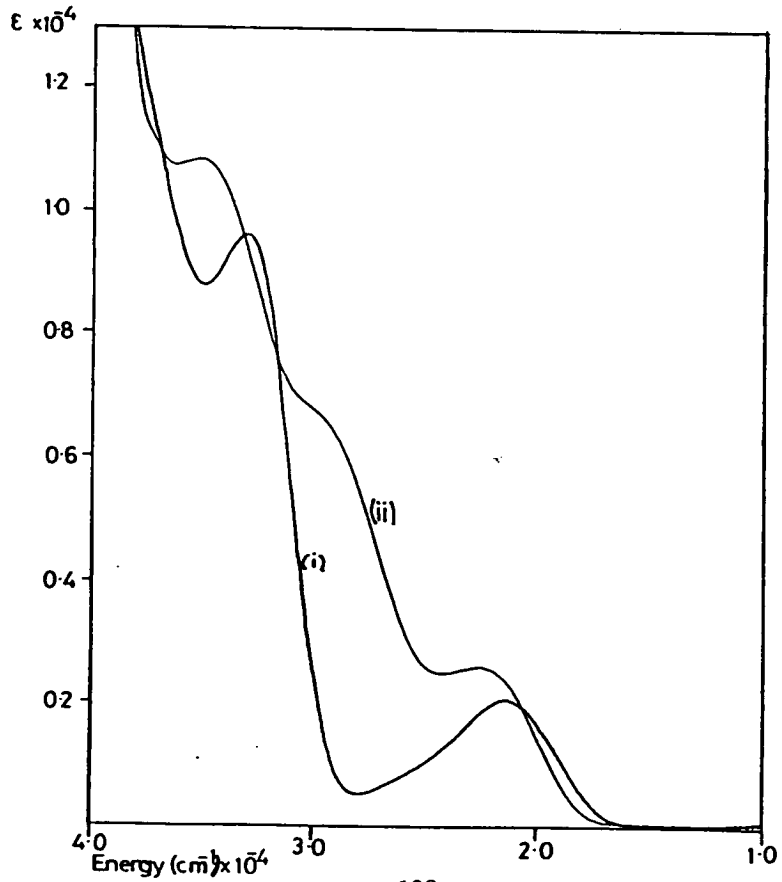

Summary

That the electrochemical oxidation and reduction of **19** induce structural change would be expected from PSEP theory. A two electron oxidation of this species should, according to this theory, cause a structural change from *nido* to *closo*. Clearly, the one characterised product of this oxidation, **22**, retains a *nido* geometry. However, how this relates to the initial product of oxidation could not be determined. Certainly this initial product, whatever its geometry, is very unstable and rapidly undergoes further reaction.

The one electron reduction of **19** again causes structural change although no analogue of *arachno*-$[B_{10}H_{14}]^{2-}$ could be isolated. Structural data on this reduction product would be interesting as its electron count appears to be intermediate between *nido* and *arachno*, and which extreme would predominate in this case is not clear.

The chlorination of **19** results in the thermodynamic stabilisation of the frontier MO's in the ruthenaboranes formed and this is reflected in the electrochemical data. However, the UV/visible spectra of these chlorinated species suggest that the overall form of the frontier MO's of **19**, **20** and **21** remains constant in all three species.

Chapter 5

Electrochemical Studies on $[BTMA]_2[M(B_{10}H_{12})_2]$ Species; M=Ni, Pd and Pt

$[NMe_4]_2[Ni(B_{10}H_{12})_2]$, $[NMe_4]_2$**8**, was the subject of one of the few previously reported electrochemical studies on metallaboranes.[63] The results of this study were initially confirmed and then compared with the redox behaviour of the palladium and platinum analogues, **11** and **10** respectively. As in Chapter 4, the nature of any redox products can be compared with those which might be expected from strict application of PSEP theory.

Anodic Electrochemistry of 8, 10 and 11.

The electrochemistry of these three species was investigated in DMF and acetonitrile. In both solvents each metallaborane exhibited a structurally similar, partially reversible oxidation wave, typified by that shown in Figure 5.1 for the platinum species in acetonitrile at 290K. $E_{1/2}$ values for all three metallaboranes in the two solvents used are shown below:

Metallaborane:	**8**	**11**	**10**
E_p^a, CH_3CN	1.24V	1.28V	1.40V
DMF	1.22V	1.26V	1.38V

It is likely that the variation in these half-wave potentials with solvent arises from the different junction potentials established between the frit of the reference electrode and the bulk solution. Bulk electrosynthesis beyond these oxidative couples in acetonitrile resulted in all cases in the decolourisation of the solution, and subsequent electrochemical investigation revealed that a complex mixture of species had been

formed. Coulometric measurements over the period of generations consistently gave values of between 6 and 8 moles of electrons per mole of compound used, suggesting that the initial oxidation product of the starting material itself undergoes further oxidation.

As discussed in Chapter 2, EHMO calculations on these systems showed the HOMO's of **8**, **11** and **10** to be more than 90% borane based. Further analysis showed that these orbitals were predominantly bonding in character within the cage framework. Depopulation of the HOMO's of these systems would therefore be expected to weaken the cage bonding, possibly leading to degradation. This is what appears to happen, the decolourisation of the solution suggestive of cleavage of the metal-boron bonds and the complex nature of the voltammetry of the product solutions indicative of a large number of degradation products.

The trend in oxidation potential, increasing as the triad is descended, is mirrored in the energies of the HOMO's of these systems obtained from the EHMO calculations:

Metallaborane:	**8**	**11**	**10**
Energy of HOMO/eV:	-10.147	-10.164	-10.311

These observations may be related to nature of the bonding between metal and borane discussed in section Chapter 2. It was noted that the larger Pt valence orbitals gave more efficient overlap with the borane fragment resulting in greater *arachno* character in the latter. This increased interaction would also result in the stabilisation of the resultant filled bonding MO.

Cathodic Electrochemistry

$[BTMA]_2$8.

$[BTMA]_2$8 displayed no electrochemical response in the range 0 to -2.5V in either DMF or acetonitrile. The previous study on this system also made no mention of any cathodic electrochemical response.

$[BTMA]_2$10

The cathodic electrochemical response of this species in acetonitrile at 290K is also shown in Figure 5.1. $E_{1/2}$ for this process occurs at -1.57V in this solvent and at -1.65V in DMF. Variable scan rate measurements showed the electron transfer process to be quasi-reversible in both solvents at both 290 and 238K. A bulk electrosynthesis in acetonitrile at -1.8V and 238K results in a rapid darkening of the initially yellow solution to deep maroon. Voltammetry of this product showed that no gross structural change had occured upon reduction, the cyclic and a.c. voltammograms being superimposible on those of the starting material, and a stirred voltammogram confirming the process at -1.57V to be oxidation. The product solution was found to be extremely air-sensitive, re-oxidation to the starting material being instantaneous upon exposure. The starting material could also be fully regenerated by a bulk electrolysis at -1.0V. A conventional time-current coulometric study on this process gave a value of the number of electrons involved in the reductive step of between one and two per mole of material present. This anomalous result was thought to be due to the high potential required to effect the reduction leading to a high background current arising from reduction of the solvent. In view of this and, especially, the air-sensitive nature of the reduced species, any subsequent characterisation relied wholly on *in-situ* spectroelectrochemical techniques. Under analogous conditions, the behaviour of this system was found to be the same in DMF.

Figure 5.1 Electrochemical Response of $[BTMA]_2$**10** in Acetonitrile at 290K.

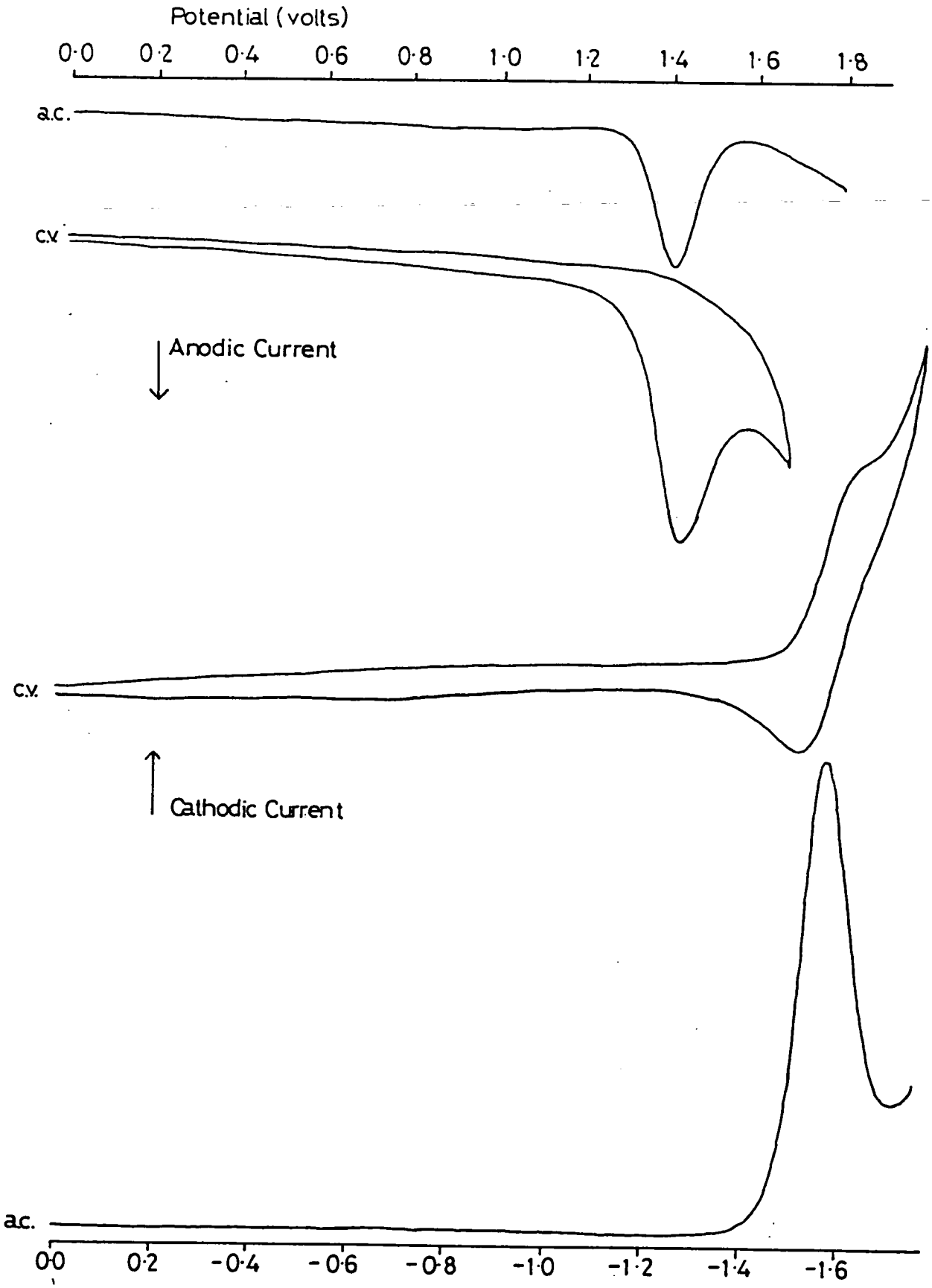

Figure 5.2 compares the UV/visible spectra of **10** in DMF and that of its reduced form obtained from an *in-situ* spectroelectrochemical study performed at 238K. The initial spectrum of **10** is dominated by two absorbances; upon reduction, the band at 36300cm^{-1} shows little change, whilst that at 26600cm^{-1} is lost, with the concomitant growth of the shoulder at 23600cm^{-1} and three other bands at 18500, 21200 and 28700cm^{-1}. The chemically reversible nature of this reductive step was confirmed by this *in-situ* study and made available the technique of controlled potential coulometry for assessment of the number of electrons involved in the reduction of **10**. This was carried out using the OTTLE cell and involves the electrochemical generation of an equilibrium mixture of **10** and its reduced form at a number of potentials near to $E_{1/2}$ for the reduction. From the absorption of these equilibrium mixtures, the number of electrons, n, involved in the reductive step can be calculated by application of the Nernst equation:

$$E = E^{o} + RT/nF\ln[O]/[R]$$

Experimentally [O]/[R] is equal to the absorbance ratio, r(ε).

$$r(\varepsilon) = [A(E) - A_R]/[A_O - A(E)]$$

Where A(E) is the absorbance at a chosen wavelength at an applied potential E, A_R is the absorbance at that wavelength of the fully reduced species and A_O the absorbance at that wavelength of the fully oxidised species.

Thus a plot of E *versus* ln r(ε) should, for a Nernstian system, give a straight line of gradient RT/nF and also the half wave potential for the process when r(ε) is zero.

The results of this study are presented in Figure 5.3 and give a value of

n=0.91±0.05 electrons involved in the reduction and a $E_{1/2}$ value of -1.67V, in reasonably good agreement with that obtained from a.c. voltammetry.

Figure 5.2 UV/visible Spectra of $[BTMA]_2$**10** (i) and its Reduced Form (ii) in DMF at 238K.

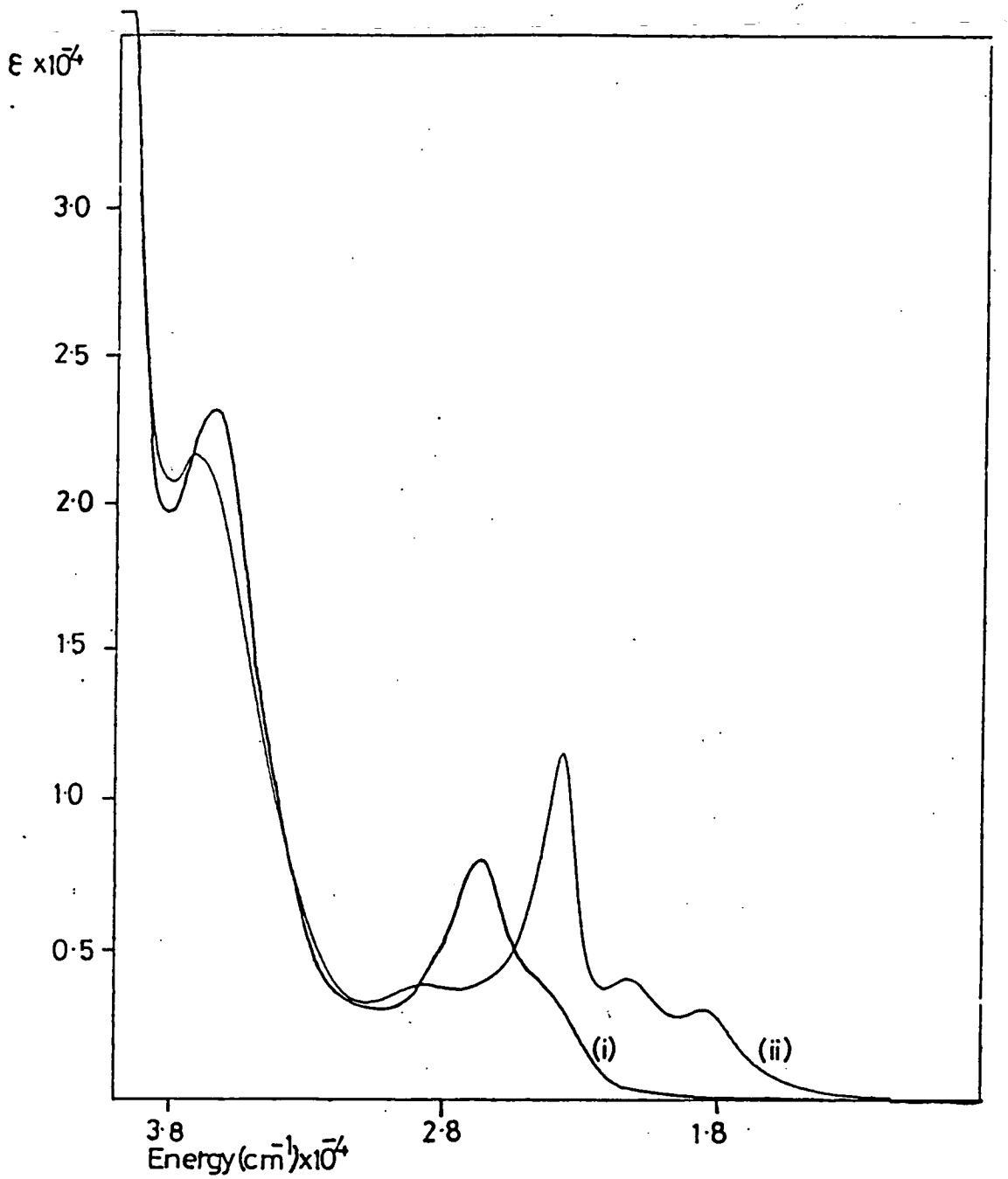

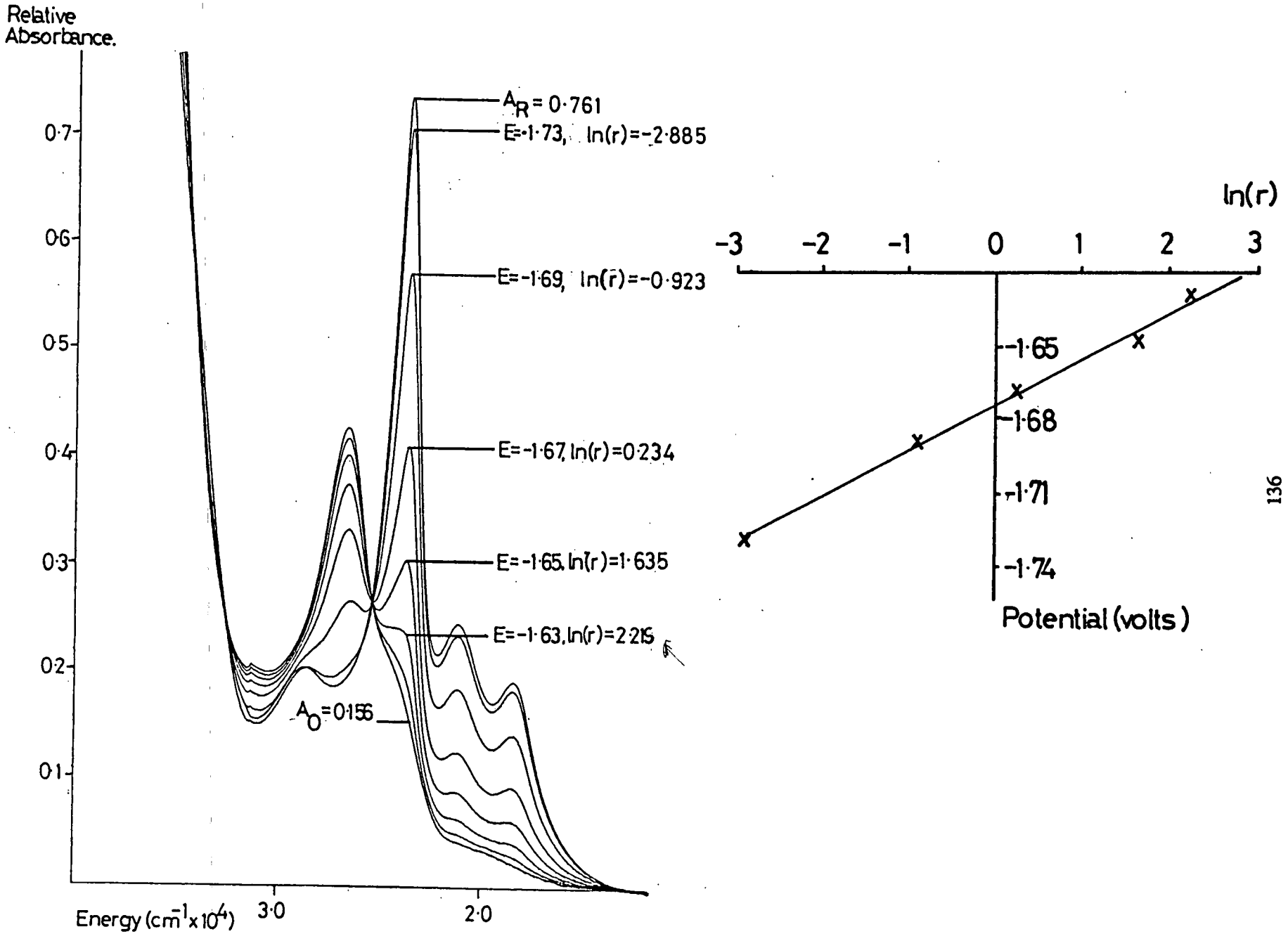

Figure 5.3 Coulometric Study of the Reduction of **10** in DMF at 238K.

The EPR spectrum of **10**$^-$ was recorded from an *in-situ* electrogeneration in the EPRESISE cell and is shown in Figure 5.4. The signal is extremely broad and, assuming the structure of **10**$^-$ retains C_{2h} molecular symmetry, cannot be easily interpreted in terms of a classic d^9 metal centre with a $d_{x^2-y^2}$ or d_{z^2} ground state. In order to assign the ground state of this system, the nature of the LUMO of **10** was investigated by an EHMO calculation. The LUMO was found to be delocalised over the platinum metal centre (45%) and its adjacent boron atoms ($B_{a/b}$,$BP_{a/b}$ Σ=41% and $B_{c/d}$, $BP_{c/d}$ Σ=7.3%), with the metal contribution being mainly $6p_x$ in character with a small, but significant, amount of $6p_z$ character. For a molecule in the point group C_{2h}, an electron in a $6p_x$ orbital would be expected to couple to both the $6p_y$ and $6p_z$, as well as (neglecting spin-orbit coupling) exhibiting a signal at the value for the free electron. What is seen, however, are two signals at g=2.021 and 1.895. In addition to these signals, satellites due to hyperfine coupling of the unpaired electron to the ^{195}Pt nucleus (I=1/2, 34%) can also be observed to low field of the signal at g=2.021 (A=268G) and to high field of that at 1.895 (A=214G). Overlap of these two signals means that the other associated satellites cannot be clearly distinguished.

The simplest interpretation of this EPR spectrum involves assignment of the signal at 1.895 to g_x. The position of this signal, relative to the that of the free electron, can be rationalised in terms of the large value of the spin-orbit coupling constant usually seen for third row transition metals:

$$g = g_e - (n\lambda/[E_{e.s.}-E_{g.s.}]) - (n\lambda^2/[E_{e.s.}-E_{g.s.}]) - \text{higher terms in } \lambda$$

where $E_{e.s.}$ is the energy of the excited state, $E_{g.s.}$ the energy of the ground state and λ the spin coupling constant.

Figure 5.4 EPR Spectrum of 10^- Recorded in DMF as a Frozen Glass at 100K.

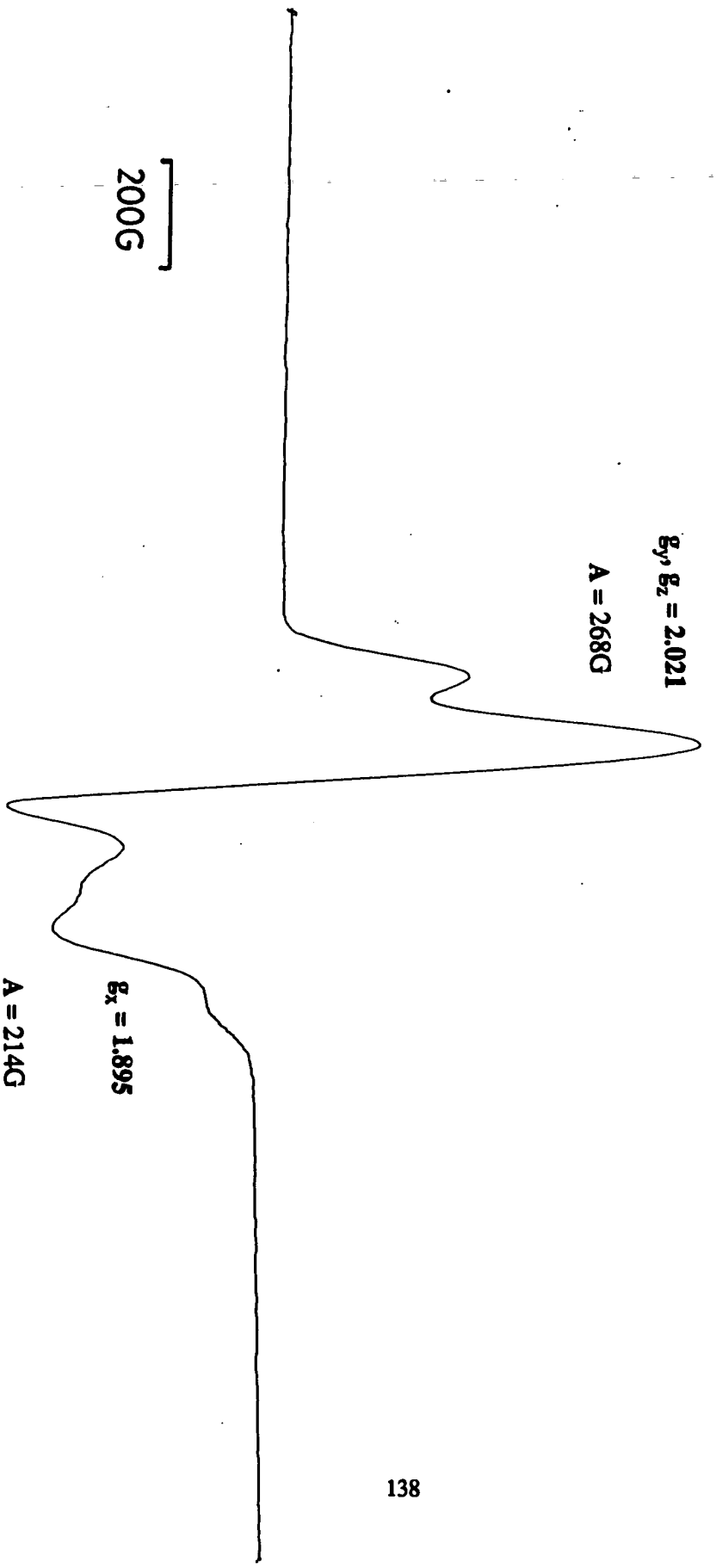

Thus for large values of λ the g_x signal shifts to high field. The other two signals, g_y and g_z are not resolved and are contained within the very broad band at g=2.021. Absolute assignment of this spectrum would require a doped-single crystal study, precluded here by the extreme air-sensitivity of **10**$^-$.

The general broadness of this EPR spectrum can be attributed to a number of factors. As previously mentioned, a significant contribution to the LUMO of **10** is made by the $6p_z$ orbital. In this orbital an electron would be expected to couple to both the other 6p orbitals and this may contribute to the broadness of the signal. In addition, the unpaired electron is in an MO which is only 45% metal based and therefore one might expect to see superhyperfine coupling to the boron atoms. Given the number of different boron environments as well as the presence of two spin-active boron nuclei (^{11}B, I=3/2, 80%; ^{10}B, I=3, 20%) it is not surprising that such superhyperfine coupling remains unresolved and leads to a general broadening of the signal.

Monomeric Pt^I species are extremely rare, resulting in a paucity of data with which to compare the EPR spectrum of **10**$^-$. The spectroelectrochemical characterisation of one such species, $[Pt(dpk)_2Cl_2]^-$ (dpk=2,2'-bipyridyl ketone), formed from the electroreduction of the neutral Pt^{II} analogue, however, was recently performed in this department. The EPR spectrum of the reduced species at 100K exhibits a rhombic signal in which two of the three anisotropic components clearly show hyperfine coupling to the ^{195}Pt nucleus. The size of these two couplings, 33.5 and 67G, are much smaller than those obtained for the platinaborane. This can be interpreted in terms of the unpaired electron having a greater metal residence time in **10**$^-$ than in the dpk species. From this it can be inferred that, of the two species, the LUMO of **10**$^-$ has the higher degree of metal character.

The results of the EPR/EHMO studies can now be used in the interpretation of the

changes in the UV/visible spectrum of **10** upon reduction. In Chapter 2, the structure of the $\{B_{10}\}$ unit in **10**, whilst intermediate between *nido* and *arachno*, was shown to contain greater *nido* character and the formal oxidation state of the platinum atom, therefore, to be slightly greater than 2. The EPR/EHMO studies revealed the LUMO of **10** to have a large amount of metal character. If this orbital is assumed to be the excited state of the low energy process in the UV/visible spectrum of **10**, this can be assigned to a borane to platinum charge transfer band. Upon reduction, the band at 26600cm^{-1} is lost whilst three lower energy processes grow in. Again assuming the LUMO to be involved, these new bands must now be due to platinum to borane charge transfer processes. An alternative interpretation of the structure of **10** would involve two fused *nido* 11-vertex cages, with two *arachno*-$\{B_{10}\}$ fragments and a formally Pt^{VI} metal centre. Any initial charge transfer processes would again occur from ligand to metal, however, the energy of these processes would increase upon reduction of the metal centre, as the electron density at that site becomes greater. Also, it seems unlikely that any platinum to borane transition in the reduced species would occur at such a low energy as that observed in the spectrum of **10**$^-$, as this would be from a, formally, Pt^V metal centre. In this way, these spectra do lend support to the conclusions drawn in Chapter 2. However the description of these absorption processes in terms of transitions between localised metal and ligand-based centres may be an over simplification even though, as has been shown, the platinum atom is not functioning as a particularily good cluster vertex.

This final point becomes even more relevant when the band at 36300cm^{-1} is considered. This is of a similar energy and shape to that exhibited by decaborane (λ_{max}=37300cm^{-1}, ε=2700moll^{-1}cm^{-1}) but is far more intense, ruling out the interpretation of this band in terms of an intra-borane "ligand" transition. In Chapter 4 the concept of an ICCT band was introduced and such a process may again account for these high energy processes in the spectrum of **10**. In this case though, the

distinction between ICCT processes and conventional metal to ligand (or ligand to metal) charge transfer processes is just as problematic as the interpretation of the structures of the $MB_{10}H_{12}$ metallaboranes themselves. What is of note, however, is that upon reduction little change in energy or intensity is seen in this band. This suggests a common electronic transition is occuring for both bands in the spectra of **10** and **10**$^-$ and therefore that the electronic structure of **10** and **10**$^-$ must be similar.

Structure of 10$^-$

The *in-situ* spectroelectrochemical studies on **10** yield little direct information on the structure of **10**$^-$. The major contributions to the LUMO are drawn below showing overall nature of this orbital to be weakly bonding. However, the electrochemical data suggest that occupation of this orbital causes no significant structural change and that the structure of **10**$^-$ is not significantly perturbed from that of **10**.

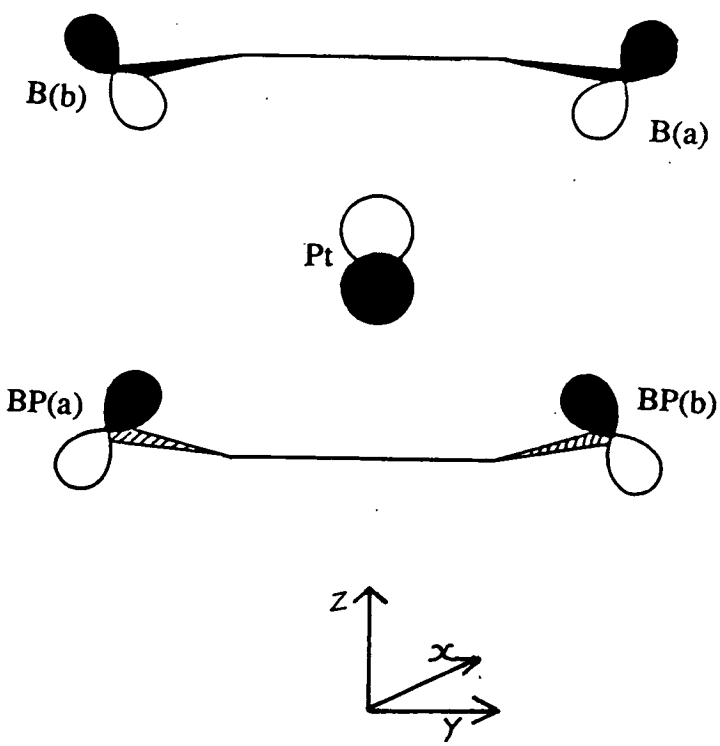

Electrosynthetic Studies at 290K

The electron transfer processes involved in the reduction of **10** in acetonitrile and DMF are quasi-reversible at 290K. However, bulk electrosynthesis in both solvents at this temperature, although still involving the passage of one mole of electrons per mole of **10** present, resulted in orange-brown, EPR-silent, air-sensitive solutions, the voltammetry of which indicated the presence of a new redox-active product. This species undergoes a partially reversible electron transfer at -0.37V in DMF and at -0.26V in acetonitrile. In addition to this major product, small amounts of other redox-active species were also noted in both solvents.

In DMF, **10** could be regenerated in approximately 90% yield by electrolysis at 0.0V, the coulometry of this process indicating the passage of one mole of electrons per mole of platinum present. Whilst the coulometry of the analogous experiment in acetonitrile was the same, the re-oxidation in this case did not regenerate **10**, but rather gave rise to four new waves in the a.c. voltammogram. The position of these waves relative to those of **10** suggests they arise from only two species:

		E_p^c	E_p^a
10		-1.57V	+1.34V
Re-oxidation Products	(a)	-1.72V	+1.22V
	(b)	-1.80V	+1.08V

Moreover, the electrochemical responses of these new species are similar to those of **10**, indicating they may be due to simple derivatives of **10**.

Little direct information on the structures of all these electrogenerated species could be obtained, due either to their air-sensitivity or to the difficulty in separating a

mixture of compounds formed in an electrolytic solution. However, a number of points can be inferred. Firstly, in both solvents the reduction products are EPR-silent, indicating that coupling of the free electron of **10**$^-$ (the probable initial product) had occurred. Because of this it is possible that these species are binuclear in nature. Secondly, the similarity of the return waves in the cyclic voltammetry of **10** in both solvents, as well as the position and shape of the electrochemical wave of the final reduced product, does imply that the same species is formed at this stage in both solvents. This is supported by the similar nature of the UV/visible spectra of the reduction product in each solvent. Therefore, the difference in behaviour observed in acetonitrile must arise as the result of re-oxidation of this reduced product rather than the reduction of **10**.

Assuming the initial product of the reduction of **10** to be **10**$^-$, however short-lived, two possible ways in which coupling of the free electron in this species could occur might be *via* a metal-metal interaction (see [i] below), or through an *exo*-polyhedral B-B linkage ([ii]).

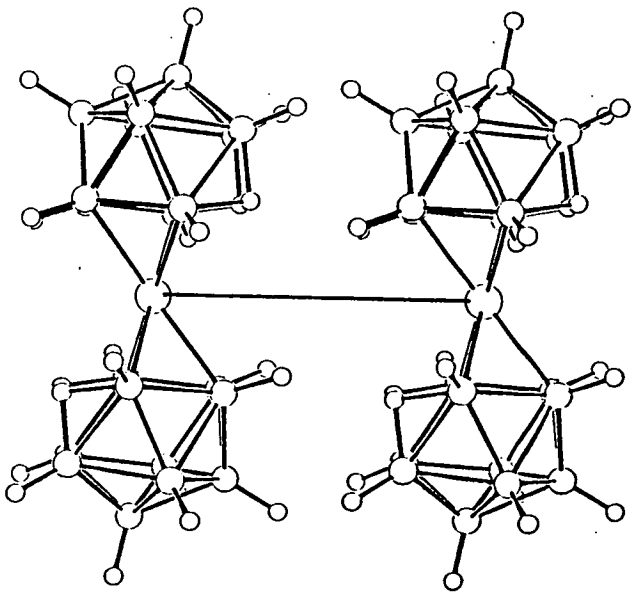

[i]

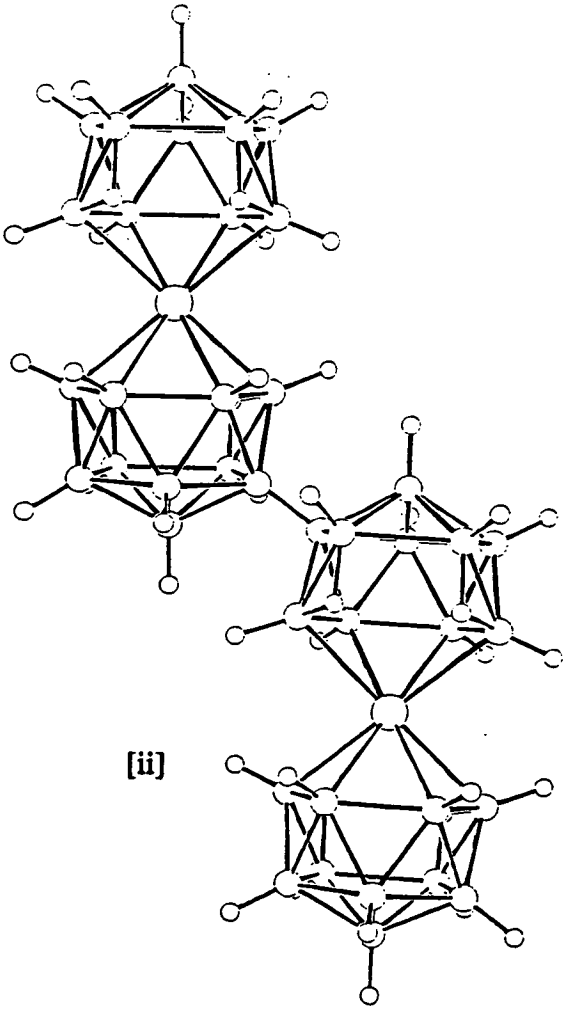

[ii]

Structure [i] represents a truely dimeric species and is similar to the types of structures thought to be formed in the reduction of several other Pt^{II} systems. For example, detailed kinetic studies on the chemically irreversible one-electron reduction of $Pt(SacSac)_2$ (SacSac=SCMeCHCMeS) revealed the subsequent chemical reaction to be second order in the starting material.[99] Also, variable temperature studies gave a positive value for the enthalpy of activation, implying the occurance of bond formation during the reaction. $[Pt(bipy)_2]^{2+}$ (bipy=2,2'-bipyridyl) also displays a similar second order process subsequent to a one-electron chemically irreversible reduction.[100] The structure of the dimeric species formed in this case is thought to be $[Pt^{I}(bipy)S]_2^{2+}$, where S is a solvent molecule, typically acetonitrile or DMF. This latter example highlights a problem in assigning the structures of electrochemically-generated binuclear species in the absence of definitive structural data, namely, whether ligand displacement is concomitant with the formation of a metal-metal bond. This would be expected if the Pt metal centres are to retain a 16 electron square planar geometry, that seen in several structurally characterised Pt^{I}-Pt^{I} dimers.[101-3] For both the dithiolate and bipy complexes mentioned above the situation is complicated by the ability of these ligands to adopt both mono- and bidentate binding modes. Likewise, how to describe the binding mode of the $\{B_{10}\}$ fragment in a structure such as [i] above is not clear.

Icosaborane chemistry has yielded a structure similar to [ii] above where two *exo*-polyhedrally-linked $\{B_{10}H_{11}\}$ cages each bond to a $\{Pt(PMe_2Ph)_2\}$ unit.[32] However, the coupling of two borane cages is usually an oxidative process, as seen in the formation of *conjuncto*-$[B_{20}H_{18}]^{2-}$ from the oxidation of *closo*-$[B_{10}H_{10}]^{2-}$ with ceric sulphate. The near total regeneration of **10** upon oxidation in DMF does favour a structure in which the minimum perturbation of the $\{Pt(B_{10}H_{12})_2\}$ unit occurs, and on this line of argument, structure [i] is the more likely form of the reduced product. This structure, as drawn, would entail a high degree of steric interaction between the

$\{B_{10}\}$ cages, which in part could be relieved by the rotation of one $\{Pt(B_{10}H_{12})_2\}$ unit by 90° about the Pt-Pt bond. However, the $^{11}B-\{^1H\}$ spectrum of the reduced species formed in acetonitrile is more complicated than would be expected from a species of such high symmetry, unless a change in the metal to borane binding mode has occurred as discussed above. Otherwise, the pattern of resonances in this spectrum is more consistent with a structure such as [ii] above which has 20 different boron environments. The fact that the free electron of $\mathbf{10}^-$ is delocalised over the entire molecule also may promote the formation of a species such as [ii], as the reactivity of the boron atoms towards a coupling reaction would be enhanced. Unfortunately though, no clear evidence for the presence or absence of a boron atom not showing coupling to a terminal hydrogen could be seen in the ^{11}B spectrum of this species.

The reduction/oxidation sequence in acetonitrile at 290K is not chemically reversible and, as discussed above, the final products of this process may be simple derivatives of **10**. These could take the form of terminal hydrogen substituted species, $[Pt(B_{10}H_{11}L)_2]^{2-}$, where L=MeCN. The two related sets of waves in the a.c. voltammetry of the final product solution could therefore arise either from isomeric forms of two such species, or from a mixture of mono- and disubstituted species. Elucidation of the nature of these species would be interesting from the point of view of determining the effects of the position and extent of substitution on $E_{1/2}$ values. The ^{11}B n.m.r. spectrum of this electrogenerated mixture yielded no structural information on the nature of these species and separation was again hampered by the vast excess of electrolyte present.

Finally, the UV/visible spectra of **10**, the binuclear reduced species and the re-oxidised mixture are compared in Figure 5.5. This shows that the initial band at $36300cm^{-1}$ varies little upon reduction and subsequent re-oxidation, interpreted above as indicative of a consistent electronic structure and metal-borane interaction. However, the lower energy bands ascribed previously to charge transfer processes in

the spectrum of **10** collapse upon reduction. This may be related to a change in the metal environment, such as a metal-metal interaction in a binuclear species. Re-oxidation gives a spectrum clearly related to that of **10** and provides further evidence for a similarity in the structures of these final products and that of **10**. The analysis of the changes in the UV/visible spectra for assessing gross molecular structure in related metallaborane systems in this way could clearly be of use in subsequent studies, and it is unfortunate that the structural characterisation of some of the species described here could not be carried out in order to test the validity of this approach.

Figure 5.5 UV/Visible Spectra of $[BTMA]_2$**10** (i), its Binuclear Reduction Product (ii) and the Re-Oxidised Mixture (iii) in Acetonitrile at 290K.

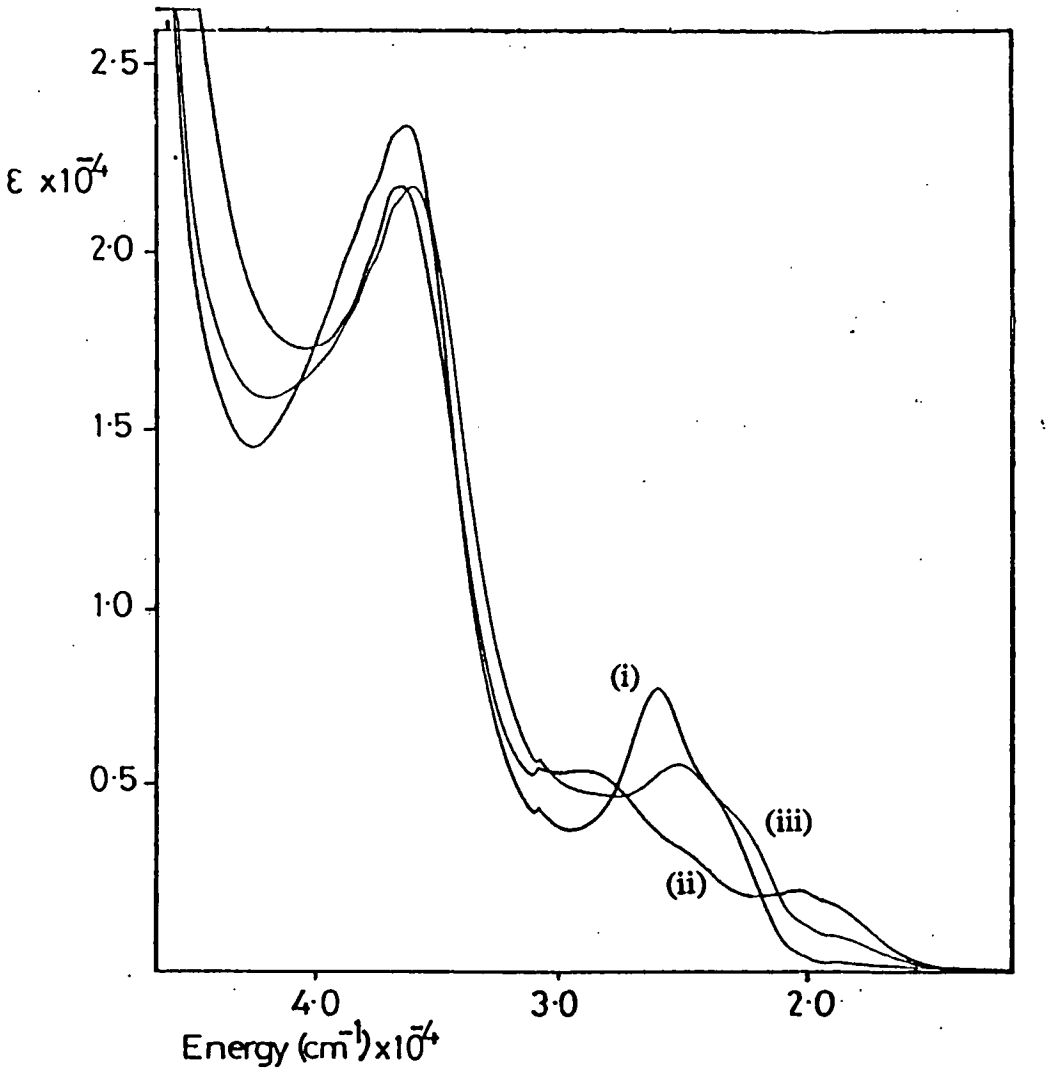

$[BTMA]_2$11

$[BTMA]_2$**11** undergoes a quasi-reversible electron transfer in both acetonitrile ($E_{1/2}$=-1.67V) and DMF ($E_{1/2}$=-1.85V) at 290K. Comparison of peak heights in the cyclic voltammograms of **11** and **10** indicated the reduction in the former also to involve one electron. However, unlike **10**, the reduction is chemically irreversible, even at lower temperatures. This meant that no analogue of **10**$^-$ could be generated in bulk form for the palladaborane. This is one of several differences between the two systems.

The low temperature electrosynthesis of **11** is extremely complex. In both acetonitrile and DMF, the pale yellow starting solution firstly turns bright green, then orange, and finally darkens to brown. A.c. voltammetry on the solution during the electrogeneration does indicate the presence of a number of intermediate species and this is confirmed by the non-isosbestic conversion seen in the *in-situ* UV/visible spectroelectrochemical study. Despite this, the major initial product of this electrogeneration does appear to be analogous to the binuclear species seen for **10** at 290K, displaying a partially reversible electron transfer at -0.15V in acetonitrile (-0.33V in DMF). However, unlike the platinum species, this product undergoes a further reaction giving rise to a new partially reversible wave ($E_{1/2}$ = +0.46V in acetonitrile, +0.51V in DMF). The rate of this final conversion is very solvent dependent; in DMF the conversion is complete in approximately two hours, whilst in acetonitrile the process requires eight hours for completion. As in the case of **10**, a.c voltammetry again shows a number of other redox-active products have been formed, but, once again, only in very small yield. Overall, these product mixtures were found to be EPR-silent.

The final electrogenerated products formed in acetonitrile and DMF can be separated from the bulk electrolyte by addition of diethyl ether. Although the

resultant brown solids are air stable, ^{11}B n.m.r. spectroscopy in acetonitrile on this crude material gave only a broad, poorly resolved spectrum. This could either be interpreted in terms of a low symmetry species involving a large number of boron environments, or in terms of a mixture of species. Preparative t.l.c. separation was therefore attempted using acetonitrile as eluant. This gave one band moving with the solvent front, electrochemical analysis of which showed it to be unchanged from the originally generated product mixture. Attempts to separate this mixture by using mixtures of solvents as eluant, by addition of dichloromethane or chloroform, led to a continuum of bands on the t.l.c. plate.

Figure 5.6 UV/Visible Spectra of $[BTMA]_2$**11** (i) and its Reduction Product (ii) Formed in Acetonitrile at 290K.

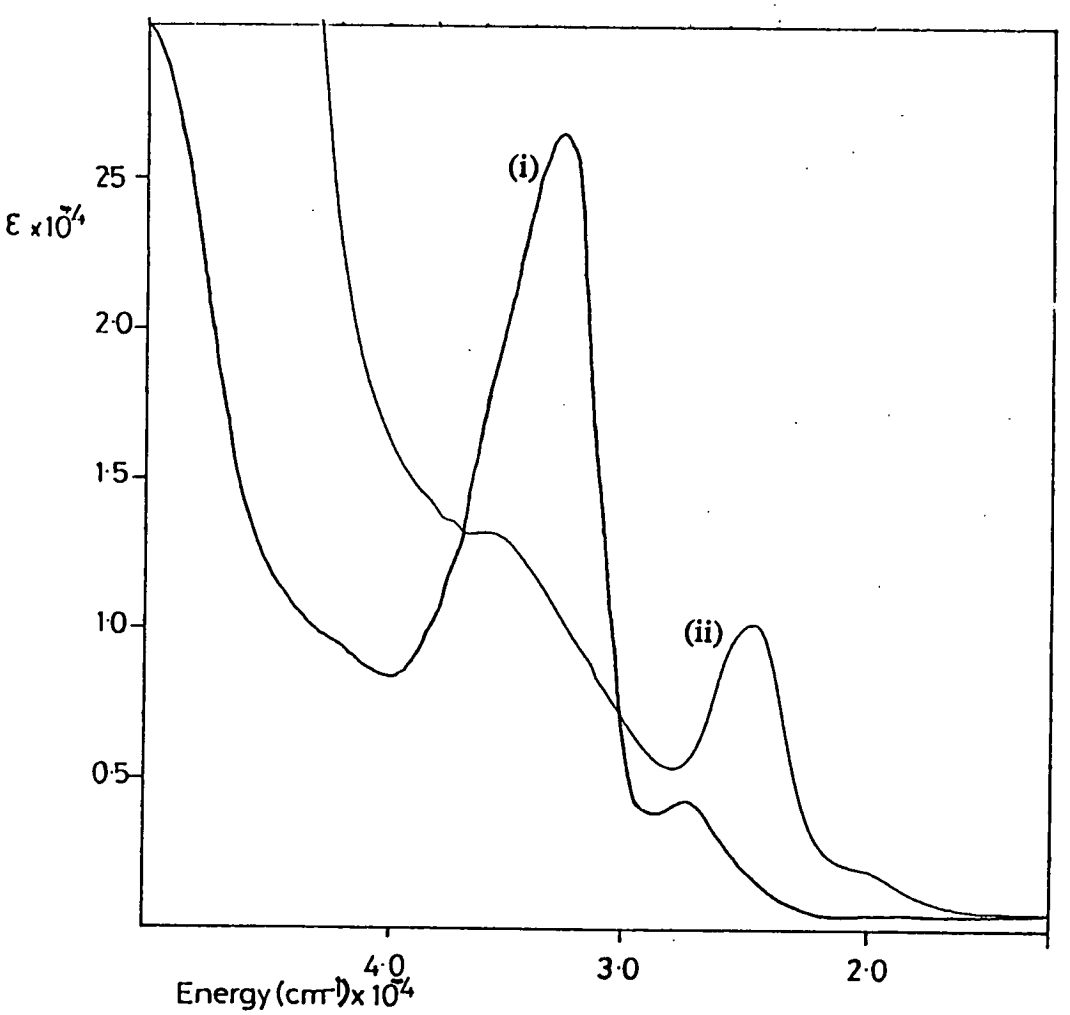

This apparent decomposition upon contact with non-coordinating solvents, as well as the solvent dependency of the final conversion in the reduction process, does suggest a non-innocent role for the solvent in the structures of these species. Oxidation of these reduced species gave no evidence for the regeneration of **11** and it was noted that a large decrease in intensity and shift in energy of the band at 32200cm^{-1} of **11** occurred upon reduction (see Figure 5.6). These last two points suggest that the structure of the final reduction product no longer contains an intact $\{Pd(B_{10}H_{12})_2\}$ unit, with the differences in the UV/visible spectra indicating a change in the nature of the interaction of the borane with the metal centre, very much in contrast to the platinum systems discussed above.

Indeed, it is perhaps surprising that **10** and **11** do exhibit such different behaviour, given their similar structures. To investigate the cause of this, the nature of the LUMO of **11** was determined from an EHMO study and compared with that of **10**, previously determined. As discussed above, the LUMO of **10** ([A], Figure 5.7, overleaf) is overall bonding in character, however occupation results in no gross change in overall structure. For **11**, the LUMO ([B] overleaf) is anti-bonding in character, not only between the metal atom and the adjacent B_4 faces, but also within those faces. This explains the instability upon reduction of the palladaborane system, which appears not only to form a binuclear species but also to undergo further reaction with solvent before sufficient stabilisation is achieved.

Figure 5.7 LUMO's of **10** [A] and **11** [B].

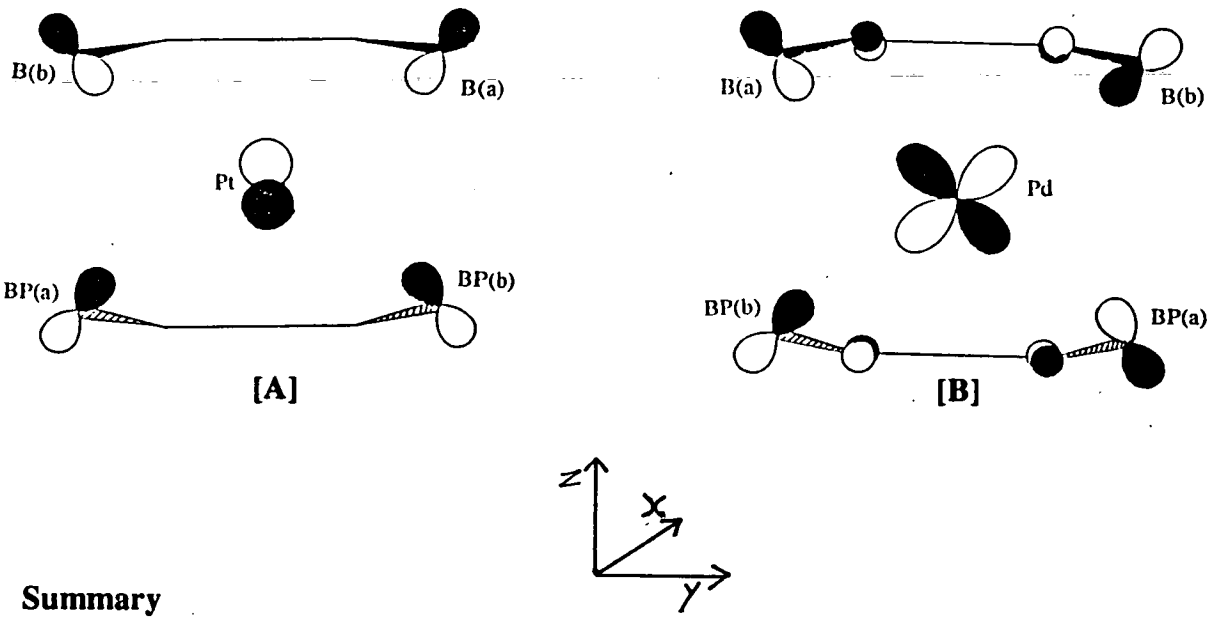

Summary

The chemical nature of the redox changes of the three metallaboranes studied here could not have been predicted from the tenets of PSEP theory. Oxidation resulted in decomposition, whereas theoretically a two-electron oxidation should entail a structural change to a *closo* system. In addition, the one-electron reduction of **10** resulted in no gross structural change at 238K. The behaviour of this species at 290K appeared similar to that of other Pt^{II} species in that a binuclear product was produced in which, however, the $\{Pt(B_{10})\}_2$ unit again appears structurally unchanged.

A more useful predictive approach might make use of EHMO calculations in which the nature of the frontier MO's are studied, and assessment of the likely effects of population changes on structure and reactivity made. The development of such an approach requires the availability of more structural data on the products of redox changes.

Chapter 6

Experimental

This chapter details the experimental procedures and techniques underlying the discussions in Chapters 2 - 5. There are four aspects of this to be described in turn here: synthetic procedures, crystallographic determinations, methods for EHMO calculations and electrochemical techniques.

Synthetic Procedures.

General Techniques

All reactions were carried out under an atmosphere of dry, oxygen-free nitrogen. Standard Schlenk techniques were employed throughout, although some subsequent manipulations were carried out in air. Preparative t.l.c. employed Kieselgel 60 F_{254} plates, prewashed in chloroform.

Dichloromethane was pretreated with KOH pellets and tetrahydrofuran and n-hexane sodium-wired before being distilled under nitrogen immediately before use, the former from CaH_2, tetrahydrofuran from sodium wire/benzophenone and n-hexane from sodium wire. Ethanol was distilled from Mg/I_2. Diethyl ether and n-pentane were dried with sodium wire. All other solvents were used as supplied.

Infrared spectra were recorded as KBr disks or as solutions in CaF_2 cells, on a Perkin-Elmer 598 double beam spectrophotometer. For solutions, a reference cell containing the solvent in use was placed in the second beam and the difference spectrum recorded.

N.m.r. spectra were recorded at ambient temperature using Bruker WP360 [^{11}B,

^{11}B-{^{1}H}, ^{11}B-^{11}B(COSY) and ^{1}H-{^{11}B selective}], Bruker WP200SY (^{11}B, ^{11}B-{^{1}H} and ^{31}P), Bruker WY80SY (^{1}H) and Jeol FX90 (^{31}P) spectrometers. Techniques describing ^{11}B-^{11}B(COSY) and ^{1}H-{^{11}B selective} have been previously published.[104, 105] Chemical shifts are quoted relative to external $SiMe_4$ (^{1}H), BF_3OEt_2 (^{11}B) and 85% H_3PO_4 (^{31}P), positive shifts to high frequency.

UV/visible spectra were recorded on a Perkin-Elmer λ9 spectrophotometer. Extinction coefficient measurements were carried out at 290K. Microanalyses were performed by the departmental service.

Starting Materials

$B_{10}H_{14}$ was sublimed before use (80°C/0.01T) or recrystallised from diethyl ether. $[Co(CO)_2DMBD]_2$,[106] $MCODCl_2$ (M=Pt, Pd),[107] $(PPh_3)_2NiCl_2$,[108] and *mer*-$RuCl_3(PMe_2Ph)_3$[109] were prepared by methods outlined in the literature.

$NaB_{10}H_{13}$[11] and $[NMe_4][B_9H_{14}]$[13] were synthesized according to published methods. [BTMA][B_9H_{14}] was prepared by an exactly analogous method to that of the [NMe_4] salt by substitution of [BTMA]Cl for [NMe_4]Cl at the appropriate point in the synthetic procedure. All other starting materials were commercially available and used as supplied.

Syntheses of $MB_{10}H_{12}$ Metallaboranes.

The literature preparations were used for $[(CO)_3CoB_{10}H_{12}]^-$ and the *bis*-boranes, $[M(B_{10}H_{12})]_2$, where M=Pt, Pd and Ni.[34] These methods give the products as $[NMe_4]^+$ salts. Their formation as $[BTMA]^+$ salts was achieved by the substitution of [BTMA]Cl for [NMe_4]Cl in the original method or by a metathesis procedure. An example of the latter is given below.

Metathesis of $[NMe_4][(CO)_3CoB_{10}H_{12}]$, $[NMe_4]$9

$[NMe_4]$9, (0.271g, 0.83mmoles) was dissolved in the minimum amount of dichloromethane and eluted on an Amberlite IR 120 Na^+ ion-exchange column (8cm, dichloromethane as eluant). The yellow/green band was collected and the solvent removed *in vacuo* giving a green powder. This was redissolved in THF (5ml) and added to a solution of [BTMA]Br (0.27g, 1.17mmoles) in H_2O. The resultant yellow solid was collected, washed with Et_2O (2 x 10ml) and dried *in vacuo* giving 0.3087g of product (yield = 93%). Thin plate-like crystals of [BTMA]**9** were grown by slow cooling of a concentrated dichloromethane solution.

Characterisation

Microanalysis. Calculated for $B_{10}C_{13}H_{28}NO_3$: %C 37.8, %H 6.82, %N 3.46.
Found: %C 37.7, %H 6.92 %N 3.48.

Infrared Spectroscopy/CH_2Cl_2: ν_{B-H} 2505cm^{-1}, ν_{C-O} 2065, 2020 and 2000cm^{-1}

Syntheses of MB_9H_{13} Metallaboranes.

6-6-6-$(PMe_2Ph)_3$-6-*nido*-RuB_9H_{13}, 19.

The method used was adapted from the originally reported preparation of this material.[37] Typically, *mer*-$RuCl_3(PMe_2Ph)_3$ (0.412g, 0.66mmoles) was suspended in degassed ethanol (20ml). $[BTMA][B_9H_{14}]$ (1.234g, 4.72mmoles) was added as a solid and the mixture heated to reflux. Upon warming, gas evolution commenced with concomitant dissolution of the solid to give a clear, bright red solution. After 15 minutes the solution was allowed to cool to room temperature and, upon standing for

2 hours, a red solid had formed. This was collected, redissolved in dichloromethane, filtered and the solvent removed *in vacuo*. Recrystallisation of the resultant solid by slow diffusion of n-hexane into a concentrated dichloromethane solution yielded dark red crystals of **19** (0.165g, 0.263mmoles, 39.9%)

Characterisation

^{11}B-{^{1}H} n.m.r., ($CDCl_3$)/p.p.m.: 12.79(2B), 10.14(2B), 2.39(1B), -1.27(2B), -23.39(1B) and -30.12(2B).

UV/visible spectrum: ν_{max}=21700cm^{-1}, (ε=1900moll^{-1}cm^{-1}), ν_{max}=33000cm^{-1}, (ε=9900moll^{-1}cm^{-1}).

2-Cl-6,6,6-$(PMe_2Ph)_3$-6-*nido*-RuB_9H_{12}, 20

Dropwise addition of a saturated solution of Cl_2 in CCl_4 to a solution of **19** (0.040g, 64.0μmoles) resulted in a colour change from red to orange. The reaction was monitored by small scale t.l.c. with chloroform as eluant which showed the appearence of a new band at R_f=0.7, in addition to the starting material (R_f=0.8). When the majority of the starting material had reacted , preparative t.l.c., again using chloroform as eluant, and collection of the band at R_f=0.7 gave **20** in 70% yield (0.030g, 44.8μmoles). Crystals of this species were grown by slow diffusion of n-hexane into a concentrated dichloromethane solution.

Characterisation

^{11}B-{^{1}H} n.m.r. ($CDCl_3$)/p.p.m.: 13.74(4B), 0.23(3B). -8.68(1B) and -30.46(1B)

UV/visible spectroscopy (CH_2Cl_2): ν_{max}=21500cm^{-1} (ε=2100mol^{-1}lcm^{-1}) and 32500cm^{-1} (ε=7800mol^{-1}lcm^{-1})

2,5-Cl_2-6,6,6-$(PMe_2Ph)_3$-6-*nido*-RuB_9H_{11}, 21.

Addition of an excess of a saturated solution of Cl_2 in CCl_4 to **19** (0.090g, 140μmoles) in dichloromethane (10ml) afforded an orange solution. Removal of the solvent *in vacuo* realised a red solid which was redissolved in the minimum amount of chloroform and separated using preparative t.l.c. with chloroform/n-hexane (1:3) as eluant. A number of bands were seen, one with R_f=0.5 was shown by ^{11}B n.m.r. spectroscopy to be **20**. Collection of the band at R_f=0.4 gave a red solid, recrystallisation of which from slow diffusion of n-hexane into a concentrated dichloromethane solution yielded small red crystals of **21** (0.011g, 15.8μmoles, 11.3%). The low yield was accounted for by the difficulty in separation of the two major bands as well as the presence of several other species, probably isomeric forms of **21** or other more highly chlorinated species.

Characterisation

^{11}B-{^1H} n.m.r. ($CDCl_3$)/p.p.m.: 16.56(1B), 15.57(1B), 11.58(1B), 9.36(1B), 0.70(3B), -12.60(1B) and -32.69(1B).

UV/visible Spectroscopy:ν_{max}=21200cm^{-1} (ε=7100moll^{-1}cm^{-1}), ν_{max}=32200cm^{-1} (ε=2100moll^{-1}cm^{-1}).

2-$(PMe_2C_6H_4)$-6,6-$(PMe_2Ph)_2$-6-*nido*-RuB_9H_{12}, 22

Bulk electrolysis on **19** (0.026g, 41.6μmoles) was performed in dichloromethane

at +1.00V and 290K using $TBAPF_6$ as electrolyte. The resultant orange solution (approximately 10ml) was transferred by pipette into a Schlenk tube whereupon addition of diethylether (50ml) precipitated the electrolyte. Filtration and removal of the solvent *in vacuo* gave a red gum. Preparative t.l.c. using chloroform as eluant of this realised a number of bands. The major one, R_f=0.7, was collected to yield **22** (0.003g, 6.19μmoles, 14.9% yield).

Characterisation

$^{11}B-\{^1H\}$ n.m.r. ($CDCl_3$)/p.p.m.: 11.40(4B), 2.37*(1B), -3.87(3B) and -31.58(1B).

^{31}P n.m.r ($CDCl_3$)/p.p.m.: 12.87(1P), 12.64(1P) and 11.87(1P).

UV/visible spectroscopy (CH_2Cl_2): 21400cm^{-1} (ε=2300$moll^{-1}cm^{-1}$), 32300cm^{-1} (ε=8300$moll^{-1}cm^{-1}$).

*: this resonance exhibits $^1J_{B-P}$=83Hz, the figure quoted is the average position of the two observed peaks.

Other Non-Boron Containing Species

$[(CO)_3Co(DMBD)][FeCl_3(CH_3CN)]$, 12$[FeCl_3(CH_3CN)]$

The method used was based on that suggested by Chauldry and Pauson.[82] $FeCl_3$ (0.088g, 0.54mmoles) was added as a solid to a solution of $[CoCO_2(DMBD)]_2$ (0.102g, 0.52mmoles) in dichloromethane (15ml), resulting in loss of the orange colour and precipitation of an olive green solid. Once the original orange colour had disappeared, the solvent was removed *in vacuo* and the resultant solid redissolved in

acetonitrile to give a deep green solution. This was filtered and crystals grown by slow diffusion of diethyl ether into a concentrated acetonitrile solution. Yield not recorded but less than 5%.

Characterisation

Infrared spectroscopy (CH_3CN): ν_{C-O}=2130, 2100, 2080cm^{-1}

$[(CO)_3Co(PPh_3)_2][BPh_4]$[90] and $[Co(en)_3]Br_3$[91] were synthesised by the literature preparations.

Crystallographic Determinations

This section describes the experimental procedures employed in the collection of data and subsequent structure solution and refinement for the crystallographic determinations presented in this work. All data were collected on an Enraf-Nonius CAD4 diffractometer, fitted with an ULT-1 low temperature device and using graphite-monochromated Mo-K_a *X* radiation, λ = 0.71069Å.

Data were corrected for Lorentz and polarisation effects (CADABS).[110] No decay or movement was noted during the duration of data collection for any of the reported structural determinations. Metal atoms were located by automatic direct methods (SHELX86)[111] or by inspection of a Patterson map (SHELX76).[112] Other atoms were located by ΔF syntheses and iterative full-matrix least-squares refinement on F. Scattering factors for C, H, B, P, N, O and Cl were those inlaid in the programs, those for Co, Pt, Pd, Fe and Ru were taken from *International Tables for X-Ray Crystallography.*[113] Geometrical calculations were performed using CALC[69] and the figures drawn using EASYORTEP.[114]

The isotropic thermal parameter = $\exp[-8\pi^2U(\sin^2\theta)/\lambda^2]$.

Anisotropic thermal parameters are defined by:

$$Uij=\exp[-2\pi^2(U11a^{*2}h^2+U22b^{*2}k^2+U33c^{*2}l^2+2U23b^*c^*kl+2U13a^*c^*hl+2U12a^*b^*hk)]$$

and the equivalent isotropic thermal parameter by:

$$Ueq = [\Sigma_i\Sigma_j Uija_i^*a_j^*a_i.a_j]/3$$

[BTMA][$(CO)_3CoB_{10}H_{12}$], [BTMA]9

Crystal Data

$C_{13}H_{28}B_{10}CoNO_3$, M=413.39, monoclinic, space group $P2_1/c$, a=10.634(5), b=14.118(5), c=14.168(4)Å, β=91.81(3)°, V=2126.0Å^3 by least squares refinement of 25 centred reflections (7<θ<13°), Z=4, D_x=1.291gcm^{-3}, μ=0.82mm^{-1}, F(000)=856.

Data collection and processing

Data collected by ω-2θ scans in 96 steps with ω scan width 0.8+0.34tanθ° at 185(1)K. Variable scan speeds between 0.87 and 2.35°min^{-1}. 4128 independent reflections measured (1≤θ≤25, h:0 to 12, k: 0 to 16, l: -16 to 16) of which 2199 with F>2.0σ(F) were retained. Analysis of variance showed anomalously poor agreement for the hk0 reflections and check intensity reflections revealed variations suggesting fluctuations in beam power during the time in which these data were collected. As a result, all hk0 data were omitted and subsequent refinement employed the remaining 1967 reflections.

Structure solution

Co position from Patterson map, all other non-hydrogen atoms from full-matrix least squares refinement/ΔF syntheses. Phenyl ring treated as a planar, rigid group (C-C=1.395Å). Upon isotropic convergance, an empirical absorption correction was applied. All non-hydrogen atoms, except phenyl C atoms, refined allowing full anisotropic thermal motion. Cage terminal hydrogen atoms were placed in idealised positions with the B-H bond (1.18Å) lying along the vector defined by the cluster centroid and the relevant boron atom. Bridging hydrogen atoms were positioned using average distances, angles and torsion angles taken from decaborane. Cage hydrogen atoms were assigned an invariant group thermal parameter ($U_{cage\text{-}H}$=0.08Å^2). Benzyl hydrogen atoms were placed in idealised positions (C-H=1.08Å) and assigned a refined group thermal parameter [$U_{benzyl\text{-}H}$=0.062(17)Å^2 at convergance]. Methyl hydrogen atoms were omitted from the structure solution. Unit weights were assigned throughout. R=0.0984, R_w=0.1108, S=4.065. Min. and max. residues in final ΔF synthesis -0.69 and 0.76eÅ^{-3} respectively.

$[BTMA]_2[Pt(B_{10}H_{12})_2]$, $[BTMA]_2$10

Crystal data

$C_{20}H_{56}B_{20}N_2Pt$, M=735.97, triclinic, space group Pbar1, *a*=9.023(3), *b*=10.440(4), *c*=11.172(3)Å, α=111.55(3), β=108.794(24), γ=101.29(3)°, *V*=865.7Å^3 by least squares refinement of 25 centred reflections, (13<θ<15°), Z=1, D_x=1.411gcm^{-3}, μ=4.11mm^{-1}, F(000)=368.

Data collection and processing

Data collected at 185(1)K by ω-2θ scans in 96 steps with ω scan width

0.8+0.34tanθ°. Variable scan speeds between 1.10 and 2.35°min^{-1}. 5403 reflections measured ($1 \leq \theta \leq 25°$, h: 0 to 10, k: -12 to 12, l: -13 to 13, h: -10 to 0, k: -12 to 12, l: -13 to 4) all of which had $F \geq 2.0\sigma F$.

Structure solution

All atoms were found from full-matrix least squares refinement/ΔF syntheses (Pt on inversion centre). Empirical absorption correction applied upon isotropic convergance and the merging afforded 3039 data (R_{merge} 0.0134). All heavy atoms were allowed full anisotropic thermal motion and all hydrogen atoms were refined with group isotropic thermal parameters [$U_{cage\text{-}H}$=0.0375(24), $U_{benzyl\text{-}H}$=0.047(4), $U_{methyl\text{-}H}$=0.041(3)Å^2 at convergence]. The weighting scheme of the form $w^{-1} = \sigma^2(F)+0.000422(F^2)$ was applied. R=0.0166, R_w=0.0212, S=1.032, min. and max. residues in final ΔF map -1.42 and 1.48eÅ^{-3} respectively (near Pt).

$[BTMA]_2[Pd(B_{10}H_{12})_2].2CH_3CN$, $[BTMA]_211.2CH_3CN$

Crystal Data

$C_{24}H_{62}B_{20}N_4Pd$, M=729.39, triclinic, space group Pbar1, *a*=9.2094(18), *b*=10.772(3), *c*=11.3707(23)Å, α=67.721(21), β=83.394(16), γ=78.801(21)°, *V*=1022.8Å^3 by least squares refinement of 25 centred reflections ($13<\theta<15°$), Z=1, D_x=1.184gcm^{-3}, μ=0.47mm^{-1}, F(000)=380.

Data collection and processing

Data collected in ω-2θ scans in 96 steps with scan width 0.8+0.34tanθ at 291(1)K. Variable scan speeds between 0.92 and 2.35°min^{-1}. 7835 reflections measured ($1 \leq \theta \leq 30°$, h: 0 to 12, k: -15 to 15, l: -16 to 16, h: -12 to 0, k: -15 to 15, l:

-16 to -2).

Structure solution

All heavy atoms located by iterative application of full-matrix least squares refinement/ΔF syntheses (Pd at inversion centre). Empirical absorption correction applied upon isotropic convergence, data merged (R_{merge} 0.0142) to give 5864 independent data of which 5850 had $F \geq 2.0\sigma F$ and were retained. All heavy atoms refined allowing full anisotropic thermal motion. Borane and benzyl hydrogen atoms freely refined with individual isotropic thermal parameters. Methyl groups treated as rigid groups (C-H=1.08Å) with separate group thermal parameters for the solvate and cationic methyl hydrogen atoms. The weighting scheme $w^{-1}=\sigma^2(F)+0.000700F^2$ was applied. R=0.0265, R_w=0.0352, S=1.128. Min. and max. residues in ΔF synthesis -1.05 and 0.52eÅ^{-3} respectively.

$[(CO)_3Co(DMBD)][FeCl_3(CH_3CN)]$, 12$[FeCl_3(CH_3CN)]$

Crystal Data

$C_{11}H_{13}CoCl_3FeNO_3$, M=428.35, monoclinic, space group $P2_1/a$, a=11.259(10), b=12.043(14), c=12.727(7)Å, β=97.53(6)°, V=1710.8Å^3 by least squares refinement of 25 centred reflections (9<θ<12°), Z=4, D_x=1.663gcm^{-3}, μ=2.29mm^{-1}, F(000)=856.

Data collection and processing

Data collected by ω-2θ scans in 96 steps with ω scan width 0.8+0.34tanθ° at 291(1)K. Variable scan speeds between 1.10 and 3.30°min^{-1}. 1699 independent reflections measured ($1 \leq \theta \leq 20°$, h: 0 to 10, k: 0 to 11, l: -12 to 12) with 1383 having $F \geq 1.0\sigma(F)$ retained.

Structure solution

Co and Fe positions from automatic direct methods, other atoms by iterative application of full-matrix least squares refinement/ΔF syntheses. Empirical absorption correction applied after isotropic convergence. Methyl groups treated as rigid groups (C-H=1.08Å), vinyl hydrogen atoms located and positionally refined. All hydrogen atoms assigned a fixed isotropic thermal parameter (U_H=0.04Å^2). Weighting scheme according to $w^{-1}=\sigma^2(F)+0.000506F^2$ applied. R=0.0321, R_w=0.0330, S=1.294, min. and max. residues in final ΔF synthesis -0.35 and 0.28eÅ^{-3} respectively .

2-Cl-6,6,6-$(PMe_2Ph)_3$-6-*nido*-RuB_9H_{12}, 20

Crystal Data

$C_{24}H_{45}B_9ClP_3Ru$, M=660.25, monoclinic, space group $P2_1/n$, *a*=9.0636(13), *b*=18.048(3), *c*=20.163(4)Å, β=96.17(6)°, *V*=3279(1)Å^3 by least-squares refinement of 25 centred reflections ($12\leq\theta\leq13°$), Z=4, D_x=1.337gcm^{-3}, μ=0.71mm^{-1}, F(000)=1360.

Data collection and Processing

Data collected by ω-2θ scans in 96 steps withω scan width 0.8+0.34tanθ°. Variable scan speeds between 0.82 and 2.35°min^{-1}. 3461 independent reflections measured ($1\leq\theta\leq20°$, h: 0 to 8, k: 0 to 17, l: -19 to 19) of which 2499 having $\theta\geq2.0\sigma(\theta)$ retained.

Ru atom position found by inspection of a Patterson map, all other non-hydrogen atoms and cage hydrogen atoms by iterative application of full-matrix least-squares refinement /ΔF syntheses. Phenyl and methyl hydrogens set in idealised positions (C-H=1.08Å), phenyl rings treated as rigid, planar groups (C-C=1.395Å). Empirical absorption correction applied after isotropic convergence. Cage hydrogen atoms located and positionally refined with a group isotropic thermal parameter [$U_{cage\text{-}H}$=0.026(8)Å^2], methyl and phenyl hydrogen atoms assigned refined group isotropic thermal parameters [$U_{methyl\text{-}H}$=0.073(9), $U_{phenyl\text{-}H}$=0.088(11)^2]. All non-hydrogen atoms allowed full anisotropic thermal motion. Weighting scheme $w^{-1}=\sigma^2(F)+0.000381F^2$ applied. R=0.0616, R_w=0.0530, S=1.126, min. and max. residues in final ΔF synthesis -0.581 and 0.536eÅ^{-3}

Extended Hückel Molecular Orbital (EHMO) Calculations

These employed a locally-modified version of the ICON8 program.[115] Some initial background to the theory and workings of this program are given here, as well as a brief description of the program output and the setting up of models for the calculations.

Background Theory

Two simplifications are central to the EHMO method. The first of these is the "orbital assumption" which states that each electron in a polyelectron environment may be treated independently and be described by a separate wavefunction, or orbital. This allows the separate treatment of each electron in terms of a one-electron Hamiltonian:

$$H_j\psi_j=E_j\psi_j$$

where H_j is a one electron operator

and ψ_j the wave function of energy, E_j.

Secondly, EHMO calculations make use of the principle of linear combination of atomic orbitals (LCAO), such that

$$\Psi = c_1\psi_1 + c_2\psi_2 + \ldots C_i\psi_i$$

where Ψ is a molecular orbital and the c terms

the coefficients of the atomic orbitals, ψ.

From these two starting points a set of secular equations can be set up:

$$\Sigma c_i(H_{ij}-ES_{ij}) = 0$$

where, H_{ij}, the resonance integral, $= \int \psi_i H \psi_j$,

H_{ii}, the coulomb integral, $= \int \psi_i H \psi_i$,

and S_{ij}, the overlap integral, $= \int \psi_i \psi_j$.

Solution of these secular equations gives the molecular orbital energies, E, and the contribution to each molecular orbital from each atomic orbital (c_i).

The EHMO Calculation

The basis set for EHMO calculations consists of the valence orbitals and electrons of the elements present. This form of calculation allows for overlap between all such atomic orbitals calculating S_{ij} and H_{ij} for all atoms. This is in contrast to Hückel calculations used for organic π-systems where $S_{ij} = 0$ for all atoms and $H_{ij} = 0$ if i and j are non-adjacent. The atomic orbitals take the form of Slater-type orbitals,[116] the radial term of which is described as:

$$R(r) = r^{n^*-1}\exp^{(-\zeta r)}$$

where $\zeta = (Z-\Sigma)/n^*$, with Z the atomic number,

S the screening constant and n^* the effective quantum number

ζ defines the diffuseness of the orbital concerned. For d-orbitals, the radial characteristics were found to be better described by linear combination of two Slater functions, the so-called double zeta potential:[117]

$$R(r)=r^{n^*-1}[c_1\exp^{(-\zeta_1 r)}+c_2\exp^{(-\zeta_2 r)}]$$

Along with values for S_{ij}s, calculated in the program, solution of the secular equations requires values for H_{ii}s and H_{ij}s. H_{ii}s are the valence shell ionisation energies (VSIE's) calculated from spectroscopic data which may be used directly or their values optimised by charge iteration. This procedure becomes important because VSIE's, derived from the neutral atom, do not accurately reflect the energies of atomic orbitals in a polyatomic, polar environment. Of the types of optimisation available, that known as METHOD 2 was employed to optimise the H_{ii}s of the metal atoms involved.

METHOD 2 makes use of a function of the form:

$$H_{ii} = -VSIE(Q)$$

$$\text{with } VSIE(Q) = AQ^2+BQ+C$$

A, B and C are defined from multiconfigurational spectral data on atoms and their charged ions.[118] The number of configurations (NCON = 1 or 3) used varied according to the availability of data.

The charge iteration calculation itself involves the cycling of EHMO results with VSIE's made a function of the atomic charges calculated in the previous cycle. For

the systems discussed in this work, convergence generally involved approximately 30 cycles.

H_{ij}s are calculated from the modified Wolfsberg-Helmholtz formula:[119, 120]

$$H_{ij}=K'S_{ij}(H_{ii}+H_{jj})/2$$

$$K'=K+\Delta^2+\Delta^4(1-K),\ K=1.75$$

$$\Delta=H_{ii}-H_{jj}/H_{ii}+H_{jj}$$

Calculation Results

A number of matrices and tables are produced as output from EHMO calculations. The most commonly used for the determination of the nature of molecular orbitals in this work are described below.

Energy Levels: A list in increasing stability of molecular orbitals with their occupancies.

Wavefunctions: The nature of a molecular orbital in terms of the contributions from each atomic orbital.

Reduced Overlap Population: An estimate of the bond strength between two atoms.

Reduced Charge Matrix: The extent of localisation of each molecular orbital on any atom.

In addition to these, of particular importance to this work was the use of fragment molecular orbital (FMO) calculations. Rather than atomic orbitals, these take as their basis sets fragment molecular orbitals generated by the ICON8 program. Of the output from an FMO calculation, that of most relevance here are the overlap matrix,

which quantifies the extent of overlap between two fragment molecular orbitals and the reduced charge matrix. The latter gives the occupation of the fragment molecular orbitals in the molecule and forms the basis of the arguments presented in Chapter 3 of this work.

$MB_{10}H_{12}$ Models for EHMO Calculations.

In all cases the models used were based upon the experimental geometries derived from crystallographic data, incorporating the modifications discussed in Chapter 3 for the borane fragments of **1-6**. Full molecular symmetry was imposed by calculating the best *pseudo*-mirror plane through the relevant atoms, which were then made to lie in this plane. The coordinates of other symmetry-related atoms were then averaged with respect to this plane. For ease of interpretation, the models were orientated such that the least squares plane through the B_4 bonding face, or in the case of the *bis*-boranes, one of the B_4 bonding faces, defined the xy plane. All geometrical manipulations were performed using CALC.

Electrochemical and Spectroelectrochemical Techniques.

Chapters 4 and 5 of this thesis are founded upon the results of a number of electrochemical experiments. The characterisation of the electrosynthetically-generated species placed special emphasis on the use of *in-situ* spectroelectrochemistry. These techniques, as well as the equipment and experimental procedure employed, are discussed below.[121]

Instrumentation

All electrochemical studies were performed using a PAR model 170 potentiostat and programmer linked to a Hewlett-Packard 704A X-Y recorder. Electronic spectroelectrochemical experiments were carried out on the Perkin-Elmer λ9

spectrophotometer. EPR spectra were obtained using a Bruker ER 081 (90/30) spectrometer and ER 200D-SRC console. Temperature control was maintained using a Bruker ER 4111 VT variable temperature control unit.

Figure 6.1 shows the standard set-up for an electrochemical experiment, displaying several important aspects common to all the electrochemical and spectroelectrochemical techniques described below. These are, in particular, a three electrode configuration consisting of a working electrode, counter electrode and reference electrode immersed in a suitable solvent system and housed in an appropriate electrochemical cell.

Electrodes

The choice of electrodes to be used depends on the experiment. In general, the working and counter electrodes should be chemically inert and stable over a wide potential range. Here, a Pt microelectrode was employed as working electrode in conjunction with a Pt counter electrode.

The reference electrode consists of a half cell of determined potential against which all other measurements are referred. An ideal reference reaction should be reversible and obey the Nernst equation, have a potential which is stable with time and have a low temperature dependence. The resistance of the reference electrode should be relatively high (in order to reduce current flow through it) and contamination of the test solution should be avoided. In practise a Ag/AgCl reference in dichloromethane was used, separated from the bulk solution by a porous glass frit.

Solvent System[122]

This consists of a solvent and a supporting electrolyte. The choice of solvent depends on the sample solubility and stability. In addition, an electrochemical

solvent should have a usable potential range, a suitably high dielectric constant, an accesible temperature range, a low vapour pressure and viscosity and not present an unreasonable danger through any toxicity. Also, the possibility of solvent interference through its donor properties should be taken into account. Purification of solvents for electrochemistry can be important as the oxidation or reduction of impurities may obscure those of the test species. Here, dichloromethane was allowed to stand over KOH pellets for a week and then was freshly distilled from P_2O_5 under an atmosphere of nitrogen. Acetonitrile was purified by the method of Walter and Ramaley[123] and, once again, freshly distilled from P_2O_5 before use. DMF was used as supplied.

The supporting electrolytes used in this work were tetrabutylammonium tetrafluoroborate and hexafluorophosphate as either 0.1M solutions (acetonitrile and DMF) or 0.5M (dichloromethane). The role of the supporting electrolyte is to reduce the resistance of the solution. The vast excess of electrolyte present, relative to the test species, also results in the structure of the double layer adjacent to the working electrode being determined by the electrolyte ions and in the elimination of migration as a means of mass transport for the test species.

Cell

The cell used is designed such that

(i) The electrode geometry is optimised to achieve a symmetric electrical field around the working electrode, and

(ii)The electrodes are placed close together in order to minimalise the effects of internal resistance. This necessitates the use of the Pt microelectrode which, having a small area, has all points on its surface effectively equidistant from the larger counter electrode.

In addition to this, the cell must allow for the purging (with Ar gas) of the solution of dissolved oxygen and also for maintenance of temperature control and the exclusion of air and moisture from the surrounding environment.

Electrochemical Analysis

All three techniques described below monitor current as a function of applied potential

Cyclic Voltammetry

In this technique the working electrode is ramped linearly from an initial potential to a switching potential and back to the initial potential. The solution is unstirred, and scan rates, v, can be in the range $20mVs^{-1}$ to $500mVs^{1}$ ($100mVs^{-1}$ for all diagrams in this text). Under the conditions outlined in the previous pages, the only means of mass transport available to the test species is that of thermal diffusion.

The nature of a cyclic voltammogram depends upon the types of processes occuring during the potential ramp and it is important to distinguish between electron transfer and any chemical reactivity or structural change subsequent to that transfer. The transfer of electrons to and from an electroactive species and can be described in one of four ways:

(i) Reversible. Electron Transfer is faster than diffusion of the test species to the electrode.

(ii) Quasi-reversible. The rate of electron transfer is similar to that of diffusion.

(ii) Irreversible. The rate of electron transfer is slower than that of diffusion.

(iv) Partially reversible. An irreversible chemical reaction follows a reversible or

quasi-reversible electron transfer.

Criteria for assessing the nature of electrochemical processes on the basis of cyclic voltametric data as well as the techniques of stirred cyclic and a.c voltammetry described below are given in Table 6.1.

A typical cyclic voltammogram for a reversible process is shown in Figure 6.2. An increase in current is observed when the potential approaches that which induces reduction (or oxidation). The rate of reaction rapidly increases with potential, consumming the reactant in the vicinity of the working electrode. At this point, the rate of diffusion of fresh material from the bulk solution becomes important and $E_p f$ occurs where these two opposing trends are equal. Thereafter, the rate of diffusion of the reactant to the electrode surface becomes the limiting factor and the current drops to a diffusion controlled limit. Beyond the switching potential the same, but opposite, processes occur giving an inversion of the initial scan.

The nature of the return wave is commonly used to assess the chemical reversibility of a system. In the ideal experiment giving rise to Figure 6.2 the symmetric shape of the cyclic voltammogram implies that no gross chemical change occurs during the timescale of the experiment and the process is said to be chemically reversible. Complete absence of a return wave implies that the initial electron transfer induces a chemical or structural change in the test species (an ec mechanism). In such cases daughter product waves are often seen. An asymmetric return wave implies at least some degree of chemical reversibility. In describing the chemical reversibility of a system it is important to stipulate the timescale of the experiment. Thus, a process reversible on the timescale of a cyclic voltammogram may, over the period of an electrosynthesis (see below) give rise to a structurally different species. However, the electrochemical regeneration of the starting material from this new species may be possible and so, overall, the process is chemically reversible.

Figure 6.1 Experimental Set-up for Conventional Electrochemistry.

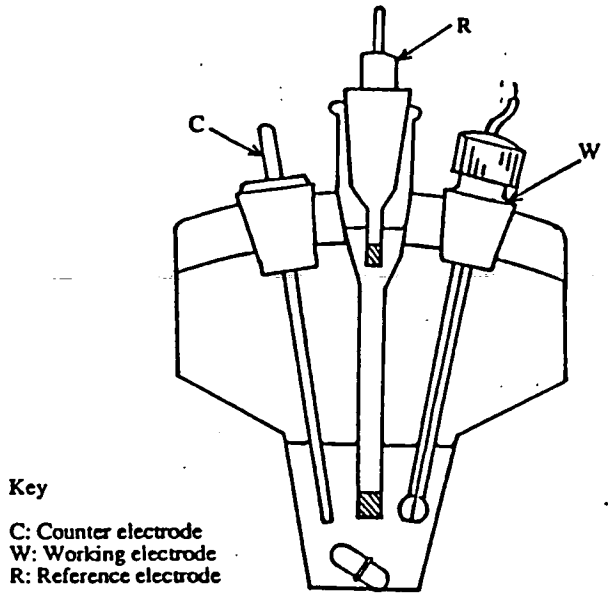

Figure 6.2 Cyclic Voltammogram for a Fully Reversible Process.

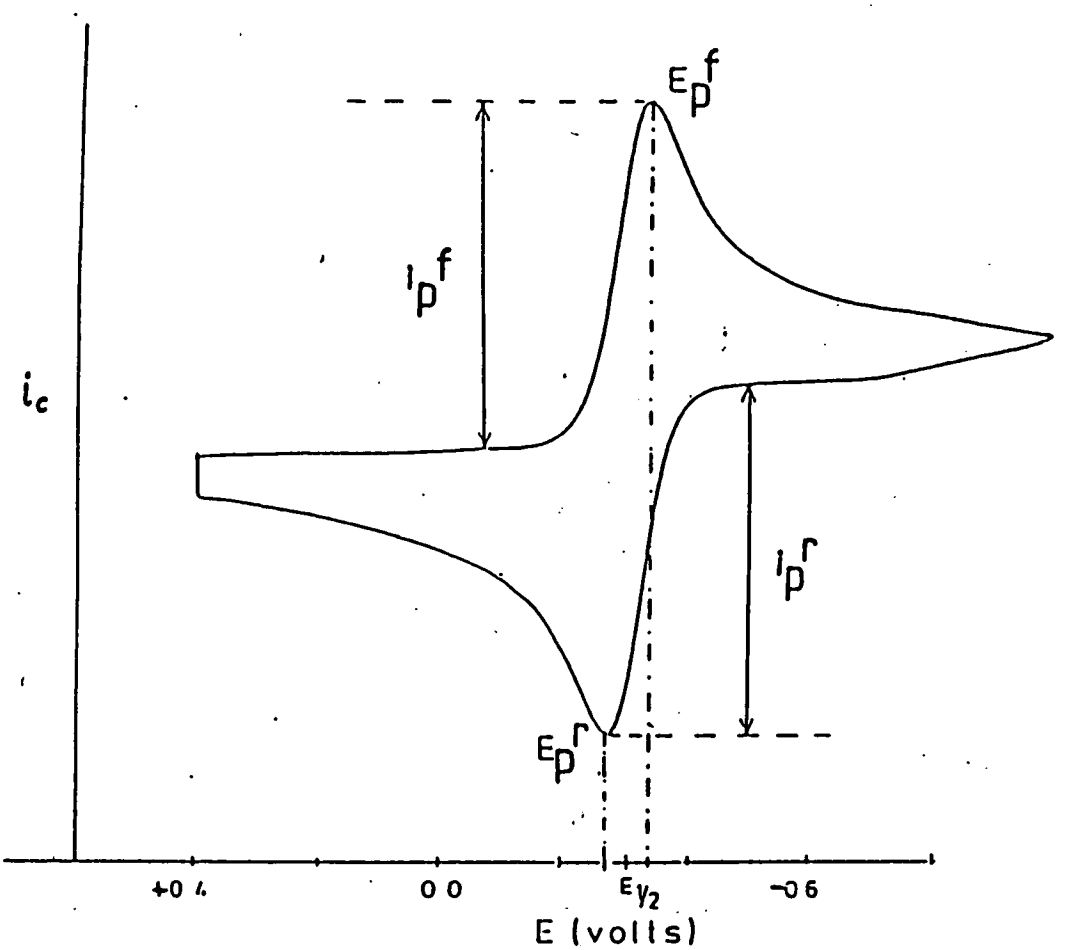

Table 6.1 Reversibility Criteria for Electron Transfer Examined Using Cyclic Voltammetry and A.c. Voltammetry.

Cyclic Voltammetry	
Reversible	E_p independent of ν
	$Epf - Epr = 59/n$ mV at 298K
	$1/2[E_p^f + E_p^r] = E_{1/2}$, independent of concentration.
	$i_p/\nu^{1/2}$ is independent of ν
	$i_p^f/i_p^r = 1$ and independent of ν
Quasi-reversible	E_p shifts with ν
	$E_p^f - E_p^r$ increases as ν increases
	$i_p/\nu^{1/2}$ is independent of ν
	i_p^f/i_p^r generally = 1
Partially reversible	E_p increases by 30/n mV for a ten-fold increase of ν, at low ν
	$i_p/\nu^{1/2}$ is independent of ν
	i_p^f/i_p^r tends to 1 as ν increases.
Irreversible	E_p shifts with ν
	$i_p/\nu^{1/2}$ is independent of ν
	There is no peak i_p^r
A.c. Voltammetry.	
Reversible	E_p is independent of ν
	$\omega^{1/2} = 90/n$ at 298K and independent of ω
	A plot i_p *vs* $\omega^{1/2}$ gives a straight line passing through the origin

Stirred Cyclic Voltammetry

This technique is applied to determine whether a given redox process is an oxidation or reduction. The experiment uses a slow ($20mVs^{-1}$), linear potential ramp at the working electrode in a uniformly stirred solution. Electron transfer at the electrode is therefore governed by diffusion and convection. A cathodic current flow, by convention up the page, indicates a reductive process, an anodic current flow (down the page) an oxidative process.

A.c. Voltammetry

Alternating current (a.c.) voltammetry involves the superimposition of a small, usually sinusoidal, alternating potential, of frequency ω, on a linear potential ramp. The resultant net a.c. current is then monitored as a function of the d.c. potential applied. A typical a.c. voltammogram for a reversible process is given in Figure 6.3. The symmetrical shape results from the need for the presence of both a reducable and oxidisable species in solution in order for an a.c. current to flow. Accordingly, the potential at the peak height corresponds to $E_{1/2}$ for the process under study, the point at which reduced and oxidised species are present in equimolar proportions. The new experimental parameter, ω (which can take values between 10 and 1000Hz), effectively controls the timescale of the experiment. This means that a.c. voltammetry often gives a better measure of any departure from reversibility than d.c. experiments. Another advantage of a.c. techniques is a much improved sensitivity, arising from the distinction in phase between the capacitive background current and the Faradaic current due to the redox processes of the test species. The latter is detected in the phase sensitive a.c. experiment. Finally, a.c. techniques give greater resolution of waves , to within 40mV (conventional cyclic voltammetry requires a separation of 150mV).

Figure 6.3 A.c. Voltammogram for a Reversible Electron Transfer *

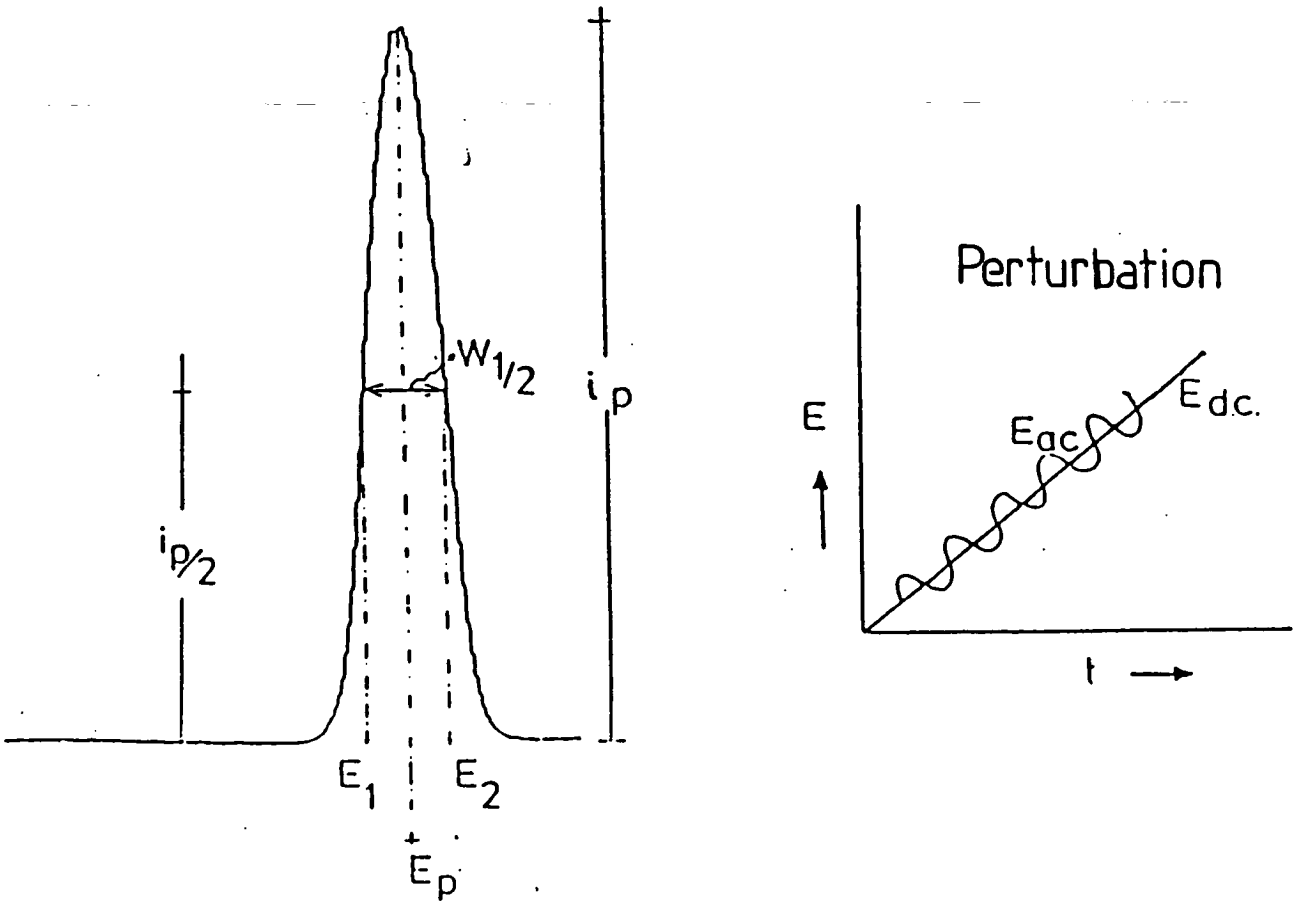

*Diagrams in the text are recorded with ν=20mVs^{-1} and ω=205Hz.

Electrosynthesis

Two types of electrosynthesis can be used; galvanostatic, in which a constant current is made to flow through the cell, and potentiostatic, in which a constant potential is selected and current monitored as a function of time. The latter technique was employed throughout this work.

Electrosyntheses were carried out in an H-cell, shown in Figure 6.4. This incorporates several adaptations from that shown in Figure 6.1. The H-cell is compartmentalised, with the working and counter electrodes separated by glass frits which avoid contamination of the products formed at the working electrode by those at the counter electrode. The working electrode compartment contains a basket Pt electrode, fritted reference and is stirred during the electrosynthesis. A Pt microelectrode is also present to examine the electrochemistry of the products. A Pt-mesh counter electrode completes the circuit. For the full generation of the reduced or oxidised species the potential applied must be 60mV beyond the couple involved.

As well as the generation of new species, coulometric measurements can also be obtained by monitoring the current passed as a function of time and calculating the charge passed, Q, as the area under the current/time curve (see Figure 6.5).

$$Q=nFM$$

n=number of moles of electrons passed,

F=Faraday's constant and M=number of moles of compound used

Figure 6.4 Electrochemical H-Cell for Bulk Electrosynthesis.

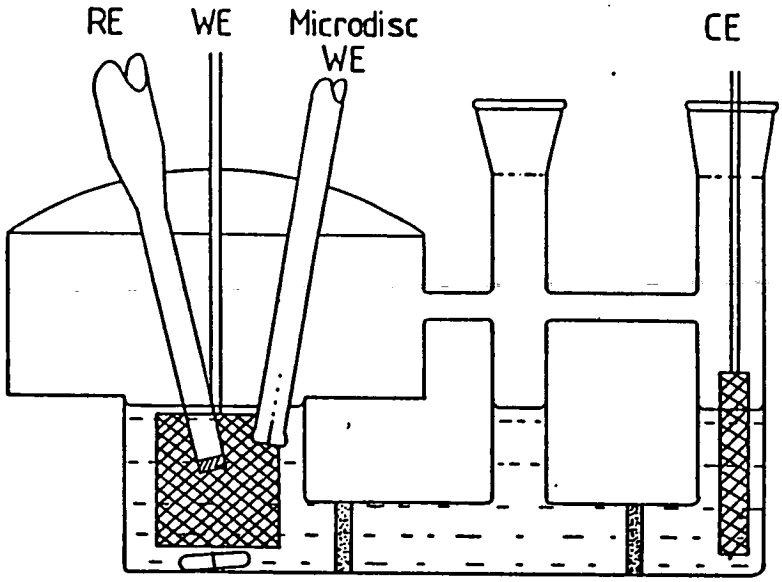

Figure 6.5 Typical Current/Time Curve for Potentiostatic Bulk Electrosynthesis

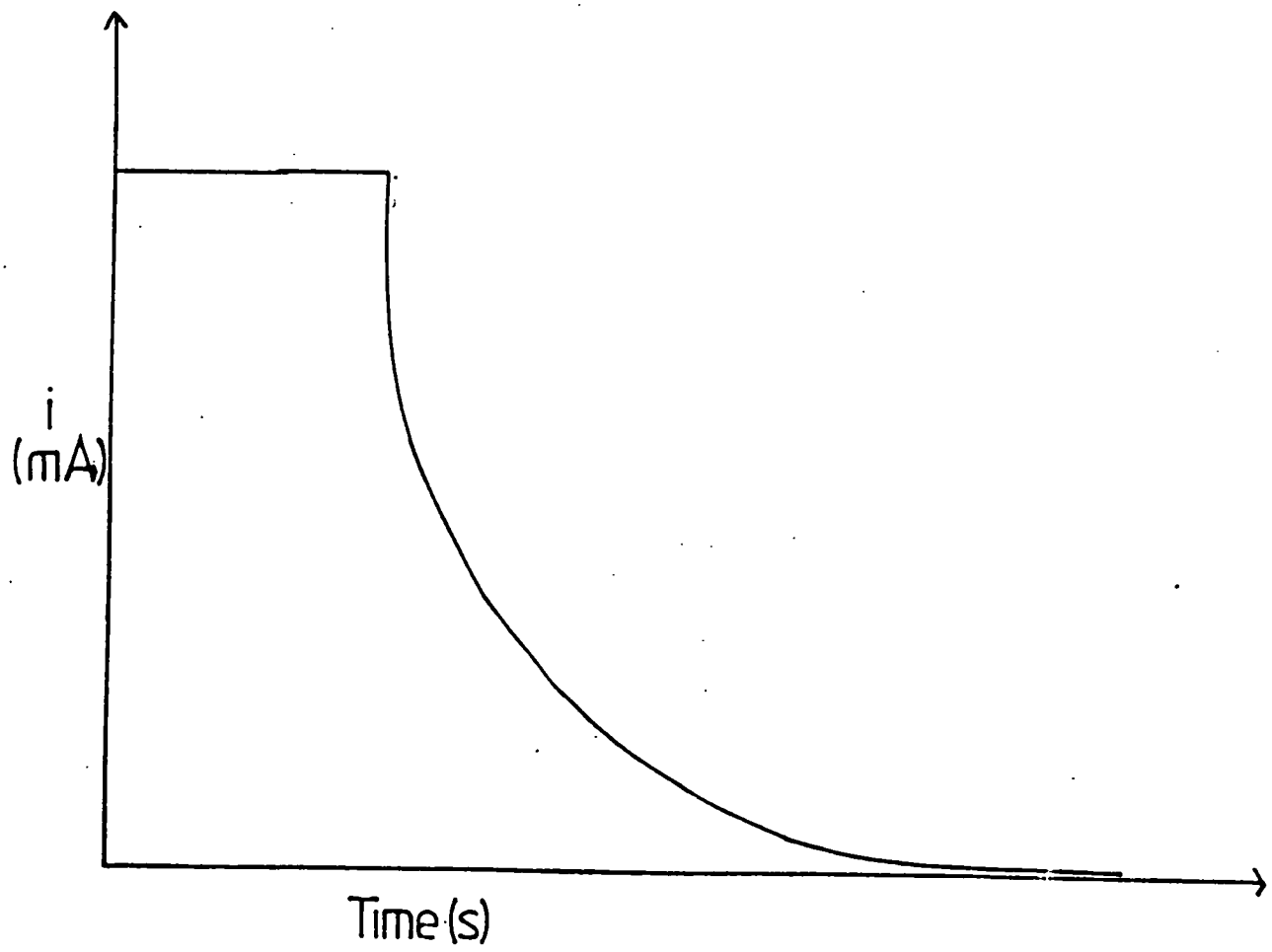

In-situ Spectroelectrochemistry

The principles behind the design of the H-cell have been adapted for the *in-situ* techniques of electronic and EPR spectroelectrochemistry. These have been developed for the study of unstable, electrochemically generated species.

Electronic Spectroelectrochemistry

This uses the Optically Transparent Thin Layer Electrode, or OTTLE, cell, the design of which is shown in Figure 6.6.[124] The Pt/Rh gauze working electrode, transparency -40%, is housed in a quartz UV/visible cell fitted with a quartz extension to act as a resevoir for the test solution. Fritted counter and reference electrodes are placed in the solution through an gas-tight PTFE top and the cell is then housed in a PTFE block in the spectrometer beam. Moisture and air are expelled from the system by flushing with dry nitrogen through the ports in this block and temperature control is maintained by varying flow rates of liquid-nitrogen cooled nitrogen and a room temperature supply.

During the course of an electrogeneration spectra are recorded every five minutes. Upon completion, the regeneration of the starting material was done routinely to assess the chemical reversibility of the system.

EPR Spectroelectrochemistry.

Electrogenerations were carried out in the electron paramagnetic resonance *in-situ* electrochemical, or EPRESI SE, cell, shown in Figure 6.7. This is once again derived from the H-cell, the cylindrical Pt working electrode and insulated Ag reference electrode being housed in a quartz EPR cell fitted with a quartz frit to separate the Pt counter electrode. Generations were performed at 240K, the product solutions being

cooled to 100K to record their EPR signal as frozen glasses.

Figure 6.6 Design of OTTLE Cell and Gas-Tight PTFE Block.

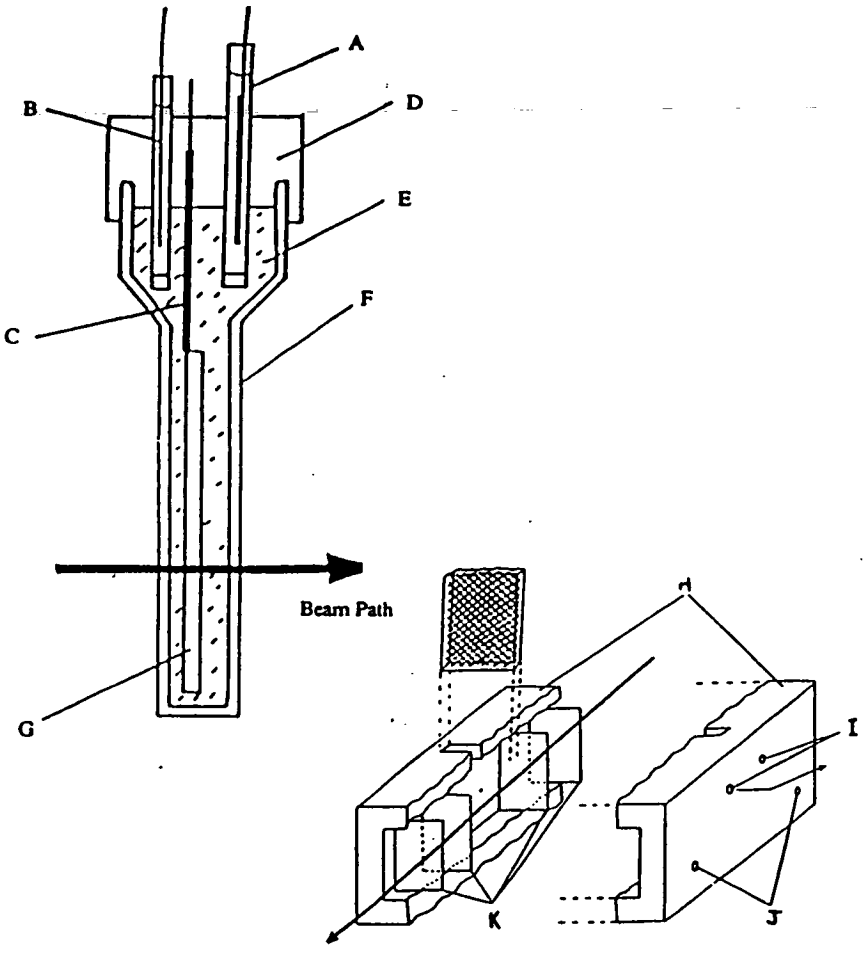

Key

A: Counter electrode
B: Reference electrode
C: Working electrode connection protected from bulk solution by PTFE sleeve
D: PTFE cell cap
E: Test solution
F: 0.1cm Infrasil quartz cell containing Pt grid working electrode
G: Pt grid working electrode
H: PTFE block
I: Variable temperature nitrogen inlet ports
J: Dry nitogen inlet ports (to prevent fogging of inner quartz windows)
K: Infrasil Quartz cell block windows

Figure 6.7 Design of EPRESI SE Cell.

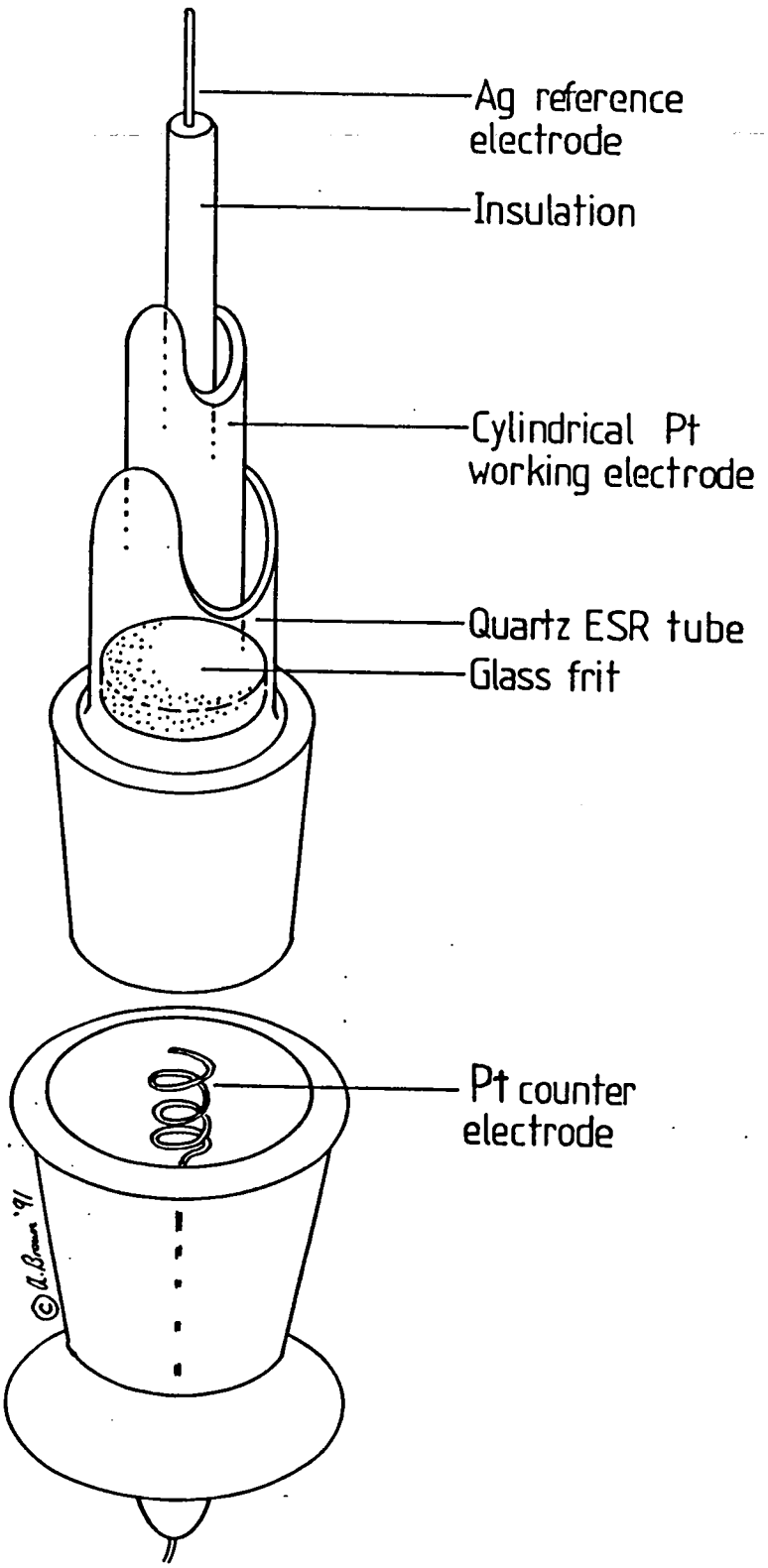

References

1. A. Stock, "Hydrides of Boron and Silicon", Cornell University Press, Ithaca, New York, 1936.

2. W. N. Lipscomb, "Boron Hydrides", Benjamin, New York, 1963.

3. K. Wade, *J. Chem. Soc., Chem. Commun.*, 1971, 792.

4. R. Hoffmann, *Angew. Chem. Int. Ed. Engl.*, 1982, **21**, 711.

5. J.S. Kasper, C.M. Lucht and D. Harker, *Acta Crystallgr.*, 1950, **3**, 436.

6. A. Tippe, W.C. Hamilton, *Inorg. Chem.*, 1969, **8**, 464.

7. R. Brill, H. Dietrich an D H. Dierks, *Acta Crystallogr.*, 1971, **27B**, 2003.

8. R.J. Pace, J. Williams and R.L. Williams, *J. Chem. Soc.*, 1961, 2196.

9. V.D. Aftandillan, H.C. Millar, G.W. Parshall and E.L. Muetterties, *Inorg. Chem.*, 1962, **1**, 734.

10. E.L. Muetterties, *Inorg. Chem.*, 1963, **2**, 647.

11. J.J. Millar and M.F. Hawthorne, *J. Am. Chem. Soc.*, 1959, **81** 4501.

12. P.H. Wilks and J.C. Carter, *J. Am. Chem. Soc.*, 1966, **88**, 3441.

13. L.E. Benjamin, S.F. Stafoej and E.A. Takos, *J. Am. Chem. Soc*, 1963, **85**, 2674.

14. M.F. Hawthorne and A.R. Pitochelli, *J. Am. Chem. Soc.*, 1959, **81**, 5519.

15. I. Dunstan, R.L. Williams and N.J. Blay, *J. Chem. Soc.*, 1960, 5012.

16. N.J. Blay, R.J. Pace and R.L. Williams, *J. Chem. Soc.*, 1962, 3416.

17. H. Schroeder, *Inorg. Chem.*, 1963, **2**, 390.

18. B. Stibr, J. Plesek and S. Hermanek, *Coll. Czech. Chem. Commun.*, 1969, **34**, 194.

19. J. Plesek, S. Hermanek and B. Stibr, *Coll. Czech. Chem. Commun.*, 1968, **33**, 691.

20. M. Hillmann and D.J. Margold, *Inorg. Chem.*, 1965, **4**, 1356.

21. N.N. Greenwood and J.H. Morris, "Mellor's Treatise on Inorganic and Theoretical Chemistry", Vol. 5, Supplement 2, Chapter 24, Longmans, London 1974.

22. M. Hillmann, *J. Am. Chem. Soc.*, 1960, **82**, 1416.

23. J.A. Dupont and M.F. Hawthorne, *J. Am. Chem. Soc.*, 1959, **81**, 4998.

24. R.E. Williams, I. Dunstan and N.J. Blay, *J. Chem. Soc.*, 1960, 5006.

25. R. Schaeffer, *J. Am. Chem. Soc.*, 1957, **79**, 1006.

26. D.E. Sands and Z. Zalkin, *Acta Crystallogr.*, 1962, **15**, 410.

27. J. Reddy and W.N. Lipscomb, *J. Chem. Phys.*, 1959, **31**, 610.

28. T.L. Heying, J.W. Ayer Jnr., S.J. Clark, D.J. Margold, H.L. Goldstein, M. Hillmann, R.J. Polak and J.W. Szmanski, *Inorg. Chem.*, 1963, **2**, 1089.

29. M.F. Hawthorne, D.C. Young and P.C. Wegner, *J. Am. Chem. Soc.*, 1965, **87**, 1818.

30. J.D. Kennedy. (a) *Prog. Inorg. Chem.*, 1984, **32**, 516. (b)1986, **34**, 211 and references therein.

31. L.G. Sneddon, J.C. Huffmann, R.O. Schaeffer and W. Streib, *Chem. Commun.*, 1972, 474.

32. S.K. Boocock, N.N. Greenwood, J.D. Kennedy, W.S. McDonald and J. Staves, *J. Chem. Soc., Dalton. Trans.*, 1981, 2573.

33. J.D. Kennedy and B. Wrachmeyer, *J. Magn. Reson.*, 1980, **38**, 529.

34. F. Klanberg, P.A. Wegner, G.W. Parshall and E.L. Muetterties, *Inorg. Chem.*, 1968, **7**, 2073.

35. N.N. Greenwood, D.S. Thomas and D.W. Waite, *J. Chem. Soc., Dalton. Trans.*, 1976, 177.

36. J.W. Lott, D.F. Gaines, H. Stenhaw and R. Schaeffer, *J. Am. Chem. Soc.*, 1973, **95**, 3042.

37. M.A. Beckett, N.N. Greenwood, J.D. Kennedy and M. Thornton-Pett, *J. Chem. Soc., Dalton. Trans.*, 1986, 795.

38. G.J. Zimmermann, L.W. Hall and L.C. Sneddon, *Inorg. Chem.*, 1980, **19**, 3642.

39. J.M. Gromek and J. Donohue, *Cryst. Struct. Commun.*, 1981, **10**, 871.

40. C.J. Fritchie Jnr., *Inorg. Chem.*, 1967, **6**, 1199.

41. J. Bould, J.E. Crook, N.N. Greenwood and J.D. Kennedy, *J. Chem. Soc., Chem. Commun.*, 1983, 949.

42. T.L. Venable, E. Sinn and R.N. Grimes, *Inorg. Chem.*, 1982, **21**, 895.

43. S.K. Boocock, N.N. Greenwood, M.J. Hails, J.D. Kennedy and W.S. McDonald, *J. Chem. Soc., Dalton. Trans.*, 1981, 1415.

44. N.N. Greenwood, M.J. Hails, J.D. Kennedy and W.S. McDonald, *J. Chem. Soc., Chem. Commun.*, 1980, 37.

45. J. Bould, N.N. Greenwood and J.D. Kennedy, *J. Chem. Soc., Dalton. Trans.*, 1984, 2477.

46. M.A. Beckett, Unpublished observations, University of Leeds, 1981-1984, discussed within reference 30.

47. M.A. Beckett, J.E. Crook, N.N. Greenwood and J.D. Kennedy, *J. Chem. Soc., Dalton. Trans.*, 1984, 1427.

48. E.B. Rupp, D.E. Smith and D.F. Shriver, *J. Am Chem. Soc.*, 1967, **89**, 5562.

49. W.E. Geiger Jnr. in "Metal Interactions with Borane Cages", ed. R.N. Grimes, Plenum Press, New York, 1982, Chapter 6.

50. J.H. Morris, H.J. Gysling and D. Reed, *Chem. Rev.*, 1985, **85**, 51.

51. E.J.M. Hamilton, *Ph.D. Thesis*, University of Edinburgh, 1990.

52. W.E. Geiger and D.E. Smith, *J. Chem. Soc., Chem. Commun.*, 1971, 8.

53. D.M.P. Mingos, M.I. Forsyth and A.J. Welch, *J. Chem. Soc., Dalton Trans.*, 1978, 1363.

54. M.F. Hawthorne, D.C. Young, T.D. Andrews, D.V. Howe, R.L. Pilling, A.P. Pitts, M. Reatjes, L.F. Warren and P.A. Wegner, *J. Am. Chem. Soc.*, 1968, **90**, 879.

55. D.F. Dustin and M.F. Hawthorne, *Inorg. Chem.*, 1973, **12**, 1380.

56. P.J. Dolan, J.H. Kindsvater and D.G. Peters, *Inorg. Chem.*, 1976, **15**, 2170.

57. N.N. Greenwood and H.J. Gysling, Unpublished Results, discussed within reference 50.

58. J.H. Morris and D. Reed, *J. Chem. Res. Synop.*, 1980, 380.

59. J.Q. Chambers, A.D. Norman, M.R. Bicknell and S.H. Cradle, *J. Am. Chem. Soc.*, 1968, **90**, 1271.

60. E.B. Rupp, D.E. Smith and D.F. Shriver, *J. Am. Chem. Soc.*, 1967, **89**, 5568.

61. B.D. Cooksley, J.D. Gorham, J.H. Morris and L. Kane, *J. Chem. Soc., Dalton. Trans.*, 1978, 141.

62. R.N. Leyden, B.P. Sullivan, R.T. Baker and M.F. Hawthorne, *J. Am. Chem. Soc.*, 1978, **100**, 3758.

63. A.R. Siedle and L.J. Todd, *Inorg. Chem.*, 1978, **15**, 2938.

64. N.N. Greenwood and J.A. Howard, *J. Chem. Soc., Dalton. Trans.*, 1976, 177.

65. D.F. Gaines, C.K. Nelson, J.C. Kurz, J.H. Morris and D. Reed, *Inorg. Chem.*, 1984, **23**, 3252.

66. J.D. Kennedy in *Multinuclear N.M.R. (N.M.R. in Inorganic and Organometallic Chemistry)*. Ed. J.Mason, Plenum Press 1986.

67. W.N. Lipscomb, R.J. Wiersema and M.F. Hawthorne, *Inorg. Chem.*, 1972, **11**, 651.

68. M.A. Beckett, J.D. Kennedy and O.W. Oliver, *J. Chem. Soc., Chem. Commun.*, 1985, 855.

69. R.O. Gould and P. Taylor, 1986. University of Edinburgh.

70. A.J. Wynd and A.J. Welch, *Acta Crystallogr.*, 1989, **C45**, 615.

71. D.S. Kendall and W.N. Lipscomb, *Inorg. Chem.*, 1973, **12**, 2915.

72. T.D. Getman, J.A. Krause and S.G. Shore, *Inorg. Chem.*, 1988, **27**, 2398.

73. A.J. Wynd, A.J. McClennan, D. Reed and A.J. Welch, *J. Chem. Soc., Dalton. Trans.*, 1987, 2761.

74. D.S. Kendall and W.N. Lipscomb, *Inorg. Chem.*, 1973, **12**, 546.

75. A.J. Wynd, A.J. Welch and R.V. Parish, *J. Chem. Soc., Dalton. Trans.*, 1990, 2185.

76. A.J. Wynd, *Ph.D. Thesis*, University of Edinburgh, 1989.

77. L.J. Guggenberger, *J. Am. Chem. Soc.*, 1972, **94**, 114.

78. J.E. Crook, *Ph.D. Thesis*, University of Leeds, 1982.

79. J.E. Crook, N.N. Greenwood, J.D. Kennedy and W.S. McDonald, *J. Chem. Soc., Dalton. Trans.*, 1984, 2487.

80. M.A. Beckett, N.N. Greenwood, J.D. Kennedy and M. Thornton-Pett, *Polyhedron*, 1985, **4**, 5059.

81. X.L.R. Fontaine, H. Fowkes, N.N. Greenwood, J.D. Kennedy and M. Thornton-Pett, *J. Chem. Soc., Chem. Commun.*, 1985, 1165.

82. F.M. Chauldry and P.L. Pauson, *J. Organomet. Chem.*, 1974, **69**, C31

83. For example, R.M. Christie, *Ph.D. Thesis* and Y.V. Roberts *Ph.D.Thesis*, University of Edinburgh, 1989 and 1991 respectively.

84. F.H. Herbstein and M.G. Reisner, *Acta Crystallogr.*, 1977, **B33**, 3304.

85. A. Immirzi, *J. Organomet. Chem.*, 1974, **78**, 65.

86. J. Cowie, E.J.M. Hamilton, J.C.V. Laurie and A.J. Welch, *J. Organomet. Chem.*, 1990, **394**, 1.

87. R.A. Kocklar and R. Petit, *J. Organomet. Chem.*, 1966, **6**, 272.

88. H. Haas and T.P. Sheline, *J. Chem. Phys.*, 1967, **47**, 2996.

89. J.E. Ellis and E.A. Flume, *J. Organomet. Chem.*, 1975, **99**, 263.

90. W. Hieber and W. Freyer, *Chem. Ber.*, 1959, **93**, 462.

91. K.H. Pearson, W.R. Howell Jnr., P.E. Reinbold and S. Kirschner, *Inorg. Synth.*, **14**, 57.

92. N.N. Greenwood, J.A. McGinnity and J.D. Owen, *J. Chem. Soc. (A)*, 1971, 809.

93. M. Thornton-Pett, Personal communication.

94. D.G. Evans and D.M.P. Mingos, *J. Organomet. Chem.*, 1982, **231**, 171

95. M. Elain, M.M.L. Chen, D.M.P. Mingos and R. Hoffmann, *Inorg. Chem.*, 1976, **15**, 1148.

96. Z.G. Lewis and A.J. Welch, *J. Chem. Soc., Dalton Trans.*, in press.

97. N.N. Greenwood, J.D. Kennedy, M. Thornton-Pett and J.D. Woollins, *J. Chem. Soc., Dalton Trans.*, 1985, 2397.

98. R.J. Sorbie, *Ph.D. Thesis*, University of Edinburgh, 1990.

99. J.H. Leslie, *Ph.D. Thesis*, University of Edinburgh, 1983.

100. L.J. Yellowlees and D.A. Robb, Unpublished results, 1990.

101. A. Modinas and P. Woodward, *J. Chem. Soc., Dalton Trans.*, 1975, 2355.

102. M.P. Brown, J.R. Fisher, S.J. Franklin, R.J. Puddephatt and K.R. Seddon, *J. Chem. Soc., Chem. Commun.*, 1978, 749.

103. D.J. Doonan, A.L. Balch, S.Z. Goldberg, R. Eisenberg and J.S. Miller, *J. Am. Chem. Soc.*, 1975, **97**, 1961.

104. J.D. Kennedy and B. Wrackmeyer, *J. Magn. Reson.*, 1980, **38**, 529.

105. (a) A. Bax and R. Freeman, *J. Magn. Reson.*, 1981, **42**, 164; 1981, **44**, 542. (b). T.L. Venable, W.C. Hutton and R.N. Grimes, *J. Am. Chem. Soc.*, 1982, **104**, 4716.

106. J. Newman and A.R. Manning, *J. Chem. Soc., Dalton Trans.*, 1973, 1593.

107. D. Drew and J.R. Doyle, *Inorg. Synth.*, **13**, 47.

108. L.M. Venanzi, *J. Chem. Soc.*, 1958, 719.

109. J. Chatt, G.J. Leigh, D.M.P. Mingos and R.J. Parke, *J. Chem. Soc.(A)*, 1968, 2636.

110. R.O. Gould and D.E. Smith, University of Edinburgh, 1986.

111. G.M. Sheldrick, University of Göttingen, Germany, 1986.

112 G.M. Sheldrick, University of Cambridge, 1976.

113. "International Tables for X-ray Crystallography", Kynoch Press, Birmingham, 1974, **4**, 99.

114. P.R. Mallinson, University of Glasgow, 1982.

115. J. Howell, A. Rossi, D. Wallace, K. Haraki and R. Hoffmann, *ICON*, Quantum Chemistry Program Exchange, Univ. Indiana, 1977, no. 344.

116. J.C. Slater, *Phys. Rev.*, 1930, **36**, 57.

117. J.W. Richardson, W.C. Nieupoort, R.R. Powell and W.F. Edjell, *J. Chem. Phys.*, 1962, **36**, 1057.

118. C.J. Ballhousen and H.B. Gray, "Molecular Orbital Theory", Benjamin, New York, 1965.

119. M. Wolfsberg and L. Helmholtz, *J. Chem. Phys.*, 1952, **20**, 837.

120. H-B.Bürgi, J.H. Ammeter, J.C. Thibealt and R. Hoffmann, *J. Am. Chem. Soc.*, 1978, **100**, 3638.

121. A.J. Bard and L.R. Faulkner. "Electrochemical Methods", John Wiley and Sons inc. New York, 1980.

122. C.K. Mann, *Electroanal. Chem.*, 1969, **3**, 57.

123. M. Walter and L. Ramaley, *Anal. Chem.*, 1973, **45**, 165.

124. G.A.Heath, L.J. Yellowlees and P.S. Braterman, *J. Chem. Soc., Chem. Commun.*, 1981, 287.

Appendix 1

The N.m.r. Misfit Method

The use of the boron chemical shifts of $MB_{10}H_{12}$ metallaboranes has often been applied to the interpretation of interactions between the metal and borane fragments in these species. Such analysis usually takes the form of specific comparisons of the chemical shifts of certain boron atoms in the metallaborane with those equivalent in *nido*-$B_{10}H_{14}$, **1**.[1] However, as outlined in Chapter 2, this approach sometimes ignores other, often contradictory, evidence. Despite this, the wide availability of high resolution n.m.r. spectroscopy, as well as the relatively rapid collection of data, compared, certainly, with X-ray methods, would make any analytical tool based solely on n.m.r. data very powerful. Therefore, in this Appendix, we report the results of a new approach to structural analysis of $MB_{10}H_{12}$ metallaboranes, the n.m.r. misfit method.

This new analysis is based on the structural r.m.s. misfit method used in Chapters 2 and 3 in this work. In it, the difference in chemical shift is calculated for equivalent boron atoms between an $MB_{10}H_{12}$ metallaborane and **1**. The r.m.s. misfit is then calculated in the same way as the structural r.m.s. misfit:

$$\text{r.m.s.misfit}_{n.m.r} = \sqrt{[\Sigma_i(\delta_i^2)/10]}$$

Where δ is the difference in chemical shift between two equivalent boron atoms

The result is an n.m.r. misfit which quantifies the change in the n.m.r. spectra when the two bridging hydrogens of **1** are replaced by a metal fragment.

Such an approach requires the unambiguous assignment of ^{11}B n.m.r. spectra of

the species involved. This can usually be performed from the interactive interpretation of both a ^{11}B-^{11}B COSY spectrum and a series of selectively decoupled-boron proton spectra. The metallaboranes studied were $[(CO)_3CoB_{10}H_{12}]^-$, **9**, the *bis*-cage species, $[M(B_{10}H_{12})_2]^{2-}$, M=Pt (**10**), Pd (**11**) and Ni (**8**), and $[PCy_3AuB_{10}H_{12}]^-$, **7**, giving examples of high, intermediate and low metal verticities respectively. In order to reduce errors in comparing the spectra of series of systems, all data were recorded on the same spectrometer at 298K, and in the same solvent (CD_3CN). The ^{11}B spectrum of **1** has been previously assigned,[2] but, again for consistency, the spectrum was re-measured under the experimental conditions described above.

The assignment of the ^{11}B spectrum of **9** serves as an example of the approach employed. The COSY spectrum of this species is shown in Figure A1.1 and the series of selectively decoupled-boron proton spectra in Figure A1.2. A common starting point in assignment is the resonance of the B(f) and B(g) atoms. As Figure A1.1 shows, this resonance should exhibit coupling to all other boron signals, the only one to do so. This is seen in the five off-diagonal peaks correlating with the resonance at -23.10p.p.m.. The simple one-dimensional ^{11}B spectrum consists, as expected, of six peaks of relative intensity 1:2:2:1:2:2. Therefore, on symmetry grounds, the two unique boron positions, B(e) and B(j), are assigned to the peaks at 19.94 and -5.09p.p.m. The off-diagonal resonances indicate that, in addition to coupling to each other and the B(f)/B(g) resonance, these two resonances both exhibit one further coupling to the resonances at -7.50 and 10.46p.p.m. respectively. These two latter peaks can be assigned to the B(h)/B(i) and B(c)/B(d) symmetry equivalent atom pairs. Selective decoupling at the frequencies corresponding to these resonances shows that the signal at -7.50p.p.m. results in the greater enhancement of the bridging hydrogen resonance at -2.91p.p.m. in the ^1H spectrum.

Figure A1.1 ^{11}B-^{11}B COSY Spectrum of [BTMA]9 in CD_3CN at 298K.

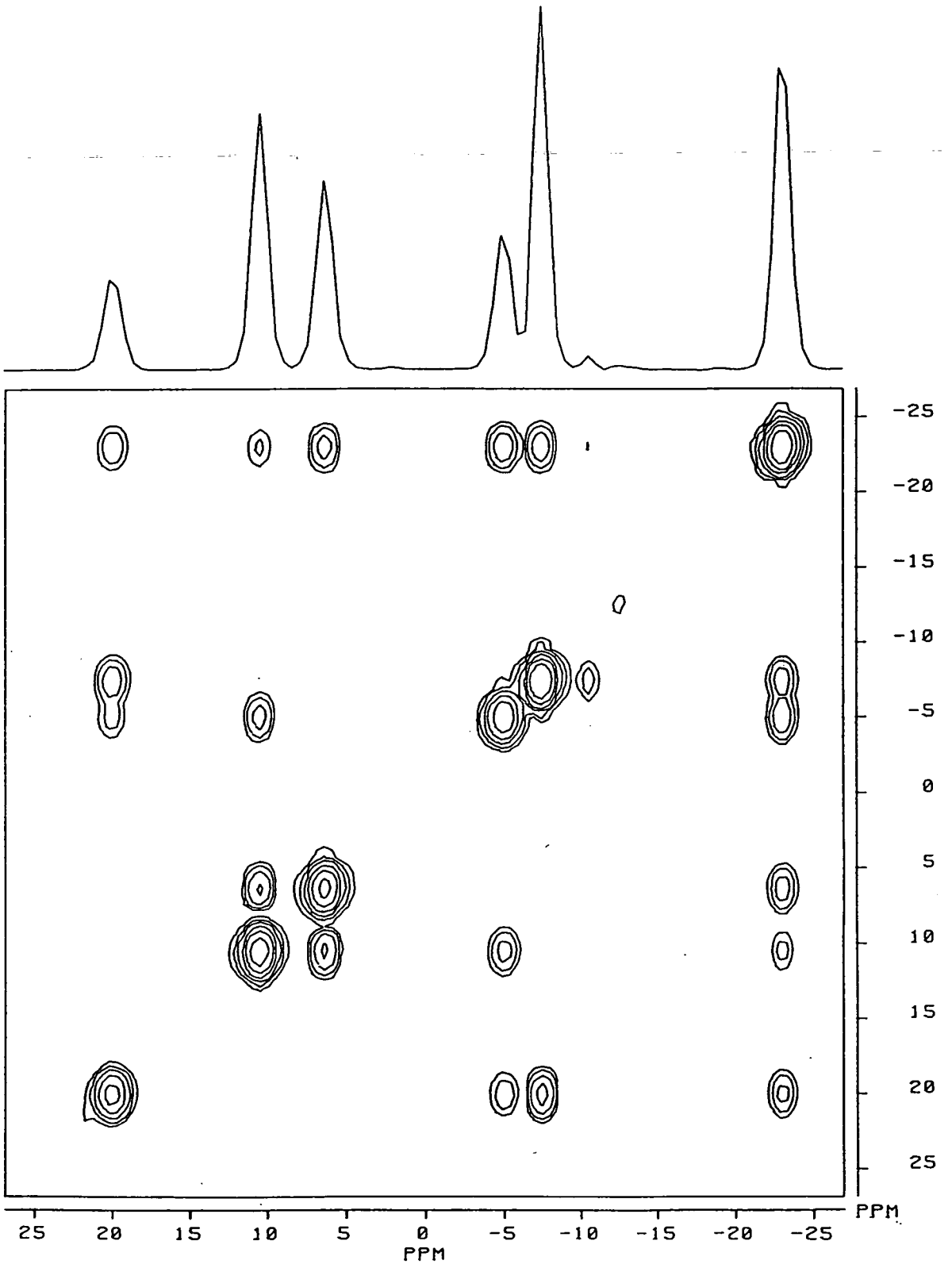

Figure A1.2 ^{1}H-{^{11}B selective} N.m.r. Spectra of [BTMA]9 in CD_3CN at 298K.

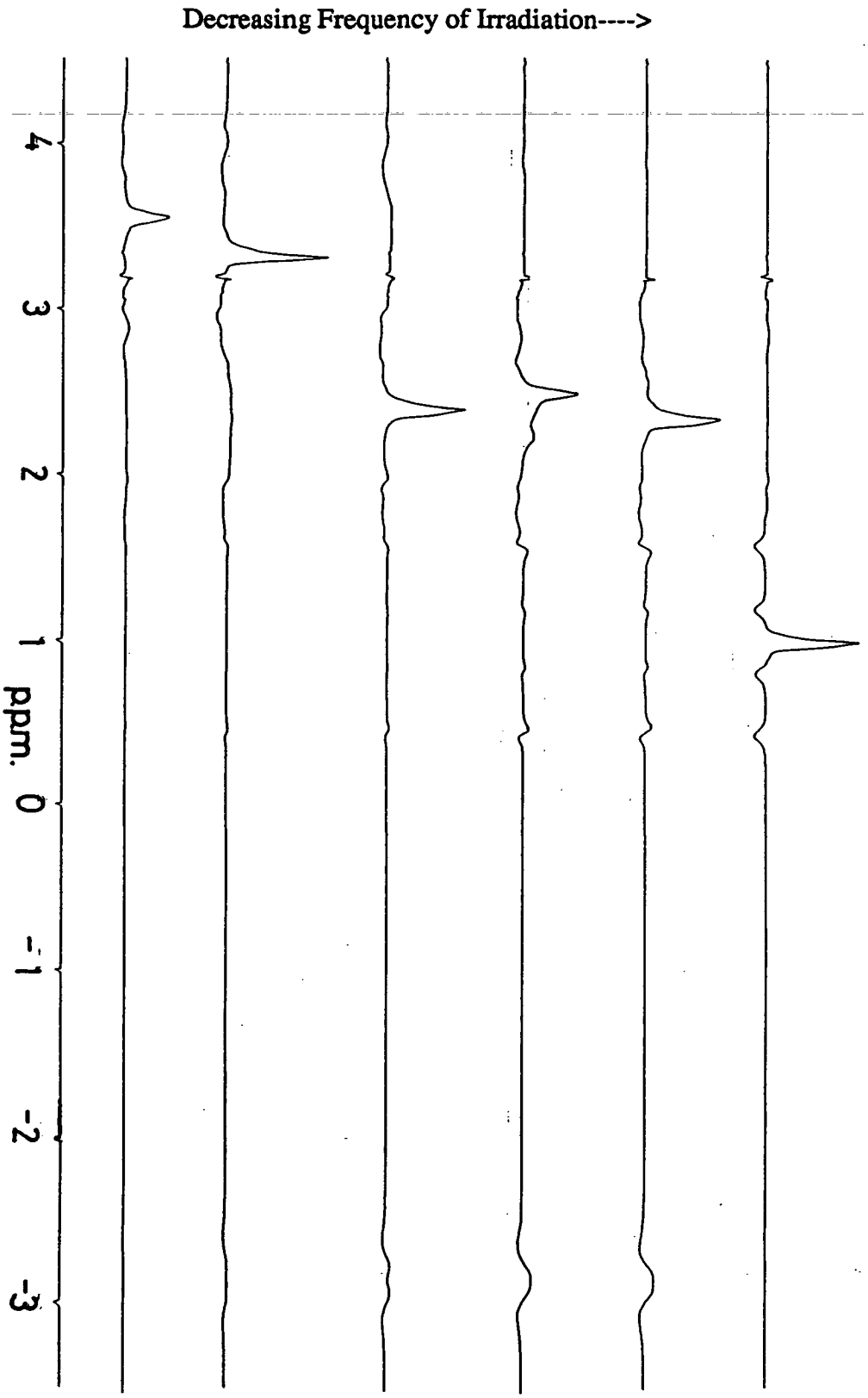

Therefore, this resonance can be attributed to B(h) and B(i), whilst that at 10.46p.p.m. must arise from B(c) and B(d). By the same token, the resonance at 19.94p.p.m. can be attributed to B(e) and that at -5.09p.p.m. to B(j). The one remaining resonance at 6.28p.p.m. is therefore assigned to B(a) and B(b). It can be seen that four out of the six selective decoupled-boron proton spectra exhibit enhancement of the bridging hydrogen signal, whereas only in the cases of irradiation at the frequencies of the B(a)/B(b) and B(h)/B(i) resonances should this occur. This apparent inconsistency probably arises from the large degree of delocalisation present in these systems. In any case, a check on the above assignment can be made by confirming the pattern of correlations seen in the original COSY spectrum. In making this check, no coupling between the B(h)/B(i) and B(a)/B(b) resonances is seen. This is, however, quite usual for a bridged boron connectivity.

The spectra of **8**, **10** and **11** were assigned in a similar fashion and are given, along with the assignment of the spectrum of **1**, in Table A1.1. The unambiguous assignment of the spectrum of **7**, however, could not be performed due to the reactivity of this species in acetonitrile. This reaction, to form $[(PCy)_2Au][Au(B_{10}H_{12})_2]$, is known to occur in refluxing acetonitrile,[3] however, even at room temperature it still occurs too rapidly to allow for the data accumulation for the COSY experiment on **7**. However, a one dimensional ^{11}B spectrum was obtained and a tentative assignment made (see Figure A1.3).

Comparison with the spectra of the other metallaboranes suggested that the extreme low frequency resonance (-29.60p.p.m.) is due B(f) and B(g). Similarily, a previous study on this and related decaboranyl systems noted that the B(a) and B(b) resonance was always to the highest frequency.[3] Assuming this also to be the case here assigns the resonance at +4.51p.p.m. to B(a) and B(b), leaving two peaks, one corresponding to one of the unique boron atoms, the other a complex signal due to the overlap of the resonances of the five remaining boron atoms. Comparing the

chemical shifts of the B(e) and B(j) atoms in the spectra of the $MB_{10}H_{12}$ species shows that the resonance due to B(j) is always to high frequency, and by analogy is therefore the single peak at -4.29p.p.m. in the spectrum of **7**. The remaining peak, of integral 5, must arise from the B(c), B(d), B(h), B(i) and B(e) atoms. Whilst it is impossible to determine the exact positions of the resonances of these atoms, they are so close together that it was felt the use of an average position (-8.50p.p.m.) in the calculation of the n.m.r. misfit for this species would not incur too large an error.

Figure A1.3 $^{11}B-\{^1H\}$ N.m.r. Spectrum of $[HNEt_3]$**7** in CD_3CN at 298K.

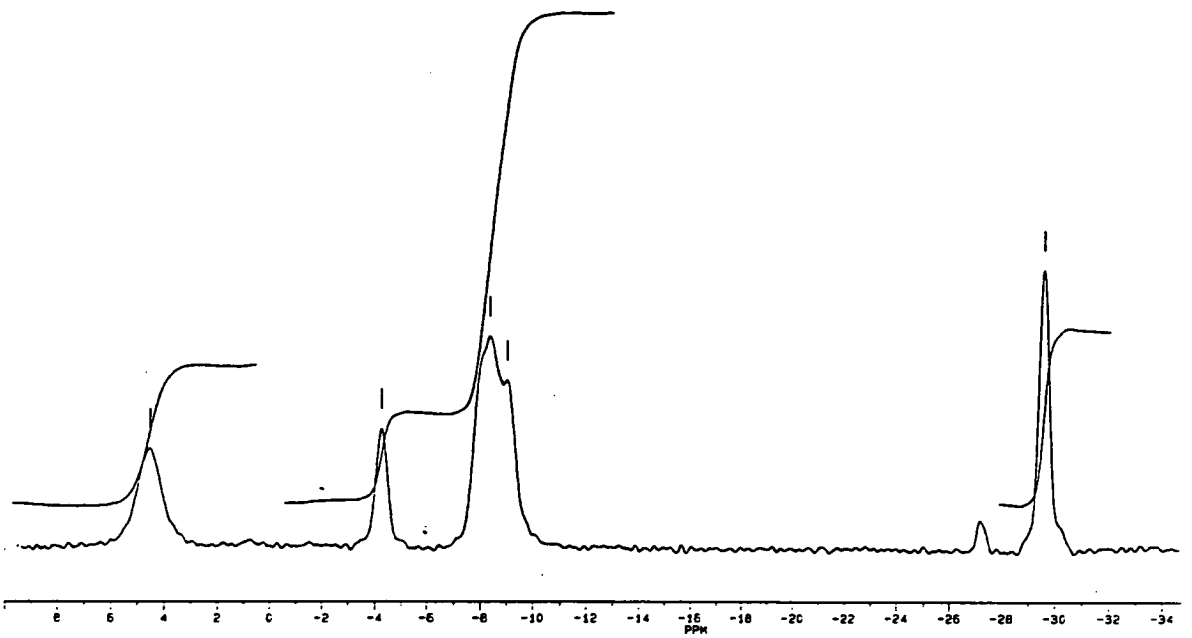

Chemical Shift/p.p.m. (Intensity)	**Assignment** (See text)
4.51 (2B)	B(a), B(b)
-4.29 (1B)	B(j)
-8.50 (5B)	B(c), B(d), B(e), B(h), B(i)
-29.60 (2B)	B(f), B(g)

Table A1.1 Assignment (p.p.m.) of the 11B-{1H} N.m.r. Spectra of **1, 8, 9, 10** and **11.**

System:	1	8	11	10	9
Position					
B(a), B(b)	12.60	11.59	12.50	7.95	6.28
B(c), B(d)	1.07	10.88	13.75	8.83	10.46
B(e)	12.60	0.95	1.78	-1.33	-5.09
B(f), B(g)	-33.96	-21.06	-23.09	-24.16	-23.10
B(h), B(i)	1.07	-3.45	-1.65	-4.66	-7.50
B(j)	12.60	8.66	11.98	9.95	19.94

The values of the n.m.r. misfit calculated from these data are shown below, along with the values of the structural r.m.s. misfit between each metallaborane and **1**.

Metallaborane:	**9**	**10**	**11**	**8**	**7**
N.m.r. Misfit/p.p.m.:	10.03	7.89	8.31	8.48	11.32
Structural R.m.s. Misfit/Å:	0.143	0.083	0.081	0.074	0.046

Although the value obtained for **7** must contain a significant error, it is immediately apparent that thereis no real correlation between the two sets of figures. However, if the n.m.r. misfits are recalculated using **9** as the standard a much better, if not exact, correlation between these results and the equivalent structural r.m.s. misfit calculation is seen.

Metallaborane:	**9**	**10**	**11**	**8**	**7**
N.m.r. Misfit/p.p.m.:	0.00	3.78	5.27	5.11	11.88
Structural R.m.s. Misfit/Å:	0.00	0.068	0.080	0.087	0.137

Whilst these initial results on the comparison of metallaborane spectra by this method are promising, clearly much more work is required to confirm the trend implicit in the above data. It seems that the n.m.r. misfit method can only be used for comparison between metallaboranes, rather than between metallaboranes and the analogous parental borane system. A possible reason for this can be seen in the data reproduced from the results of the FMO calculations performed in Chapter 3 in Tables A1.2.

These calculations investigated the occupations of the frontier MO's of the $\{B_{10}H_{12}\}^{2-}$ fragments in several metallaborane and borane systems. Here, we see that in the cases of high, intermediate and low verticity, as modelled by **18'**, **10'** and **7'**

respectively, the deoccupation of the **1a'** and **2a'** occupied MO's of the $\{B_{10}H_{12}\}^{2-}$ fragments is approximately the same; the real distinction in verticity results from the varying degree of deoccupation of the **1a''** and occupation of the **3a'** MO's. Compared with these systems, the deoccupation of the **1a'** and **2a'** orbitals of this fragment in **1** is far greater, and this may lie behind the difficulty in comparing the ^{11}B spectrum of **1** with those of the metallaboranes. The detailed electronic structure of the two types of system may simply be too different to allow for close comparison by the n.m.r. misfit method.

Table A1.2 Occupations (e) of Frontier MO's of $\{B_{10}H_{12}\}^{2-}$ in Metallaboranes and **1**.

System	Added Fragment	1a'	2a'	1a''(HOMO)	3a'(LUMO)
18'	$\{Ir(PH_3)_3\}^+$	1.800	1.939	1.269	0.766
10'	$\{Au(B_{10}H_{12})\}^+$	1.791	1.895	0.970	0.082
7'	$\{AuPH_3\}^+$	1.826	1.853	1.861	0.054
1	$\{H..H\}^{2+}$	1.607	1.585	1.124	0.010
$[Me_2TlB_{10}H_{12}]^-$	$\{Me_2Tl\}^+$	1.913	1.647	1.568	0.010

These differences in fragment frontier MO occupancy could be rationalised in terms of the structures of the boranes and metallaboranes (see Chapter 3). However, the sensitivity of the n.m.r. technique to the precise electronic environment of each nucleus may mean that even subtle variations in structure may lead to anomalies in the size of the n.m.r. misfit. In relation to this last point, it would be interesting to calculate the n.m.r. misfit of the thallaborane, $[Me_2TlB_{10}H_{12}]^-$, as, as is shown in

Table A1.2, the deoccupation of the **1a'** and **2a'** MO's is quite different in this system compared to that seen in the other metallaboranes.

Thus, whilst some promising results were obtained using this n.m.r. misfit method, its further use for structural analysis must treated with a degree of scepticism until either a greater bulk of supporting data is built up or the precise correlation between electronic structure and chemical shift is made.

Experimental

General methods and instrumentation outlined in Chapter 6 were employed. N.m.r. spectra were recorded on a Bruker WP360 spectrometer. The synthesis of PCy_3AuCl followed the published method.[4] Syntheses of Cy_3AuMe and $[HNEt_3][Cy_3PAuB_{10}H_{12}]$ were made by the methods developed in this department and have been outlined elsewhere.[3]

References

1. S.K. Boocock, N.N. Greenwood, J.D. Kennedy, W.S. McDonald and J. Staves, *J. Chem. Soc., Dalton Trans.*, 1981, 2573.

2. D.F. Gaines, C.K. Nelson, J.C. Kunz, J.H. Morris and D. Reed, *Inorg. Chem.*, 1984, **23**, 3252.

3. A.J. Wynd, *Ph.D. Thesis*, University of Edinburgh, 1989; A.J. Wynd, A.J. McLennan, D. Reed and A.J. Welch, *J. Chem. Soc., Dalton Trans.*, 1987, 2761; A.J. Wynd, A.J. Welch and R.V. Parish, *J. Chem. Soc., Dalton Trans.*, 1990, 2185.

4. A.J. Carty and A. Efraty, *Inorg. Chem.*, 1969, **8**, 543.

Appendix 2.

Reaction of 6-(p-cymene)-6-*nido*-RuB_9H_{13}

with Ethanolic Sodium Hydroxide

Introduction

As described in Chapter 1, decaborane undergoes a deboronation reaction in ethanolic alkali to give the *arachno* anion $[B_9H_{14}]^-$. The structure of 6-(p-cymene)-6-*nido*-RuB_9H_{13},**23**, along with those of the several other known *nido*-6-metalladecaboranes, has been interpreted as being derived from that of decaborane by the replacement of a {BH} fragment with an isolobal metal fragment. Therefore, the reaction of this ruthenaborane with ethanolic sodium hydroxide was carried out to study to what extent, if any, the isolobal replacement causes variation in the reaction chemistry of these isostructural species. Strict analogy with borane chemistry would suggest the formation of an arachno-$[MB_8H_{13}]^-$ metallaborane, as yet unreported in the literature.

Synthesis and Spectroscopic Characterisation of Products.

23 was treated with one equivalent of sodium hydroxide in ethanol. In contrast to the reaction of decaborane under these conditions, no immediate colour change or subsequent gas evolution was noted. After about two hours a slight lightening of the reaction mixture was seen and at this point the solvent was removed *in vacuo*. ^{11}B and $^{11}B-\{^1H\}$ n.m.r. spectra of the crude reaction mixture suggested a mixture of products had been formed and all the starting material had been consumed.

Chromatographic separation yielded one major product, the ^{11}B and $^{11}B-\{^{1}H\}$ n.m.r. spectra of which are presented in Figure A2.1.

Several structural details are apparent from these spectra. Firstly, the product seems to have a low molecular symmetry, with eight boron resonances in the decoupled ^{11}B spectrum. The integral of the peak at -4.45p.p.m. is twice that of the others and, assuming this is the coincidental overlap of two boron resonances, the overall spectrum indicates the presence of nine different boron environments in the molecule. It seems likely therefore that deboronation of **23** has not occurred. Another feature was the absence of any coupling to the resonance at +44.77p.p.m. in the ^{11}B spectrum, suggesting that substitution of a terminal hydrogen had occurred. Finally, and most interestingly, the signal at -15.45p.p.m. in the proton decoupled spectrum clearly displays a second coupling in the ^{11}B spectrum. This extra coupling of 43Hz is in addition to the single $B-H_{terminal}$ bond coupling, typically of the order of 150Hz exhibited by the eight lower frequency resonances and strongly suggests the presence of an *endo*-H atom. Figure A2.2 shows a series of eight selectively decoupled boron-proton spectra corresponding to irradiation at each of the eight boron resonances which give further information on the nature of the product. Firstly, irradiation at the lowest frequency boron resonance sharpens the lowest frequency proton resonance. The position of this signal indicates a metal hydride, which can be assigned as bridging a boron-metal connectivity. The other spectra in this series confirm the association of a terminal hydrogen with each of the other boron atoms, as well as the second proton resonance associated with the boron resonance at -15.45p.p.m. The resonances at -1.55p.p.m. and -2.37p.p.m. can be tentatively assigned as being due to two bridging hydrogens. However, only one resonance appears associated with a metal-boron bridge.

Figure A2.1 ^{11}B and ^{11}B-{^{1}H} N.m.r. Spectra of the Product of the Reaction of NaOH/EtOH with **23**.

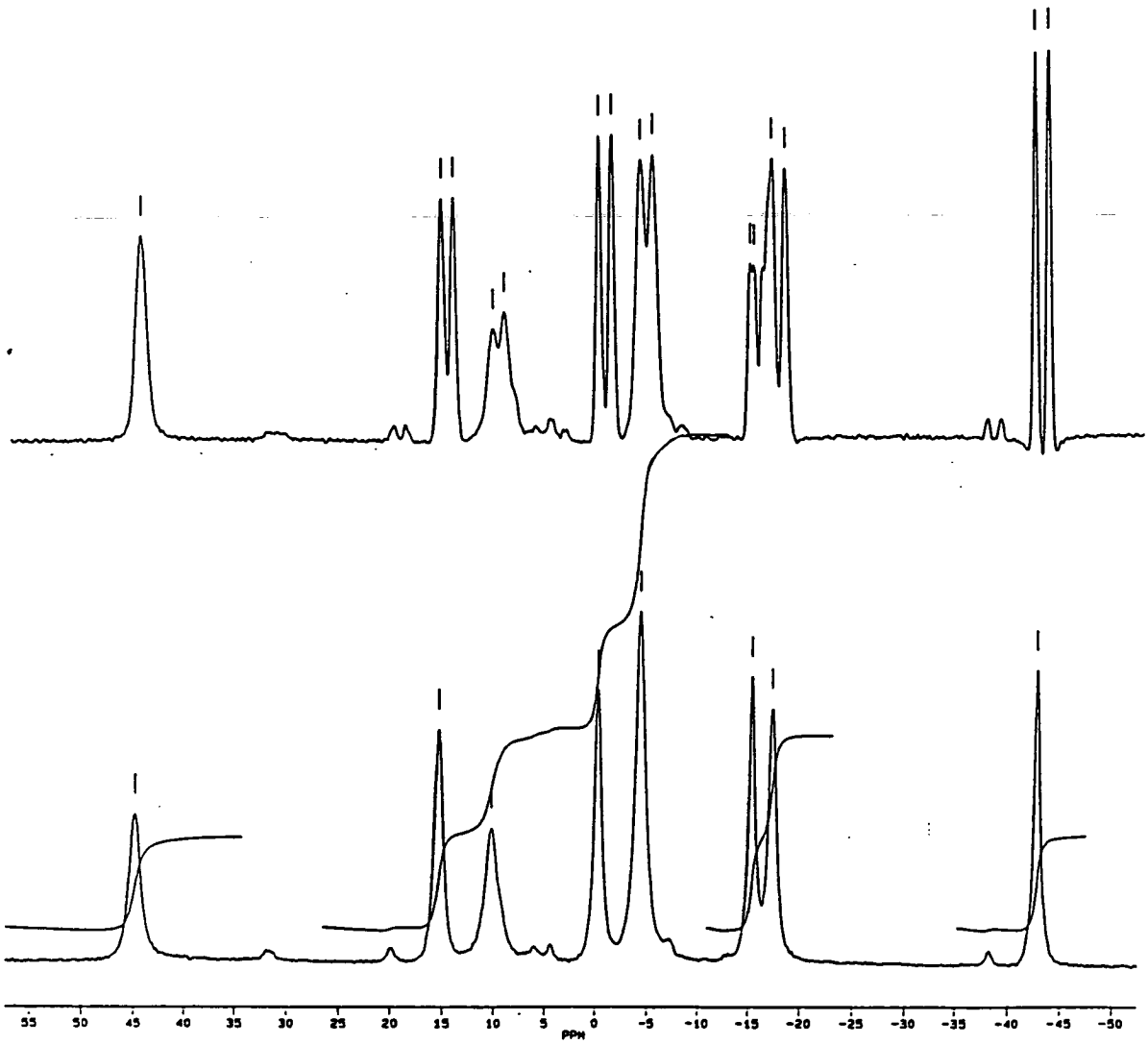

Figure A2.2 ^{1}H-{^{11}B selective} Spectra.

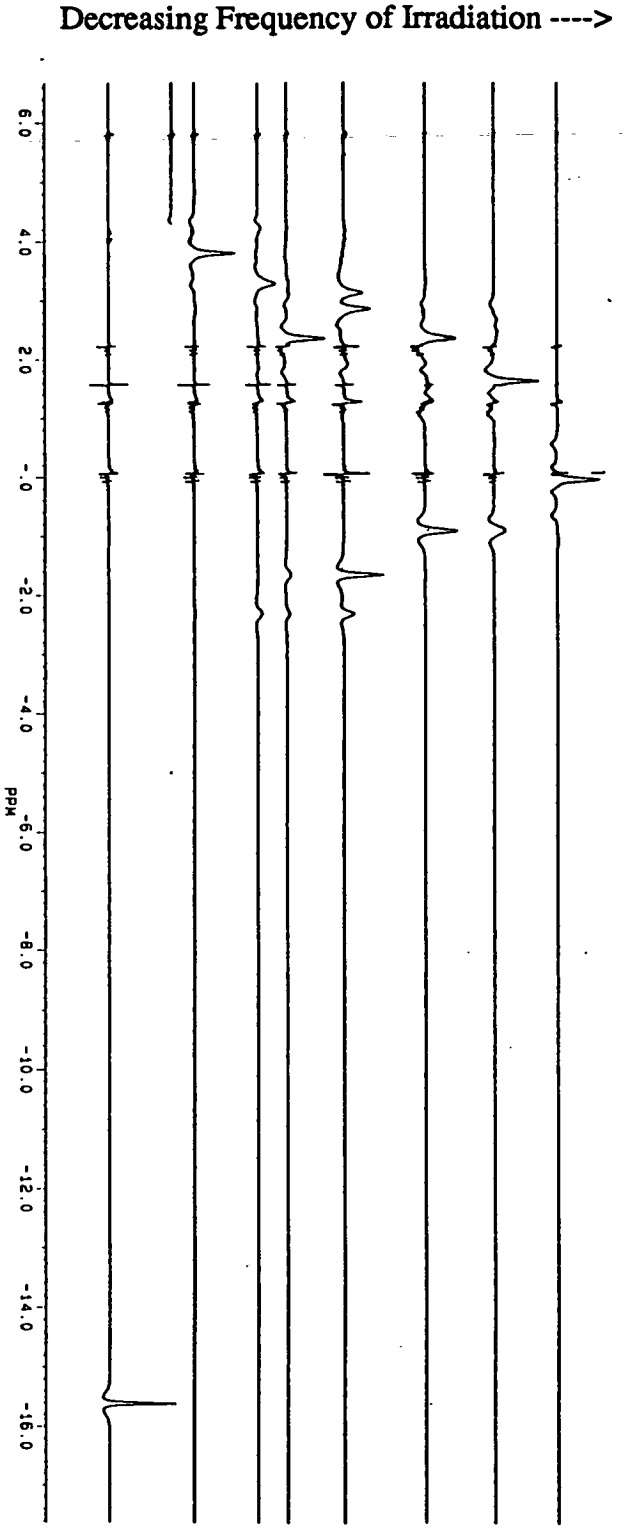

Attempts to assign the full molecular structure of the product by a ^{11}B - ^{11}B COSY experiment were frustrated by the lack of off-diagonal peaks in this spectrum. The situation was further complicated by the coincidental resonances and the close proximity of the two resonances at -15.44 and -17.45p.p.m. To fully characterise this species, therefore, it was necessary to undertake an X-ray crystallographic study.

Crystallographic Analysis

The crystallographic study reveals that the product is the substituted *nido*-5-metalladecaborane, 5-(p-cymene)-6-OEt-5-*nido*-RuB_9H_{12}, **24**. It also confirms the conclusions drawn from the spectroscopic studies: terminal hydrogen substitution has occurred at the 6 position whilst an *endo* hydrogen is bound to B(7). During the course of the reaction a cluster rearrangement has occurred to yield the product which is once again a structural analogue of $B_{10}H_{14}$, but with the isolobal replacement of {BH} by the metal fragment now occuring at the 5 position. The major difference between the two species is that in **24** the B(6)-B(7) connectivity is not bridged.

24 crystallises in the orthorhombic space group $P2_12_12_1$ with eight molecules per unit cell and two independent molecules present in the asymmetric fraction. Crystallographic analysis shows these two molecules to be a racemic mixture of two enantiomers. A perspective view of each molecule (hereafter referred to as molecules A and B) is given in Figures A2.3. Tables A2.1a and A2.1b list the positions of non-hydrogen atoms of each molecule along with the associated equivalent isotropic thermal parameters. Table A2.2 compares selected interatomic distances for each molecule and Table A2.3 selected interbond angles. Tables A2.4a and A2.4b list anisotropic thermal parameters for the two molecules and Tables A2.5a and A2.5b detail the positions of refined and calculated hydrogen atoms.

Figure A2.3 Molecular Stuctures of Molecules A and B of **24**

Molecule A

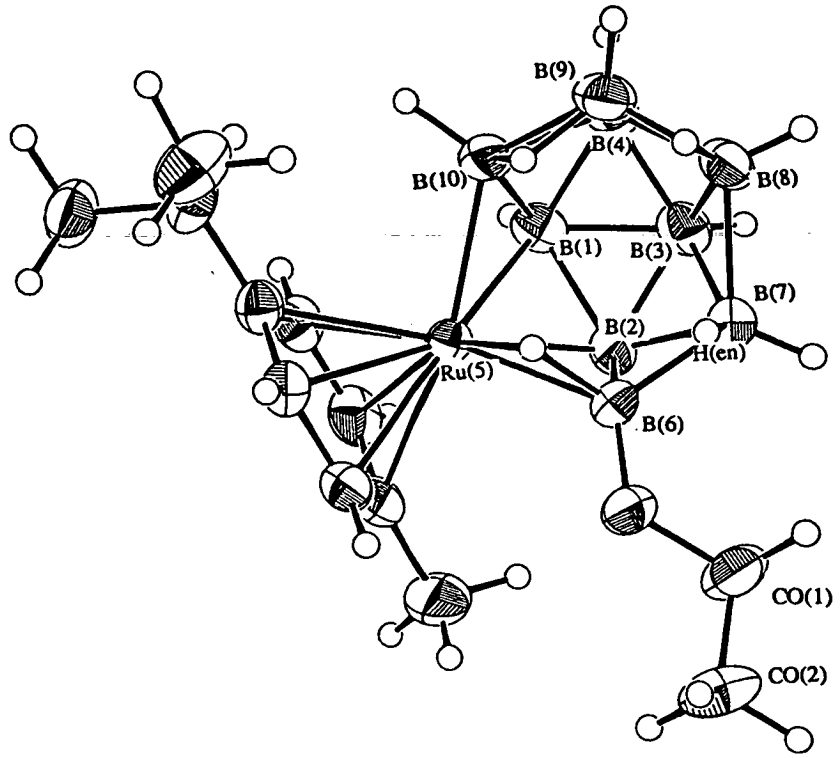

Molecule B

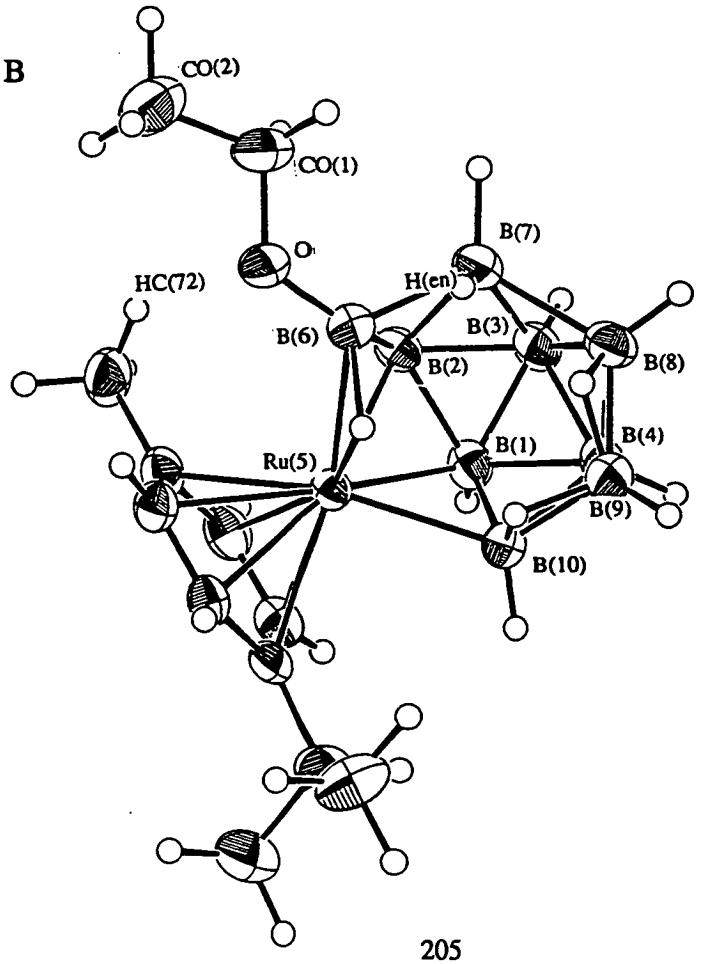

Table A2.1a Atomic Positions of Non-Hydrogen Atoms and Equivalent Isotropic Thermal Parameters ($Å^2$) for Molecule A of **24**.

	x	y	z	Ueq
Ru(5)	-0.13431(3)	-0.06967(2)	-0.19864(1)	0.0286(1)
B(1)	-0.0634(4)	0.0413(3)	-0.1783(3)	0.0383(25)
B(6)	-0.1653(4)	-0.0343(3)	-0.30567(25)	0.0387(25)
B(10)	-0.2056(5)	0.0296(3)	-0.1399(3)	0.040(3)
B(4)	-0.1605(5)	0.11914(25)	-0.1693(3)	0.042(3)
B(8)	-0.2245(5)	0.1314(3)	-0.2548(3)	0.044(3)
B(7)	-0.1474(5)	0.0646(3)	-0.3200(3)	0.0426(25)
B(9)	-0.3033(5)	0.0956(3)	-0.1800(3)	0.044(3)
B(2)	-0.0434(4)	0.01251(25)	-0.2670(3)	0.0359(25)
B(3)	-0.0773(5)	0.1061(3)	-0.2470(3)	0.043(3)
C(1)	-0.0176(4)	-0.16770(22)	-0.22459(25)	0.0419(24)
C(2)	-0.1339(4)	-0.19066(21)	-0.21996(23)	0.0405(21)
C(5)	-0.0408(4)	-0.11516(23)	-0.10498(25)	0.0435(25)
C(3)	-0.2039(4)	-0.17881(21)	-0.15931(24)	0.0367(23)
C(4)	-0.1591(4)	-0.14188(21)	-0.09947(21)	0.0379(22)
C(6)	0.0286(4)	-0.12769(23)	-0.1654(3)	0.0437(25)
C(7)	0.0554(4)	-0.1809(3)	-0.2897(3)	0.056(3)
C(8)	-0.2270(4)	-0.1321(3)	-0.03220(22)	0.0476(25)
C(9)	-0.3576(5)	-0.1320(3)	-0.0418(3)	0.067(3)
C(10)	-0.1895(5)	-0.1937(3)	0.0189(3)	0.068(3)
O	-0.1740(3)	-0.08335(16)	-0.36133(14)	0.0446(16)
CO(1)	-0.1451(6)	-0.0619(3)	-0.43222(22)	0.065(3)
CO(2)	-0.1420(5)	-0.1283(3)	-0.4781(3)	0.068(3)

Table A2.1b. Atomic Positions of Non-Hydrogen Atoms and Equivalent Isotropic Thermal Parameters ($Å^2$) for Molecule B of **24**.

	x	y	z	Ueq
Ru(5)	-0.12901(3)	-0.41958(1)	-0.61044(1)	0.0300(1)
B(6)	-0.1574(4)	-0.4543(3)	-0.71807(24)	0.0376(24)
B(10)	-0.1941(5)	-0.5216(3)	-0.5539(3)	0.043(3)
B(1)	-0.0514(4)	-0.5296(3)	-0.5915(3)	0.041(3)
B(2)	-0.0341(5)	-0.49893(25)	-0.6805(3)	0.040(3)
B(7)	-0.1346(5)	-0.5510(3)	-0.7348(3)	0.044(3)
B(3)	-0.0618(5)	-0.5929(3)	-0.6628(3)	0.046(3)
B(4)	-0.1434(6)	-0.6101(3)	-0.5847(3)	0.049(3)
B(9)	-0.2901(5)	-0.5893(3)	-0.5950(3)	0.052(3)
B(8)	-0.2095(5)	-0.6209(3)	-0.6705(3)	0.048(3)
C(1)	-0.0231(4)	-0.31691(24)	-0.63618(25)	0.0457(25)
C(2)	0.0293(4)	-0.3570(3)	-0.5791(3)	0.049(3)
C(3)	-0.0338(4)	-0.37350(25)	-0.51754(25)	0.0433(24)
C(4)	-0.1537(4)	-0.35124(22)	-0.50923(22)	0.0398(22)
C(5)	-0.2071(4)	-0.31494(24)	-0.56602(23)	0.0396(23)
C(6)	-0.1425(4)	-0.29784(22)	-0.62867(23)	0.0428(23)
C(7)	0.0468(5)	-0.2992(3)	-0.7008(3)	0.066(3)
C(8)	-0.2168(4)	-0.3682(3)	-0.44074(23)	0.048(3)
C(9)	-0.1788(5)	-0.3148(3)	-0.38274(24)	0.063(3)
C(10)	-0.3516(5)	-0.3695(4)	-0.4482(3)	0.074(4)
O	-0.1723(3)	-0.40398(17)	-0.77145(15)	0.0455(16)
CO(1)	-0.1407(5)	-0.4218(3)	-0.84312(22)	0.060(3)
CO(2)	-0.1510(5)	-0.3534(3)	-0.8869(3)	0.071(4)

Table A2.2. Comparison of Selected Interatomic Distances (Å) in Molecules A and B of **24**.

Molecule A		Molecule B	
Ru(5)-B(1)	2.202(5)	Ru(5)-B(1)	2.210(5)
Ru(5)-B(2)	2.226(5)	Ru(5)-B(2)	2.232(5)
Ru(5)-B(6)	2.153(5)	Ru(5)-B(6)	2.156(5)
Ru(5)-B(10)	2.264(5)	Ru(5)-B(10)	2.262(5)
Ru(5)-H(56)	1.59(5)	Ru(5)-H(56)	1.65(4)
Ru(5)-C(1)	2.269(4)	Ru(5)-C(1)	2.268(5)
Ru(5)-C(2)	2.232(4)	Ru(5)-C(2)	2.202(5)
Ru(5)-C(3)	2.257(4)	Ru(5)-C(3)	2.225(5)
Ru(5)-C(4)	2.306(4)	Ru(5)-C(4)	2.299(4)
Ru(5)-C(5)	2.223(5)	Ru(5)-C(5)	2.257(5)
Ru(5)-C(6)	2.213(5)	Ru(5)-C(6)	2.241(4)
B(1) -B(2)	1.773(7)	B(1) -B(2)	1.784(7)
B(1) -B(3)	1.760(7)	B(1) -B(3)	1.775(8)
B(1) -B(4)	1.797(7)	B(1) -B(4)	1.798(8)
B(1) -B(10)	1.777(7)	B(1) -B(10)	1.771(8)
B(1) -HB(1)	1.11(5)	B(1) -HB(1)	1.05(4)
B(2) -B(3)	1.781(7)	B(2) -B(3)	1.766(8)
B(2) -B(6)	1.777(7)	B(2) -B(6)	1.762(7)
B(2) -B(7)	1.812(7)	B(2) -B(7)	1.800(7)
B(2) -HB(2)	1.15(5)	B(2) -HB(2)	1.20(4)
B(3) -B(4)	1.762(7)	B(3) -B(4)	1.769(8)
B(3) -B(7)	1.762(8)	B(3) -B(7)	1.765(8)
B(3) -B(8)	1.733(8)	B(3) -B(8)	1.752(8)
B(3) -HB(3)	1.16(5)	B(3) -HB(3)	0.96(5)
B(4) -B(8)	1.785(8)	B(4) -B(8)	1.798(8)
B(4) -B(9)	1.683(8)	B(4) -B(9)	1.712(8)
B(4) -B(10)	1.792(7)	B(4) -B(10)	1.801(8)
B(4) -HB(4)	1.15(4)	B(4) -HB(4)	1.08(4)
B(6) -B(7)	1.827(7)	B(6) -B(7)	1.802(7)
B(6) -H(56)	1.44(5)	B(6) -H(56)	1.40(4)
B(7) -B(8)	1.938(8)	B(7) -B(8)	1.951(8)
B(7) -HB(7)	1.25(4)	B(7) -HB(7)	1.05(4)
B(7) -H(en)	0.94(5)	B(7) -H(en)	1.23(4)
B(8) -B(9)	1.794(8)	B(8) -B(9)	1.789(8)
B(8) -HB(8)	1.06(5)	B(8) -HB(8)	1.02(4)
B(8) -H(89)	1.25(5)	B(8) -H(89)	1.24(4)
B(9) -B(10)	1.797(8)	B(9) -B(10)	1.814(8)
B(9) -HB(9)	0.90(5)	B(9) -HB(9)	1.12(4)
B(9) -H(89)	1.27(5)	B(9) -H(89)	1.14(4)
B(9) -H(910)	1.28(5)	B(9) -H(910)	1.24(5)
B(10)-HB(10)	1.07(5)	B(10)-HB(10)	1.17(4)
B(10)-H(910)	1.31(5)	B(10)-H(910)	1.20(5)
B(6) - O	1.382(6)	B(6) - O	1.372(6)
O -CO(1)	1.435(6)	O -CO(1)	1.440(6)
CO(1)-CO(2)	1.486(8)	CO(1)-CO(2)	1.497(8)

Table A2.3. Comparison of Selected Interbond Angles(°) for Molecules A and B of **24**.

Molecule A		Molecule B	
B(1) -Ru(5)-B(2)	47.2(2)	B(1) -Ru(5)-B(2)	47.3(2)
B(1) -Ru(5)-B(10)	46.9(2)	B(1) -Ru(5)-B(10)	46.6(2)
B(2) -Ru(5)-B(6)	47.9(2)	B(2) -Ru(5)-B(6)	47.3(2)
Ru(5)-B(1) -B(2)	67.1(2)	Ru(5)-B(1) -B(2)	67.0(2)
Ru(5)-B(1) -B(10)	68.4(2)	Ru(5)-B(1) -B(10)	68.2(3)
B(2) -B(1) -B(3)	60.5(3)	B(2) -B(1) -B(3)	59.5(3)
B(3) -B(1) -B(4)	59.4(3)	B(3) -B(1) -B(4)	59.3(3)
B(4) -B(1) -B(10)	60.2(3)	B(4) -B(1) -B(10)	60.6(3)
Ru(5)-B(2) -B(1)	65.7(2)	Ru(5)-B(2) -B(1)	65.7(2)
Ru(5)-B(2) -B(6)	63.9(2)	Ru(5)-B(2) -B(6)	64.1(2)
B(1) -B(2) -B(3)	59.4(3)	B(1) -B(2) -B(3)	60.0(3)
B(3) -B(2) -B(7)	58.7(3)	B(3) -B(2) -B(7)	59.3(3)
B(6) -B(2) -B(7)	61.2(3)	B(6) -B(2) -B(7)	60.8(3)
B(1) -B(3) -B(2)	60.1(3)	B(1) -B(3) -B(2)	60.5(3)
B(1) -B(3) -B(4)	61.4(3)	B(1) -B(3) -B(4)	61.0(3)
B(2) -B(3) -B(7)	61.5(3)	B(2) -B(3) -B(7)	61.3(3)
B(4) -B(3) -B(8)	61.4(3)	B(4) -B(3) -B(8)	61.4(3)
B(7) -B(3) -B(8)	67.3(3)	B(7) -B(3) -B(8)	67.4(3)
B(1) -B(4) -B(3)	59.3(3)	B(1) -B(4) -B(3)	59.7(3)
B(1) -B(4) -B(10)	59.4(3)	B(1) -B(4) -B(10)	58.9(3)
B(3) -B(4) -B(8)	58.5(3)	B(3) -B(4) -B(8)	58.8(3)
B(8) -B(4) -B(9)	62.2(3)	B(8) -B(4) -B(9)	61.2(3)
B(9) -B(4) -B(10)	62.2(3)	B(9) -B(4) -B(10)	62.1(3)
Ru(5)-B(6) -B(2)	68.2(2)	Ru(5)-B(6) -B(2)	68.6(2)
B(2) -B(6) -B(7)	60.4(3)	B(2) -B(6) -B(7)	60.7(3)
B(2) -B(6) - O	132.6(4)	B(2) -B(6) - O	134.5(4)
B(2) -B(7) -B(3)	59.8(3)	B(2) -B(7) -B(3)	59.4(3)
B(2) -B(7) -B(6)	58.5(3)	B(2) -B(7) -B(6)	58.6(3)
B(3) -B(7) -B(8)	55.6(3)	B(3) -B(7) -B(8)	56.0(3)
B(3) -B(8) -B(4)	60.1(3)	B(3) -B(8) -B(4)	59.7(3)
B(3) -B(8) -B(7)	57.0(3)	B(3) -B(8) -B(7)	56.6(3)
B(4) -B(8) -B(9)	56.1(3)	B(4) -B(8) -B(9)	57.0(3)
B(4) -B(9) -B(8)	61.7(3)	B(4) -B(9) -B(8)	61.8(3)
B(4) -B(9) -B(10)	61.9(3)	B(4) -B(9) -B(10)	61.4(3)
Ru(5)-B(10)-B(1)	64.7(2)	Ru(5)-B(10)-B(1)	65.2(2)
B(1) -B(10)-B(4)	60.5(3)	B(1) -B(10)-B(4)	60.4(3)
B(4) -B(10)-B(9)	55.9(3)	B(4) -B(10)-B(9)	56.5(3)
B(6) - O -CO(1)	121.4(4)	B(6) - O -CO(1)	120.9(4)
O -CO(1)-CO(2)	109.4(4)	O -CO(1)-CO(2)	108.4(4)

Table A2.4a. Anisotropic Thermal Parameters (Å^2) for Molecule A of **24**.

	U11	U22	U33	U23	U13	U12
Ru(5)'	0.0299(1)	0.0262(1)	0.0296(2)	-0.0001(1)	-0.0024(1)	-0.0027(2)
B(1)	0.0427(27)	0.0319(23)	0.0402(27)	-0.0034(21)	-0.0107(23)	-0.0037(21)
B(6)	0.0411(26)	0.0385(24)	0.0364(25)	0.0000(21)	0.0033(21)	0.0007(20)
B(10)	0.0551(32)	0.0322(24)	0.0341(26)	-0.0026(21)	0.0018(24)	-0.0001(23)
B(4)	0.0522(32)	0.0294(23)	0.0431(27)	-0.0018(20)	-0.0088(24)	-0.0019(21)
B(8)	0.0598(34)	0.0379(27)	0.0353(26)	0.0054(22)	-0.0085(25)	-0.0021(26)
B(7)	0.0543(29)	0.0366(23)	0.0367(23)	0.0049(20)	0.0003(24)	-0.0033(25)
B(9)	0.0504(29)	0.0366(26)	0.0442(29)	0.0001(22)	0.0126(25)	0.0030(23)
B(2)	0.0359(24)	0.0318(23)	0.0400(27)	0.0051(20)	0.0017(21)	-0.0071(20)
B(3)	0.0500(29)	0.0305(24)	0.0498(30)	0.0063(23)	0.0082(25)	-0.0075(22)
C(1)	0.0419(25)	0.0326(21)	0.0511(26)	0.0014(20)	0.0043(22)	0.0083(19)
C(2)	0.0520(25)	0.0296(18)	0.0399(21)	-0.0054(17)	-0.0036(25)	-0.0048(22)
C(5)	0.0500(26)	0.0374(23)	0.0432(25)	0.0034(21)	-0.0150(22)	-0.0053(20)
C(3)	0.0382(24)	0.0263(19)	0.0455(24)	-0.0006(18)	-0.0010(21)	-0.0038(18)
C(4)	0.0538(27)	0.0292(19)	0.0307(20)	0.0063(16)	-0.0049(19)	0.0034(18)
C(6)	0.0359(23)	0.0377(22)	0.0576(29)	0.0061(21)	-0.0071(22)	0.0028(19)
C(7)	0.0575(30)	0.0421(24)	0.0673(33)	-0.0038(23)	0.0235(27)	0.0053(23)
C(8)	0.0675(30)	0.0457(25)	0.0295(22)	0.0007(19)	-0.0018(22)	-0.0069(24)
C(9)	0.0607(32)	0.0922(38)	0.0481(27)	-0.0079(27)	0.0155(28)	0.0002(34)
C(10)	0.0958(43)	0.0592(31)	0.0490(28)	0.0147(26)	-0.0012(30)	0.0014(32)
O	0.0635(18)	0.0414(16)	0.0289(14)	-0.0016(12)	-0.0039(14)	-0.0019(15)
CO(1)	0.1052(44)	0.0583(27)	0.0313(21)	0.0048(20)	0.0049(29)	-0.0060(35)
CO(2)	0.0732(36)	0.0812(35)	0.0491(27)	-0.0111(26)	0.0092(32)	0.0104(34)

Table A2.4b. Anisotropic Thermal Parameters (Å^2) for Molecule B of **24**.

	U11	U22	U33	U23	U13	U12
Ru(5)	0.0293(2)	0.0315(1)	0.0292(2)	0.0013(1)	-0.0033(1)	-0.0002(2)
B(6)	0.0430(27)	0.0412(24)	0.0285(21)	0.0024(19)	-0.0010(21)	-0.0004(21)
B(10)	0.0524(31)	0.0417(26)	0.0344(26)	0.0061(22)	-0.0038(24)	-0.0060(25)
B(1)	0.0381(27)	0.0378(25)	0.0483(30)	0.0076(23)	-0.0084(24)	0.0045(22)
B(2)	0.0465(28)	0.0318(23)	0.0422(28)	-0.0019(21)	0.0014(23)	0.0061(22)
B(7)	0.0565(30)	0.0387(23)	0.0375(25)	-0.0032(20)	0.0021(27)	-0.0044(27)
B(3)	0.0493(29)	0.0352(27)	0.0545(32)	0.0021(24)	-0.0022(26)	0.0097(24)
B(4)	0.0625(34)	0.0380(24)	0.0470(28)	0.0094(22)	-0.0107(30)	-0.0012(28)
B(9)	0.0586(33)	0.0478(31)	0.0502(32)	0.0100(26)	-0.0003(27)	-0.0161(28)
B(8)	0.0615(35)	0.0336(28)	0.0483(32)	0.0026(24)	-0.0071(28)	-0.0065(26)
C(1)	0.0475(26)	0.0379(23)	0.0517(28)	-0.0018(21)	0.0008(22)	-0.0120(21)
C(2)	0.0359(24)	0.0529(27)	0.0579(30)	-0.0120(24)	-0.0052(23)	-0.0133(22)
C(3)	0.0427(24)	0.0446(24)	0.0426(25)	-0.0059(21)	-0.0142(22)	-0.0039(20)
C(4)	0.0410(25)	0.0413(21)	0.0370(22)	-0.0051(18)	-0.0052(19)	-0.0005(19)
C(5)	0.0398(24)	0.0405(23)	0.0384(23)	-0.0058(19)	-0.0027(20)	0.0039(20)
C(6)	0.0529(26)	0.0330(19)	0.0424(22)	0.0011(17)	-0.0026(24)	-0.0018(22)
C(7)	0.0729(35)	0.0656(33)	0.0603(33)	0.0053(27)	0.0108(29)	-0.0303(29)
C(8)	0.0553(28)	0.0591(28)	0.0303(21)	-0.0050(21)	-0.0017(21)	0.0093(24)
C(9)	0.0816(38)	0.0666(31)	0.0408(25)	-0.0122(25)	-0.0030(26)	0.0052(29)
C(10)	0.0570(33)	0.1107(47)	0.0541(30)	0.0025(32)	0.0076(29)	-0.0039(35)
O	0.0554(18)	0.0460(16)	0.0350(15)	0.0060(13)	0.0037(14)	0.0021(15)
CO(1)	0.0771(34)	0.0677(30)	0.0366(22)	0.0107(22)	0.0115(26)	0.0099(35)
CO(2)	0.0770(40)	0.0890(39)	0.0479(28)	0.0314(28)	-0.0004(30)	-0.0037(35)

Table A2.5a. Positions of Refined and Calculated Hydrogen-atoms for Molecule A of **24**.

	x	y	z
HB(1)	0.013(4)	0.045(3)	-0.1421(25)
HB(10)	-0.216(4)	0.023(3)	-0.0843(25)
HB(4)	-0.148(4)	0.1679(24	-0.1314(22)
HB(8)	-0.243(4)	0.184(3)	-0.2779(24)
HB(7)	-0.126(4)	0.0852(22	-0.3816(22)
H(en)	-0.220(4)	0.039(3)	-0.3185(25)
HB(9)	-0.355(4)	0.120(3)	-0.1529(24)
HB(2)	0.050(4)	-0.0026(24	-0.2863(24)
HB(3)	0.000(5)	0.144(3)	-0.264(3)
H(56)	-0.243(4)	-0.054(3)	-0.2490(23)
H(910)	-0.306(4)	0.026(3)	-0.174(3)
H(89)	-0.312(4)	0.090(3)	-0.2469(25)
HC(2)	-0.163(4)	-0.2092(24	-0.2570(22)
HC(3)	-0.282(4)	-0.1934(23	-0.1607(22)
HC(5)	-0.013(4)	-0.0869(22	-0.0718(22)
HC(6)	0.116(4)	-0.1053(21	-0.1677(20)
HC(71)	0.143	-0.159	-0.282
HC(72)	0.015	-0.154	-0.334
HC(73)	0.061	-0.239	-0.230
HC(8)	-0.206	-0.079	-0.011
HC(91)	-0.382	-0.088	-0.078
HC(92)	-0.400	-0.123	0.009
HC(93)	-0.386	-0.184	-0.063
HC(101)	-0.237	-0.188	0.068
HC(102)	-0.096	-0.190	0.029
HC(103)	-0.209	-0.247	-0.004
HO(1)	-0.211	-0.024	-0.452
HO(2)	-0.059	-0.036	-0.433
HO(3)	-0.120	-0.112	-0.532
HO(4)	-0.228	-0.154	-0.478
HO(5)	-0.077	-0.167	-0.459

Table A2.5b. Positions of Refined and Calculated Hydrogen-Atoms for Molecule B of **24**.

	x	y	z
HB(10)	-0.204(4)	-0.5158(23	-0.4927(23)
HB(1)	0.027(4)	-0.5352(24	-0.5619(23)
HB(2)	0.060(4)	-0.4782(23	-0.7020(22)
HB(7)	-0.110(4)	-0.5721(23	-0.7845(22)
H(en)	-0.232(4)	-0.5201(24	-0.7369(22)
HB(3)	-0.014(4)	-0.6308(24	-0.6840(24)
HB(4)	-0.128(4)	-0.6524(22	-0.5455(21)
HB(9)	-0.372(4)	-0.6187(22	-0.5762(21)
HB(8)	-0.242(4)	-0.6671(25	-0.6937(21)
H(56)	-0.239(4)	-0.4363(23	-0.6650(21)
H(89)	-0.308(4)	-0.5966(25	-0.6537(24)
H(910)	-0.287(4)	-0.5217(24	-0.5848(24)
HC(2)	0.113(4)	-0.3816(22	-0.5845(21)
HC(3)	-0.002(4)	-0.3977(23	-0.4789(23)
HC(5)	-0.294(4)	-0.2962(23	-0.5706(22)
HC(6)	-0.183(4)	-0.2733(23	-0.6682(24)
HC(71)	-0.008	-0.269	-0.737
HC(72)	0.077	-0.350	-0.725
HC(73)	0.122	-0.266	-0.686
HC(8)	-0.191	-0.423	-0.426
HC(91)	-0.225	-0.328	-0.334
HC(92)	-0.200	-0.259	-0.399
HC(93)	-0.084	-0.320	-0.374
HC(101)	-0.376	-0.408	-0.490
HC(102)	-0.383	-0.315	-0.462
HC(103)	-0.391	-0.387	-0.399
HO(1)	-0.051	-0.442	-0.845
HO(2)	-0.200	-0.464	-0.863
HO(3)	-0.128	-0.366	-0.941
HO(4)	-0.092	-0.312	-0.866
HO(5)	-0.241	-0.334	-0.885

Figures A2.3 clearly shows the enantiomeric relationship of the two molecules. The orientation of the p-cymene moiety is the same in each case, with the single methyl group lying *cis* to the ethoxy group on B(6). Whilst there is some evidence for a stabilising hydrogen bonding interaction in Molecule A [HC(72)···O = 2.539(6)Å] this is not the case in Molecule B [no H···O distances < 3Å]. It seems more likely therefore that the preferred orientation arises as a result of either steric constraints, with the smaller single methyl rather than the bulkier *iso*-propyl group adjacent to the cage substituent, or of the different *trans* influences exerted on the p-cymene moiety by the borane cage. Tables A2.2 and A2.3 reveal that any significant differences in structure between the two molecules reside only in the exo-polyhedral ligands and that the $\{RuB_9\}$ units can therefore be treated together.

Similar cluster rearrangements to that seen here have been noted in other *nido*-6-metalladecaborane systems especially when subjected to nucleophilic attack. Greenwood, Kennedy and co-workers observed that treatment of 6-(C_6Me_6)-6-*nido*-RuB_9H_{13} with phosphines (PPh_3 or PMe_2Ph) gave rise to metalladecaboranes with the {areneRu} unit in the 5 position and terminal hydrogen substitution by phosphine in the 7 position.[1] A species closely related to **24**, 5-(C_6Me_6)-6-OMe-5-*nido*-RuB_9H_{12}, formed in the reaction of *closo*-$[B_{10}H_{10}]^{2-}$ with $[RuCl_2(C_6Me_6)]_2$ in methanol, has also been reported by the same group.[2] However, in this study the B(6)-B(7) connectivity was described as carrying a bridging hydrogen atom. Comparison of the position of the H(6,7) bridge in the methoxy derivative and the *endo*-hydrogen in **24** reveals them to be similarily disposed relative to their neighbouring boron atoms. Taking the average for the two independent molecules of **24**, H(en)-B(6)=1.50(6)Å and H(en)-B(5)=1.09(7)Å for this species. In the methoxy derivative, the equivalent distances, H(6,7)-B(6) and H(6,7)-B(5), are 1.53(3)Å and 1.13(3)Å respectively. This, in conjunction with the spectroscopic data on **24**, suggests that H(6,7) in the the methoxy derivative is also more correctly

described as an *endo*-hydrogen.

EHMO Studies.

The presence of the *endo*-hydrogen in the structure of **24** is unusual in that this feature is normally associated with low connected sites in the more open *arachno* stuctures (for example *arachno*-$[B_{10}H_{14}]^{2-}$ and *arachno*-$[B_9H_{14}]^-$). Because of this EHMO calculations were performed on a number of substituted boranes and metalladecaboranes to ascertain whether the *endo* hydrogen in **24** arises as a result of the influence of the metal and/or the ethoxy group at B(6).

The models employed for this study were constructed such that the bridging hydrogens near the site of substitution were placed symmetrically over the 5-6 and 6-7 connectivities. Inspection of the reduced overlap matrix (ROM) then gives an estimate of the strength of bonding between the hydrogen bridge and its neighbouring atoms and an indication towards which vertex any asymmetry should lie. Over a series of calculations, the extent of that asymmetry should also become apparent.

Five such symmetrisised models were set up. $B_{10}H_{14}$, 5-OH-$B_{10}H_{13}$ and 6-OH-$B_{10}H_{13}$ were derived from the experimental geometry of $B_{10}H_{14}$ itself with the H(5,6) and H(6,7) bridging hydrogens positioned using average bond distances from that structure. B-O bonds were placed along the vector of the substituted B-H bond (B-O = 1.38Å), and hydroxyl hydrogens were positioned such that the torsion angle with the boron atom oppposite on the open face of the cage [*ie.* B(9) or B(8)] was 180° (O-H = 1.04Å, B-O-H = 109.47°). The structures of two metallaboranes were also similarily adapted: 6-(C_5Me_5)-6-*nido*-CoB_9H_{13}[3] and 5-(p-cymene)-5-*nido*-RuB_9H_{13}, the latter derived from **24** by placing a terminal hydrogen atom along the B-O vector (B-H = 1.15Å). H(5,6) and H(6,7) were positioned using average bond distances, angles and torsions found in the

experimental geometries of the parent metallaboranes.

Table A2.6 gives the ROM data from these calculations. Firstly, for $B_{10}H_{14}$ a slightly higher value is obtained with B(5). This difference, although small, appears significant when the asymmetry observed in the structure of $B_{10}H_{14}$ is taken into account. This asymmetry arises because the higher connected B(5) atom carries a relatively lower positive charge than the three (cluster) connected B(6) atom and is therefore more attractive to the (protonic) bridging hydrogen. That this effect is enhanced when an ethoxy group is placed at B(6) can be rationalised in terms of the electronegative oxygen atom removing yet more electron density from B(6). The electronegativity of the oxygen atom is such that with the ethoxy group at B(5) the asymmetry seen in $B_{10}H_{14}$ is reversed.

Table A2.6 ROM Data for Substituted Boranes and Metallaboranes.

Model	Atom Pair:	B(6)-H(5,6)	B(5)-H(5,6)	B(6)-H(6,7)	B(7)-H(6,7)
$B_{10}H_{14}$		0.4250	0.4327		
5-OH-B10H13		0.4386	0.4197		
6-OH-$B_{10}H_{13}$		0.4120	0.4457		
6-(C_5H_5)-6-*nido*-Co-B_9H_{13}[a]		0.2586	0.3992		
5-(p-cymene)-5-*nido*-Ru-B_9H_{13}[b]		0.3601	0.2518	0.4091	0.4253

[a] Co AO Parameters used: H_{ii}'s(eV): -9.21(4s), -5.29(4p), -13.18(3d); $\zeta_{4s}=\zeta_{4p}=2.0$; $\zeta^1_{3d}=5.35$, $\zeta^2_{3d}=2.10$, $c_1=0.5680$, $c_2=0.6060$. [b] Ru AO parameters used; H_{ii}'s(eV): -10.4(5s), -6.87(5p), -14.90(5d); $\zeta_{5s}=2.08$, $\zeta_{4p}=2.04$, $\zeta^1_{4d}=5.38$, $\zeta^2_{4d}=2.3$; $c_1=0.5340$, $c_2=0.6365$

In the cobaltaborane the effect of the electropositive metal fragment is far greater than that of a {BH} group in the same site. However, this effect is still not enough to

cause the loss of bridging character, a fact confirmed by both crystallographic and spectroscopic studies on this species.[4] In the ruthenaborane the effect of the metal is again to push the protonic bridge towards the adjacent boron, although here the effect is reduced, due presumably to the low connectivity of B(6). In addition to this, however, an increase, relative to $B_{10}H_{14}$, in the asymmetry of the H(67) bridge is also seen. It appears therefore that the *endo* hydrogen observed in the structure of **24** arises as a result of both the terminal hydrogen substitution by the ethoxy group and the metallotropic shift of the {(p-cymene)Ru} fragment.

Comparison of Reactivities of 23 and Decaborane

The deboronation reaction of $B_{10}H_{14}$ finds no parallel in the chemistry of **23** under the conditions used here. One possible reason for this is in the distribution of charge around the open faces of each system. As mentioned in Chapter 1, the deboronation of $B_{10}H_{14}$ is thought to proceed *via* an initial deprotonation and then a nucleophilic attack by OH^- at the B(6) (or 9) position, the lowest connected and therefore most δ^+ sites. An EHMO calculation on $B_{10}H_{14}$ with experimental geometry confirms this, the net charge on B(6) and B(9) being +0.517, that on the other four facial borons +0.348. However, a similar calculation on 6-(C_5Me_5)-5-*nido*-CoB_9H_{13} shows much less variation in the charge distribution: the average charge on B(5) and B(7) is +0.682, on B(8) and B(10) +0.643 and on B(9) +0.677. Therefore, from charge considerations, the effect of the metal is to make its adjacent boron atoms at least as likely a site for an initial deprotonation and any subsequent nucleophilic attack as the other facial boron atoms. Indeed the uniform charge distribution may explain the low yield of **24** obtained in the reaction, with the number of available sites for nucleophilic attack leading to a number of products. A possible mechanism for the formation of **24**, based on the above assumption, can be advanced and is summarised in Figure A2.4.

Figure A2.4 Possible Mechanism of Formation of **24** from **23**.

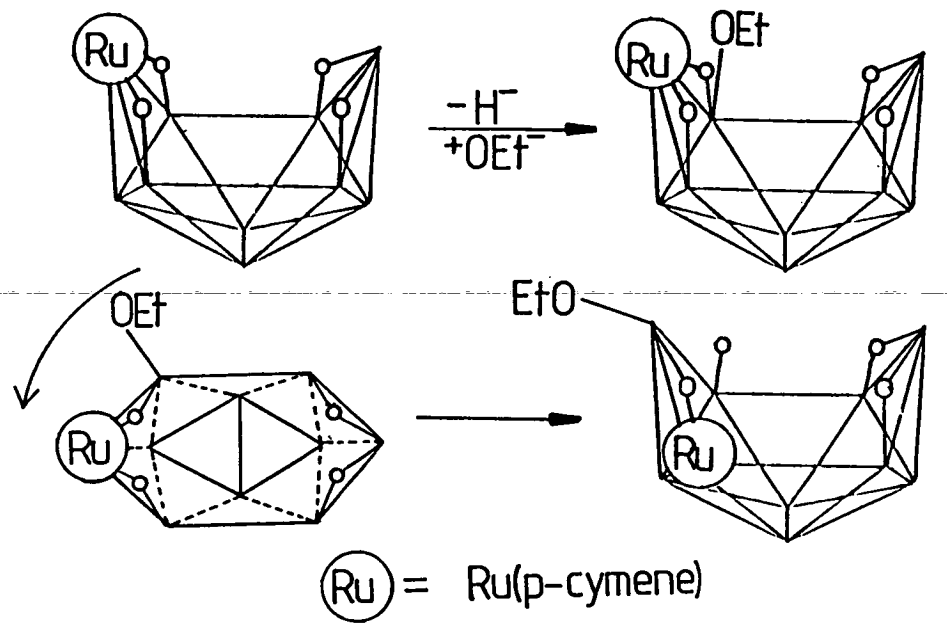

The first step involves deprotonation and nucleophilic attack at B(5), forming a substituted intermediate. The formation of the final product can then be envisaged by the rotation of the upper six facial borons relative to the four basal borons. A driving force for this process may be that, upon substitution, the ethoxy group removes electron density from B(5), making it relatively more positively charged, a situation more commonly associated with low connected sites.

Returning to the reaction giving the methoxy derivative described earlier, a possible intermediate may be a *nido*-6-metalladecaborane which then goes on to react with methanol in the fashion outlined above to give the final product.

Finally, in this case at least, whilst the isolobal analogy provides rationalisation of the structures of related boranes and metallaboranes, the extension of this principle to the reaction chemistry of structural analogues is not straightforward. Any prediction of the reactivity of a molecule requires a greater understanding of the electronic structure of the species concerned.

Experimental

General techniques and instruments used were as those described in Chapter 6. $[RuCl_2(C_{10}H_{14})]_2$ was synthesised from the literature preparation.[5]

6-(p-cymene)-6-*nido*-Ru-B_9H_{13}, **23**.

Synthesis

The synthesis of **23** followed a similar route to that detailed for the formation of the C_6Me_6 analogue.[2].

$[RuCl_2(C_{10}H_{14})]_2$ (0.448g, 1.46mmoles) was added as a solid to a solution of $[BTMA][B_9H_{14}]$ (1.564g, 5.99mmoles) in dichloromethane (20ml) and left to stir for 48 hours. After this time the solvent was removed *in vacuo*, the resultant brown solid redissolved in the minimum amount of dichloromethane and chromatographed on a fluorasil column (100-200 mesh, 12x1.5cm, dichloromethane as eluant). A mobile yellow band was collected , which, upon removal of solvent *in vacuo*, afforded **23** (0.343g, 0.99mmoles, 68% yield).

Characterisation

$^{11}B-\{^1H\}$ n.m.r.($CDCl_3$)/p.p.m.: 21.53 (2B), 15.67(2B), 6.37(1B), 0.21(2B), -18.53(1B) and -28.28(1B).

Microanalysis. Calculated for $C_{10}H_{27}B_9Ru$: %C 34.7, %H 7.82;
Found %C 34.2, %N 7.72.

5-(p-cymene)-6-OEt-5-*nido*-RuB_9H_{12}, 24

Synthesis

23 (0.102g, 0.26mmoles) was added as a solid to a solution of NaOH (0.011g, 0.28mmoles) in ethanol (10ml). After 2 hours a loss of intensity in the colour of the solution was noted and the solvent was removed *in vacuo*. The resultant brown solid was dissolved in the minimum amount of dichloromethane and eluted on a fluorasil column (100-200 mesh, 8x1.5cm, dichloromethane as eluant). A mobile yellow band was collected which, upon removal of the solvent *in vacuo* gave **24** in high purity (0.034g, 0.09mmoles, 34%). Crystals of this species were grown by slow diffusion of n-hexane into a concentrated dichloromethane solution.

Characterisation

^{11}B-{^1H} n.m.r. ($CDCl_3$)/p.p.m.: 44.76(1B), 15.23(1B), 10.13(1B), -0.37(1B), -4.45(2B), -15.45(1B), -17.45(1B) and -42.93(1B).

Single crystal X-ray analysis

Crystal Data

$C_{12}H_{31}B_9ORu$, M=389.3, orthorhombic, space group $P2_12_12_1$, a=11.310(3), b=18.146(11), g=18.926(4)Å, V=3884(3)Å^3 by least-squares refinement of 25 centred reflections ($14<\theta<15^o$), Z=8, two independent molecules per asymmetric fraction , D_x=1.331gcm^{-3}, μ=0.764mm^{-1}, F(000)=1568.

Data collection and processing

Data collected in ω-2θ scans in 96 steps with ω scan width 0.8+0.34tanθ^{o} at 291(1)K. Variable scan speeds between 0.92 and 2.35°min^{-1}. 3854 independent reflections measured ($1 \leq \theta \leq 25^{o}$, h: 0 to 13, k: 0 to 21, l: 0 to 22) of which 3578 with $F > 2.0\sigma(F)$ retained.

Structure Solution

Ru atom position from inspection of the Patterson map, all other non-hydrogen atoms and cage and phenyl hydrogens from iterative application of full-matrix least-squares refinement/ΔF syntheses. Upon isotropic convergence, absolute configuration was established by parallel refinement of both enantiomers. Empirical absorption correction applied. Methyl and methine hydrogens set in idealised positions (C-H=1.08Å). Refinement proceeded in two blocks, corresponding to the two molecules present (molecules A and B). Cage, phenyl and alkyl hydrogens assigned refined, group isotropic thermal parameters [$U_{cage\text{-}H(A)}$=0.055(4), $U_{cage\text{-}H(B)}$=0.045(4), $U_{phenyl\text{-}H(A)}$=0.038(6), $U_{phenyl\text{-}H(B)}$=0.044(6), $U_{alkyl\text{-}H(A)}$=0.095(5) and $U_{alkyl\text{-}H(B)}$=0.116(6)Å^2 at convergence]. Weighting scheme of the form $w^{-1}=\sigma^2(F)+0.000660F^2$ applied. R=0.0254, R_w=0.0321, S=0.940, min. and max. residues in final ΔF synthesis -0.20 and 0.18eÅ^{-3} respectively.

References

1. M. Bown, X.L.R. Fontaine, N.N. Greenwood and J.D. Kennedy, *J. Organomet. Chem.*,

1988, **325**, 233.

2. M. Bown, N.N. Greenwood and J.D. Kennedy, *J.Chem. Soc., Dalton Trans.*,

1988, 925.

3. T.L. Venable and R.L. Grimes, *Inorg. Chem.*, 1982, **21**, 887.

4. T.L. Venable, E. Sinn and R.L. Grimes, *Inorg. Chem.*, 1982, **21**, 895.

5. M.A. Bennett, T.N. Huang, T.W. Matheson and A.K. Smith, *Inorg. Chem.*,

1982, **21**, 75.

Appendix 3: Lectures, Courses and Meetings Attended

Recent Advances in Inorganic Chemistry.

Drs. A.J. Welch, L.J. Yellowlees, S.K. Chapman and M. Schröder

Electroanalytical Methods.

Dr. H.H. Girault

EPR Spectroscopy.

Dr R.E.P. Winnpenny

Departmental Research Seminars and Colloquia

Inorganic Section Meetings

Intraboron IX, X and XI, Annual Meetings of United Kingdom Boron Chemists, 1989, 1990, 1991.

University of Strathclyde Inorganic Club (USIC) Meetings, 1989, 1990.

Imeboron VII, International Meeting on Boron Chemistry, Torun, Poland, 1990

Butler Postgraduate Electrochemistry Meetings, 1989, 1990.

B.C.A. Residential Crystallography School, Aston, Birmingham, April, 1989.

Appendix 4: Published Work

Certain of the results presented in this thesis have published, The references for these papers are:

S.A. Macgregor, L.J. Yellowlees and A.J. Welch, *Acta Crystallogr.*, 1990, **C46**, 551.

S.A. Macgregor, L.J. Yellowlees and A.J. Welch, *Acta Crystallogr.*, **C46**, 1399.

S.A. Macgregor, J.A. Scanlon, L.J. Yellowlees and A.J. Welch, *Acta Crystallogr.*, 1991, **C47**, 513.

S.A. Macgregor, L.J. Yellowlees and A.J. Welch, *Acta Crystallogr.*, 1991, **C47**, 536

A reprint of each paper is included.

In addition, the following papaers have been accepted for publication:

When is a Vertex not a Vertex? An Analysis of the Structures of $MB_{10}H_{12}$ Metallaboranes. S.A. Macgregor, A.J. Wynd, N. Moulden, R.O. Gould, P. Taylor, L.J. Yellowlees and A.J. Welch, *J. Chem Soc., Dalton Trans.*, in press.

5-(p-cymene)-6-OEt-5-ruthenadecaborane(12), S.A. Macgregor, L.J. Yellowlees and A.J. Welch, *Acta Crystallogr.*, Section C, in press.

Acta Cryst. (1990). C46, 551–554

Structure of Benzyltrimethylammonium 7,7,7-Tricarbonyldodecahydro-7-cobalta-*nido*-undecaborate(1 −)

BY STUART A. MACGREGOR, LESLEY J. YELLOWLEES AND ALAN J. WELCH

Department of Chemistry, University of Edinburgh, Edinburgh EH9 3JJ, Scotland

(*Received* 12 *June* 1989; *accepted* 10 *July* 1989)

Abstract. $[PhCH_2NMe_3][7,7,7\text{-}(CO)_3\text{-}7\text{-}CoB_{10}H_{12}]$, $C_{10}H_{16}N^+.B_{10}C_3CoH_{12}O_3^-$, $M_r = 413{\cdot}39$, monoclinic, $P2_1/c$, $a = 10{\cdot}634\ (5)$, $b = 14{\cdot}118\ (5)$, $c = 14{\cdot}168\ (4)$ Å, $\beta = 91{\cdot}81\ (3)°$, $V = 2126{\cdot}0$ Å^3, $Z = 4$, $D_x = 1{\cdot}291$ Mg m^{-3}, Mo $K\alpha$, $\lambda = 0{\cdot}71069$ Å, $\mu = 0{\cdot}82$ mm^{-1}, $F(000) = 856$, $T = 185\ (1)$ K, $R = 0{\cdot}0985$ for 1967 independent observed reflections. The anion has effective C_s molecular symmetry, with one carbonyl ligand lying *endo* to the open face of the cage. R.m.s. misfit calculations suggest that the $B_{10}H_{12}$ moiety is better described as the *arachno* fragment $\{B_{10}H_{12}\}^{4-}$, and hence that the formal metal oxidation state is +3, the overall geometry of the cobaltaborane approximating to that of the *nido* fragment of an icosahedron.

0108-2701/90/040551-04$03.00

Introduction.

At their simplest level metallaboranes and metallahetereoboranes can be viewed in two ways, either as complexes between a metal and a (hetero)borane ligand, or as heteroboranes in which the metal atom occupies a polyhedral vertex. In many cases these two views are entirely complementary and semantical.

Recent studies (Wynd, Welch & Parish, 1989; Wynd, 1988) from this laboratory, however, suggest that in some systems a distinction can be made

Table 1. *Coordinates and equivalent isotropic displacement parameters of refined atoms with e.s.d.'s in parentheses*

	x	y	z	U_{eq}*(Å^2)
Co(7)	0·24060 (16)	0·09793 (13)	0·02488 (11)	0·0272 (8)
C(A)	0·1186 (12)	0·0919 (10)	0·1115 (8)	0·035 (7)
O(A)	0·0437 (9)	0·0923 (8)	0·1666 (7)	0·052 (6)
C(B)	0·2480 (13)	−0·0270 (11)	0·0047 (10)	0·046 (9)
O(B)	0·2585 (12)	−0·1056 (7)	−0·0096 (8)	0·067 (8)
C(C)	0·3785 (12)	0·1193 (7)	0·0940 (7)	0·025 (6)
O(C)	0·4700 (9)	0·1334 (8)	0·1393 (7)	0·054 (7)
B(1)	0·1382 (13)	0·2187 (12)	−0·1682 (10)	0·032 (8)
B(2)	0·1912 (12)	0·1041 (11)	−0·1239 (9)	0·030 (7)
B(3)	0·1065 (15)	0·1871 (12)	−0·0546 (11)	0·038 (9)
B(4)	0·1554 (13)	0·3037 (11)	−0·0803 (10)	0·031 (8)
B(5)	0·2699 (14)	0·2938 (10)	−0·1690 (9)	0·029 (8)
B(6)	0·2903 (14)	0·1716 (12)	−0·1970 (9)	0·033 (8)
B(8)	0·2139 (14)	0·2538 (10)	0·0256 (10)	0·031 (8)
B(9)	0·3189 (13)	0·3225 (10)	−0·0528 (10)	0·028 (8)
B(10)	0·4066 (15)	0·2341 (11)	−0·1304 (10)	0·034 (8)
B(11)	0·3587 (13)	0·1120 (10)	−0·1022 (9)	0·029 (7)
C(2)	0·6362	0·3520	0·0755	0·033 (3)
C(3)	0·6220	0·3772	0·1697	0·041 (3)
C(4)	0·7269	0·4028	0·2255	0·044 (3)
C(5)	0·8461	0·4033	0·1871	0·040 (3)
C(6)	0·8603	0·3781	0·0928	0·034 (3)
C(1)	0·7554	0·3524	0·0370	0·027 (3)
C(7)	0·7716 (11)	0·3232 (9)	−0·0646 (8)	0·027 (3)
N(1)	0·7568 (8)	0·4026 (7)	−0·1370 (6)	0·026 (5)
C(8)	0·7726 (14)	0·3593 (11)	−0·2326 (9)	0·045 (9)
C(9)	0·8522 (12)	0·4808 (8)	−0·1203 (10)	0·039 (8)
C(10)	0·6257 (11)	0·4476 (9)	−0·1355 (9)	0·034 (7)

*$U_{eq} = (1/3)\Sigma_i\Sigma_j U_{ij} a_i^* a_j^* \mathbf{a}_i.\mathbf{a}_j$.

Table 2. *Internuclear distances (Å) and selected interbond angles (°) with e.s.d.'s in parentheses*

Co(7)—C(A)	1·816 (13)	B(4)—B(8)	1·754 (21)
Co(7)—C(B)	1·788 (15)	B(4)—B(9)	1·789 (20)
Co(7)—C(C)	1·763 (11)	B(5)—B(6)	1·785 (21)
Co(7)—B(2)	2·158 (14)	B(5)—B(9)	1·758 (20)
Co(7)—B(3)	2·187 (16)	B(5)—B(10)	1·753 (21)
Co(7)—B(8)	2·219 (15)	B(6)—B(10)	1·768 (21)
Co(7)—B(11)	2·237 (14)	B(6)—B(11)	1·726 (20)
C(A)—O(A)	1·133 (16)	B(8)—B(9)	1·871 (20)
C(B)—O(B)	1·135 (19)	B(9)—B(10)	1·924 (21)
C(C)—O(C)	1·165 (15)	B(10)—B(11)	1·845 (21)
B(1)—B(2)	1·818 (20)		
B(1)—B(3)	1·714 (22)		
B(1)—B(4)	1·735 (21)		
B(1)—B(5)	1·756 (21)		
B(1)—B(6)	1·807 (21)		
B(2)—B(3)	1·790 (21)		
B(2)—B(6)	1·778 (20)	C(1)—C(7)	1·512 (14)
B(2)—B(11)	1·801 (20)	C(7)—N(1)	1·525 (15)
B(3)—B(4)	1·768 (22)	N(1)—C(8)	1·500 (17)
B(3)—B(8)	1·844 (21)	N(1)—C(9)	1·513 (16)
B(4)—B(5)	1·783 (20)	N(1)—C(10)	1·533 (16)

C(A)—Co(7)—C(B)	95·6 (6)	B(1)—B(5)—B(6)	61·4 (8)
C(A)—Co(7)—C(C)	103·4 (6)	B(4)—B(5)—B(9)	60·7 (8)
C(B)—Co(7)—C(C)	102·6 (6)	B(6)—B(5)—B(10)	60·0 (8)
B(2)—Co(7)—B(3)	48·7 (6)	B(9)—B(5)—B(10)	60·5 (8)
B(2)—Co(7)—B(11)	48·3 (5)	B(1)—B(6)—B(2)	61·0 (8)
B(3)—Co(7)—B(8)	49·5 (6)	B(1)—B(6)—B(5)	58·5 (8)
Co(7)—C(A)—O(A)	176·8 (12)	B(2)—B(6)—B(11)	61·8 (8)
Co(7)—C(B)—O(B)	176·6 (13)	B(5)—B(6)—B(10)	59·1 (8)
Co(7)—C(C)—O(C)	179·6 (10)	B(10)—B(6)—B(11)	63·7 (9)
B(2)—B(1)—B(3)	60·8 (8)	Co(7)—B(8)—B(3)	64·4 (7)
B(2)—B(1)—B(6)	58·7 (8)	B(3)—B(8)—B(4)	58·8 (8)
B(3)—B(1)—B(4)	61·7 (9)	B(4)—B(8)—B(9)	59·0 (8)
B(4)—B(1)—B(5)	61·4 (8)	B(4)—B(9)—B(5)	60·3 (8)
B(5)—B(1)—B(6)	61·1 (8)	B(4)—B(9)—B(8)	57·2 (8)
Co(7)—B(2)—B(3)	66·5 (7)	B(5)—B(9)—B(10)	56·7 (8)
Co(7)—B(2)—B(11)	68·1 (6)	B(5)—B(10)—B(6)	60·9 (8)
B(1)—B(2)—B(3)	56·7 (8)	B(5)—B(10)—B(9)	56·9 (8)
B(1)—B(2)—B(6)	60·3 (8)	B(6)—B(10)—B(11)	57·0 (8)
B(6)—B(2)—B(11)	57·7 (8)	Co(7)—B(11)—B(2)	63·5 (6)
Co(7)—B(3)—B(2)	64·8 (7)	B(2)—B(11)—B(6)	60·5 (8)
Co(7)—B(3)—B(8)	66·2 (7)	B(6)—B(11)—B(10)	59·2 (8)
B(1)—B(3)—B(2)	62·5 (9)	C(2)—C(1)—C(7)	120·2 (7)
B(1)—B(3)—B(4)	59·8 (9)	C(6)—C(1)—C(7)	119·8 (7)
B(4)—B(3)—B(8)	58·1 (8)	C(1)—C(7)—N(1)	115·3 (9)
B(1)—B(4)—B(3)	58·6 (8)	C(7)—N(1)—C(8)	107·2 (9)
B(1)—B(4)—B(5)	59·9 (8)	C(7)—N(1)—C(9)	112·1 (9)
B(3)—B(4)—B(8)	63·1 (9)	C(7)—N(1)—C(10)	111·7 (9)
B(5)—B(4)—B(9)	59·0 (8)	C(8)—N(1)—C(9)	110·3 (9)
B(8)—B(4)—B(9)	63·8 (8)	C(8)—N(1)—C(10)	108·1 (9)
B(1)—B(5)—B(4)	58·7 (8)	C(9)—N(1)—C(10)	107·5 (9)

between the formalisms of metal–ligand complex and heteroborane, in that all metallaboranes and metallaheteroboranes are metal–ligand complexes, but not all are *properly* described as heteroboranes. The distinction relies on assessment of the 'verticity' of the metal atom – the extent to which it acts as a true cluster vertex and not simply a bridge between several B atoms. Analysis of structural data on MB$_{10}$H$_{12}$ metallaboranes reveals subtle trends in verticity that, *inter alia*, appear to be a function of the position of M in the Periodic Table (Wynd, Macgregor, Yellowlees & Welch, 1990).

Unfortunately, limited data are available for cases where M is a 'typical' transition metal, in spite of the fact that many such species are known (Kennedy, 1986). The only representative compound to have been crystallographically characterized is [7-(CO)-1,7,7-(PPh$_3$)$_3$-7-IrB$_{10}$H$_{11}$] (Crook, 1982), a derivative of the MB$_{10}$H$_{12}$ cluster type, which awaits full publication. Therefore, to understand fully the emerging patterns in verticity amongst MB$_{10}$H$_{12}$ metallaboranes, we have resynthesized [7,7,7-(CO)$_3$-7-CoB$_{10}$H$_{12}$]$^-$ (Klanberg, Wegner, Parshall & Muetterties, 1968), using cobalt, a 'typical' transition metal, for the purpose of the crystallographic study reported herein. Suitable crystals were afforded as the [PhCH$_2$NMe$_3$]$^+$ salt.

Experimental. Compound prepared as [NMe$_4$]$^+$ salt, converted to Na$^+$ salt by ion exchange chromatography, and precipitated from aqueous solution as [PhCH$_2$NMe$_3$]$^+$ salt by addition of an aqueous solution of benzyltrimethylammonium bromide; purity checked by IR spectroscopy (CH_2Cl_2 solution, ν_{B-H} 2505, $\nu_{C\equiv O}$ 2065, 2020, and 2000 cm^{-1}) and microanalysis (found: C, 37·7; H, 6·92; N, 3·48%. $C_{13}H_{28}B_{10}CoNO_3$ requires: C, 37·8; H, 6·83; N, 3·39%); small yellow plates grown by slow cooling of a CH_2Cl_2 solution containing hexane; crystal, 0·5 × 0·27 × 0·05 mm, mounted on an Enraf–Nonius CAD-4 diffractometer (Mo $K\alpha$ X-radiation, graphite monochromator, ULT-1 low-temperature attachment); cell parameters and orientation matrix from least-squares refinement of the setting angles ($7 < \theta < 13°$) of 25 centred reflections; data collection by ω–2θ scans in 96 steps with ω scan width ($0·8 + 0·34\tan\theta$)°; data (h: 0 to 12, k: 0 to 16, l: −16 to 16) measured for $1 \le \theta \le 25°$ over 110 X-ray hours; corrections for Lorentz and polarization effects applied (Gould & Smith, 1986); 4128 independent reflections measured, of which 2199 [$F \ge 2·0\sigma(F)$]

retained; structure solution *via* Patterson synthesis (Co) and iterative full-matrix least-squares refinement (on $F/\Delta F$ syntheses (C, O, B, N) (Sheldrick, 1976); analysis of variance revealed anomalously poor agreement for *hk*0 reflections, and analysis of the intensities of two check reflections as functions of time suggested fluctuations in beam power during the period over which these data were measured. Consequently all *hk*0 reflections omitted from data set; empirical absorption correction (Walker & Stuart, 1983) applied to remaining 1967 reflections (correction factors 0·782–1·141); all non-H atoms except benzyl C atoms refined with anisotropic thermal parameters; phenyl C atoms treated as regular planar hexagon (C—C = 1·395 Å); cage H and benzyl H atoms set in idealized positions, the former assigned an (invariant) isotropic thermal parameter ($U_{cage\text{-}H}$ = 0·08 Å^2), and the latter a (refined) group thermal parameter [$U_{benzyl\text{-}H}$ = 0·062 (17) Å^2 at convergence]; methyl H atoms not included in calculations; unit weights assigned throughout; 207 variables, data:variable ratio > 9·5:1; max. shift/e.s.d. in final cycle < 0·02; R = 0·0985, attributed to size and quality of crystal; max. and min. residues in final difference Fourier synthesis 0·76 and −0·69 e Å^{-3} respectively; scattering factors for C, H, B, N and O inlaid in *SHELX*76. Those for Co from *International Tables for X-ray Crystallography* (1974); Fig. 1 drawn using *EASYORTEP* (Mallinson & Muir, 1985); molecular geometry calculations *via CALC* (Gould & Taylor, 1986).

Discussion. The anion has effective, non-crystallographically imposed, C_s molecular symmetry about the plane containing Co(7), B(5), and B(1). Table 1* lists the coordinates of refined atoms and equivalent isotropic thermal parameters, whilst Table 2 collates internuclear distances and selected interbond angles determined. A perspective view of the anion is presented in Fig. 1.

A recent study of $[Cy_3PAu(B_{10}H_{12})]^-$ (Cy = cyclo-C_6H_{11}) (Wynd, Welch & Parish, 1989) and analysis of the structures of several $MB_{10}H_{12}$ congeners already in the literature (Wynd, 1988; Wynd, Macgregor, Yellowlees & Welch, 1990) have shown that the $\{B_{10}\}$ portions of a number of these species are geometrically more similar to the $\{B_{10}\}$ fragment of $B_{10}H_{14}$ (Brill, Dietrich & Dierks, 1971) than to the corresponding $\{B_{10}\}$ fragment of $[B_{11}H_{13}]^{2-}$ (Fritchie, 1967), *i.e.* that the $\{B_{10}\}$ unit is better described as $\{B_{10}H_{12}\}^{2-}$, a *nido* fragment of an octadecahedron, than $\{B_{10}H_{12}\}^{4-}$, an *arachno* fragment of an icosahedron.

This analysis has been based on the results of 'r.m.s. misfit' calculations (Gould & Taylor, 1986). Application of the same analysis to the $\{B_{10}\}$ fragment of the present compound affords r.m.s. misfit values of 0·147 Å *versus* $B_{10}H_{14}$ and 0·070 Å *versus* $[B_{11}H_{13}]^{2-}$, on the basis of which the $\{B_{10}H_{12}\}$ unit in this species appears to be formally present as $\{B_{10}H_{12}\}^{4-}$, *i.e.* $[(CO)_3CoB_{10}H_{12}]^-$ appears to be better described as a true *nido*-icosahedral species, in which the metal atom is formally in the +3 oxidation state. Current studies are directed towards independent measurement of the oxidation state of Co in the compound. The 'verticity' of the metal atom (Wynd, 1988; Wynd, Macgregor, Yellowlees & Welch, 1990) is calculated to be 69·1%. We are currently assessing the utility of a number of structural parameters for polyhedral classification, and for the present compound these include: B(2)—B(3) 1·790 (21); B(9)—B(10) 1·924 (21); B(8)···B(11) 3·136 (20) Å; and displacement of the Co atom from the least-squares plane through the B(8)B(9)B(10)-B(11) sequence 0·321 (15) Å.

The $Co(CO)_3$ unit is orientated such that it conforms to the effective mirror plane through the cage, and the C(C)O(C) carbonyl ligand is *endo* to the open polyhedral face. C—Co—C angles are not equal. Those involving C(C) average 103·0 (8)°, whilst C(A)—Co—C(B) is 95·6 (6)°. Moreover, the Co—C(C) bond is the shortest of its type and the C(C)—O(C) bond the longest of its type, but unfortunately the general lack of high precision in the model is such that the differences involved are

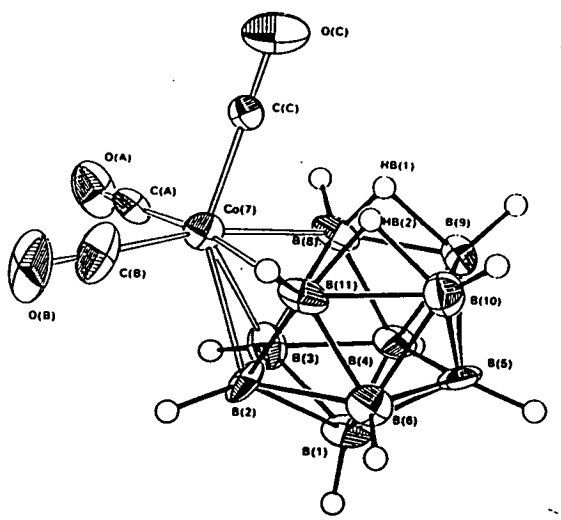

Fig. 1. Perspective view of [7,7,7-(CO)$_3$-7-$CoB_{10}H_{12}$]$^-$ (50% thermal ellipsoids, except for the H atoms which have an artificial radius of 0·1 Å for clarity).

* Lists of structure factors, anisotropic thermal parameters and H-atom parameters have been deposited with the British Library Document Supply Centre as Supplementary Publication No. SUP 52406 (17 pp.). Copies may be obtained through The Technical Editor, International Union of Crystallography, 5 Abbey Square, Chester CH1 2HU, England.

not strictly statistically significant. Nevertheless, taken together these results are not inconsistent with the conclusion that there is more π back bonding from Co to C(C)O(C) than to the other carbonyl ligands. This point is one of several that we are currently addressing through extended Hückel molecular orbital calculations on $[(CO)_3CoB_{10}H_{12}]^-$ and related species.

Distances and angles within the $[PhCH_2NMe_3]^+$ cation are unexceptional and fully consistent with those determined in recent studies in this department (Mitchell & Welch, 1987; Wynd & Welch, 1989).

We thank the SERC for support (SAM) and the Callery Chemical Company for a generous gift of $B_{10}H_{14}$.

References

Brill, R., Dietrich, H. & Dierks, H. (1971). *Acta Cryst.* B27, 2003–2018.

Crook, J. E. (1982). PhD thesis. Univ. of Leeds, England.

Fritchie, C. J. (1967). *Inorg. Chem.* 6, 1199–1203.

Gould, R. O. & Smith, D. E. (1986). *CADABS*. A program for data reduction. Univ. of Edinburgh, Scotland.

Gould, R. O. & Taylor, P. (1986). *CALC*. A program for molecular geometry calculations. Univ. of Edinburgh, Scotland.

International Tables for X-ray Crystallography (1974). Vol. IV. Birmingham: Kynoch Press. (Present distributor Kluwer Academic Publishers, Dordrecht.)

Kennedy, J. D. (1986). *Prog. Inorg. Chem.* 34, 211–434.

Klanberg, F., Wegner, P. A., Parshall, G. W. & Muetterties, E. L. (1968). *Inorg. Chem.* 7, 2072–2077.

Mallinson, P. & Muir, K. W. (1985). *J. Appl. Cryst.* 18, 51–53.

Mitchell, G. F. & Welch, A. J. (1987). *J. Chem. Soc. Dalton Trans.* pp. 1017–1025.

Sheldrick, G. M. (1976). *SHELX76*. Program for crystal structure determination and refinement. Univ. of Cambridge, England.

Walker, N. G. & Stuart, D. (1983). *Acta Cryst.* A39, 158–166.

Wynd, A. J. (1988). PhD thesis. Univ. of Edinburgh, Scotland.

Wynd, A. J., Macgregor, S. A., Yellowlees, L. J. & Welch, A. J. (1990). Work in progress.

Wynd, A. J. & Welch, A. J. (1989). *Acta Cryst.* C45, 615–617.

Wynd, A. J., Welch, A. J. & Parish, R. V. (1989). *J. Chem. Soc. Dalton Trans.* Submitted.

Acta Cryst. (1990). C46, 1399–1402

Structure of $[PhCH_2NMe_3]_2[(B_{10}H_{12})_2Pt]$

BY STUART A. MACGREGOR, LESLEY J. YELLOWLEES AND ALAN J. WELCH

Department of Chemistry, University of Edinburgh, Edinburgh EH9 3JJ, Scotland

(*Received* 7 *August* 1989; *accepted* 10 *November* 1989)

Abstract. $[PhCH_2NMe_3]_2^{2+}.[Pt(B_{10}H_{12})_2]^{2-}$, M_r = 735·97, triclinic, $P\bar{1}$, a = 9·023 (3), b = 10·440 (4), c = 11·172 (3) Å, α = 111·55 (3), β = 108·794 (24), γ = 101·29 (3)°, V = 865·7 Å^3, Z = 1, D_x = 1·411 Mg m^{-3}, Mo $K\alpha$, λ = 0·71069 Å, μ = 4·111 mm^{-1}, $F(000)$ = 368, T = 185 (1) K, R = 0·0166 for 3039 independent observed reflections. The anion resides on a crystallographic inversion centre, and is slightly, but significantly, distorted from C_{2h} point symmetry as a result of crystal packing. Molecular-geometry calculations suggest that the $\{B_{10}H_{12}\}$ ligand does not fit particularly well with either a *nido*-$\{B_{10}H_{12}\}^{2-}$ or an *arachno*-$\{B_{10}H_{12}\}^{4-}$ formalism.

Introduction. The precise structures of metallaboranes of the general family $MB_{10}H_{12}$ are of current interest because the $\{B_{10}H_{12}\}$ ligand could formally be present in such species as either the *nido* fragment $\{B_{10}H_{12}\}^{2-}$ or the *arachno* fragment $\{B_{10}H_{12}\}^{4-}$. The structural differences between these are subtle (the pattern of connectivities is exactly the same), and only recently have they really been successfully delineated *via* application of the 'root-mean-square misfit' technique (Wynd, 1988; Wynd, Welch & Parish, 1990; Macgregor, Yellowlees & Welch, 1990).

It is important to attempt to distinguish between the formalisms of $\{B_{10}H_{12}\}^{2-}$ and $\{B_{10}H_{12}\}^{4-}$ ligands in $MB_{10}H_{12}$ metallaboranes for two reasons. Firstly, it allows access to the formal oxidation state of the metal in the complex, something that is very rarely probed. Cases where independent measurement of the metal oxidation state is possible are welcome, since these afford a check on the validity of the approach to distinction of the two formalisms. Secondly, it allows assessment of the 'verticity' of the metal atom, *i.e.* (the rough measure of) the extent to which it is truly involved in cluster skeletal bonding, as opposed to acting as a simple bridge between several B atoms.

The dianion $[(B_{10}H_{12})_2Pt]^{2-}$ has been known for many years (Klanberg, Wegner, Parshall & Muetterties, 1968). Although it is well accepted that its gross structure is the same as that of the crystallographically characterized anions $[(B_{10}H_{12})_2Ni]^{2-}$ (Guggenberger, 1972) and $[(B_{10}H_{12})_2Au]^-$ (Wynd & Welch, 1987), molecular parameters are not known, and so the precise form of the $\{B_{10}H_{12}\}$ ligand in this species cannot be assessed. To remedy this we have resynthesized $[(B_{10}H_{12})_2Pt]^{2-}$ for the purposes of the accurate structural study described herein. Suitable crystals were afforded as the $[PhCH_2NMe_3]^+$ salt.

Experimental. The salt $[PhCH_2NMe_3]_2[(B_{10}H_{12})_2Pt]$ was prepared in an analogous manner to that which previously afforded the $[NMe_4]$ salt (Klanberg, Wegner, Parshall & Muetterties, 1968), and its purity confirmed by microanalysis (found: C, 32·3; H, 7·49; N, 3·83%. $C_{20}H_{56}B_{20}N_2Pt$ requires: C, 32·7; H, 7·62; N, 3·81%); golden-yellow blocks grown by slow diffusion of diethyl ether into an acetonitrile solution at 243 K; slightly irregular crystal, *ca* 0·3 × 0·25 × 0·15 mm, mounted in glass capillary and slowly cooled to 185 (1) K on an Enraf–Nonius CAD-4

0108-2701/90/081399-04$03.00

diffractometer (Mo $K\alpha$ radiation, graphite monochromator, ULT-1 attachment); orientation matrix and cell parameters from least-squares refinement of the setting angles ($13 < \theta < 15°$) of 25 centred reflections; data collection by ω–2θ scans in 96 steps with ω-scan width $(0{\cdot}8 + 0{\cdot}34\tan\theta)°$; nearly one full sphere of data (h: 0 to 10, k: −12 to 12, l: −13 to 13; h: −10 to 0, k: −12 to 12, l: −13 to 4) measured for $1 \le \theta \le 25°$ over *ca* 82 X-ray hours with no perceptible crystal movement or decay (average net intensity of the $52\bar{1}$ and $\bar{6}11$ reflections varied between 98·3 and 101·5% of their mean values); 5403 intensities corrected for Lorentz and polarization effects (Gould & Smith, 1986), all having $F \ge 6{\cdot}0\sigma(F)$; solution *via* iterative application of full-matrix least-squares refinement (on F)/ΔF syntheses (Pt at inversion centre) (Sheldrick, 1976); empirical absorption correction (Walker & Stuart, 1983) following isotropic convergence (correction factors 0·828–1·262); merging afforded 3039 data (R_{merge} 0·0134); all non-H atoms allowed anisotropic thermal vibration, and all H atoms freely refined with group isotropic thermal parameters [$U_{cage\ H} = 0{\cdot}0375\ (24)$, $U_{benzyl\ H} = 0{\cdot}047\ (4)$, $U_{methyl\ H} = 0{\cdot}041\ (3)$ Å^2 at convergence]; the weighting scheme $w^{-1} = \sigma^2(F) + 0{\cdot}000422(F^2)$ afforded satisfactory analysis of variance against parity group, abs(h), abs(k), abs(l), $(F/F_{max})^{1/2}$, and $\sin\theta$; 283 variables, data:variable ratio > 10·7:1; max. shift/e.s.d. in final cycle < 0·02; $R = 0{\cdot}0166$, $wR = 0{\cdot}0212$, $S = 1{\cdot}032$; max. and min. residues in final ΔF synthesis 1·48 and −1·42 e Å^{-3} respectively (near Pt); scattering factors for C, H, B and N inlaid in *SHELX*76. Those for Pt from *International Tables for X-ray Crystallography* (1974); figures drawn using *EASYORTEP* (Mallinson & Muir, 1985) and *PLUTO* (Motherwell, 1976); molecular-geometry calculations (including r.m.s. misfit calculations) *via CALC* (Gould & Taylor, 1986).

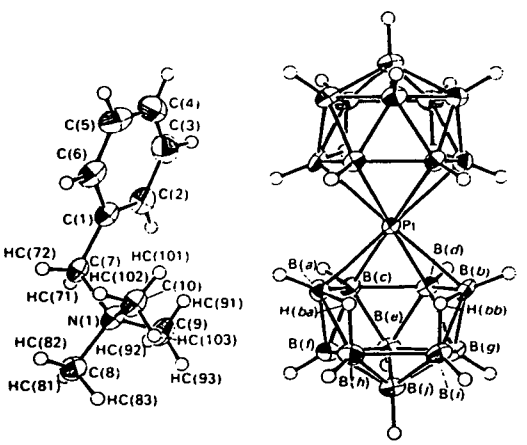

Fig. 1. Perspective view of the $[(B_{10}H_{12})_2Pt]^{2-}$ anion and one $[PhCH_2NMe_3]^+$ cation (50% thermal ellipsoids, except for H atoms which have an artificial radius of 0·1 Å for clarity).

Table 1. *Fractional atomic coordinates and equivalent isotropic temperature factors*

$U_{eq} = (1/3)\sum_i\sum_j U_{ij}a_i^*a_j^*\mathbf{a}_i.\mathbf{a}_j$

	x	y	z	U_{eq}(Å^2)
Pt	0·00000	0·00000	0·00000	0·0218 (1)
C(1)	0·7779 (3)	0·4894 (3)	0·3868 (3)	0·0351 (17)
C(2)	0·7429 (4)	0·3618 (3)	0·2671 (3)	0·0444 (20)
C(3)	0·7363 (4)	0·2313 (4)	0·2751 (4)	0·0576 (25)
C(4)	0·7666 (4)	0·2291 (4)	0·4028 (5)	0·066 (3)
C(5)	0·8051 (4)	0·3564 (4)	0·5237 (4)	0·062 (3)
C(6)	0·8090 (4)	0·4861 (4)	0·5154 (3)	0·0449 (20)
C(7)	0·7967 (3)	0·6335 (3)	0·3830 (3)	0·0340 (17)
N(1)	0·6346 (3)	0·66296 (25)	0·33214 (23)	0·0331 (14)
C(8)	0·6803 (4)	0·8187 (3)	0·3547 (4)	0·0445 (21)
C(9)	0·5272 (4)	0·5620 (4)	0·1775 (3)	0·0436 (21)
C(10)	0·5377 (4)	0·6451 (4)	0·4148 (3)	0·0417 (20)
B(a)	0·1163 (4)	0·2424 (3)	0·0634 (3)	0·0307 (17)
B(c)	0·0954 (3)	0·1181 (3)	−0·1060 (3)	0·0290 (17)
B(d)	−0·1101 (4)	−0·0279 (3)	−0·2201 (3)	0·0293 (17)
B(b)	−0·2605 (3)	−0·0253 (3)	−0·1484 (3)	0·0317 (18)
B(i)	−0·2739 (4)	0·1574 (4)	−0·0997 (3)	0·0368 (19)
B(j)	−0·1517 (4)	0·2480 (3)	−0·1597 (3)	0·0368 (19)
B(e)	−0·0583 (4)	0·1316 (3)	−0·2430 (3)	0·0337 (18)
B(g)	−0·2627 (4)	0·0548 (3)	−0·2619 (3)	0·0334 (18)
B(f)	0·0675 (4)	0·2894 (3)	−0·0763 (3)	0·0346 (19)
B(h)	−0·0505 (4)	0·3169 (3)	0·0253 (3)	0·0377 (20)

Discussion. Fig. 1 shows a perspective view of the dianion and one adjacent cation. The $[(B_{10}H_{12})_2Pt]^{2-}$ anion resides on a crystallographic inversion centre; the $[C_6H_5CH_2NMe_3]^+$ cation crystallizes in general space. Table 1* lists fractional coordinates of refined atoms (excluding H atoms), and Table 2 details selected interatomic distances and interbond angles. Fig. 1 also shows the numbering scheme adopted; we have chosen to number the B atoms in the anion as B(a)–B(j) (Fig. 2b) to avoid any prejudice about the best description of the $\{B_{10}H_{12}\}$ fragment. If formally present as *nido*-$\{B_{10}H_{12}\}^{2-}$ this would be numbered as in Fig. (2a), whereas if the best description was that of *arachno*-$\{B_{10}H_{10}\}^{4-}$ the appropriate numbering scheme would be that of Fig. (2c).

In fact, use of the r.m.s. misfit approach places the $\{B_{10}H_{12}\}$ fragment of the present complex essentially equidistant from idealized *nido*-B_{10} and *arachno*-B_{10} cages, since the r.m.s misfit values are 0·085 Å *versus* $B_{10}H_{14}$ (Brill, Dietrich & Dierks, 1971) and 0·125 Å *versus* the appropriate B_{10} fragment of $[B_{11}H_{13}]^{2-}$

* Lists of structure factors, H-atom positions, additional interatomic distances and interbond angles and anisotropic thermal parameters have been deposited with the British Library Document Supply Centre as Supplementary Publication No. SUP 52783 (24 pp.). Copies may be obtained through The Technical Editor, International Union of Crystallography, 5 Abbey Square, Chester CH1 2HU, England.

Table 2. *Selected bond lengths* (Å) *and angles* (°)

Pt—B(*a*)	2·274 (3)	B(*c*)—B(*d*)	1·825 (5)
Pt—B(*c*)	2·231 (3)	B(*c*)—B(*e*)	1·776 (5)
Pt—B(*d*)	2·215 (3)	B(*c*)—B(*f*)	1·779 (5)
Pt—B(*b*)	2·295 (3)	B(*d*)—B(*b*)	1·784 (5)
C(1)—C(2)	1·385 (5)	B(*d*)—B(*e*)	1·772 (5)
C(1)—C(6)	1·386 (5)	B(*d*)—B(*g*)	1·791 (5)
C(1)—C(7)	1·498 (4)	B(*d*)—B(*i*)	1·821 (5)
C(2)—C(3)	1·388 (6)	B(*b*)—B(*g*)	1·754 (5)
C(3)—C(4)	1·373 (6)	B(*i*)—B(*j*)	1·758 (5)
C(4)—C(5)	1·382 (6)	B(*i*)—B(*g*)	1·783 (5)
C(5)—C(6)	1·386 (6)	B(*i*)—B(*h*)	1·987 (5)
C(7)—N(1)	1·525 (4)	B(*j*)—B(*e*)	1·769 (5)
N(1)—C(8)	1·499 (4)	B(*j*)—B(*g*)	1·776 (5)
N(1)—C(9)	1·489 (5)	B(*j*)—B(*f*)	1·775 (5)
N(1)—C(10)	1·495 (4)	B(*j*)—B(*h*)	1·748 (5)
B(*a*)—B(*c*)	1·781 (5)	B(*e*)—B(*g*)	1·770 (5)
B(*a*)—B(*f*)	1·754 (5)	B(*e*)—B(*f*)	1·767 (5)
B(*a*)—B(*h*)	1·828 (5)	B(*f*)—B(*h*)	1·779 (5)

B(*a*)—Pt—B(*c*)	46·55 (12)	B(*e*)—B(*d*)—B(*g*)	59·56 (19)
B(*c*)—Pt—B(*d*)	48·46 (2)	Pt—B(*b*)—B(*d*)	64·36 (14)
B(*d*)—Pt—B(*b*)	46·56 (12)	B(*d*)—B(*b*)—B(*g*)	60·81 (19)
C(2)—C(1)—C(6)	119·3 (3)	B(*i*)—B(*b*)—B(*g*)	59·77 (19)
C(2)—C(1)—C(7)	121·3 (3)	B(*b*)—B(*i*)—B(*g*)	58·23 (19)
C(6)—C(1)—C(7)	119·3 (3)	B(*j*)—B(*i*)—B(*g*)	60·19 (20)
C(1)—C(2)—C(3)	120·4 (3)	B(*j*)—B(*i*)—B(*b*)	55·23 (19)
C(2)—C(3)—C(4)	119·8 (4)	B(*i*)—B(*j*)—B(*g*)	60·58 (20)
C(3)—C(4)—C(5)	120·3 (4)	B(*i*)—B(*j*)—B(*h*)	69·05 (21)
C(4)—C(5)—C(6)	119·8 (4)	B(*e*)—B(*j*)—B(*g*)	59·91 (19)
C(1)—C(6)—C(5)	120·3 (3)	B(*e*)—B(*j*)—B(*f*)	59·83 (19)
C(1)—C(7)—N(1)	115·67 (25)	B(*f*)—B(*j*)—B(*h*)	60·66 (20)
C(7)—N(1)—C(8)	107·85 (24)	B(*c*)—B(*e*)—B(*d*)	61·90 (18)
C(7)—N(1)—C(9)	111·01 (24)	B(*c*)—B(*e*)—B(*f*)	60·30 (19)
C(7)—N(1)—C(10)	111·24 (24)	B(*d*)—B(*e*)—B(*g*)	60·74 (19)
C(8)—N(1)—C(9)	108·8 (3)	B(*j*)—B(*e*)—B(*g*)	60·24 (19)
C(8)—N(1)—C(10)	108·83 (25)	B(*j*)—B(*e*)—B(*f*)	60·25 (19)
C(9)—N(1)—C(10)	109·1 (3)	B(*d*)—B(*g*)—B(*h*)	60·43 (19)
Pt—B(*a*)—B(*c*)	65·46 (15)	B(*d*)—B(*g*)—B(*e*)	59·70 (19)
B(*c*)—B(*a*)—B(*f*)	60·45 (19)	B(*h*)—B(*g*)—B(*i*)	62·00 (19)
B(*f*)—B(*a*)—B(*h*)	59·51 (19)	B(*i*)—B(*g*)—B(*j*)	59·23 (19)
Pt—B(*c*)—B(*a*)	67·99 (15)	B(*j*)—B(*g*)—B(*e*)	59·85 (19)
Pt—B(*c*)—B(*d*)	65·30 (14)	B(*a*)—B(*f*)—B(*c*)	60·53 (19)
B(*a*)—B(*c*)—B(*f*)	59·02 (18)	B(*a*)—B(*f*)—B(*h*)	62·33 (20)
B(*d*)—B(*c*)—B(*e*)	58·96 (18)	B(*c*)—B(*f*)—B(*e*)	60·09 (19)
B(*e*)—B(*c*)—B(*f*)	59·61 (19)	B(*j*)—B(*f*)—B(*c*)	59·93 (19)
Pt—B(*d*)—B(*c*)	66·24 (14)	B(*j*)—B(*f*)—B(*h*)	58·93 (20)
Pt—B(*d*)—B(*b*)	69·07 (15)	B(*a*)—B(*h*)—B(*f*)	58·15 (19)
B(*c*)—B(*d*)—B(*e*)	59·14 (18)	B(*i*)—B(*h*)—B(*j*)	55·72 (19)
B(*b*)—B(*d*)—B(*g*)	58·77 (18)	B(*j*)—B(*h*)—B(*f*)	60·41 (20)

(Fritchie, 1967). Misfits for the B_{10} cages of $[(B_{10}H_{12})_2Ni]^{2-}$ and $[(B_{10}H_{12})_2Au]^-$ *versus* these standards are similar, *viz* 0·080, 0·136 Å (Ni) and 0·107, 0·110 Å (Au) respectively. Naturally, mutual r.m.s. misfit values between the three $[(B_{10}H_{12})_2M]$ anions are considerably lower (Ni–Au 0·065, Ni–Pt 0·029, Pt–Au 0·054 Å). The verticity of the Pt atom is calculated to be 40·1%.

We have previously (Macgregor, Yellowlees & Welch, 1990) identified a number of key parameters that may ultimately be of use in classifying the $\{B_{10}H_{12}\}$ ligand, and in the present determination the values of these are as follows: B(*c*)–B(*d*) 1·825 (5), B(*h*)–B(*i*) 1·987 (5), B(*a*)···B(*b*) 3·347 (7) Å; height of Pt above the B(*a*)B(*h*)B(*i*)B(*b*) plane 0·537 (3) Å.

Although it appears that the $[(B_{10}H_{12})_2Pt]^{2-}$ anion might have non-crystallographic C_{2h} point-group symmetry, there are small but significant distortions within the polyhedron that do not accord with this. Specifically, B(*b*)—B(*d*)—B(*c*) is wider than B(*a*)—B(*c*)—B(*d*) by 1·93 (32)°, allowing Pt—B(*a*) to be shorter than Pt—B(*b*) [Δ = 0·021 (4) Å] whilst at the same time Pt—B(*c*) is *longer* than Pt—B(*d*) [Δ = 0·016 (4) Å]. Since there is no obvious intramolecular reason for this slight but apparently real asymmetry,

Fig. 2. Numbering schemes for B_{10} ligands and their interrelationship; (*a*) *nido*-B_{10}; (*b*) present complex; (*c*) *arachno*-B_{10}.

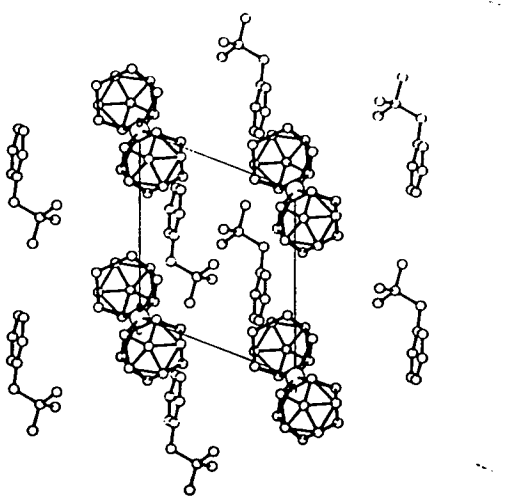

Fig. 3. Packing diagram down the crystallographic *c* axis.

it is likely that its origin lies in crystal-packing effects. Although there are no $H_{cage}\cdots H_{cation}$ contacts $< 2{\cdot}6$ Å, it is clear from the packing diagram (Fig. 3) that the two sides of the $\{B_{10}H_{12}\}$ ligand [that containing B(*a*) and that containing B(*b*)] experience quite different crystal environments. Distances and angles within the $[PhCH_2NMe_3]^+$ cation are quite normal (*e.g.* Mitchell & Welch, 1987; Wynd & Welch, 1989; Macgregor, Yellowlees & Welch, 1990).

We thank the SERC for support (SAM) and the Callery Chemical Company for a generous gift of $B_{10}H_{14}$.

References

Brill, R., Dietrich, H. & Dierks, H. (1971). *Acta Cryst.* B27, 2003–2018.

Fritchie, C. J. (1967). *Inorg. Chem.* 6, 1199–1203.

Gould, R. O. & Smith, D. E. (1986). *CADABS*. Program for data reduction. Univ. of Edinburgh, Scotland.

Gould, R. O. & Taylor, P. (1986). *CALC*. Program for molecular geometry calculations. Univ. of Edinburgh, Scotland.

Guggenberger, L. J. (1972). *J. Am. Chem. Soc.* 94, 114–119.

Internatinal Tables for X-ray Crystallograpy (1974). Vol. IV. Birmingham: Kynoch Press. (Present distributor Kluwer Academic Publishers, Dordrecht.)

Klanberg, F., Wegner, P. A., Parshall, G. W. & Muetterties, E. L. (1968). *Inorg. Chem.* 7, 2072–2077.

Macgregor, S. A., Yellowlees, L. J. & Welch, A. J. (1990). *Acta Cryst.* C46, 551–554.

Mallinson, P. & Muir, K. W. (1985). *J. Appl. Cryst.* 18, 51–53.

Mitchell, G. F. & Welch, A. J. (1987). *J. Chem. Soc. Dalton Trans.* pp. 1017–1025.

Motherwell, W. D. S. (1976). *PLUTO*. Program for molecular and crystal structure illustrations. Univ. of Cambridge, England.

Sheldrick, G. M. (1976). *SHELX76*. Program for crystal structure determination. Univ. of Cambridge, England.

Walker, N. G. & Stuart, D. (1983). *Acta Cryst.* A39, 158–166.

Wynd, A. J. (1988). PhD Thesis. Univ. of Edinburgh, Scotland.

Wynd, A. J. & Welch, A. J. (1987). *J. Chem. Soc. Chem. Commun.* pp. 1174–1176.

Wynd, A. J. & Welch, A. J. (1989). *Acta Cryst.* C45, 615–617.

Wynd, A. J., Welch, A. J. & Parish, R. V. (1990). *J. Chem. Soc. Dalton Trans.* In the press.

Acta Cryst. (1991). C47, 513–516

Structure of $[PhCH_2NMe_3]_2[(B_{10}H_{12})_2Pd]$ Acetonitrile Solvate

BY STUART A. MACGREGOR, JAMES A. SCANLAN, LESLEY J. YELLOWLEES AND ALAN J. WELCH

Department of Chemistry, University of Edinburgh, Edinburgh EH9 3JJ, Scotland

(*Received* 24 *June* 1990; *accepted* 29 *August* 1990)

Abstract. $[PhCH_2NMe_3]_2^{2+}.[Pd(B_{10}H_{12})_2]^{2-}.2CH_3CN$, $M_r = 729{\cdot}39$, triclinic, $P\bar{1}$, $a = 9{\cdot}2094$ (18), $b = 10{\cdot}772$ (3), $c = 11{\cdot}3707$ (23) Å, $\alpha = 67{\cdot}721$ (21), $\beta = 83{\cdot}394$ (16), $\gamma = 78{\cdot}801$ (21)°, $V = 1022{\cdot}8$ Å^3, $Z = 1$, $D_x = 1{\cdot}184$ Mg m^{-3}, Mo $K\alpha$, $\lambda = 0{\cdot}71069$ Å, $\mu = 0{\cdot}470$ mm^{-1}, $F(000) = 380$, $T = 291$ (1) K, $R = 0{\cdot}0265$ for 5850 independent observed reflections. The palladaborane anion has effective C_{2h} molecular symmetry (C_i imposed). The $\{B_{10}\}$ fragment has a geometry close to intermediate between that of *nido*-$\{B_{10}H_{12}\}^{2-}$ and *arachno*-$\{B_{10}H_{12}\}^{4-}$, and the verticity of the Pd atom is 39·4%.

Introduction. We are involved in a major research programme which critically examines the structures of metallaboranes and metallaheteroboranes. The aims of the work are firstly to measure the extent to which the metal atom present can be regarded as a true cluster vertex, and then to determine the factors responsible for the 'verticity' of the metal. The family of metallaboranes represented by $MB_{10}H_{12}$ is particularly useful in this respect, since the $\{B_{10}H_{12}\}$ ligand appears able to accommodate both metal vertices and (non-vertex) metal bridges with only subtle, but nevertheless measureable, structural change. In brief, if the metal is formally present as a polyhedral vertex the $\{B_{10}H_{12}\}$ ligand is formally the *arachno* fragment $\{B_{10}H_{12}\}^{4-}$, whereas for a bridging metal atom the polyhedral unit is merely the *nido* species $\{B_{10}H_{12}\}^{2-}$.

We have previously shown that clear examples of both types of metallaborane exist. Thus, in [7,7,7-$(CO)_3$-*nido*-7-$CoB_{10}H_{12}]^-$ (Macgregor, Yellowlees & Welch, 1990*a*) the Co atom, formally Co^{3+}, is a true polyhedral vertex (high verticity), whereas in (the superficially structurally similar) [5,6,9,10-μ_4-$\{AuP(C_6H_{11})_3\}$-*nido*-$B_{10}H_{12}]^-$ (Wynd, Welch & Parish, 1990), the Au atom, formally Au^+, is not (low verticity).

We recently showed (Macgregor, Yellowlees & Welch, 1990*b*) that metallaboranes of the type $[(B_{10}H_{12})_2M]^{n-}$ [M = Ni, $n = 2$ (Guggenberger, 1972); M = Pt, $n = 2$ (Macgregor, Yellowlees & Welch, 1990*b*); M = Au, $n = 1$ (Wynd & Welch, 1987)] are particularly interesting in that they show intermediate behaviour, *i.e.* the $\{B_{10}H_{12}\}$ fragments of the molecules have structures that lie between those expected for $\{B_{10}H_{12}\}^{2-}$ and $\{B_{10}H_{12}\}^{4-}$, resulting in metal verticities that are neither high nor low. The situation was further complicated by the fact that the platinaborane structure appeared to suffer from an unusual asymmetry which we were forced to conclude was the result of crystal packing effects. Seeking further data on the $[(B_{10}H_{12})_2M]^{n-}$

0108-2701/91/030513-04$03.00

metallaboranes, we have resynthesized the palladium derivative ($n = 2$) for the purposes of the structural study reported here. This will furnish precise stereochemical information on a complete group of analogous metallaboranes from the first, the second, and the third transition series. Fortuitously, $[PhCH_2NMe_3][(B_{10}H_{12})_2Pd]$ crystallizes from acetonitrile/diethyl ether with two molecules of acetonitrile solvate whereas the platinum analogue is solvate free, allowing additional comment on the possible influence of packing forces on the structure of the latter.

Experimental. The salt $[PhCH_2NMe_3][(B_{10}H_{12})_2Pd]$ was prepared by a modified version of a published procedure (Klanberg, Wegner, Parshall & Muetterties, 1968), and wine-red crystals grown by the slow diffusion of diethyl ether into an acetonitrile solution at 243 K; single crystal, 0·3 × 0·3 × 0·2 mm, removed from solvent mixture and quickly covered with silicone grease, then sealed inside a Lindemann capillary; mounted on an Enraf–Nonius CAD-4 diffractometer (Mo $K\alpha$ radiation, graphite monochromator); cell parameters and orientation matrix from least-squares refinement of the setting angles ($13 < \theta < 15°$) of 25 centred reflections; data collection by ω–2θ scans in 96 steps with ω scan width ($0{\cdot}8 + 0{\cdot}34\tan\theta$)°; data ($h$: 0 to 12, k: −15 to 15, l: −16 to 16. h: −12 to 0, k: −15 to 15, l −16 to −2) measured for $1 \le \theta \le 30°$ over 202 X-ray hours; corrections for Lorentz and polarization effects applied (Gould & Smith, 1986); 7835 reflections measured; structure solution *via* iterative full-matrix least-squares refinement (on F)/ΔF syntheses (Pd atom at origin) (Sheldrick, 1976); empirical absorption correction (Walker & Stuart, 1983) applied after isotropic convergence (correction factors 0·793–1·313); data merged ($R_{merge} = 0{\cdot}0142$) to give 5864 independent reflections of which 5850 [$F \ge 2{\cdot}0\sigma(F)$] retained; all non-H atoms refined with anisotropic thermal parameters; borane, phenyl and methylene H atoms freely refined (including individual isotropic thermal parameters), and CH_3 moieties treated as rigid groups, with separate group thermal parameters for H atoms of the benzyltrimethylammonium cation and the acetonitrile solvate; weighting scheme $w^{-1} = \sigma^2(F) + 0{\cdot}000700F^2$; 313 variables, data:variable ratio > 18:1; max. shift/e.s.d. in final cycle < 0·13 (H atom); $R = 0{\cdot}0265$, $wR = 0{\cdot}0352$, $S = 1{\cdot}128$; max. and min. residues in final ΔF synthesis 0·52 and −1·05 e Å^{-3}, respectively; scattering factors for C, H, B and N inlaid in *SHELX76*. Those for Pd from *International Tables for X-ray Crystallography* (1974, Vol. IV); Fig. 1 drawn using *EASYORTEP* (Mallinson & Muir, 1985); molecular geometry calculations *via CALC* (Gould & Taylor, 1986).

Table 1. *Fractional coordinates of non-H atoms and equivalent isotropic thermal parameters*

$U_{eq} = (1/3)\Sigma_i\Sigma_j U_{ij}a_i^*a_j^*\mathbf{a}_i.\mathbf{a}_j.$

	x	y	z	U_{eq}(Å^2)
Pd	0·00000	0·00000	0·00000	0·0318 (1)
B(a)	0·05941 (14)	−0·22922 (12)	0·11364 (12)	0·0379 (3)
B(b)	0·22174 (13)	0·01148 (12)	−0·11556 (11)	0·0373 (3)
B(c)	0·00450 (14)	−0·18732 (13)	−0·04241 (12)	0·0380 (3)
B(d)	0·09237 (13)	−0·05590 (13)	−0·16722 (11)	0·0367 (3)
B(j)	0·31487 (14)	−0·27865 (13)	−0·04638 (12)	0·0404 (3)
B(g)	0·28606 (14)	−0·11884 (13)	−0·17461 (11)	0·0393 (3)
B(i)	0·35679 (14)	−0·13439 (13)	−0·02919 (12)	0·0398 (3)
B(e)	0·15571 (14)	−0·23081 (13)	−0·13862 (12)	0·0405 (3)
B(f)	0·14379 (15)	−0·33020 (12)	0·02590 (13)	0·0406 (3)
B(h)	0·26101 (14)	−0·27731 (13)	0·10615 (12)	0·0393 (3)
C(1)	0·22667 (13)	0·06314 (14)	0·36903 (12)	0·0469 (3)
C(2)	0·20236 (15)	−0·04673 (14)	0·48024 (13)	0·0531 (3)
C(3)	0·31791 (15)	0·03825 (16)	0·27166 (12)	0·0559 (3)
C(4)	0·26626 (17)	−0·17689 (15)	0·49152 (15)	0·0614 (3)
C(5)	0·35606 (17)	−0·20146 (16)	0·39376 (16)	0·0673 (3)
C(6)	0·38256 (16)	−0·09320 (17)	0·28410 (14)	0·0667 (3)
C(7)	0·14763 (14)	0·20338 (15)	0·35198 (13)	0·0532 (3)
N(1)	0·22615 (14)	0·28558 (12)	0·40039 (11)	0·0495 (3)
C(8)	0·12703 (20)	0·41814 (16)	0·38372 (18)	0·0735 (3)
C(9)	0·25637 (22)	0·21256 (16)	0·53771 (15)	0·0835 (3)
C(10)	0·36641 (18)	0·31553 (18)	0·32580 (19)	0·0820 (3)
C($A1$)	0·70103 (20)	−0·40641 (17)	0·13582 (17)	0·0735 (3)
C($A2$)	0·69530 (21)	−0·44438 (16)	0·27029 (18)	0·0758 (3)
N($A1$)	0·69141 (25)	−0·47402 (19)	0·37764 (19)	0·1333 (3)

Discussion. Table 1* lists coordinates of refined non-H atoms and equivalent isotropic thermal parameters, and Table 2 details internuclear distances and selected interbond angles. The palladaborane anion is viewed in perspective in Fig. 1. Cage atoms are labelled B(a) to B(j), as in the platinum analogue, to reflect the ambiguity in formal classification (*nido* or *arachno*) of the B_{10} residue. The compound crystallizes with no unusually short contacts between ions.

Although this structural study was performed at room temperature, the high quality of the crystal, the relatively high θ_{max}, and the measurement of more than one asymmetric fraction of data combine to afford a result that is highly accurate, as evidenced by the low e.s.d.'s on the molecular parameters. Although the anion has crystallographically required C_i symmetry, the *effective* point group is C_{2h}. Thus, in the present compound there is no evidence of the small but real distortion of the MB_8 coordination sphere that is observed in $[(B_{10}H_{12})_2Pt]^{2-}$ (Macgregor, Yellowlees & Welch, 1990*b*). The fact that the palladium species reported here has a totally different *crystal* structure to its platinum analogue is wholly consistent with our previous suggestion (Macgregor, Yellowlees & Welch, 1990*b*) that the

* Lists of structure factors, H-atom positions and anisotropic thermal parameters have been deposited with the British Library Document Supply Centre as Supplementary Publication No. SUP 53524 (38 pp.). Copies may be obtained through The Technical Editor, International Union of Crystallography, 5 Abbey Square, Chester CH1 2HU, England.

Table 2. *Interatomic distances* (Å) *and interbond angles* (°)

Pd—B(*a*)	2·2988 (13)	B(*i*)—B(*h*)	1·9837 (19)
Pd—B(*b*)	2·2955 (12)	B(*i*)—H(*i*)	1·050 (3)
Pd—B(*c*)	2·2375 (14)	B(*i*)—H(*bb*)	1·252 (3)
Pd—B(*d*)	2·2357 (13)	B(*e*)—B(*f*)	1·7713 (19)
B(*a*)—B(*c*)	1·7659 (19)	B(*e*)—H(*e*)	1·029 (3)
B(*a*)—B(*f*)	1·7603 (19)	B(*f*)—B(*h*)	1·7839 (19)
B(*a*)—B(*h*)	1·8292 (19)	B(*f*)—H(*f*)	0·984 (3)
B(*a*)—H(*a*)	1·131 (3)	B(*h*)—H(*ba*)	1·302 (3)
B(*a*)—H(*ba*)	1·214 (3)	B(*h*)—H(*h*)	1·053 (3)
B(*b*)—B(*d*)	1·7639 (18)	C(1)—C(2)	1·3974 (20)
B(*b*)—B(*g*)	1·7528 (18)	C(1)—C(3)	1·3883 (20)
B(*b*)—B(*i*)	1·8254 (18)	C(1)—C(7)	1·4942 (20)
B(*b*)—H(*bb*)	1·283 (3)	C(2)—C(4)	1·3744 (22)
B(*b*)—H(*b*)	1·101 (3)	C(2)—H(2*C*)	1·007 (3)
B(*c*)—B(*d*)	1·8249 (19)	C(3)—C(6)	1·3854 (22)
B(*c*)—B(*e*)	1·7720 (19)	C(3)—H(3*C*)	0·938 (3)
B(*c*)—B(*f*)	1·7814 (19)	C(4)—C(5)	1·3843 (24)
B(*c*)—H(*c*)	1·158 (3)	C(4)—H(4*C*)	0·731 (4)
B(*d*)—B(*g*)	1·7854 (18)	C(5)—C(6)	1·3828 (24)
B(*d*)—B(*e*)	1·7743 (19)	C(5)—H(5*C*)	0·926 (4)
B(*d*)—H(*d*)	1·096 (3)	C(6)—H(6*C*)	0·904 (4)
B(*j*)—B(*g*)	1·7799 (19)	C(7)—H(1*C*7)	0·897 (3)
B(*j*)—B(*i*)	1·7558 (19)	C(7)—H(2*C*7)	0·991 (3)
B(*j*)—B(*e*)	1·7789 (19)	C(7)—N(1)	1·5231 (19)
B(*j*)—B(*f*)	1·7782 (19)	N(1)—C(8)	1·4955 (23)
B(*j*)—B(*h*)	1·7529 (19)	N(1)—C(9)	1·4893 (22)
B(*j*)—H(*j*)	1·114 (3)	N(1)—C(10)	1·4813 (23)
B(*g*)—B(*i*)	1·7838 (19)	C(*A*1)—C(*A*2)	1·422 (3)
B(*g*)—B(*e*)	1·7716 (19)	C(*A*2)—N(*A*1)	1·137 (3)
B(*g*)—H(*g*)	1·009 (3)		

B(*a*)—Pd—B(*c*)	45·80 (5)	B(*g*)—B(*d*)—H(*d*)	121·59 (19)
B(*b*)—Pd—B(*d*)	45·80 (5)	B(*e*)—B(*d*)—H(*d*)	121·22 (19)
B(*c*)—Pd—B(*d*)	48·15 (5)	B(*g*)—B(*j*)—B(*i*)	60·59 (7)
B(*a*)—Pd—B(*b'*)	86·30 (5)	B(*g*)—B(*j*)—B(*e*)	59·71 (7)
B(*a*)—Pd—B(*d'*)	95·75 (5)	B(*g*)—B(*j*)—H(*j*)	122·99 (19)
B(*c*)—Pd—B(*b'*)	95·95 (5)	B(*i*)—B(*j*)—B(*h*)	68·86 (8)
Pd—B(*a*)—B(*c*)	65·27 (6)	B(*e*)—B(*j*)—B(*f*)	59·73 (8)
Pd—B(*a*)—H(*a*)	117·15 (18)	B(*f*)—B(*j*)—B(*h*)	60·68 (8)
B(*c*)—B(*a*)—B(*f*)	60·69 (8)	B(*f*)—B(*j*)—H(*j*)	115·84 (19)
B(*c*)—B(*a*)—H(*a*)	131·05 (19)	B(*h*)—B(*j*)—H(*j*)	113·71 (19)
B(*f*)—B(*a*)—B(*h*)	59·56 (7)	B(*b*)—B(*g*)—B(*d*)	59·80 (7)
B(*f*)—B(*a*)—H(*a*)	123·05 (19)	B(*b*)—B(*g*)—B(*i*)	62·14 (7)
B(*h*)—B(*a*)—H(*a*)	117·61 (19)	B(*b*)—B(*g*)—B(*e*)	110·86 (9)
B(*h*)—B(*a*)—H(*ba*)	45·27 (16)	B(*b*)—B(*g*)—H(*g*)	119·52 (20)
Pd—B(*b*)—B(*d*)	65·31 (6)	B(*d*)—B(*g*)—B(*e*)	59·84 (7)
Pd—B(*b*)—H(*b*)	117·12 (18)	B(*d*)—B(*g*)—H(*g*)	126·27 (21)
B(*d*)—B(*b*)—B(*g*)	61·02 (7)	B(*j*)—B(*g*)—B(*i*)	59·03 (7)
B(*d*)—B(*b*)—H(*b*)	129·55 (19)	B(*j*)—B(*g*)—B(*e*)	60·12 (7)
B(*g*)—B(*b*)—B(*i*)	59·76 (7)	B(*j*)—B(*g*)—H(*g*)	120·51 (21)
B(*g*)—B(*b*)—H(*b*)	122·30 (19)	B(*i*)—B(*g*)—H(*g*)	119·54 (20)
B(*i*)—B(*b*)—H(*bb*)	43·29 (15)	B(*e*)—B(*g*)—H(*g*)	121·75 (21)
B(*i*)—B(*b*)—H(*b*)	118·39 (19)	B(*b*)—B(*i*)—B(*g*)	58·10 (7)
Pd—B(*c*)—B(*a*)	68·93 (6)	B(*b*)—B(*i*)—H(*i*)	119·73 (20)
Pd—B(*c*)—B(*d*)	65·87 (6)	B(*h*)—B(*i*)—H(*bb*)	44·62 (15)
Pd—B(*c*)—H(*c*)	114·22 (17)	B(*j*)—B(*i*)—B(*g*)	60·37 (7)
B(*a*)—B(*c*)—B(*f*)	59·50 (7)	B(*j*)—B(*i*)—B(*h*)	55·50 (7)
B(*a*)—B(*c*)—H(*c*)	120·93 (18)	B(*j*)—B(*i*)—H(*i*)	123·94 (20)
B(*d*)—B(*c*)—B(*e*)	59·09 (7)	B(*g*)—B(*i*)—H(*i*)	123·63 (20)
B(*d*)—B(*c*)—H(*c*)	118·11 (18)	B(*h*)—B(*i*)—H(*i*)	121·46 (20)
B(*e*)—B(*c*)—B(*f*)	59·80 (8)	B(*h*)—B(*i*)—H(*bb*)	94·73 (16)
B(*e*)—B(*c*)—H(*c*)	116·44 (18)	B(*c*)—B(*e*)—B(*d*)	61·94 (7)
B(*f*)—B(*c*)—H(*c*)	120·04 (18)	B(*c*)—B(*e*)—B(*f*)	60·36 (8)
Pd—B(*d*)—B(*b*)	68·89 (6)	B(*c*)—B(*e*)—H(*e*)	121·49 (20)
Pd—B(*d*)—B(*c*)	65·97 (6)	B(*d*)—B(*e*)—B(*g*)	60·46 (7)
Pd—B(*d*)—H(*d*)	110·70 (18)	B(*d*)—B(*e*)—H(*e*)	122·84 (20)
B(*b*)—B(*d*)—B(*g*)	59·18 (7)	B(*j*)—B(*e*)—B(*g*)	60·17 (7)
B(*b*)—B(*d*)—H(*d*)	117·43 (19)	B(*j*)—B(*e*)—B(*f*)	60·11 (8)
B(*c*)—B(*d*)—B(*e*)	58·97 (7)	B(*j*)—B(*e*)—H(*e*)	122·64 (20)
B(*c*)—B(*d*)—H(*d*)	120·28 (19)	B(*g*)—B(*e*)—H(*e*)	119·99 (20)
B(*g*)—B(*d*)—B(*e*)	59·69 (7)	B(*f*)—B(*e*)—H(*e*)	117·66 (20)

Table 3. *Root-mean-square misfit values* (Å), *and percentage verticities, for the series* $[(B_{10}H_{12})_2M]^{2-}$ (M = Ni, Pd, Pt)

Compound	Misfit *vs* $B_{10}H_{14}$	Misfit *vs* $[B_{11}H_{13}]^{2-}$	% Verticity	Reference
$[(B_{10}H_{12})_2Ni]^{2-}$	0·080	0·136	36·1	Guggenberger (1972)
$[(B_{10}H_{12})_2Pd]^{2-}$	0·084	0·127	39·4	This work
$[(B_{10}H_{12})_2Pt]^{2-}$	0·085	0·125	42·6	Macgregor, Yellowlees & Welch (1990*b*)

Mutual misfits (Å)

$[(B_{10}H_{12})_2Ni]^{2-}$ *vs* $[(B_{10}H_{12})_2Pd]^{2-}$	0·030
$[(B_{10}H_{12})_2Ni]^{2-}$ *vs* $[(B_{10}H_{12})_2Pt]^{2-}$	0·029
$[(B_{10}H_{12})_2Pd]^{2-}$ *vs* $[(B_{10}H_{12})_2Pd]^{2-}$	0·011

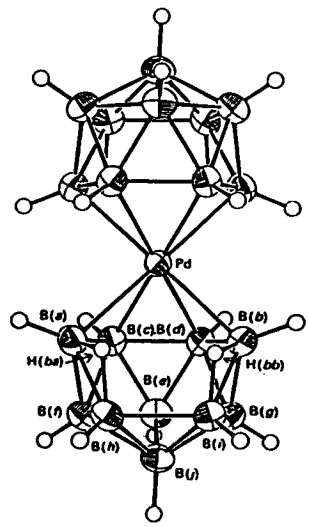

Fig. 1. Perspective view of, and atom-labelling scheme for, the $[Pd(B_{10}H_{12})_2]^{2-}$ anion (30% thermal ellipsoids, except for H atoms which have an artificial radius of 0·1 Å for clarity).

structural distortion in the platinaborane is due to crystal packing effects.

Root-mean-square misfit calculations (Wynd, Macgregor, Gould, Taylor, Yellowlees & Welch, 1990) on the $\{B_{10}\}$ fragment of the palladaborane afford (mis)fits of 0·084 Å *versus* $B_{10}H_{14}$ (Brill, Dietrich & Dierks, 1971) and 0·127 Å *versus* $[B_{11}H_{13}]^{2-}$ (Fritchie, 1967). The verticity of the Pd atom is calculated to be 39·4%. These data position $[(B_{10}H_{12})_2Pd]^{2-}$ nicely between $[(B_{10}H_{12})_2Ni]^{2-}$ (Guggenberger, 1972) and $[(B_{10}H_{12})_2Pt]^{2-}$ (Macgregor, Yellowlees & Welch, 1990*b*) (Table 3), but clearly show that the greatest similarity is between the palladium and platinum analogues. Other key molecular parameters that may ultimately be useful in formal classification of the $\{B_{10}H_{12}\}$

ligand in the present compound are as follows: B(*c*)—B(*d*) 1·8249 (19), B(*h*)—B(*i*) 1·9837 (19), B(*a*)···B(*b*) 3·352 (2) Å; height of Pd above the B(*a*)B(*h*)B(*i*)B(*b*) plane 0·5693 (22) Å.

We thank the SERC for support (SAM), and the Callery Chemical Company for a generous gift of decaborane.

References

BRILL, R., DIETRICH, H. & DIERKS, H. (1971). *Acta Cryst.* B27, 2003–2018.

FRITCHIE, C. J. (1967). *Inorg. Chem.* 6, 1199–1203.

GOULD, R. O. & SMITH, D. E. (1986). *CADABS*. Program for data reduction. Univ. of Edinburgh, Scotland.

GOULD, R. O. & TAYLOR, P. (1986). *CALC*. Program for molecular geometry calculations. Univ. of Edinburgh, Scotland.

GUGGENBERGER, L. J. (1972). *J. Am. Chem. Soc.* 94, 114–119.

KLANBERG, F., WEGNER, P. A., PARSHALL, G. W. & MUETTERTIES, E. L. (1968). *Inorg. Chem.* 7, 2072–2077.

MACGREGOR, S. A., YELLOWLEES, L. J. & WELCH, A. J. (1990*a*). *Acta Cryst.* C46, 551–554.

MACGREGOR, S. A., YELLOWLEES, L. J. & WELCH, A. J. (1990*b*). *Acta Cryst.* C46, 1399–1402.

MALLINSON, P. & MUIR, K. W. (1985). *J. Appl. Cryst.* 18, 51–53.

SHELDRICK, G. M. (1976). *SHELX76*. Program for crystal structure determination. Univ. of Cambridge, England.

WALKER, N. G. & STUART, D. (1983). *Acta Cryst.* A39, 158–166.

WYND, A. J., MACGREGOR, S. A., GOULD, R. O., TAYLOR, P., YELLOWLEES, L. J. & WELCH, A. J. (1990). Work in progress.

WYND, A. J. & WELCH, A. J. (1987). *J. Chem. Soc. Chem. Commun.* pp. 1174–1176.

WYND, A. J., WELCH, A. J. & PARISH, R. V. (1990). *J. Chem. Soc. Dalton Trans.* pp. 2185–2193.

Acta Cryst. (1991). C47, 536–539

Tricarbonyl[(1,2,3,4-η)-2,3-dimethylbutadiene]cobalt Acetonitriletrichloroferrate(1 −)

BY STUART A. MACGREGOR, LESLEY J. YELLOWLEES AND ALAN J. WELCH

Department of Chemistry, University of Edinburgh, Edinburgh EH9 3JJ, Scotland

(*Received* 21 *June* 1990; *accepted* 28 *August* 1990)

Abstract. $[Co(C_6H_{10})(CO)_3][Fe(Cl)_3(C_2H_3N)]$, M_r = 428·35, monoclinic, $P2_1/a$, a = 11·259 (10), b = 12·043 (4), c = 12·727 (7) Å, β = 97·53 (6)°, V = 1710·8 Å^3, Z = 4, D_x = 1·663 Mg m^{-3}, Mo $K\alpha$, λ = 0·71069 Å, μ = 2·291 mm^{-1}, $F(000)$ = 856, T = 291 (1) K, R = 0·032 for 1383 independent observed reflections. The title compound, an archetypal Co^{I} species, was studied in the hope of gaining further information about $[7,7,7\text{-}(CO)_3\text{-}7\text{-}CoB_{10}H_{12}]^-$, which had previously been described formally as a Co^{III} complex. Comparison of Co—CO distances and C—O IR stretching frequencies lends support to this conclusion.

Introduction. Recently (Macgregor, Yellowlees & Welch, 1990) we reported that analysis of the structure of the anion $[7,7,7\text{-}(CO)_3\text{-}7\text{-}CoB_{10}H_{12}]^-$ (1) implied that the $\{B_{10}H_{12}\}$ moiety in this species could best be described as the *arachno* fragment $\{B_{10}H_{12}\}^{4-}$, and therefore that the formal oxidation state of the Co atom was +3.

In an attempt to gain further information on this system we describe here the results of a structural study of the cation $[(CO)_3Co(dmbd)]^+$ (2) [dmbd = 2,3-dimethylbutadiene, η-$CH_2C(Me)C(Me)CH_2$]. This species has been selected for comparison with the cobaltaborane anion since (i) it contains a directly analogous metal coordination sphere (a tricarbonyl unit and an acyclic η^4-bonded ligand) and (ii) the oxidation state of cobalt in the title compound is clearly known (+1). Spectroscopic evidence for the cation $[(CO)_3Co(dmbd)]^+$ was first furnished in 1974 (Chauldry & Paulson, 1974), but no bulk preparation and characterization was carried out. Here we report the isolation of (2) as its $[FeCl_3(NCMe)]^-$ salt.

Experimental. Compound prepared as the $[FeCl_3(NCMe)]^-$ salt by oxidation of a CH_2Cl_2 solution of $[Co(CO)_2(dmbd)]_2$ with $FeCl_3$, removal of solvent *in vacuo*, and extraction of the resultant solid into acetonitrile; identity checked by IR spectroscopy (KBr disc, ν_{C-O} = 2130, 2100 and 2080 cm^{-1}), and established by diffraction study; marine blue crystal, 0·2 × 0·2 × 0·3 mm, mounted on an Enraf–Nonius CAD-4 diffractometer (Mo $K\alpha$ radiation, graphite monochromator); cell parameters and orientation matrix from least-squares refinement of the setting angles ($9 < \theta < 12°$) of 25 centred reflections; data collection by ω–2θ scans in 96 steps with ω scan width (0·8 + 0·34tanθ)°; data (h: 0 to 10, k: 0 to 11, l: −12 to 12) measured for $1 \le \theta \le 20°$ over 18 X-ray hours; corrections for Lorentz and polarization effects applied (Gould & Smith, 1986); 1699 indepen-

0108-2701/91/030536-04$03.00

dent reflections measured, of which 1383 [$F \geq 1{\cdot}0\sigma(F)$] retained; structure solution *via* automatic direct methods (Co,Fe) (Sheldrick, 1986), and iterative full-matrix least-squares refinement (on $F/\Delta F$ syntheses (Cl, O, N, C, H) (Sheldrick, 1976); empirical absorption correction (Walker & Stuart, 1983) applied after isotropic convergence (maximum and minimum correction factors 1·053 and 0·933, respectively); CH_3 moieties treated as rigid groups; vinyl H atoms located and positionally refined; all H atoms given a fixed isotropic thermal parameter ($U_H = 0{\cdot}04$ Å^2); weighting scheme $w^{-1} = \sigma^2(F) + 0{\cdot}000506F^2$; model refined in two blocks of 68 and 137 variables, data:variable ratio > 10:1; max. shift/e.s.d. in final cycle < 0·06; $R = 0{\cdot}032$, $wR = 0{\cdot}033$, $S = 1{\cdot}294$; max. and min. residues in final ΔF synthesis 0·28 and $-0{\cdot}35$ e Å^{-3}, respectively; scattering factors for C, H, N, O and Cl inlaid in *SHELX76* (Sheldrick, 1976), those for Co and Fe from *International Tables for X-ray Crystallography* (1974, Vol. IV); Fig. 1 drawn using *EASYORTEP* (Mallinson & Muir, 1985); molecular geometry calculations *via CALC* (Gould & Taylor, 1986).

Table 1. *Coordinates of refined atoms and equivalent isotropic thermal parameters* (Å^2)

$U_{eq} = (1/3)\sum_i\sum_j U_{ij}a_i^*a_j^*\mathbf{a}_i.\mathbf{a}_j$.

	x	y	z	U_{eq}
Fe	0·22731 (6)	0·52612 (5)	0·69958 (5)	0·0231 (4)
Cl(1)	0·33475 (12)	0·46608 (11)	0·57326 (9)	0·0409 (8)
Cl(2)	0·34165 (11)	0·61722 (10)	0·83185 (9)	0·0328 (8)
Cl(3)	0·10651 (12)	0·40022 (11)	0·76295 (10)	0·0414 (9)
N(1)	0·1174 (4)	0·6387 (4)	0·6165 (3)	0·035 (3)
C(10)	0·0509 (5)	0·6898 (4)	0·5610 (4)	0·034 (3)
C(11)	−0·0364 (4)	0·7552 (4)	0·4906 (4)	0·039 (3)
Co	0·69182 (6)	0·43230 (6)	0·81949 (5)	0·0251 (4)
C(1)	0·7827 (5)	0·3509 (4)	0·9218 (4)	0·034 (4)
O(1)	0·8410 (4)	0·3033 (3)	0·9855 (3)	0·045 (3)
C(2)	0·5438 (6)	0·3696 (4)	0·8211 (4)	0·034 (4)
O(2)	0·4504 (4)	0·3338 (3)	0·8254 (3)	0·049 (3)
C(3)	0·7531 (4)	0·3602 (4)	0·7113 (4)	0·028 (3)
O(3)	0·7927 (3)	0·3197 (3)	0·6445 (3)	0·042 (3)
C(4)	0·6628 (5)	0·5538 (4)	0·9292 (4)	0·034 (4)
HC(41)	0·585 (4)	0·581 (4)	0·906 (4)	*
HC(42)	0·672 (4)	0·533 (4)	1·006 (4)	*
C(5)	0·7608 (4)	0·5837 (4)	0·8768 (4)	0·022 (3)
C(6)	0·7399 (4)	0·5865 (4)	0·7645 (4)	0·023 (3)
C(7)	0·6222 (5)	0·5584 (4)	0·7177 (4)	0·028 (3)
HC(71)	0·553 (4)	0·580 (4)	0·751 (4)	*
HC(72)	0·619 (4)	0·549 (4)	0·651 (4)	*
C(8)	0·8848 (4)	0·6017 (4)	0·9367 (4)	0·033 (3)
C(9)	0·8387 (4)	0·6087 (4)	0·6983 (4)	0·031 (3)

*U_{iso} fixed at 0·04 Å^2.

Discussion. Table 1* lists the coordinates of refined atoms and equivalent isotropic thermal parameters, and Table 2 details internuclear distances and interbond angles between these. The cation (2) has effective, non-crystallographically imposed, C_s symmetry about the plane containing CoC(2)O(2), and the midpoint of the C(5)—C(6) bond, and the $\{Co(CO)_3\}$ unit is oriented such that one carbonyl ligand, C(2)O(2), lies over the open edge of the dmbd ligand (see Fig. 1). This (*endo*) conformation is analogous to that observed in the cobaltaborane anion (1), confirming the similarities of the metal coordination spheres in both species.

Table 3 summarizes Co—CO and C—O distances for (1) and (2) (parameters related by the effective mirror planes present in both species are averaged). The bond angles are highly similar, the only perceptible difference being a slight widening of C(1)—Co—C(3) in (1). Co—CO bonds are consistently shorter in the cobaltaborane anion than in the cobalt–dmbd cation, and are thus not inconsistent with a greater formal metal oxidation state in the former species. However, at least two other differences (discussed below) between (1) and (2) could contribute to this result, making it somewhat difficult to factorize out the causes. The C—O distances in (2) are marginally shorter than those in (1), but the

Table 2. *Internuclear distances* (Å) *and interbond angles* (°)

Fe—Cl(1)	2·2540 (14)	C(1)—O(1)	1·130 (7)
Fe—Cl(2)	2·2642 (14)	C(2)—O(2)	1·144 (7)
Fe—Cl(3)	2·2554 (15)	C(3)—O(3)	1·122 (6)
Fe—N(1)	2·035 (4)	C(4)—C(5)	1·408 (7)
N(1)—C(10)	1·140 (7)	C(4)—HC(41)	0·94 (5)
C(10)—C(11)	1·469 (7)	C(4)—HC(42)	0·99 (5)
Co—C(1)	1·831 (5)	C(5)—C(6)	1·418 (7)
Co—C(2)	1·832 (6)	C(5)—C(8)	1·516 (7)
Co—C(3)	1·837 (5)	C(6)—C(7)	1·420 (7)
Co—C(4)	2·077 (6)	C(6)—C(9)	1·504 (7)
Co—C(5)	2·076 (5)	C(7)—HC(71)	0·97 (5)
Co—C(6)	2·082 (5)	C(7)—HC(72)	0·85 (5)
Co—C(7)	2·082 (5)		

Cl(1)—Fe—Cl(2)	112·32 (5)	C(6)—Co—C(7)	39·90 (20)
Cl(1)—Fe—Cl(3)	116·40 (5)	Co—C(1)—O(1)	177·9 (5)
Cl(1)—Fe—N(1)	100·94 (13)	Co—C(2)—O(2)	177·0 (5)
Cl(2)—Fe—Cl(3)	111·76 (5)	Co—C(3)—O(3)	177·4 (5)
Cl(2)—Fe—N(1)	108·13 (13)	Co—C(4)—C(5)	70·2 (3)
Cl(3)—Fe—N(1)	106·22 (13)	Co—C(4)—HC(41)	105 (3)
Fe—N(1)—C(10)	170·6 (4)	Co—C(4)—HC(42)	119 (3)
N(1)—C(10)—C(11)	179·0 (6)	C(5)—C(4)—HC(41)	121 (3)
C(1)—Co—C(2)	101·27 (25)	C(5)—C(4)—HC(42)	123 (3)
C(1)—Co—C(3)	92·85 (24)	HC(41)—C(4)—HC(42)	111 (4)
C(1)—Co—C(4)	91·26 (23)	Co—C(5)—C(4)	70·2 (3)
C(1)—Co—C(5)	94·16 (22)	Co—C(5)—C(6)	70·3 (3)
C(1)—Co—C(6)	124·83 (22)	Co—C(5)—C(8)	125·4 (3)
C(1)—Co—C(7)	164·30 (23)	C(4)—C(5)—C(6)	116·6 (4)
C(2)—Co—C(3)	104·20 (24)	C(4)—C(5)—C(8)	121·7 (4)
C(2)—Co—C(4)	93·41 (24)	C(6)—C(5)—C(8)	121·6 (4)
C(2)—Co—C(5)	131·06 (22)	Co—C(6)—C(5)	69·9 (3)
C(2)—Co—C(6)	130·45 (22)	Co—C(6)—C(7)	70·0 (3)
C(2)—Co—C(7)	92·24 (23)	Co—C(6)—C(9)	126·2 (3)
C(3)—Co—C(4)	160·74 (23)	C(5)—C(6)—C(7)	116·0 (4)
C(3)—Co—C(5)	121·21 (21)	C(5)—C(6)—C(9)	122·1 (4)
C(3)—Co—C(6)	91·69 (21)	C(7)—C(6)—C(9)	121·7 (4)
C(3)—Co—C(7)	91·51 (22)	Co—C(7)—C(6)	70·1 (3)
C(4)—Co—C(5)	39·64 (20)	Co—C(7)—HC(71)	100 (3)
C(4)—Co—C(6)	70·63 (20)	Co—C(7)—HC(72)	119 (3)
C(4)—Co—C(7)	79·90 (22)	C(6)—C(7)—HC(71)	120 (3)
C(5)—Co—C(6)	39·88 (18)	C(6)—C(7)—HC(72)	111 (3)
C(5)—Co—C(7)	70·75 (20)	HC(71)—C(7)—HC(72)	123 (4)

* Lists of structure factors, H-atom positions and anisotropic thermal parameters have been deposited with the British Library Document Supply Centre as Supplementary Publication No. SUP 53518 (12 pp.). Copies may be obtained through The Technical Editor, International Union of Crystallography, 5 Abbey Square, Chester CH1 2HU, England.

unfortunately high e.s.d.'s associated with the structural study of (1) prevent detailed comparison.

In addition to a higher oxidation state resulting in shorter Co—CO distances (by dint of the smaller radius of Co^{3+} *versus* Co^{+}), both the overall charge on the metal complexes and the nature of the η-bonded ligand *trans* to the carbonyl functions could influence the Co—CO bond lengths. Thus, *if the formal metal oxidation states in both* (1) *and* (2) *were the same*, both the higher negative charge on (1) and the presence of an η-bonded ligand face composed of B atoms rather than C atoms might reasonably be expected to increase the electron density at the metal atom, resulting in greater Co—CO π back bonding and shorter Co—CO distances.

To an extent, the influence of the difference in overall charge between (1) and (2) on the extent of Co—CO back bonding can be assessed by consideration of CO stretching frequencies. The $\{M(CO)_3\}$ fragment has local C_{3v} symmetry, giving rise to C—O stretches of a_1 and e symmetry. Table 4 lists the 'a_1' and 'e' IR stretching frequencies for the family of d^6 complexes $[CpM(CO)_3]^n$ ($Cp = \eta$-C_5H_5; M = Fe, n = +1; M = Mn, n = 0; M = Cr, n = −1) and for (2) and (1). In moving from the (cationic) Fe complex to the (anionic) Cr complex the frequency of the a_1 stretch decreases by 170 cm^{-1} and that of the e stretch by 250 cm^{-1} (as more electron density is available for M—CO back bonding).

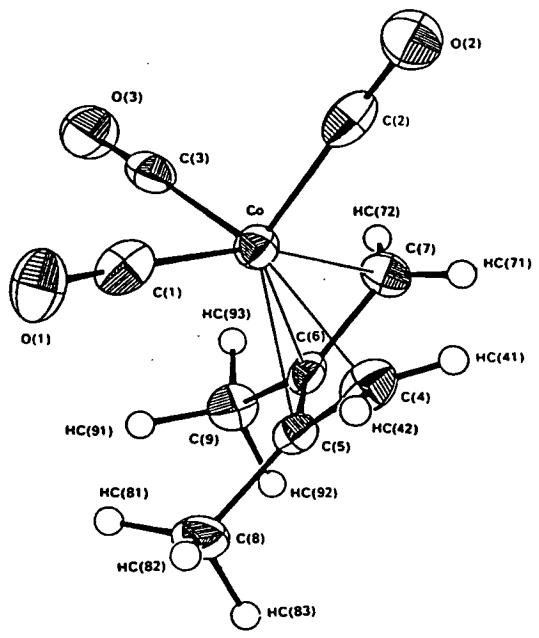

Fig. 1. Perspective view of, and atomic numbering scheme adopted for, the cation $[Co(C_6H_{10})(CO)_3]^+$ (50% thermal ellipsoids, except for H atoms which have an artificial radius of 0·1 Å for clarity).

Table 3. *Comparison of key molecular parameters* (Å, °) *for* (1) *and* (2)

	$[7,7,7\text{-}(CO)_3\text{-}7\text{-}CoB_{10}H_{12}]^-$ (1)	$[(CO)_3Co(dmbd)]^+$ (2)
Co—C(1,3)	1·802 (14)	1·834 (5)
Co—C(2)	1·763 (11)	1·832 (6)
C(1,3)—O(1,3)	1·134 (18)	1·126 (7)
C(2)—O(2)	1·165 (15)	1·144 (7)
C(1,3)—Co—C(2)	102·97 (58)	102·74 (25)
C(1)—Co—C(3)	95·58 (63)	92·85 (24)

Table 4. *Carbonyl IR stretching frequencies* (cm^{-1}) *in complexes containing* $\{M(CO)_3\}$ *fragments*

Complex	'a_1' stretch	'e' stretch	Reference
$[CpFe(CO)_3]^-$	2070	2127	Kochhar & Pettit (1966)
$[CpMn(CO)_3]$	2025	1945	Haas & Sheline (1967)
$[CpCr(CO)_3]^-$	1900	1776*	Ellis & Flum (1975)
$[(CO)_3Co(dmbd)]^+$ (2)	2130	2090*	This work
$[(CO)_3CoB_{10}H_{12}]^-$ (1)	2065	2010*	Macgregor, Yellowlees & Welch (1990)

* Components of 'e' stretch resolved; average value given.

In moving from the (cationic) (2) to the (anionic) (1), the changes are considerably smaller (65 and 80 cm^{-1}, respectively). This implies that considerably less electron density is available to the metal centre in (1) than is expected from overall charge considerations alone. Given that the non-carbonyl ligand in (1) is anticipated to be a somewhat stronger donor than that in (2) (Cowie, Hamilton, Laurie & Welch, 1990), this analysis of IR stretching frequencies appears to lend support to the idea that the metal atom in (1) *is* formally in a higher oxidation state than that in (2). Indeed, this result is fully consistent with analysis of the dimensions of the borane ligand in (1) (Macgregor, Yellowlees & Welch, 1990), and with the results of XANES studies on (1) in comparison to those on standard Co^{I} and Co^{III} compounds (Wynd, Macgregor, Gould, Taylor, Yellowlees & Welch, 1990).

Bond distances and angles within the metallabutadiene moiety of (2) are entirely consistent with those found in a large number of isoelectronic iron analogues (Herbstein & Reisner, 1977). As has previously been described by Immirzi (1974) for iron–butadiene systems, we find that the *syn* and *anti* H atoms of the dmbd ligand are displaced out of the C(4)C(5)C(6)C(7) plane, the former by (average) 0·172 Å away from Co, and the latter by (average) 0·516 Å towards Co.

As far as we can ascertain, the anion in the current study, $[FeCl_3(NCMe)]^-$, has not previously been structurally characterized. The environment around the Fe atom is slightly distorted from tetahedral; the Cl—Fe—Cl angles average 113·5 (1)°, whilst N—Fe—Cl averages 105·1 (2)°. The angle at the

acetonitrile N atom is significantly bent away from 180°, whilst the sequence N(1)–C(10)–C(11) is linear.

We thank the SERC for a research studentship (SAM), and the Callery Chemical Company for continued support of this project.

References

CHAUDRY, F. M. & PAULSON, P. L. (1974). *J. Organomet. Chem.* 69, C31–C32.

COWIE, J., HAMILTON, E. J. M., LAURIE, J. C. V. & WELCH, A. J. (1990). *J. Organomet. Chem.* 394, 1–13.

ELLIS, J. E. & FLUM, E. A. (1975). *J. Organomet. Chem.* 99, 263–268.

GOULD, R. O. & SMITH, D. E. (1986). *CADABS*. Program for data reduction. Univ. of Edinburgh, Scotland.

GOULD, R. O. & TAYLOR, P. (1986). *CALC*. Program for molecular geometry calculations. Univ. of Edinburgh, Scotland.

HAAS, H. & SHELINE, T. P. (1967). *J. Chem. Phys.* 47, 2996–3021.

HERBSTEIN, F. H. & REISNER, M. G. (1977). *Acta Cryst.* B33, 3304–3317.

IMMIRZI, A. (1974). *J. Organomet Chem.* 76, 65–71.

KOCKHAR, R. K. & PETTIT, R. (1966). *J. Organomet. Chem.* 6, 272–278.

MACGREGOR, S. A., YELLOWLEES, L. J. & WELCH, A. J. (1990). *Acta Cryst.* C46, 551–554.

MALLINSON, P. & MUIR, K. W. (1985). *J. Appl. Cryst.* 18, 51–53.

SHELDRICK, G. M. (1976). *SHELX76*. Program for crystal structure determination. Univ. of Cambridge, England.

SHELDRICK, G. M. (1986). *SHELX86*. Program for the solution of crystal structures. Univ. of Göttingen, Federal Republic of Germany.

WALKER, N. G. & STUART, D. (1983). *Acta Cryst.* A39, 158–166.

WYND, A. J., MACGREGOR, S. A., GOULD, R. O., TAYLOR, P., YELLOWLEES, L. J. & WELCH, A. J. (1990). Work in progress.